UNIVERSIDAD DE CHILE
FACULTAD DE CIENCIAS FÍSICAS Y MATEMÁTICAS
DEPARTAMENTO DE INGENIERÍA CIVIL

IMPROVED FINITE ELEMENT MODEL OF A TALL BUILDING IN SANTIAGO OF CHILE USING SEISMIC RECORDS

TESIS PARA OPTAR AL GRADO DE MAGÍSTER EN CIENCIAS DE LA INGENIERÍA, MENCIÓN INGENIERÍA ESTRUCTURAL, SÍSMICA Y GEOTÉCNICA

MEMORIA PARA OPTAR AL TÍTULO DE INGENIERO CIVIL

MATÍAS EDUARDO GARRIDO GAMBOA

PROFESOR GUÍA:
RUBÉN BOROSCHEK KRAUSKOPF

MIEMBROS DE LA COMISIÓN:
HAMED EBRAHIMIAN CHELEKHANE
CARLOS VENTURA ZAMORA

SANTIAGO DE CHILE
2021

RESUMEN DE LA MEMORIA PARA OPTAR AL GRADO DE MAGÍSTER EN CIENCIAS DE LA INGENIERÍA MENCIÓN INGENIERÍA ESTRUCTURAL, SÍSMICA Y GEOTÉCNICA Y AL TÍTULO DE INGENIERO CIVIL
POR: MATÍAS EDUARDO GARRIDO GAMBOA
FECHA: AGOSTO 2021
PROF. GUÍA: RUBÉN BOROSCHEK KRAUSKOPF

MODELO DE ELEMENTOS FINITOS MEJORADO DE UN EDIFICIO ALTO EN SANTIAGO DE CHILE UTILIZANDO REGISTROS SISMICOS

Históricamente los modelos estructurales utilizados para el diseño estructural se han desarrollado utilizando parámetros consensuados (el amortiguamiento, el nivel de agrietamiento de elementos de hormigón armado, la magnitud y distribución de masas y acciones, etc.). Algunos de estos parámetros han sido confirmados en ensayos de laboratorio y en los pocos edificios instrumentados que han estado bajo el efecto de sismos severos. Por mucho tiempo fue casi imposible ajustar directamente los parámetros básicos que usamos en los modelos (masa, rigidez, y disipación). Se tenía antecedentes de respuesta (amplitudes de aceleración, desplazamiento, etc.), de parámetros modales medidos (periodos, forma y amortiguamientos modales), y el ajuste para determinar los parámetros básicos que generaban esta condición se realizaba por prueba y error. Esta labor arrojaba cientos de posibles modelos que podían cumplir con la respuesta observada.

El procedimiento utilizado en este trabajo de investigación está basado en el trabajo de Ebrahimian *et al.*, 2018 [1], es robusto y permite determinar con precisión los parámetros básicos que dan un modelo apropiado, pero además informa la incertidumbre asociada a ellos. Se abre la posibilidad de mejorar nuestras técnicas de modelamiento utilizando los parámetros que definimos en el diseño. Para validar la metodología se utiliza como ejemplo el Edificio de la Cámara Chilena de la Construcción (CChC), que cuenta desde 1997 con 12 sensores uniaxiales de aceleración, 4 de ellos ubicados en su base y el resto distribuido en otros tres pisos de la estructura. Desde su instalación, el sistema de sensores ha registrado la respuesta dinámica del edificio para temblores leves, de mediana intensidad, y de movimiento fuerte.

El trabajo de tesis presentado tiene como objetivo mejorar las predicciones del modelo de elementos finitos (EF) del Edificio de la Cámara Chilena de la Construcción (CChC) a través de la actualización de sus parámetros base (módulo de elasticidad, distribución de masas, etc.). Para lo anterior, se utiliza una técnica novedosa que consiste en la actualización del modelo de elementos finitos. La idea detrás del algoritmo consiste en modelar la incertidumbre de los parámetros del modelo con una función de distribución de probabilidad (PDF). Dicha PDF se actualiza en un proceso iterativo con el fin de disminuir la discrepancia entre la respuesta real de la estructura y la estimada por el modelo numérico. Los resultados muestran que el algoritmo satisfactoriamente logra reducir las discrepancias entre las mediciones y la respuesta del modelo numérico respecto al modelo inicial. Esta metodología es un gran avance y una herramienta muy útil en la profesión.

RESUMEN DE LA MEMORIA PARA OPTAR AL GRADO DE MAGÍSTER EN CIENCIAS DE LA INGENIERÍA MENCIÓN INGENIERÍA ESTRUCTURAL, SÍSMICA Y GEOTÉCNICA Y AL TÍTULO DE INGENIERO CIVIL
POR: MATÍAS EDUARDO GARRIDO GAMBOA
FECHA: AGOSTO 2021
PROF. GUÍA: RUBÉN BOROSCHEK KRAUSKOPF

IMPROVED FINITE ELEMENT MODEL OF A TALL BUILDING IN SANTIAGO OF CHILE USING SEISMIC RECORDS

Historically the structural models used for structural design have been developed using accepted parameters (damping, the level of cracking of reinforced concrete elements, the magnitude and distribution of masses and actions, among others). Some model parameters have been confirmed in laboratory tests and in the few instrumented buildings that have been under the effect of severe earthquakes. For a long time, estimate the parameters that we use in the models (mass, stiffness, and dissipation) was hard work. The previous engineers have backgrounds about the response (accelerations amplitude, displacements, among others), the modal parameters (modal periods, mode shapes, and modal damping). The model parameters that allowed the above conditions were selected through the trial and error process. From this procedure, hundreds of possible models were obtained that arrive at the observed response.

The current thesis work continues the research conducted by Ebrahimian *et al.*, 2018 [1] on the parameters' estimation for non-linear models. The algorithm proposed is robust and determines with precision the basic parameters to derive an appropriate model. In addition, notice the uncertainties associated with the parameters. The possibility to improve our model techniques using the model parameters defined in structural design standards stays open. The methodology is validated using the Chilean Chamber of Construction Building (CChC). Since 1997, a monitoring network with 12 uniaxial accelerometers located at four different levels of the structure (including its base) has strong-motion records and ambient records of the building. Since its installation, the sensor system has recorded the building's dynamic response to slight, medium-intensity, and strong-motion earthquakes.

The thesis work presented aims to improve the predictions of the finite element model (EF) of the Chilean Chamber of Construction Building (CChC) through updating its parameters (modulus of elasticity, mass distribution, etc.). For the above, a novel technique is used that consists of update the finite element model. The idea behind the algorithm is to model the uncertainty of the model parameters with a probability distribution function (PDF). The PDF is updated in an iterative process to reduce the discrepancy between the actual response of the structure and that estimated by the numerical model. The results show that the algorithm successfully manages to decrease the misfit between the measurements and the response of the numerical model. This methodology is an innovative and practical tool in the profession.

A mis dos ángeles en la Tierra
mis padres...

Acknowledgment

I would like to give my sincere gratitude to my guide in this work, Professor Rubén Boroschek. His constant support, confidence, patience, and experience in the field were fundamental to carrying out this work. In addition, the advice delivered served me for my professional growth during the stage. I am very grateful for the time dedicated and the opportunity it gave me to develop this work, which I was able to acquire a large number of tools.

On the other hand, I want to thank Professor Hamed Ebrahimian, whom I had the opportunity to meet at this stage. His experience, time, and his classes were fundamental to putting theory into practice. I also appreciate the chance to meet other students from other parts of the world. Which helped me open my mind to pursue new opportunities and the motivation to continue studying. Among the students, I want to highlight my future collaborator, Sina Zolfaghary. We started this world of Bayesian filters together. He was great support for the development of the programming codes and a great co-worker.

Finally, I would like to thank my parents, Nelly and Juan Carlos, for their unlimited support and affection at each stage of this process. Each achievement of my life I owe to them. To my brothers, Martín and Carlos, for the good times, we had, and that each one helped me in his own way. Also, my sincere appreciation to my lifelong friends, which this path gifted me. My best friends Danko, Tomás, Gastón, and Gabriel... thanks for accompanying me to school and to university, and for good times. Finally, to the lovely people I met in the final stage of this journey. I love you so much.

Table of Contents

List of Tables

List of Figures

Chapter 1

Introduction

1.1. Introduction and Motivation

All structures, including infrastructures such as bridges, roads, and buildings, are frequently disturbed by vibrations. These vibrations may cause changes in the physical and mechanical properties of the structural elements. In the field of structural engineering, systems identification (SID) refers to methods and techniques that allow the identification of these structures' properties, using input-output or output-only data [2, 1]. Researchers have used SID methods to study the changes in the properties of structures for different types of disturbances. For example, Boroschek *et al.* identified the variations in the modal parameters of the Chamber Chilean of Construction building under environmental conditions [3, 4] and for seismic events [5, 6], using accelerations records measured in the building. This study concluded that environmental variables, such as temperature, humidity, wind, affect the modal properties, which in the case of periods, reaches 1-2 % variability, 7 % for heavy rains and winds, and 4-9 % for slight and moderate earthquakes in the absence of damage.

1.1.1. Systems Identification techniques applied in Civil Engineering

Chile is considered a natural laboratory due to its high seismicity, which has allowed the observation of the structural response of buildings, bridges, ports, among other structures. The large number of seismic events has been the primary motivation to instrument different structures with sensors and study their structural response. The reader is referred to Boroschek *et al.* [6, 7, 8] and Moroni *et al.* [9, 10] for an in-depth literature survey on this subject, which presents results associated with the dynamic response of the structures for different seismic events. One of the most important seismic events was recorded on February 27, 2010, hereinafter called the 27F event. Chile was affected by an earthquake of magnitude 8.8, whose epicenter was located 43 kilometers south-west of the town of Cobquecura, VIII Region [11]. The National Accelerometer Network of the Civil Engineering Department(RENADIC) recorded ground accelerations of over 0.50g and durations of over 120 seconds. Also, the coastal areas were affected by earthquakes and tsunamis. The event damaged roads, train tracks, ports, airports, and buildings due to the effects of ground vibrations and site liquefaction [12, 13, 14].

System identification (SID) refers to methods and techniques used to identify a characteris-

tics model of structures using input-output or output-only data [2, 1]. The SID has played a fundamental role in detecting changes of state in structural response. Extensive research efforts have entered into the framework of Structural Health Monitoring (S.H.M.) implementing techniques that enable the detection of such damage to structures [15]. Moreover, many recent studies have been conducted in this area, e.g. Doebling *et al.* 1996 [16, 17]; Carden & Fanning, 2004 [18]; Yan *et al.*, 2007 [19]; Caroca, 2012 [20]; and Villalpando, 2019 [21].

System identification can be classified mainly into the frequency domain and time domain-based methods [2]. Both families of methods analyze the structures dynamic response through a continuous monitoring of their vibrations. Some of the identification methods used are Power Spectral Density (PSD), Multiple Input – Multiple Output (MIMO), Stochastic Subspace Identification (SSI), among others [3, 6, 22, 23]. These methods allow the estimation of the systems' modal properties, that is, vibration frequencies, modal damping ratios, and mode shapes. In theory, these properties are time-invariant for linear elastic systems. The previous techniques can be extended to non-linear behavior structures, where modal properties are time-variant, through methods based on estimation windows [5, 24].

1.1.2. Finite Element Model Updating Techniques

Another approach used in the field of system identification are algorithms based on non-linear or linear finite element (FE) model updating in the time of frequency domain. Model updating seeks to improve the finite element model, reducing the discrepancy between the real structure measurements and the FE-predicted response. Several methods have been proposed and employed for FE model updating. Different approaches are studied in Alkayem *et al.*, 2018 [25] and are summarized in Figure 1.1.

The FE model updating techniques use the input-output data or only the system's output to identify the parameters that model the non-linearity in the structural response. A family of these methods uses a Bayesian approach, where the parameters' uncertainties are modeled as a probability distribution function (PDF) and propagate with different techniques. Some of these methods are Kalman Filter (KF) [26, 27], the Extended Kalman Filter (EKF) [2, 28], the Unscented Kalman Filter (UKF) [29], and the methods based on Markov Chain Monte Carlo (MCMC) simulation [30, 31]. Finally, Ebrahimian *et al.* developed a Bayesian FE model updating method for joint input-parameter estimation. The method was validated for numerical simulation cases [2, 1].

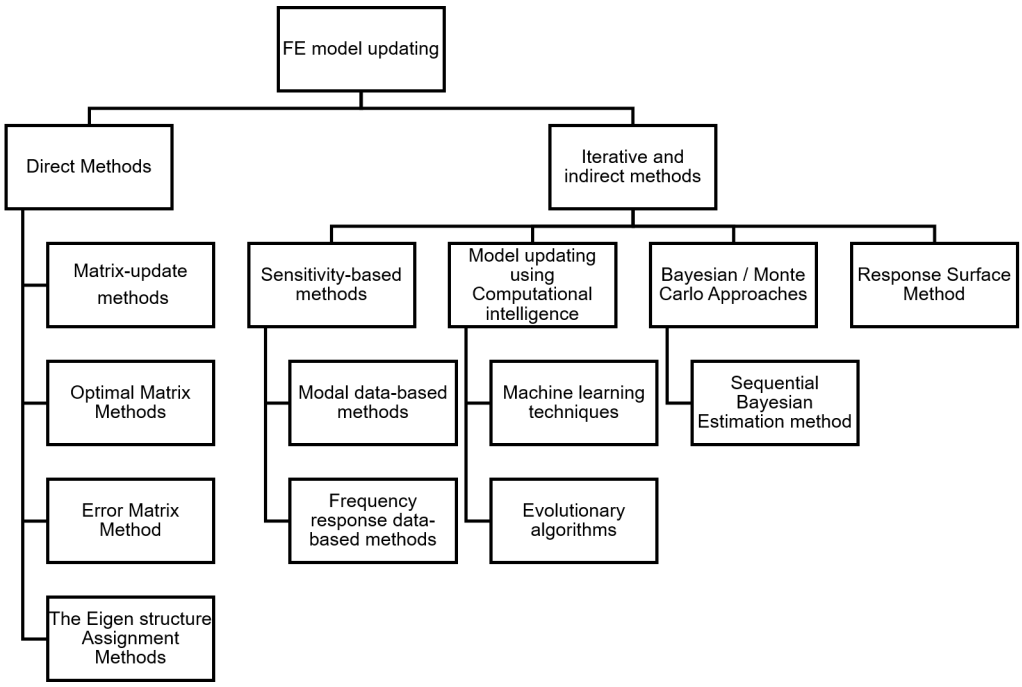

Figure 1.1: FE model updating approaches (Figure adapted from ref. [25]).

The present work aims to improve the Finite Element Model of the Chilean Chamber of Construction (CChC) Building located in Santiago, Chile, using the sequential FE model updating algorithm proposed by Ebrahimian *et al.* [1].

The CChC Building has a structure of concrete walls, typically used in Chile, and since 1997 to date, has 12 uni-axial accelerometers. Lazcano *et al.* [3] between the months of April-December 2007, compiled the acceleration records in the CChC Building, and evaluated the relationship between rain, temperature, humidity and wind and the modal parameters of the structure. They concluded the frequencies' variations under environmental conditions reach 7 % for heavy rains and winds, and 1 % for other weather conditions [3]. Carreño *et al.* [5] identified the variations on the modal parameters of the building during earthquakes of low to high intensity and concluded that for the 27F earthquake, the frequencies of the first two translational modes decreased 35 % during the seismic event, and there was a permanent decrease of 18 % on average compared to the initial values [5].

1.2. Objectives

1.2.1. General Objective

The objective of this thesis is to improve the Finite Element Model prediction of a tall building located in Santiago, Chile, using accelerations records and the Sequential Finite Element (FE) Model Updating technique proposed by Ebrahimian *et al.* [1].

1.2.2. Specific Objectives

a) Review the literature on model updating algorithms.

b) Implement the sequential FE model updating technique proposed by Ebrahimian *et al.* [1].

c) Review previous studies of the CChC Building and convert the FE model presented in Boroschek and Yáñez, 2000 [7] to the open-source FE analysis software framework OpenSees [32].

d) To identify the building's modal parameters for the seismic records used in the study through the algorithm Multi-Output Error State Space (MOESP) [33].

e) Carry out an identifiability assessment to select the FE model parameters that provide more information on the structural response given the available data set [34].

f) Identify the set of model parameters that will reduce the difference between the accelerations measured in the structure and the prediction of the FE model for each available seismic event, and study the variability of these parameters.

1.3. Dissertation outline

This research work has been divided into seven chapters. The content of each chapter is described below.

- Chapter 1, describes the research's objectives and the outline of each chapter.
- Chapter 2, the model updating technique theory used in the present dissertation is described and a simulation case is presented for algorithm validation.
- Chapter 3, the structure under study and the instrumentation system is described. The structural details are commented and the structural plans are presented.
- Chapter 4, the seismic record data obtained from the CChC Building instrumentation system is presented. The maximum accelerations, magnitude, intensity, epicenters, and hypocenters depths are summarized to characterize and classify seismic events. The Spectrogram and MOESP identification techniques are used to identify the modal parameters of the building in the absence of damage and with damage.
- Chapter 5, the finite element model of the building is presented and the assumptions are described. The process used to export the FE model to OpenSees and their validation is presented. In addition, an identifiability assessment is performed to a selection of parameters to estimate.
- Chapter 6, the results and their analysis are presented. The variability of the parameters obtained with the algorithm for seismic events between 1997-2014 is presented. Along with the relative root-mean-square error (RRMSE) between the measurements and the FE model's prediction.
- Chapter 7, the algorithm performance for different seismic earthquakes are commented on. Finally, recommendations are given to continue with the work.

Chapter 2

Sequential Finite Element Model Updating for Joint estimation of Parameters and Input Forces

This chapter presents the sequential finite element model update theory (also called the posterior maximum sequential estimation method) proposed by Ebrahimian *et al.* [1] to improve model prediction of finite elements using acceleration records. The idea behind updating the FE model with Bayesian filters is to characterize the uncertainties of the FE model parameters and the input forces with a probability distribution function (PDF). Then, the uncertainties of the model parameters and the input forces are propagated through the model to calculate the simulated response. Finally, the stochastic prediction of the FE model is compared with the real structural response, and then the parameter estimates and the input estimates are sequentially updated using Bayesian inferences.

2.1. Output-Only Non-linear system and input identification

The equation of motion of the finite element model at time step i ($i = 1, 2, ..., k$, where k denotes the total number of time steps) is expressed as

$$\boldsymbol{M}(\boldsymbol{\theta})\,\ddot{\boldsymbol{q}}_i(\boldsymbol{\theta}) + \boldsymbol{C}(\boldsymbol{\theta})\,\dot{\boldsymbol{q}}_i(\boldsymbol{\theta}) + \boldsymbol{\gamma}_i(\boldsymbol{q}_{1:i}(\boldsymbol{\theta}), \boldsymbol{\theta}) = \boldsymbol{f}_i(\boldsymbol{\theta}) \tag{2.1}$$

where $\boldsymbol{M}(\boldsymbol{\theta}) \in \mathbb{R}^{n_{dof} \times n_{dof}}$ = mass matrix; $\boldsymbol{C}(\boldsymbol{\theta}) \in \mathbb{R}^{n_{dof} \times n_{dof}}$ = damping matrix; $\boldsymbol{\gamma}_i(\boldsymbol{q}_{1:i}(\boldsymbol{\theta}), \boldsymbol{\theta}) \in \mathbb{R}^{n_{dof} \times 1}$ = history-dependent internal resisting force vector; $\ddot{\boldsymbol{q}}_i(\boldsymbol{\theta})$, $\dot{\boldsymbol{q}}_i(\boldsymbol{\theta})$, $\boldsymbol{q}_i(\boldsymbol{\theta}) \in \mathbb{R}^{n_{dof} \times 1}$ = nodal acceleration, velocity, and displacement response vectors, respectively; $\boldsymbol{\theta} \in \mathbb{R}^{n_\theta \times 1}$ = vector of unknown FE model parameters; $\boldsymbol{f}_i(\boldsymbol{\theta}) \in \mathbb{R}^{n_{dof} \times 1}$ = dynamic load vector; n_{dof} = number of degrees of freedom; and n_θ = number of unknown parameters. In the case of uniform seismic excitation (rigid base), $\boldsymbol{f}_i(\boldsymbol{\theta}) = -\boldsymbol{M}(\boldsymbol{\theta})\boldsymbol{L}\ddot{\boldsymbol{u}}_i^g$, where $\boldsymbol{L} \in \mathbb{R}^{n_{dof} \times n_{\ddot{u}^g}}$ = base acceleration influence matrix and $\ddot{\boldsymbol{u}}_i^g \in \mathbb{R}^{n_{\ddot{u}^g} \times 1}$ denotes the seismic input ground acceleration vector. Equation 2.1 indicates that the FE model prediction depends on an unknown parameter vector and the input load vector. The nodal response vector at each time step can be determined using a recursive numerical integration rule, such as the Newmark-beta method, obtaining at each time step the non-linear system equations that can be solved iteratively

with the Newton-Raphson method [35]. Therefore, the nodal response vector of the FE model at time step i can be expressed as a non-linear function of the FE model parameter vector ($\boldsymbol{\theta}$), and time history of the input ground acceleration vector $\left(\ddot{\boldsymbol{u}}_{1:i}^{g} = \left[(\ddot{\boldsymbol{u}}_{1}^{g})^{T}, (\ddot{\boldsymbol{u}}_{2}^{g})^{T}, ..., (\ddot{\boldsymbol{u}}_{i}^{g})^{T}\right]^{T}\right)$:

$$\hat{\boldsymbol{y}}_i = \boldsymbol{h}_i\left(\boldsymbol{\theta}, \ddot{\boldsymbol{u}}_{1:i}^{g}\right) \tag{2.2}$$

where $\hat{\boldsymbol{y}}_i \in \mathbb{R}^{n_y \times 1}$ denotes the structural response quantity predicted by the FE model at time step i ($i = 1, 2, ..., k$), n_y is the number of observation points (or the number of sensors) deployed in the structure, and $\boldsymbol{h}_i(...)$ is the response function of the FE model at time step i, which, in general, is a non-linear function of $\boldsymbol{\theta}$ and $\ddot{\boldsymbol{u}}_{1:i}^{g}$. The measured response vector of the structure, $\boldsymbol{y}_i$, is related to the FE-predicted responses, $\hat{\boldsymbol{y}}_i$, as ([2, 1])

$$\boldsymbol{v}_i\left(\boldsymbol{\theta}, \ddot{\boldsymbol{u}}_{1:i}^{g}\right) = \boldsymbol{y}_i - \hat{\boldsymbol{y}}_i \tag{2.3}$$

where $\boldsymbol{v}_i \in \mathbb{R}^{n_y \times 1}$ is the simulation error vector, which accounts for the misfit between the measured and FE-predicted responses of the structure. The FE model misfit stems from the output measurement noise, parameters uncertainties, and model uncertainties. The model uncertainties are referred to geometric simplifications adopted when devising the finite element model, and the assumptions made when defining boundary conditions (e.g., soil-structure interaction), which result in an inherent discrepancy between the FE model prediction and the measured structural response [36]. The uncertainties in the finite element model parameters are because these values are sensitive to weather conditions, operational demands, or damage presence [4, 6, 8]. In the absence of model uncertainties, the simulation error due to model parameter uncertainty is minimized through the parameter estimation process, and $\boldsymbol{v}_i$ in Equation 2.3 accounts only for the measurement noise.

Given an unbiased estimate $\boldsymbol{\theta}$ and $\ddot{\boldsymbol{u}}_{1:i}^{g}$, and assuming that the simulation error can be modeled as a stationary, zero-mean, and independent Gaussian white noise process [37], the likelihood function is given by,

$$p\left(\boldsymbol{y}_i|\boldsymbol{\theta}, \ddot{\boldsymbol{u}}_{1:i}^{g}\right) = p\left(\boldsymbol{v}_i\right) \tag{2.4}$$

$$\begin{aligned} p\left(\boldsymbol{y}_i|\boldsymbol{\theta}, \ddot{\boldsymbol{u}}_{1:i}^{g}\right) &= \frac{1}{(2\pi)^{n_y/2}\,|\boldsymbol{R}|^{1/2}}\, e^{-\frac{1}{2}\boldsymbol{v}_i^{T}\,\boldsymbol{R}^{-1}\,\boldsymbol{v}_i} \\ &= \frac{1}{(2\pi)^{n_y/2}\,|\boldsymbol{R}|^{1/2}}\, e^{-\frac{1}{2}\left(\boldsymbol{y}_i - \boldsymbol{h}_i\left(\boldsymbol{\theta}, \ddot{\boldsymbol{u}}_{1:i}^{g}\right)\right)^{T}\,\boldsymbol{R}^{-1}\,\left(\boldsymbol{y}_i - \boldsymbol{h}_i\left(\boldsymbol{\theta}, \ddot{\boldsymbol{u}}_{1:i}^{g}\right)\right)} \end{aligned} \tag{2.5}$$

where $|\boldsymbol{R}|$ denotes the determinant of the diagonal matrix $\boldsymbol{R} \in \mathbb{R}^{n_y \times n_y}$, which is the (time-invariant) covariance matrix of the simulation error vector (i.e., $\boldsymbol{R} = E\left(\boldsymbol{v}_i \boldsymbol{v}_i^{T}\right)$, $\forall i$) and $p\left(\boldsymbol{y}_i|\boldsymbol{\theta}, \ddot{\boldsymbol{u}}_{1:i}^{g}\right)$ is referred to as the likelihood function. In the Bayesian optimal estimation for output-only non-linear systems algorithm proposed by Ebrahimian *et al.* [1], the FE model parameter vector and the values of the seismic input ground acceleration at each time step are time-invariant unknown parameters, which are modeled with probability distribution functions (PDF). FE model updating aims to find and estimate the unknown parameters vector (here, the model parameters and input actions), such that their joint posterior PDF, given the measured output response of the structure, is maximized. This is referred to as the maximum a posterior (MAP) estimate.

$$\left(\hat{\boldsymbol{\theta}}, \hat{\ddot{\boldsymbol{u}}}^g_{1:k} | \boldsymbol{y}_{1:k}\right)_{\text{MAP}} = \underset{\left(\boldsymbol{\theta}, \ddot{\boldsymbol{u}}^g_{1:k}\right)}{\arg\max}\ p\left(\boldsymbol{\theta}, \ddot{\boldsymbol{u}}^g_{1:k} | \boldsymbol{y}_{1:k}\right) \tag{2.6}$$

in which $\boldsymbol{y}_{1:k} = \left[\boldsymbol{y}_1^T, \boldsymbol{y}_2^T, ..., \boldsymbol{y}_k^T\right]^T$, is the time history vector of the measured responses of the structure.

2.2. Sequential Finite Element Model Updating using Model Linearization

The MAP estimation problem is solved with a sequential estimation approach that improves the computational efficiency compared with methods that used a batch optimization algorithm [1]. The scheme proposed by Ebrahimian *et al.* [2, 1] consists of solving the estimation problem iteratively at each estimation window to estimate the posterior mean vector and covariance matrix of the unknown model parameters (which include the input time history). For the last, the posterior joint PDF of the FE model parameters and base acceleration discrete-time history is maximized at each estimation window using an iterative linearization approach. Once reached the convergence, the posterior mean estimates and covariance matrix of the estimation parameters are then transferred to the next estimation window and used as prior information to solve the MAP estimation problem at the subsequent estimation window. The sequential MAP estimation method is equivalent to a sequential iterative Extended Kalman Filter (EKF) method [2, 1].

Using Bayes' rule, the posterior joint PDF of the FE model parameters and input ground motion (Equation 2.6) can be rewritten as follows

$$p\left(\boldsymbol{\theta}, \ddot{\boldsymbol{u}}^g_{1:k} | \boldsymbol{y}_{1:k}\right) = \frac{p\left(\boldsymbol{y}_{1:k} | \boldsymbol{\theta}, \ddot{\boldsymbol{u}}^g_{1:k}\right) p\left(\boldsymbol{\theta}, \ddot{\boldsymbol{u}}^g_{1:k}\right)}{p\left(\boldsymbol{y}_{1:k}\right)} \tag{2.7}$$

where $p\left(\boldsymbol{y}_{1:k} | \boldsymbol{\theta}, \ddot{\boldsymbol{u}}^g_{1:k}\right) = \prod_{i=1}^{k} p\left(\boldsymbol{v}_i\right)$, $p\left(\boldsymbol{\theta}, \ddot{\boldsymbol{u}}^g_{1:k}\right)$ is the prior joint PDF of the unknown model parameters including the unknown input ground motion, and $p\left(\boldsymbol{y}_{1:k}\right)$ is a normalizing constant. Considering the above, an extended unknown parameter vector is defined as $\boldsymbol{\psi} = \left[\boldsymbol{\theta}^T, \left(\ddot{\boldsymbol{u}}^g_{1:k}\right)^T\right]^T$, then, the Equation 2.7 is rewritten as

$$p\left(\boldsymbol{\psi} | \boldsymbol{y}_{1:k}\right) = \frac{p\left(\boldsymbol{y}_{1:k} | \boldsymbol{\psi}\right) p\left(\boldsymbol{\psi}\right)}{p\left(\boldsymbol{y}_{1:k}\right)} \tag{2.8}$$

Assume that m^{th} estimation window spans from time step t_1^m to time step t_2^m, where the window size is defined as $t_l = t_2^m - t_1^m$, the extended unknown parameter vector is redefined as $\boldsymbol{\psi}_m = \left[\boldsymbol{\theta}^T, \left(\ddot{\boldsymbol{u}}^{g,m}_{t_1^m:t_2^m}\right)^T\right]^T$, where $\boldsymbol{\psi}_m \in \mathbb{R}^{(n_\theta + t_l \times n_{\ddot{u}^g})}$. Furthermore considering that $p\left(\boldsymbol{y}_{t_1^m:t_2^m} | \boldsymbol{\psi}_m\right) = \prod_{i=t_1^m}^{t_2^m} p(\boldsymbol{v}_i)$, and assuming a Gaussian distribution for the prior joint PDF, the natural logarithm of the posterior joint PDF of the extended unknown parameter vector can be derived as [1]

$$\log\left(p\left(\boldsymbol{\psi}_m|\boldsymbol{y}_{t_1^m:t_2^m}\right)\right) = c + \log\left(p\left(\boldsymbol{y}_{t_1^m:t_2^m}|\boldsymbol{\psi}_m\right)\right) + \log\left(p\left(\boldsymbol{\psi}_m\right)\right) \tag{2.9}$$

where $c = -\log\left(p\left(\boldsymbol{y}_{t_1^m:t_2^m}\right)\right)$ is a normalization constant. In this equation, the time history of the base acceleration from time step 1 to $t_1^m - 1$, that is, $\ddot{\boldsymbol{u}}^{g,m}_{1:t_1^m-1}$, is assumed to be deterministic and equal to the mean estimates obtained from the previous estimation sequences. When Equation 2.5 is substituted for the likelihood function into Equation 2.9 and a Gaussian distribution for the prior joint PDF is assumed, it follows that

$$\begin{aligned}\log\left(p\left(\boldsymbol{\psi}_m|\boldsymbol{y}_{t_1^m:t_2^m}\right)\right) = k_o \ ... \\ -\frac{1}{2}\left(\boldsymbol{y}_{t_1^m:t_2^m} - \boldsymbol{h}_{t_1^m:t_2^m}\left(\boldsymbol{\psi}_m, \ddot{\boldsymbol{u}}^g_{1:t_1^m-1}\right)\right)^T \widetilde{\boldsymbol{R}}^{-1}\left(\boldsymbol{y}_{t_1^m:t_2^m} - \boldsymbol{h}_{t_1^m:t_2^m}\left(\boldsymbol{\psi}_m, \ddot{\boldsymbol{u}}^g_{1:t_1^m-1}\right)\right) \ ... \\ -\frac{1}{2}\left(\boldsymbol{\psi}_m - \hat{\boldsymbol{\psi}}_m^-\right)^T\left(\hat{\boldsymbol{P}}^-_{\psi,m}\right)^{-1}\left(\boldsymbol{\psi}_m - \hat{\boldsymbol{\psi}}_m^-\right)\end{aligned} \tag{2.10}$$

where k_o is a constant, $\hat{\boldsymbol{\psi}}_m^-$ and $\hat{\boldsymbol{P}}^-_{\psi,m}$ are the prior mean vector and the covariance matrix of the extended unknown parameter vector at the m^{th} estimation window. $\widetilde{\boldsymbol{R}} \in \mathbb{R}^{(t_l \times n_y)\times(t_l \times n_y)}$ is a block-diagonal matrix, in which the diagonals denote the simulation error covariance matrix $\boldsymbol{R}$.

$$\widetilde{\boldsymbol{R}} = \begin{bmatrix} (\boldsymbol{R})_{n_y\times n_y} & \boldsymbol{0} & ... & \boldsymbol{0} \\ \boldsymbol{0} & (\boldsymbol{R})_{n_y\times n_y} & \vdots & \boldsymbol{0} \\ \vdots & \vdots & \ddots & \vdots \\ \boldsymbol{0} & \boldsymbol{0} & \cdots & (\boldsymbol{R})_{n_y\times n_y} \end{bmatrix}_{(t_l\times n_y)\times(t_l\times n_y)} \tag{2.11}$$

To find the MAP estimate of $\boldsymbol{\psi}_m$, the posterior joint PDF presented in Equation 2.9 is maximized, that is, $\partial \log\left(p\left(\boldsymbol{\psi}_m|\boldsymbol{y}_{t_1^m:t_2^m}\right)\right)/\partial\boldsymbol{\psi}_m = \boldsymbol{0}$. Therefore,

$$\begin{aligned}\left(\frac{\partial \boldsymbol{h}_{t_1^m:t_2^m}\left(\boldsymbol{\psi}_m, \hat{\ddot{\boldsymbol{u}}}^g_{1:t_1^m-1}\right)}{\boldsymbol{\psi}_m}\right)^T \widetilde{\boldsymbol{R}}^{-1}\left(\boldsymbol{y}_{t_1^m:t_2^m} - \boldsymbol{h}_{t_1^m:t_2^m}\left(\boldsymbol{\psi}_m, \hat{\ddot{\boldsymbol{u}}}^g_{1:t_1^m-1}\right)\right) - ... \\ \left(\hat{\boldsymbol{P}}^-_{\psi,m}\right)^{-1}\left(\boldsymbol{\psi}_m - \hat{\boldsymbol{\psi}}_m^-\right) = \boldsymbol{0}\end{aligned} \tag{2.12}$$

Using the first-order Taylor approximation of $\boldsymbol{h}_{t_1^m:t_2^m}\left(\boldsymbol{\psi}_m, \hat{\ddot{\boldsymbol{u}}}^g_{1:t_1^m-1}\right)$ at $\hat{\boldsymbol{\psi}}_m^-$, its possible solve iteratively the Equation 2.12 as

$$\begin{aligned}\boldsymbol{h}_{t_1^m:t_2^m}\left(\boldsymbol{\psi}_m, \hat{\ddot{\boldsymbol{u}}}^g_{1:t_1^m-1}\right) \approx \boldsymbol{h}_{t_1^m:t_2^m}\left(\hat{\boldsymbol{\psi}}_m^-, \hat{\ddot{\boldsymbol{u}}}^g_{1:t_1^m-1}\right) + ... \\ \left.\frac{\partial \boldsymbol{h}_{t_1^m:t_2^m}\left(\boldsymbol{\psi}_m, \hat{\ddot{\boldsymbol{u}}}^g_{1:t_1^m-1}\right)}{\partial\boldsymbol{\psi}_m}\right|_{\boldsymbol{\psi}_m=\hat{\boldsymbol{\psi}}_m^-}\left(\boldsymbol{\psi}_m - \hat{\boldsymbol{\psi}}_m^-\right) + \text{H.O.T.}\end{aligned} \tag{2.13}$$

The matrix $\left.\frac{\partial \boldsymbol{h}_{t_1^m:t_2^m}\left(\boldsymbol{\psi}_m, \hat{\ddot{\boldsymbol{u}}}^g_{1:t_1^m-1}\right)}{\partial\boldsymbol{\psi}_m}\right|_{\boldsymbol{\psi}_m=\hat{\boldsymbol{\psi}}_m^-} \in \mathbb{R}^{(t_l\times n_y)\times n_\theta}$ represents the FE response sensitivities with respect to the extended unknown parameter vector, evaluated at the prior mean values. This matrix is denoted by $\boldsymbol{C}$ hereafter. Substituting Equation 2.13 in Equation 2.12, neglecting the higher order terms of the first-order approximation equation, the MAP estimate of $\boldsymbol{\psi}_m$ is equal to [1]

$$\hat{\boldsymbol{\psi}}_m^+ = \hat{\boldsymbol{\psi}}_m^- + \boldsymbol{K}\left(\boldsymbol{y}_{t_1^m:t_2^m} - \boldsymbol{h}_{t_1^m:t_2^m}\left(\hat{\boldsymbol{\psi}}_m^-, \hat{\ddot{\boldsymbol{u}}}^g_{1:t_1^m-1}\right)\right) \tag{2.14}$$

in which $\boldsymbol{\psi}_m^+$ is the posterior mean estimate of $\boldsymbol{\psi}_m$, $\boldsymbol{K}$ is the Kalman gain matrix [26], and is calculate as [1]

$$\boldsymbol{K} = \left(\boldsymbol{C}^T\widetilde{\boldsymbol{R}}^{-1}\boldsymbol{C} + \left(\hat{\boldsymbol{P}}^-_{\psi,m}\right)^{-1}\right)^{-1}\boldsymbol{C}^T\widetilde{\boldsymbol{R}}^{-1} \tag{2.15}$$

An iteratively prediction-correction procedure is performed using the posterior mean estimate ($\boldsymbol{\psi}_m^+$) aims to improve the FE model predictions. As mention above, the process is equivalent to the Extended Kalman Filter (EKF) method for parameter-only estimation. Following the EKF procedure, the prior covariance matrix $\hat{\boldsymbol{P}}^-_{\psi,m}$ is updated to the posterior covariance matrix $\hat{\boldsymbol{P}}^+_{\psi,m}$ at each prediction-correction iteration as in [1, 26]

$$\hat{\boldsymbol{P}}^+_{\psi,m} = (\boldsymbol{I} - \boldsymbol{K}\boldsymbol{C})\,\hat{\boldsymbol{P}}^-_{\psi,m}\,(\boldsymbol{I} - \boldsymbol{K}\boldsymbol{C})^T + \boldsymbol{K}\widetilde{\boldsymbol{R}}\boldsymbol{K}^T \tag{2.16}$$

Furthermore, to improve the convergence characteristics of the iterative prediction-correction procedure, a disturbance matrix is added to the posterior covariance matrix at each iteration to provide the prior covariance matrix for the next iteration, i.e., [2, 1]

$$\hat{\boldsymbol{P}}^-_{\psi,m} = \hat{\boldsymbol{P}}^+_{\psi,m} + \boldsymbol{Q} \tag{2.17}$$

where $\boldsymbol{Q} \in \mathbb{R}^{(n_\theta + t_l \times n_{\ddot{u}^g}) \times (n_\theta + t_l \times n_{\ddot{u}^g})}$ is a diagonal matrix with small positive diagonal entries (relative to the diagonal entries of matrix $\hat{\boldsymbol{P}}^+_{\psi,m}$). The matrix $\boldsymbol{Q}$ is referred to as the process noise covariance matrix [26].

In summary, the prior information is used to solve the MAP problem through a first-order approximation approach, and the mean vector estimate and the covariance matrix are updated by Equations 2.14 and 2.16 in each iteration to improve the FE model prediction. Once time the convergence is reached in an estimation window (i.e., until Equation 2.14 is solved within a specified tolerance level), the posterior information is transferred to the next estimation window. The parameters estimates are transferred directly from one estimation window to the next and used as initial estimates, but the time history input estimates transference is not direct. The process is described in detail in the following section.

2.3. Transference of the Extended Parameter vector between Consecutive Estimation Windows

The following section describes the procedure used by Ebrahimian *et al.* [1] to transfer the mean estimation vector between two subsequent estimation windows. Every time the MAP estimation problem is solved, the estimation windows are divided into two parts, the first part is the non-overlap zone. When the estimations are transferred to next window, the non-overlap zone is concatenated with the deterministic input vector for the next iterations. The second part, however, is transferred to the next estimation window and used as the initial estimate for the next estimation sequence. Through the conditional posterior covariance matrix given known values for the first part of the estimated input time history, it is possible

to transfer the uncertainties of the FE model parameters and the uncertainties associated with the second part of the time history of estimated input in the $(m-1)^{th}$ window to the subsequent estimation window m^{th}, based on the previous covariance matrix of the extended parameter vector for the previous estimation window.

In the current section the overlap length between two consecutive windows will be denoted as t_o in number of time steps, and t_s is the sliding rate, is defined as $t_s = t_l - t_o$. For the $(m-1)^{th}$ estimation window, suppose the final posterior mean estimate of the extended parameter vector is defined as

$$\hat{\boldsymbol{\psi}}^{+}_{m-1} = \left[\hat{\boldsymbol{\theta}}^{T}_{m-1}, \left(\hat{\ddot{\boldsymbol{u}}}^{g,m-1}_{t_1^{m-1}:t_1^{m-1}+t_s-1}\right)^{T}, \left(\hat{\ddot{\boldsymbol{u}}}^{g,m-1}_{t_1^{m-1}+t_s:t_2^{m-1}}\right)^{T}\right]^{T} \tag{2.18}$$

The final posterior estimate of the covariance matrix of the extended parameter vector for the $(m-1)^{th}$ estimation window is correspondingly partitioned as

$$\hat{\boldsymbol{P}}^{+}_{\psi,m-1} = \begin{bmatrix} \hat{\boldsymbol{P}}_{\theta,\theta} & \hat{\boldsymbol{P}}_{\theta,\ddot{u}^{g,1}} & \hat{\boldsymbol{P}}_{\theta,\ddot{u}^{g,2}} \\ \hat{\boldsymbol{P}}_{\ddot{u}^{g,1},\theta} & \hat{\boldsymbol{P}}_{\ddot{u}^{g,1},\ddot{u}^{g,1}} & \hat{\boldsymbol{P}}_{\ddot{u}^{g,1},\ddot{u}^{g,2}} \\ \hat{\boldsymbol{P}}_{\ddot{u}^{g,2},\theta} & \hat{\boldsymbol{P}}_{\ddot{u}^{g,2},\ddot{u}^{g,1}} & \hat{\boldsymbol{P}}_{\ddot{u}^{g,2},\ddot{u}^{g,2}} \end{bmatrix} \tag{2.19}$$

where $\hat{\ddot{\boldsymbol{u}}}^{g,m-1}_{t_1^{m-1}:t_1^{m-1}+t_s-1}$ and $\hat{\ddot{\boldsymbol{u}}}^{g,m-1}_{t_1^{m-1}+t_s:t_2^{m-1}}$ are denoted as $\ddot{\boldsymbol{u}}^{g,1}$ and $\ddot{\boldsymbol{u}}^{g,2}$, respectively. The prior mean estimate of the extended parameter vector for the m^{th} estimation window is defined as

$$\hat{\boldsymbol{\psi}}^{-}_{m} = \left[\hat{\boldsymbol{\theta}}^{T}_{m-1}, \left(\hat{\ddot{\boldsymbol{u}}}^{g,m}_{t_1^{m}:t_1^{m}+t_o}\right)^{T}, \left(\hat{\ddot{\boldsymbol{u}}}^{g,m}_{t_1^{m}+t_o+1:t_2^{m}}\right)^{T}\right]^{T} \tag{2.20}$$

where $\hat{\ddot{\boldsymbol{u}}}^{g,m}_{t_1^{m}:t_1^{m}+t_o} = \hat{\ddot{\boldsymbol{u}}}^{g,m-1}_{t_1^{m-1}+t_s:t_2^{m-1}}$ is transferred from the previous window and $\hat{\ddot{\boldsymbol{u}}}^{g,m}_{t_1^{m}+t_o+1:t_2^{m}}$ is initialized as a zero vector, that is $\hat{\ddot{\boldsymbol{u}}}^{g,m}_{t_1^{m}+t_o+1:t_2^{m}} = \boldsymbol{0}$. The conditional posterior covariance matrix of the estimation parameters that are transferred from the $(m-1)^{th}$ to m^{th} estimation windows can be derived as

$$\hat{\boldsymbol{P}}_{\theta,\ddot{u}^{g,2}|\ddot{u}^{g,1}} = \begin{bmatrix} \hat{\boldsymbol{P}}_{\theta,\theta} & \hat{\boldsymbol{P}}_{\theta,\ddot{u}^{g,2}} \\ \hat{\boldsymbol{P}}_{\ddot{u}^{g,2},\theta} & \hat{\boldsymbol{P}}_{\ddot{u}^{g,2},\ddot{u}^{g,2}} \end{bmatrix} - \begin{bmatrix} \hat{\boldsymbol{P}}_{\theta,\ddot{u}^{g,1}} \\ \hat{\boldsymbol{P}}_{\ddot{u}^{g,2},\ddot{u}^{g,1}} \end{bmatrix} \left(\hat{\boldsymbol{P}}_{\ddot{u}^{g,1},\ddot{u}^{g,1}}\right)^{-1} \begin{bmatrix} \hat{\boldsymbol{P}}_{\theta,\ddot{u}^{g,1}} \\ \hat{\boldsymbol{P}}_{\ddot{u}^{g,2},\ddot{u}^{g,1}} \end{bmatrix}^{T} \tag{2.21}$$

The prior covariance matrix for the m^{th} estimation window is defined as

$$\hat{\boldsymbol{P}}^{-}_{\psi,m} = \begin{bmatrix} \hat{\boldsymbol{P}}_{\theta,\ddot{u}^{g,2}|\ddot{u}^{g,1}} & \boldsymbol{0} \\ \boldsymbol{0} & \hat{\boldsymbol{P}}^{-}_{\ddot{u}^{g,2},\ddot{u}^{g,2}} \end{bmatrix} \tag{2.22}$$

where $\hat{\boldsymbol{P}}^{-}_{\ddot{u}^{g,2},\ddot{u}^{g,2}}$ is the prior covariance matrix of $\hat{\ddot{\boldsymbol{u}}}^{g,m}_{t_1^{m}+t_o+1:t_2^{m}}$, which is selected as a diagonal matrix with identical entries, that is, $\hat{\boldsymbol{P}}^{-}_{\ddot{u}^{g,2},\ddot{u}^{g,2}} = (p)^2\mathbb{I}_{t_s\times t_s}$, where $\mathbb{I}$ is the identity matrix and p is the prior standard deviation (SD) of the random base accelerations sampled in the time interval $t_1^m + t_o + 1 : t_2^m$ at the m^{th} estimation window.

2.4. FE response sensitivities using FDM

The FE model parameters sensitivity was calculated with the Finite Difference Method (FDM). The FDM method is implemented by perturbing the estimation parameters one at a time based on a central difference method with unequal spacing. If the parameter $\boldsymbol{\psi}_j$ is perturbed to $\Delta\psi_j$, then the sensitivity of structural response for the parameter can be approximated through the finite difference method as follow

$$\frac{\partial \boldsymbol{h}\left(\boldsymbol{\psi}_m, \ddot{\boldsymbol{u}}^g_{1:t_1^m-1}\right)}{\partial \psi_j} \approx \frac{\boldsymbol{h}\left(\boldsymbol{\psi}_m + \Delta\psi_j \boldsymbol{e}_j, \ddot{\boldsymbol{u}}^g_{1:t_1^m-1}\right) - \boldsymbol{h}\left(\boldsymbol{\psi}_m, \ddot{\boldsymbol{u}}^g_{1:t_1^m-1}\right)}{\Delta\psi_j} \tag{2.23}$$

Where the $\boldsymbol{e}_j$ is the j^{th} standard basis vector, the vector $\boldsymbol{\psi}_m + \Delta\psi_j \boldsymbol{e}_j$ results from perturbing only the j^{th} component of $\boldsymbol{\psi}_m$, and $\partial \boldsymbol{h}\left(\boldsymbol{\psi}_m, \ddot{\boldsymbol{u}}^g_{1:t_1^m-1}\right)/\partial\psi_j$ represents the j^{th} column of the Jacobian matrix.

The Bayesian FE model updating algorithm was implemented in MATLAB [38], which calls in each step of prediction-correction to OpenSeesSP platform [32, 39] in parallel for FE response sensitivity computation. To view the enhance of the parallel computation in comparison with a single-core computation, the speed-up time studies can be reviewed in Chapter 5.

As mentioned above, a linear-elastic FE model is used in the current work. Therefore, to improve the computational efficiency of the algorithm, the sensitivity of the unknown ground input was calculated using the theory for linear time-invariant systems (LTI) with the impulse response function (IRF), which can be consulted in Appendix A. The above reduces the number of times the numerical model must be run, from $n_{\boldsymbol{\theta}} + (t_l \times n_{\ddot{u}^g})$ to $n_{\boldsymbol{\theta}} + n_{\ddot{u}^g}$ times. The theory was implemented with the help of Dr. Hamed Ebrahimian [40].

2.5. Correction for Constraints

To avoid the non-physical values for FE model parameters estimates, an upper- and lower-bound constraints methodology was used. The idea behind this is to correct the Gaussian PDF of the parameters estimates each time these exceed the bounds defined by the user. The corrected estimates are calculated as the mean of the truncated PDF. Once the estimates calculated reach values into the range defined, the covariances are updated and the algorithm continues to the next iteration. For more information, the readers can be derived to [26, 41], and the algorithm was implemented in [42].

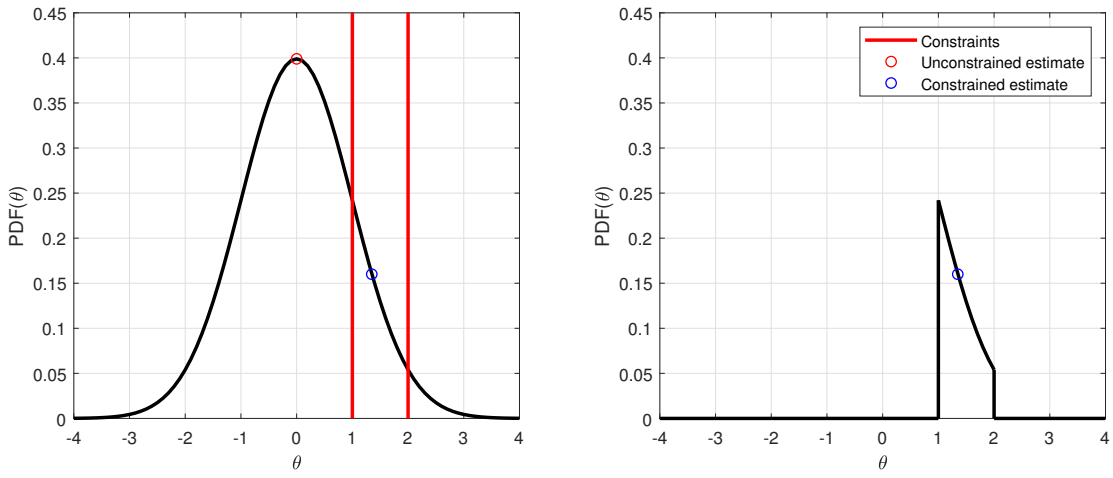

Figure 2.1: Method proposed by Simon, where the constrained estimate is the centroid of the truncated PDF: (a) Unconstrained PDF; (b) constrained PDF (Figure adapted from ref. [41]).

2.6. Adaptive Scaling of the Unknown Model Parameters

The correct convergence of the estimation algorithm depends directly on the sensitivity matrix. Due to different orders in the values between the unknown model parameters and unknown input time history, it is necessary to scale the parameters at each iteration aim to improve the performance of the estimation algorithm. The scaling adaptively method allows the FE model response to have relatively similar sensitivities concerning different estimation parameters at each estimation point [40].

In general, one part of the sensitivity matrix is associated with FE model parameters, and the other part is associated with input time history. The idea behind this is to calculate the scale factors for the FE model parameters, which aim to obtain a sensitivity matrix with values of the same order. For the above, a scaled vector is defined as

$$\boldsymbol{\theta}^s = \boldsymbol{A}\boldsymbol{\theta} \tag{2.24}$$

in which $\boldsymbol{A} \in \mathbb{R}^{n_\theta \times n_\theta}$ is a diagonal scaling matrix. It is noted that the vector of the unknown input time history remains unscaled. The parameters scaling factors (i.e., the diagonal entries of matrix $\boldsymbol{A}$ denoted by a_n, $n = 1 \rightarrow n_\theta$) are calculated to result in equal corresponding diagonal entries in the Fisher Information Matrix (FIM) of the scaled parameters, which is approximated as

$$\boldsymbol{I}^s = (\boldsymbol{C}_\theta^s)^T(\boldsymbol{C}_\theta^s) \tag{2.25}$$

wherein $\boldsymbol{C}_\theta^s$ denotes the FE response sensitivity matrix concerning the scaled FE model parameter vector. Likewise, the FIM of the non-scaled parameters are calculated as

$$\boldsymbol{I} = (\boldsymbol{C}_\theta)^T(\boldsymbol{C}_\theta) \tag{2.26}$$

Calculating the finite element model response sensitivity (Equation 2.2) for the parameters vector, and applying the chain rule to compute the derivative of a composite function, we obtain

$$\frac{\partial \boldsymbol{h}}{\partial \boldsymbol{\theta}} = \frac{\partial \boldsymbol{h}}{\partial \boldsymbol{\theta}^s}\frac{\partial \boldsymbol{\theta}^s}{\partial \boldsymbol{\theta}} \tag{2.27}$$

$$\boldsymbol{C}_\theta = \boldsymbol{C}_\theta^s \boldsymbol{A} \tag{2.28}$$

Taking Equations 2.25 and 2.28 is possible to get a relation between the FIM of the model parameters and the scaled model parameters as shown below [43]

$$\boldsymbol{I} = \boldsymbol{A}^T \boldsymbol{I}^s \boldsymbol{A} \tag{2.29}$$

The diagonal entries of the FIM of the non-scaled parameters are calculated as follows

$$(\boldsymbol{I})_n = a_n^2 (\boldsymbol{I}^s)_n \tag{2.30}$$

Therefore, because the unknown input time history remains unscaled, the FIM corresponding to the vector of unknown input ground motion will be the same for non-scaled and scaled parameters. Given the above, the mean value of the Fisher Information Matrix associated with the unknown input time history is taken as a reference value and equal to $(\boldsymbol{I}^s)_n$. Considering the previous statement, and using the definition of FIM (Equation 2.26), Equation 2.30 can be rewritten as

$$\left(\frac{\partial \boldsymbol{h}}{\partial \theta_n}\right)^T \left(\frac{\partial \boldsymbol{h}}{\partial \theta_n}\right) = a_n^2 \,\text{mean}\left[\text{diag}\left(\left(\frac{\partial \boldsymbol{h}}{\partial \ddot{\boldsymbol{u}}^{g,m}_{t_1^m:t_2^m}}\right)^T \left(\frac{\partial \boldsymbol{h}}{\partial \ddot{\boldsymbol{u}}^{g,m}_{t_1^m:t_2^m}}\right)\right)\right] \tag{2.31}$$

Then the scale factor for the n^{th} model parameter in the m^{th} estimation window is calculated as follows

$$a_n = \sqrt{\frac{\left(\frac{\partial \boldsymbol{h}}{\partial \theta_n}\right)^T \left(\frac{\partial \boldsymbol{h}}{\partial \theta_n}\right)}{\text{mean}\left[\text{diag}\left(\left(\frac{\partial \boldsymbol{h}}{\partial \ddot{\boldsymbol{u}}^{g,m}_{t_1^m:t_2^m}}\right)^T \left(\frac{\partial \boldsymbol{h}}{\partial \ddot{\boldsymbol{u}}^{g,m}_{t_1^m:t_2^m}}\right)\right)\right]}} \tag{2.32}$$

Finally, the posterior unknown extended parameter vector and the posterior covariance matrix are re-defined as

$$\hat{\boldsymbol{\psi}}_m^+ = \left[(\boldsymbol{A}\boldsymbol{\theta}_m)^T \left(\hat{\ddot{\boldsymbol{u}}}^{g,m}_{t_1^m:t_2^m}\right)^T\right]^T \tag{2.33}$$

$$\hat{\boldsymbol{P}}^+_{\psi,m} = \begin{bmatrix} \boldsymbol{A}\hat{\boldsymbol{P}}_{\theta,m}\boldsymbol{A}^T & \boldsymbol{0} \\ \boldsymbol{0} & \hat{\boldsymbol{P}}_{\ddot{u}^g,m} \end{bmatrix} \tag{2.34}$$

Therefore, the magnitude of the FE response sensitivity vector with respect to each scaled model parameters is equal to the mean magnitude of FE response sensitivity vectors with respect to the unknown discrete values of the input motion histories.

2.7. Algorithm

Algorithm 1, below, is a procedure summary of the sequential FE model updating for the joint estimation of the model parameters and the input motion time histories, used in this work.

Algorithm 1: Sequential FE model updating algorithm for joint estimation of model parameters and input motion time histories.

---

1. Determine the start and end points of the estimation windows -i.e., t_1^m, t_2^m, where $m = 1, 2, ..., N$ and N is the number of estimation windows.

2. Set the initial values: $\hat{\boldsymbol{\theta}}_0$, $\hat{\boldsymbol{P}}_{\theta_0}$, $\hat{\ddot{\boldsymbol{u}}}^g_{t_1^0:t_2^0} = \boldsymbol{0}$, and $\hat{\boldsymbol{P}}_{\ddot{u}^g_0}$.

3. Set the scaling factor as the inverse of the initial values of the model parameters, i.e., $a_n = 1/\theta_{0,n}$. Set up $\hat{\boldsymbol{\psi}}^+_{0,0} = \left[\left(\boldsymbol{A}\hat{\boldsymbol{\theta}}_0\right)^T, \left(\hat{\ddot{\boldsymbol{u}}}^g_{0,t_1^1:t_2^1}\right)^T\right]^T$ and $\hat{\boldsymbol{P}}^+_{\psi,0,0} = \begin{bmatrix} \boldsymbol{A}\hat{\boldsymbol{P}}_{\theta_0}\boldsymbol{A}^T & \boldsymbol{0} \\ \boldsymbol{0} & \hat{\boldsymbol{P}}_{\ddot{\boldsymbol{u}}^g_0} \end{bmatrix}$.

4. for *m=1,...,N* **do**

- **4.1.** Retrieves the posterior estimates of the mean vector and covariance matrix of the extended parameter vector (i.e., $\hat{\boldsymbol{\psi}}^+_{m,0}$ and $\hat{\boldsymbol{P}}_{\psi,m,0}$) from the last estimation window (i.e., $\hat{\boldsymbol{\psi}}^+_{m-1}$ and $\hat{\boldsymbol{P}}_{\psi,m-1}$).
- **4.2.** Define the process noise covariance matrix $\boldsymbol{Q}$ and the simulation error covariance matrix $\boldsymbol{R}$. Set up $\widetilde{\boldsymbol{R}}$.
- **4.3.** Set $\hat{\boldsymbol{\psi}}^-_{m,0} = \hat{\boldsymbol{\psi}}^-_m$ where $\hat{\boldsymbol{\psi}}^-_m$ is defined in Equation 2.20.
- **4.4.** Set $\hat{\boldsymbol{P}}^-_{\psi,m,0} = \hat{\boldsymbol{P}}^-_{\psi,m}$ where $\hat{\boldsymbol{P}}^-_{\psi,m}$ is defined in Equation 2.22.
- **4.5 while** $|\hat{\boldsymbol{\psi}}^+_{m,i} - \hat{\boldsymbol{\psi}}^+_{m,i-1}| > \text{tol}_1 \times |\hat{\boldsymbol{\psi}}^+_{m,i-1}|$ *or* $i \leq \text{tol}_2$ **do**
  - **Comment:** tol_1 = tolerance limit for relative change in the estimated parameter vector, i denotes the iteration number, and tol_2 = maximum number of iterations.
  - **4.5.1.** Set $\hat{\boldsymbol{\psi}}^-_{m,i} = \hat{\boldsymbol{\psi}}^+_{m,i-1}$ and $\hat{\boldsymbol{P}}^-_{\psi,m,i} = \hat{\boldsymbol{P}}^+_{\psi,m,i-1} + \boldsymbol{Q}$.
  - **4.5.2.** Obtain the FE responses using $\hat{\boldsymbol{\psi}}^-_{m,i}$; i.e., $\hat{\boldsymbol{y}}_{t_1^m:t_2^m} = \boldsymbol{h}_{t_1^m:t_2^m}\left(\hat{\boldsymbol{\psi}}^-_{m,i}, \hat{\ddot{\boldsymbol{u}}}^g_{1:t_1^m-1}\right)$. Obtain the FE response sensitivities using a finite difference method. Set up the sensitivity matrix with respect to the scaled model parameters, $\boldsymbol{C}^s$.
  - **4.5.3.** Compute the Kalman gain matrix:
    $$\boldsymbol{K} = \left((\boldsymbol{C}^s)^T \widetilde{\boldsymbol{R}}^{-1}\boldsymbol{C}^s + \left(\hat{\boldsymbol{P}}^-_{\psi,m,i}\right)^{-1}\right)^{-1}(\boldsymbol{C}^s)^T \widetilde{\boldsymbol{R}}^{-1}$$
  - **4.5.4.** Find the corrected estimates of the mean vector and covariance matrix of the extended parameter vector:
    $$\hat{\boldsymbol{\psi}}^+_{m,i} = \hat{\boldsymbol{\psi}}^-_{m,i} + \boldsymbol{K}\left(\boldsymbol{y}_{t_1^m:t_2^m} - \boldsymbol{h}_{t_1^m:t_2^m}\left(\hat{\boldsymbol{\psi}}^-_{m,i}, \hat{\ddot{\boldsymbol{u}}}^g_{1:t_1^m-1}\right)\right)$$
    $$\hat{\boldsymbol{P}}^+_{\psi,m,i} = (\boldsymbol{I} - \boldsymbol{K}\boldsymbol{C}^s)\hat{\boldsymbol{P}}^-_{\psi,m,i}(\boldsymbol{I} - \boldsymbol{K}\boldsymbol{C}^s)^T + \boldsymbol{K}\widetilde{\boldsymbol{R}}\boldsymbol{K}^T$$
  - **4.5.5.** Correct for constraints.
  - **4.5.6.** Update the model parameter scaling factors using Equation 2.32. Update $\hat{\boldsymbol{\psi}}^+_{m,i}$ and $\hat{\boldsymbol{P}}^+_{\psi,m,i}$ based on the new model parameters scale factors.
  - **4.5.7** Set up $i = i + 1$.
- **end**

end

2.8. Simulation Case

An output-only simulation case is performed for algorithm validation. The FE model consists of an elastic frame structure, as shown in Figure 2.2. The parameters that will be estimated are the elastic modulus of the columns per story denoted by E_1 for the 1st story, E_2 for the 2nd story, and E_3 for the 3rd story. The true value for elastic modulus was defined in 29000 [ksi]. In addition, the mass and stiffness proportional Rayleigh damping coefficients, denoted as α and β, respectively, will also be estimated. The mass was fixed to get a period equal to $T_1 = 1.015$[sec]. Also, the input ground motion will be considered unknown, and the measured structural response time histories consist of the floor absolute acceleration response at the first, and second floor, and the relative roof displacement response. The acceleration response time histories are polluted with statistically independent, zero-mean, 1 %g root-mean-square (RMS) Gaussian white noise processes, whereas the displacement response time history is polluted with a zero-mean, 1-mm RMS, Gaussian white noise. The "El Centro" earthquake (PGA $= 0.319g$) was used for the simulation, with a time-step equal to 0.02 [sec]. The damping ratio was fixed in 2 % for the 1st and 3rd modes ($T_1 = 1.015$ [sec], $T_3 = 0.250$ [sec]).

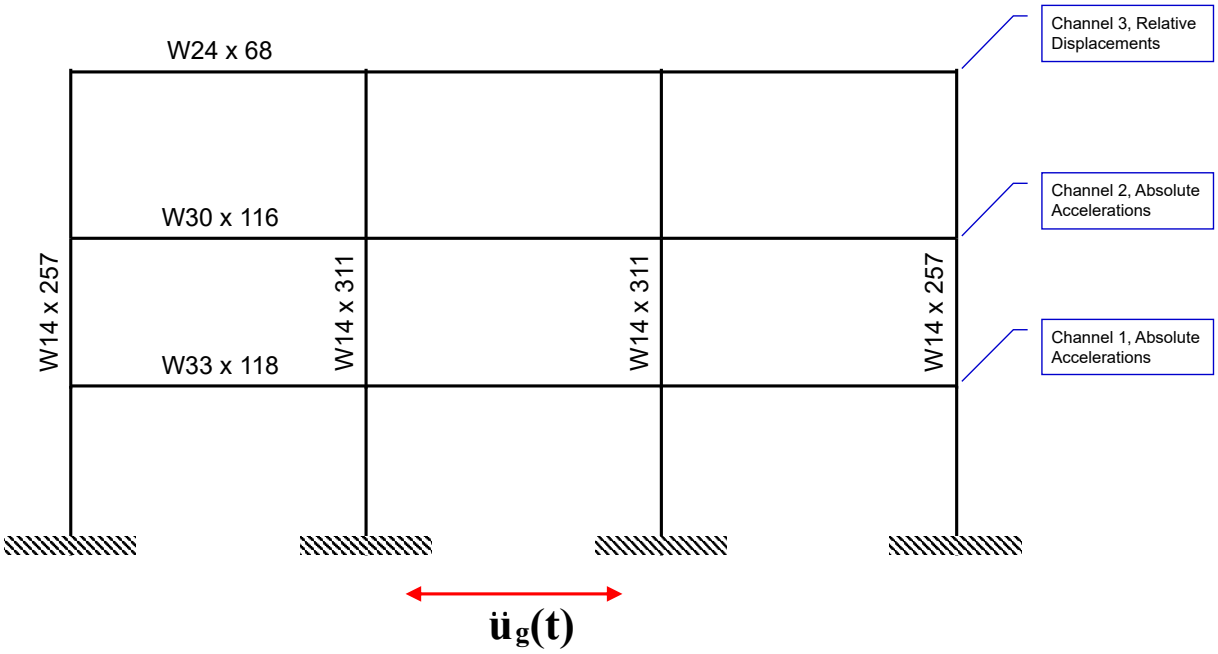

Figure 2.2: Elastic frame model used for algorithm validation (Figure adapted from ref. [32]).

The initial values were selected as $\hat{\boldsymbol{\theta}}_0 = 0.80\boldsymbol{\theta}^{true}$, and the covariances matrices of the initial estimates are were selected as $\hat{\boldsymbol{P}}_{\theta_0} = (0.01)^2\mathbb{I}_{n_\theta \times n_\theta}$ for the FE model parameters, and $\hat{\boldsymbol{P}}_{\ddot{\boldsymbol{u}}^{g,0}} = (0.05)^2\mathbb{I}_{t_l \times t_l}$ for the unknown input vector. The coefficients represent the FE model parameters variances of the initial estimate and the variances of the base acceleration at each discrete time, also quantifies the uncertainty of these parameters. The process noise covariance matrix $\boldsymbol{Q}$ is defined as a diagonal matrix with entries equal to 10^{-4} for the FE model parameters and unknown inputs, and constant throughout the estimation process. Finally, the simulation error covariance matrix $\boldsymbol{R}$ was defined as a diagonal matrix where the entries were estimated as 1 %g RMS for accelerations response time histories and 1-mm RMS for displacements response time histories; the mentioned values represent the measurement noise variances.

The estimation window was defined with a length equal to 100-time steps, with an overlap between windows equal to 20-time steps. In general, the parameters of the filter ($\hat{\boldsymbol{P}}_{\psi}^{+}$, $\boldsymbol{Q}$, and $\boldsymbol{R}$) selected depends on the user's experience. For more details, the readers can be referred to Ebrahimian *et al.*, 2018 [1].

Table 2.1: Comparison of finite element model parameter estimation results for the sequential maximum a posterior estimation method.

Parameter ID	**Final estimates of FE model parameters** ($\hat{\boldsymbol{\theta}}/\boldsymbol{\theta}^{true}$)	**Final estimates of coefficient of variation (%)** ($C.O.V.(\hat{\boldsymbol{\theta}})$)
E_1	1.025	0.069
E_2	1.004	0.086
E_3	0.997	0.062
α	0.948	0.826
β	1.018	0.846

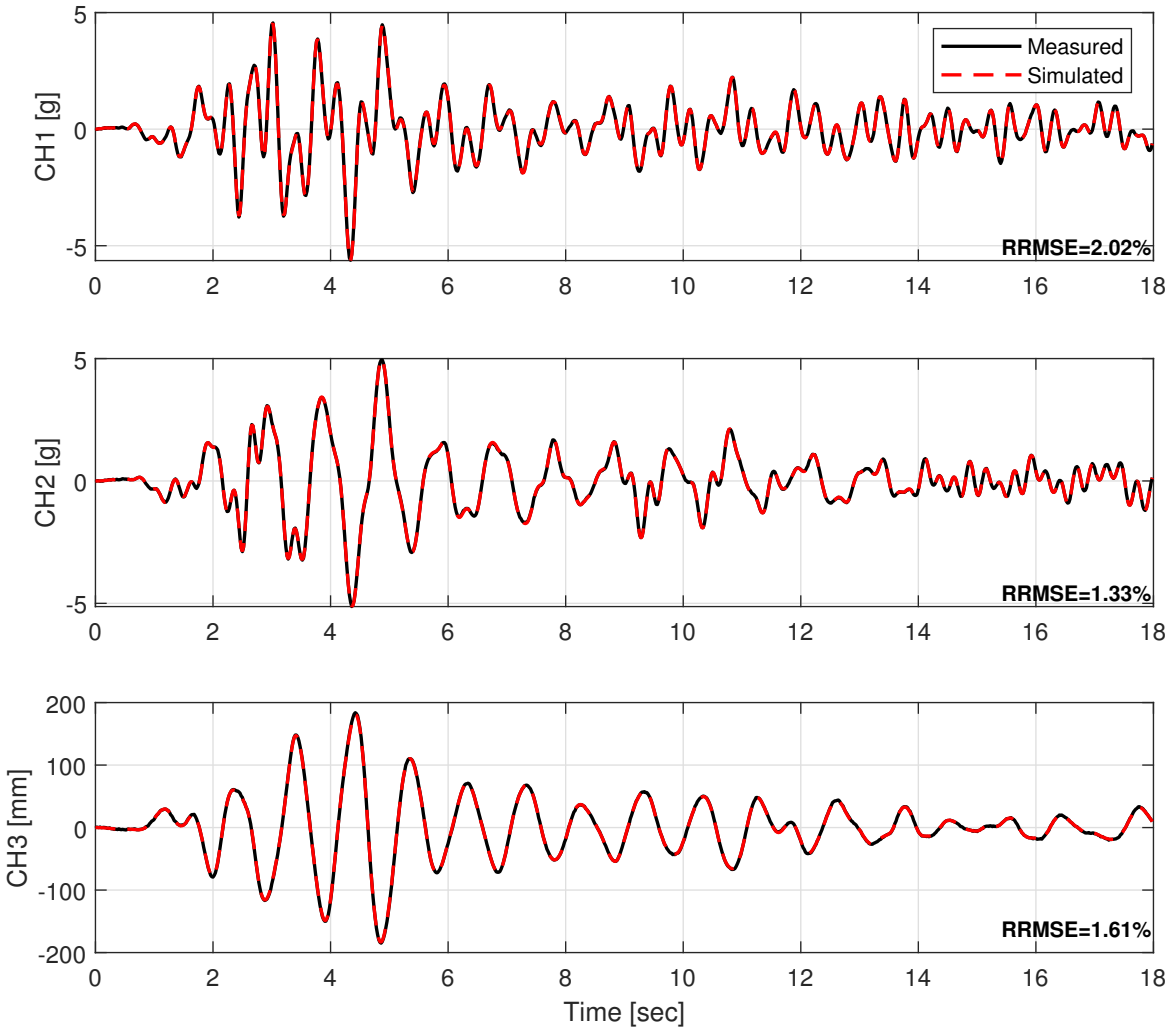

Figure 2.3: Comparison of the measured structural response with the structural responses predicted using the final-updated FE model.

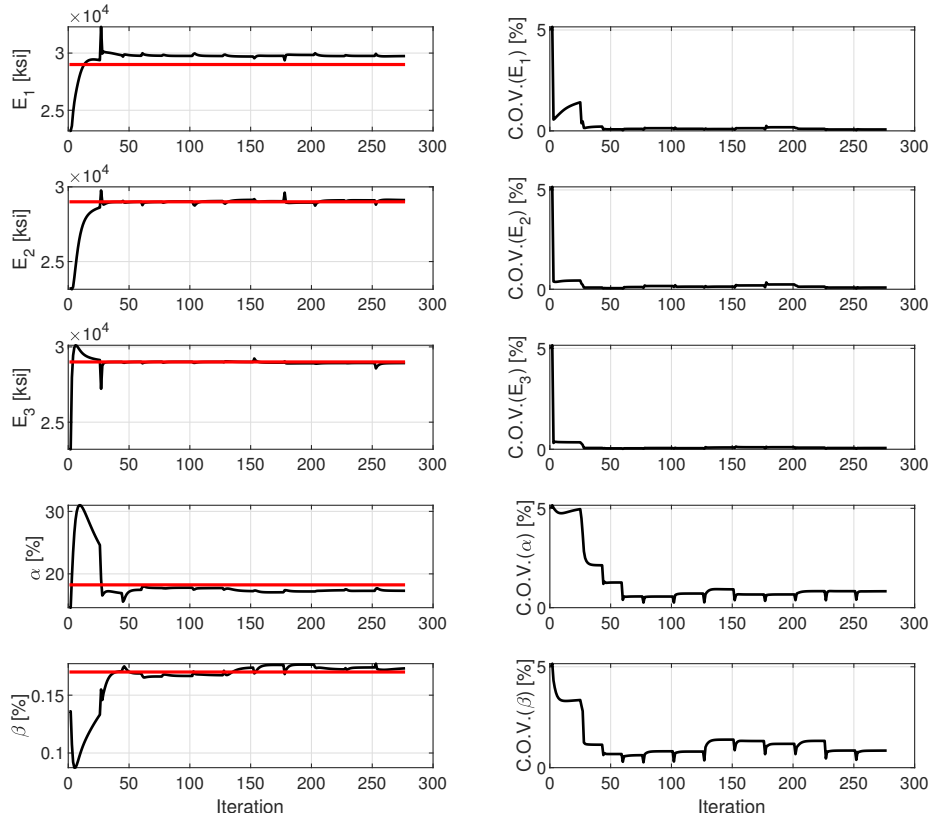

Figure 2.4: Time-histories of the posterior mean (left) and coefficient of variation (right) of the final-updated model parameters.

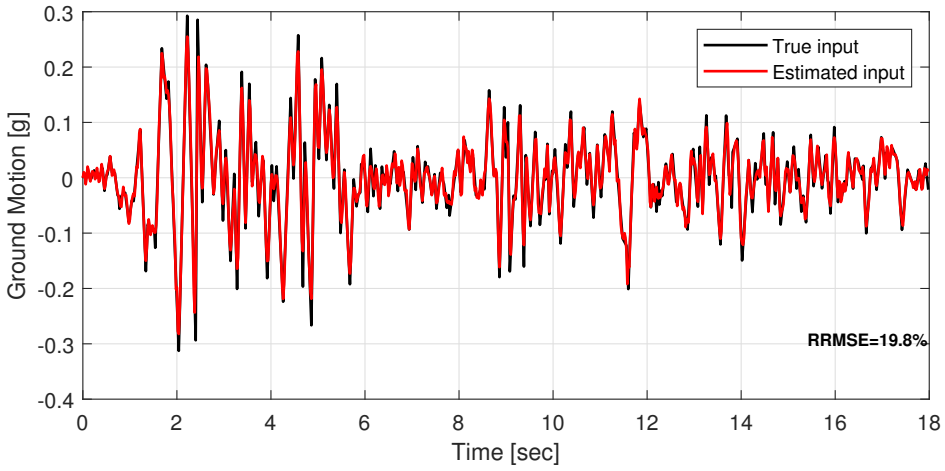

Figure 2.5: Comparison of the actual and estimated base acceleration time histories.

Figure 2.3 shows the measured structural response (simulated) and the elastic frame model prediction using the model parameters estimates (Table 2.1), and the input ground motion (Figure 2.5) estimate through the model updating process. The relative difference between both signals is measured with the metric relative-root-mean-square error (RRMSE) and was calculated as follows

$$\mathrm{RRMSE}(\hat{\ddot{\boldsymbol{u}}}^{g}_{1:k})(\,\%) = \sqrt{\frac{\sum_{i=1}^{k}\left(\hat{\ddot{\boldsymbol{u}}}^{g}_{i} - \ddot{\boldsymbol{u}}^{g,\mathrm{true}}_{i}\right)^{2}}{\sum_{i=1}^{k}\left(\ddot{\boldsymbol{u}}^{g,\mathrm{true}}_{i}\right)^{2}}} \times 100 \tag{2.35}$$

The RRMSE appears due to the intrinsic measurement noise of the channels (which was simulated adding 1 % of the white noise), and the final uncertainties associated with final estimated parameters (C.O.V.) and the unknown input vector. The coefficient of variation (C.O.V.) is used to quantify the confidence of the estimations; therefore, the estimated parameter values with larger C.O.V. include larger estimation uncertainties. This will be used later to assess the confidence of the estimates when using the algorithm for actual measurements. With this, the algorithm is validated, and it can be seen that it is a powerful tool for the joint estimation of parameters and input forces.

Chapter 3

Description of the Building

The structure under study in this thesis corresponds to the Chilean Chamber of Construction (CChC) Building. The building is located in the commune of Providencia, Santiago, Chile. The structural system was designed by the office Lagos, Contreras, and Associates, and the building was built in 1987. The Chilean Chamber of Construction Building has been instrumented since 1997 with 12 uniaxial acceleration sensors and a central recording unit.

Figure 3.1: (a) North-east, (b) south-west, and (c) north-west views of the building.

Figure 3.2: The Chilean Chamber of Construction Building during its construction (1987).

3.1. Structural Characteristics of the Building

The building has 20 stories above ground level and four basement stories; the total height is 77.7 meters from the top of the foundation system to the roof slab and 66.6 meters from ground level. The structural system consists of a dual frame-wall structural design of reinforced concrete with a predominance of the wall system for resistance to lateral loads. The structural walls are concentrated in the area corresponding to elevators and stairs; the rest of the structural elements correspond to reinforced concrete beams and columns. The density of structural walls for shear stress control, defined as the ratio between the walls area and the plant area, is between 3 and 6 % [44]. Table 3.1 note the increase in density in the basement stories, due to the presence of perimeter walls.

Table 3.1: Structural wall density per floor of the CChC Building (Carreño, 2009 [5]).

Story	**Floor height** [m]	**Elevation** [m]	**Plant area** [m^2] (A_{plant})	**Top wall area** [m^2] (A_{wall})	$\frac{A_{wall}}{A_{plant}}$ [%]
20	3.3	77.7	851	23.8	2.8
19	3.3	74.4	918	32.8	3.6
18	3.3	71.1	918	32.8	3.6
17	3.3	67.8	877	32.5	3.7
16	3.3	64.5	957	34.6	3.6
15	3.3	61.2	957	34.6	3.6
14	3.3	57.9	957	34.6	3.6
13	3.3	54.6	957	34.6	3.6
12	3.3	51.3	957	46.0	4.8
11	3.3	48	957	46.0	4.8
10	3.3	44.7	957	46.0	4.8
9	3.3	41.4	957	46.0	4.8
8	3.3	38.1	957	52.0	5.4
7	3.3	34.8	957	52.0	5.4
6	3.3	31.5	957	52.0	5.4
5	3.3	28.2	957	52.0	5.4
4	3.3	24.9	957	52.0	5.4
3	3.3	21.6	1794	68.7	3.8
2	3.6	18.3	1794	68.7	3.8
1	3.6	14.7	1479	67.1	4.5
Z	3.3	11.1	2090	132.7	6.3
S1	2.6	7.8	2090	132.7	6.3
S2	2.6	5.2	2090	132.7	6.3
S3	2.6	2.6	2090	132.7	6.3
Total:			29432.0	1439.6	4.9

Regarding the soil's mechanical report, the foundation system is located on soil composed mainly of dense gravel, corresponding to soil type II according to the Chilean seismic standard, NCh433. Of.72 [45]. The perimetral walls are founded on spread footings of 40 centimeters thick, while the structural columns are on square footings of 280 or 360 centimeters long linked through a concrete beam (Figure 3.3).

Finally, the slabs thickness is enough to resist gravity loads and punching shear failure in columns. The floor's slabs located above the ground are 15 centimeters thick, and the slabs situated below the ground are 17 centimeters thick. The 1^{st} floor slab is 20 centimeters thick to transmit the seismic shear from core structural walls to perimeter walls.

3.2. Structural Plans

In the next section, the structural details of the building are shown. The floors located above ground level have a plane of symmetry on axis 5. Due to the above, the mode shapes of the first two translational modes of vibrations don't have a predominant direction.

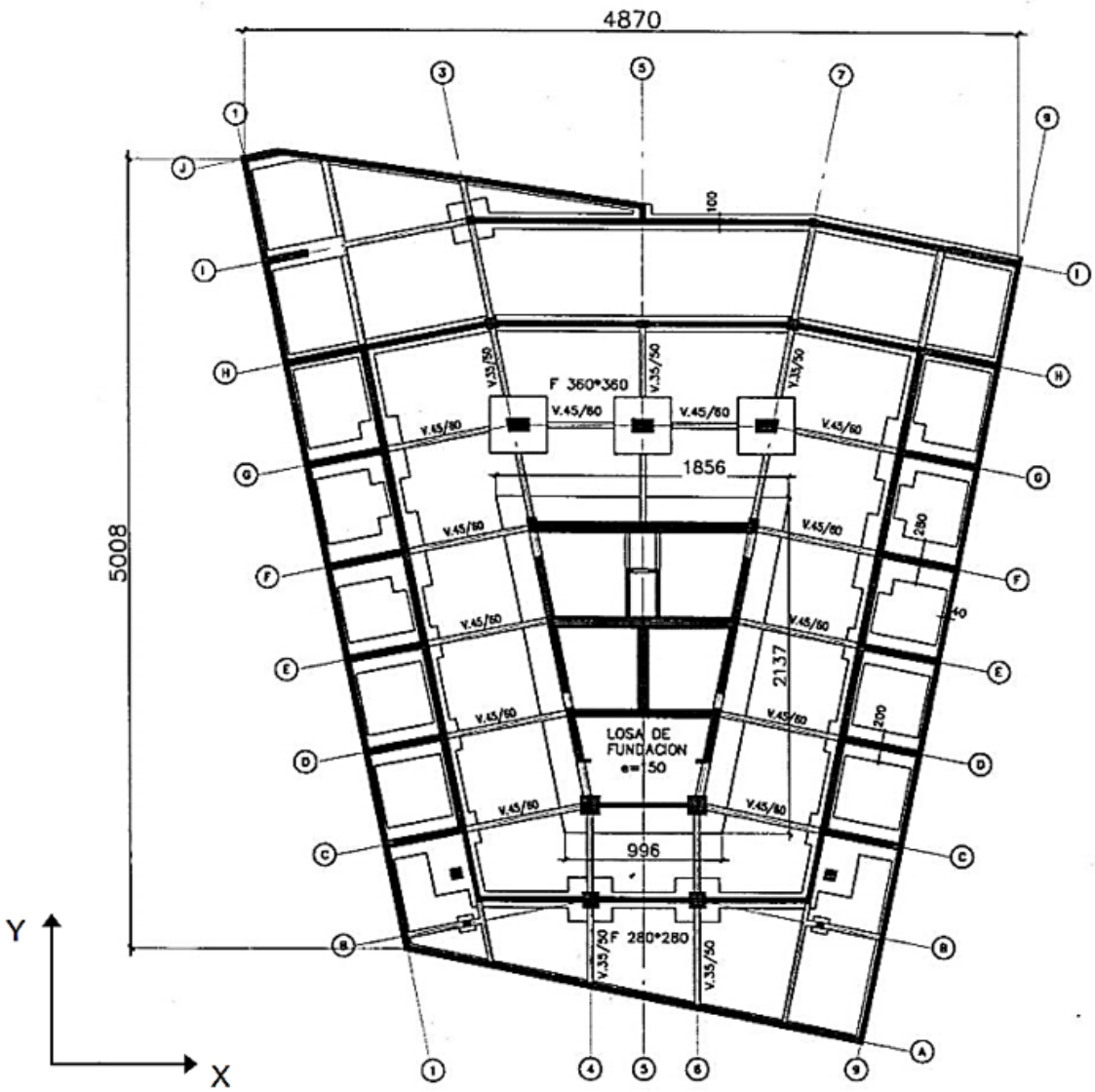

Figure 3.3: Foundation structural details. CChC Building [5].

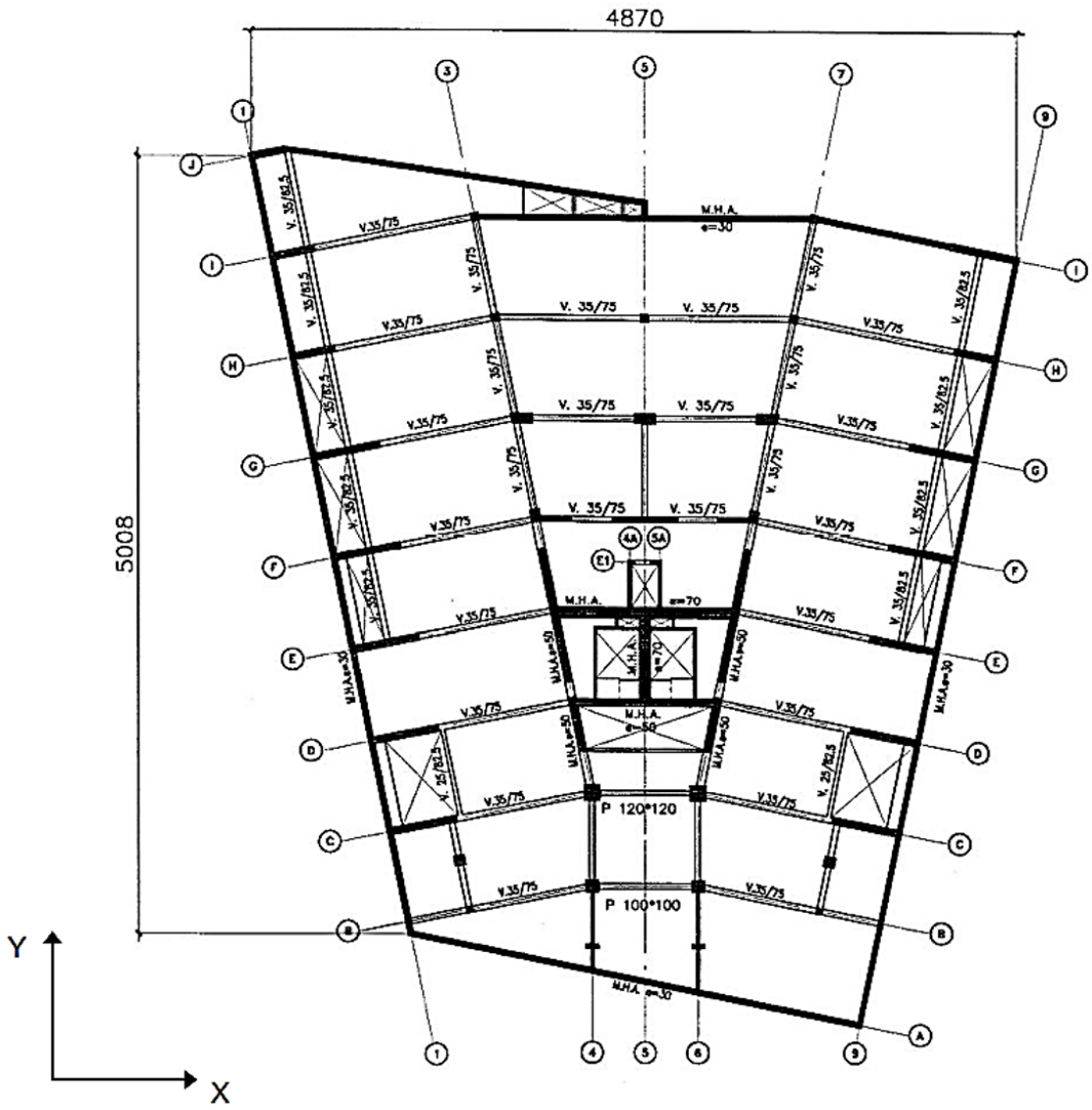

Figure 3.4: Zocalo structural details. CChC Building [5].

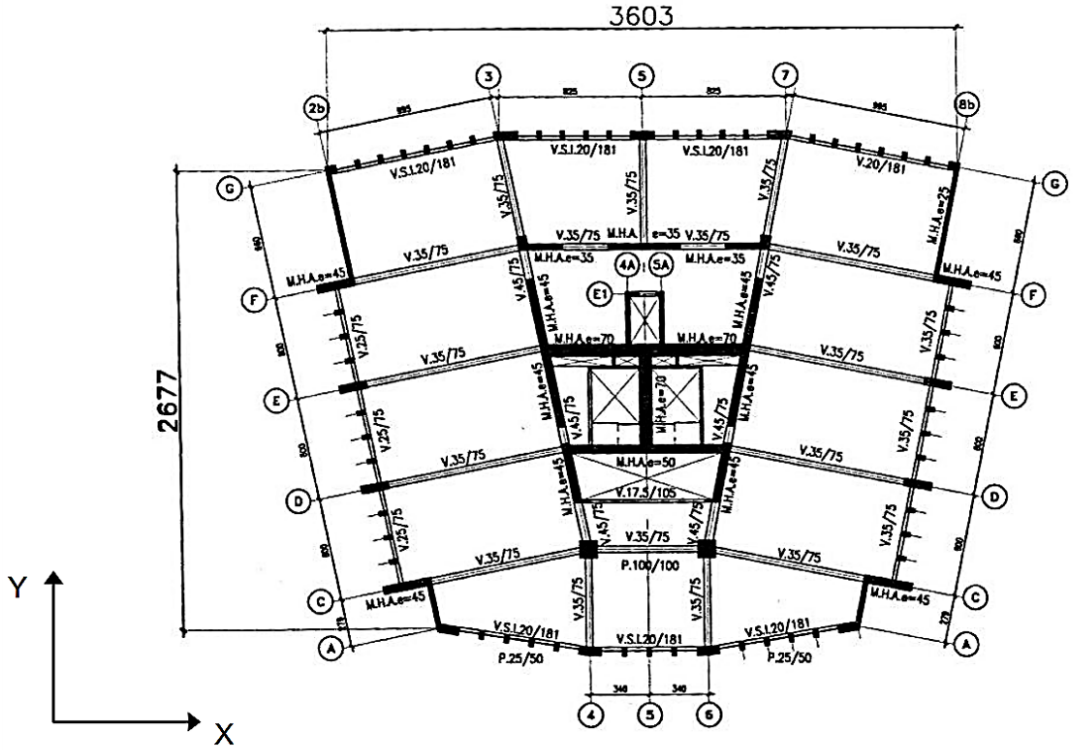

Figure 3.5: 5^{th}-8^{th} floors structural details. CChC Building [5].

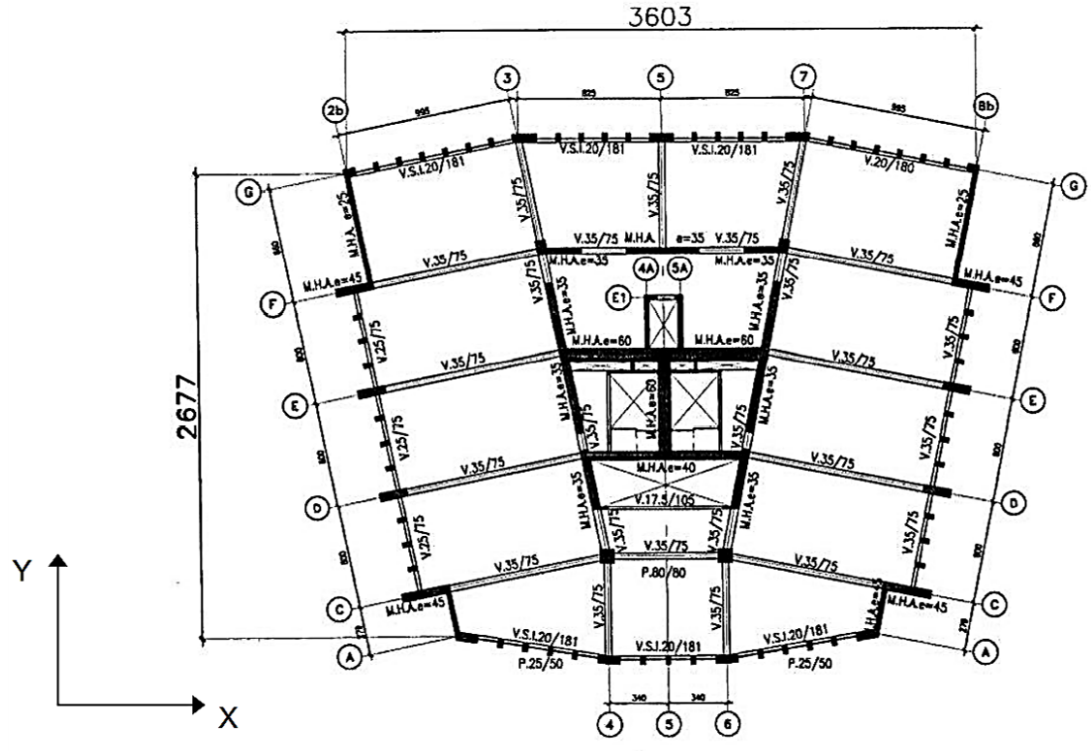

Figure 3.6: 9^{th}-12^{th} floors structural details. CChC Building [5].

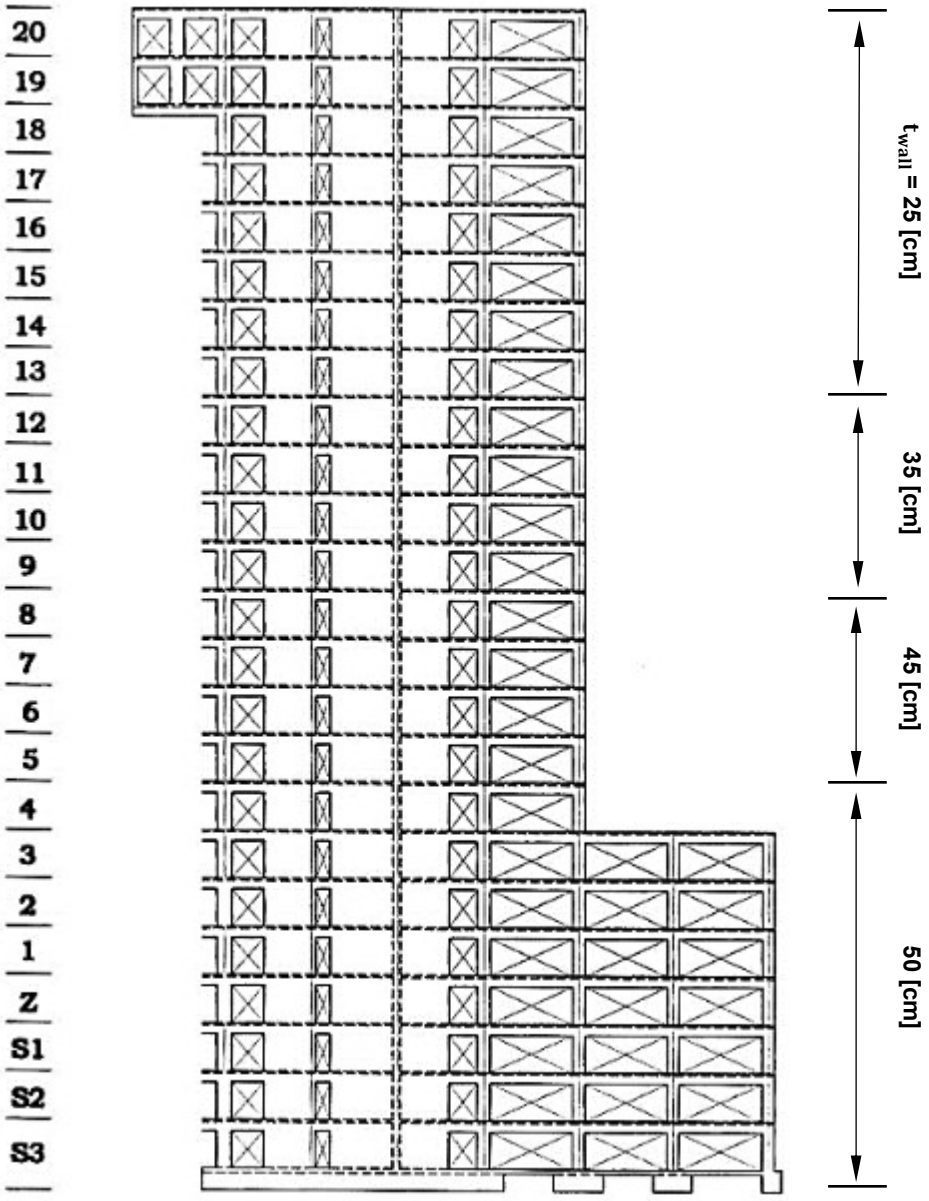

Figure 3.7: 7 and 3-axes elevations (dimensions in the figure specify walls thickness in each story). CChC Building [5].

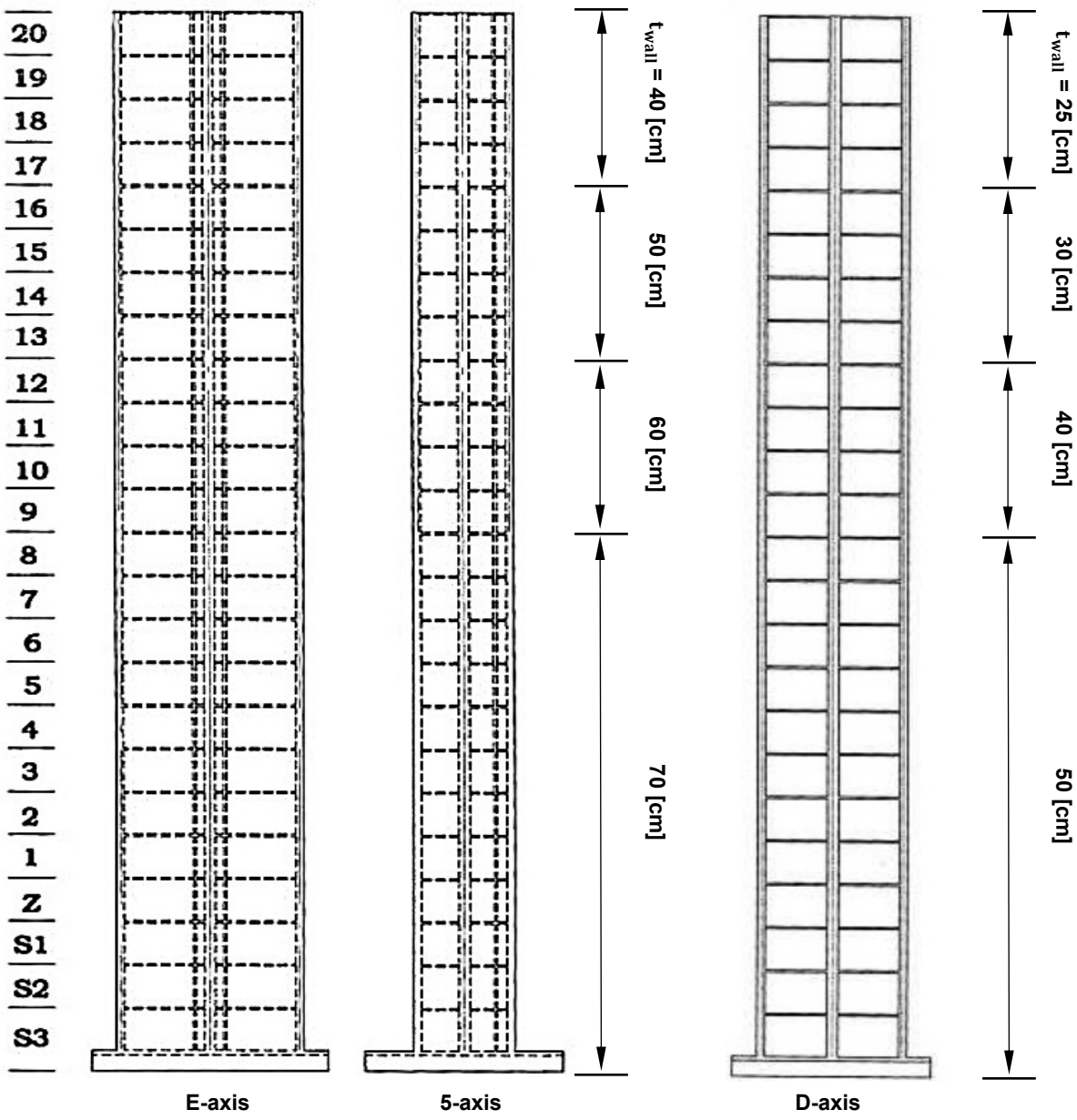

Figure 3.8: E, 5, and D-axes elevations (dimensions in the figure specify walls thickness in each story). CChC Building [5].

3.3. Instrumentation System of the Building

The Chilean Chamber of Construction Building has been instrumented since 1997 with 12 uni-axial acceleration sensors, 4 of them located at the base and the rest distributed on the 1^{st}, 12^{th}, and 19^{th} floors of the building [7]. The sensors were distributed to study the spatial motion of the building, and measure displacements, floor distortions, torsion, and structural walls rotation to foundation level, among other aspects.

The sensor used is a force-balanced accelerometer, model FBA-11 from Kinemetric brand, which captures absolute accelerations. The measurement equipment has an acquisition sys-

tem, model K2 of the Kinemetric Altus^{TM} series.

The sensor system records the accelerations both from seismic events and for environmental micro-vibrations. The sensors' locations are shown in Table 3.2 and Figure 3.9.

Table 3.2: Sensors location on the building \cite{Carreno2009}.

Channel	**Sensors location - Direction**
1	Basement 3 - EW
2	Basement 3 - NS
3	Basement 3 - V1
4	Basement 3 - V2
5	Ground Level - EW
6	Ground Level - NS
7	Ceiling Floor 11^{th} - EW, north side
8	Ceiling Floor 11^{th} - NS, east side
9	Ceiling Floor 11^{th} - EW, south side
10	Ceiling Floor 18^{th} - EW, north side
11	Ceiling Floor 18^{th} - NS, east side
12	Ceiling Floor 18^{th} - EW, south side

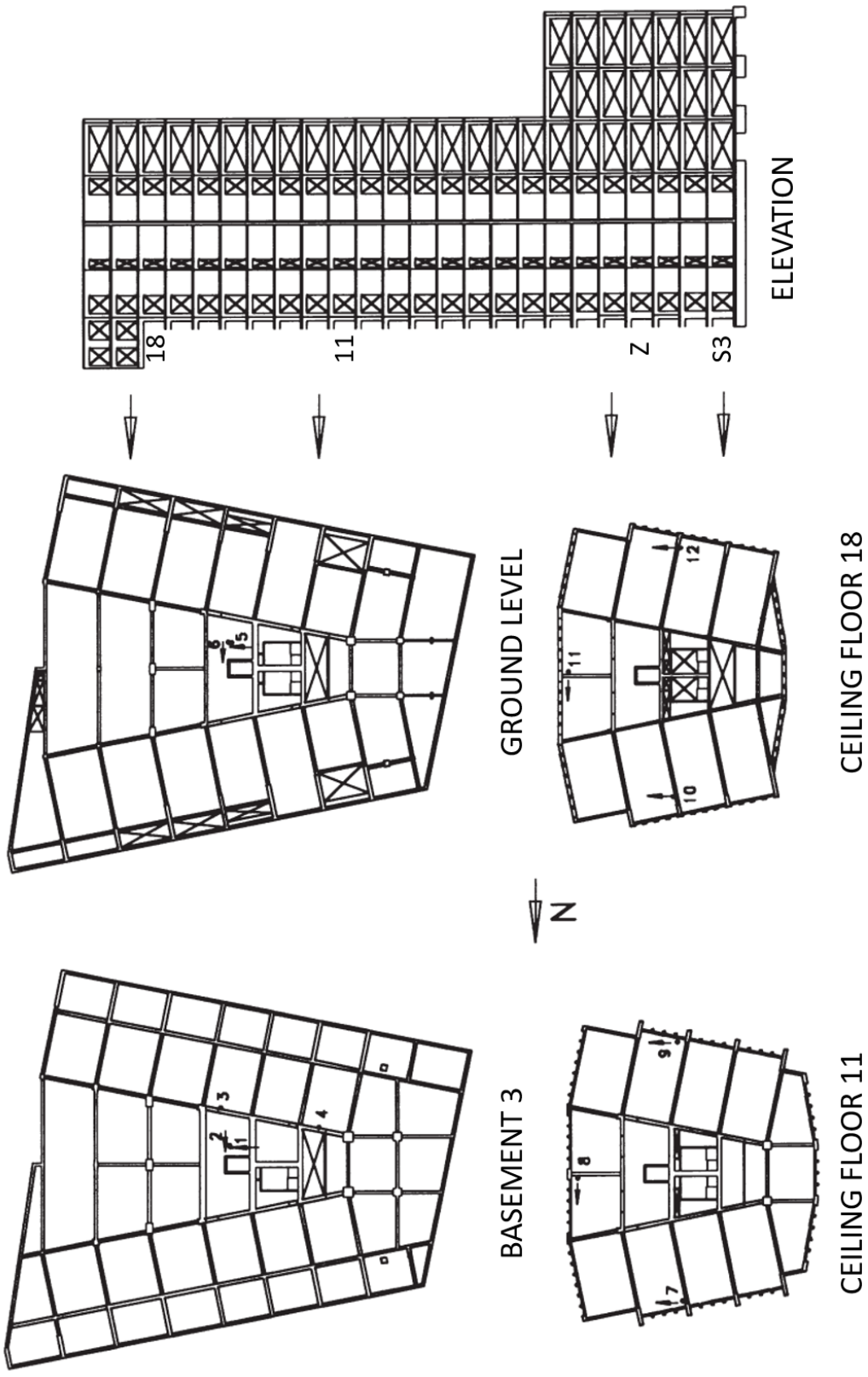

Figure 3.9: Scheme about the location of the sensors on the building [7].

3.4. Previous Studies

In previous studies, the authors identified the building's modal properties and correlated the mentioned parameters for environmental and seismic conditions. The results presented in these investigations are summarized below.

3.4.1. Environmental conditions

In 2008, Lazcano recompiled the micro-vibration accelerations records of the CChC Building, joint with meteorological data, rain, temperature, humidity, and wind. The conclusions were that for environmental conditions, the frequencies of the building change in a range of 1-2 %, for heavy rains and winds the variations reach 7 % [3], and the damping ratios values are between 0.8-2 % [46]. Lazcano summarized the building's modal parameters identified by Valdés & Castillo [3] (Table 3.3).

Table 3.3: The CChC modal properties from previous studies (Lazcano, 2008 [3]).

Mode	**Identified by Frequency Domain Method (Records date: 1997-1999)**		**Identified by SSI Method (Records date: 1997)**		**Identified by SSI Method (Records date: 2004)**	
	Frequency [Hz]	**Damping ratios [%]**	**Frequency [Hz]**	**Damping ratios [%]**	**Frequency [Hz]**	**Damping ratios [%]**
1	1.04	1.10	1.053	1.84	1.021	1.02
2	1.07	1.00	1.067	0.45	1.024	0.92
3	1.63	0.60	1.618	0.55	1.552	0.97
4	3.56-3.63	1.50	3.582	1.17	3.489	1.58
5	3.53-3.60	1.50	3.608	2.11	3.495	2.39
6	-	-	4.097	1.96	3.94	1.74
7	4.80	1.20	4.842	1.31	4.649	0.91

Table 3.3 shows a slight decrease in frequencies between 1997 and 2004. The slight variation in frequencies values cannot be associated with structural damage.

3.4.2. Strong earthquakes conditions

Carreño (2010), concluded that for a small and moderate earth-quake with an absence of damage, the dynamic parameters of the CChC Building change in a range between 4-9 % for the frequencies [6], and damping ratios differ between 1-9 % [46].

The earthquake dated February 27, 2010, whose magnitude was $M_w = 8.8$ (or event 27F for brevity), has been recognized as one of the largest recorded earthquakes in history. Regarding the reports [6], the structure suffered minor and moderate damage related to non-structural elements (partitions, ceiling, etc.) and some visible shear cracks in the perimeter façade elements (Figure 3.10).

Carreño & Boroschek (2011) compared the dynamic parameters of the CChC Building before and after the 27F seismic event [6]. The results are presented in Table 3.4 and Table 3.5. On average, the frequencies reduced their value by 18 % (Figure 3.11), while the damping ratios

don't show a clear trend (Figure 3.12).

Table 3.4: Evolution of frequencies for ambient conditions. Before and after the 27F event (Carreño & Boroschek, 2011 [6])

Mode	**Frequencies before 27F [Hz]**	**Frequencies after 27F [Hz]**	**Relative difference [%]**
1	1.01	0.84	16.83
2	1.03	0.86	16.50
3	1.54	1.22	20.78
4	3.45	2.91	15.65
5	3.44	2.86	16.86
6	4.62	3.67	20.56

Table 3.5: Evolution of damping ratios for ambient conditions. Before and after the 27F earthquake (Carreño & Boroschek, 2011 [6]).

Mode	**Damping ratios before 27F [%]**	**Damping ratios after 27F [%]**	**Relative difference [%]**
1	0.6	0.6	0.0
2	0.7	0.6	14.3
3	0.6	0.8	33.3
4	1.1	1.1	0.0
5	1.2	1.1	8.3
6	1.1	1.1	0.0

Figure 3.10: Structural and non-structural damage for 27F event in the CChC Building (Photos: Bartolomé & Caroca, 2010 [47]).

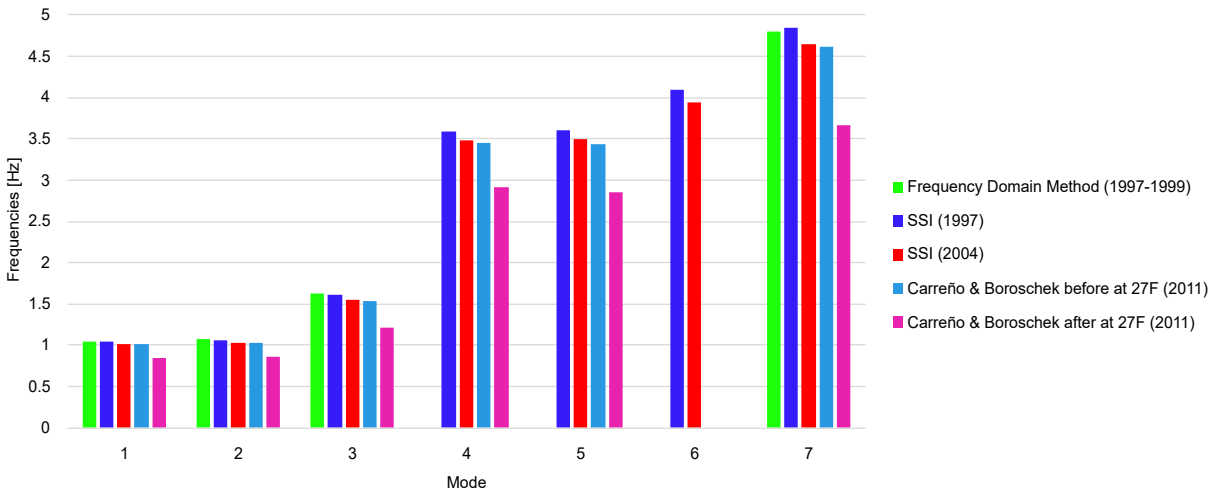

Figure 3.11: CChC Building's frequencies identified for different conditions.

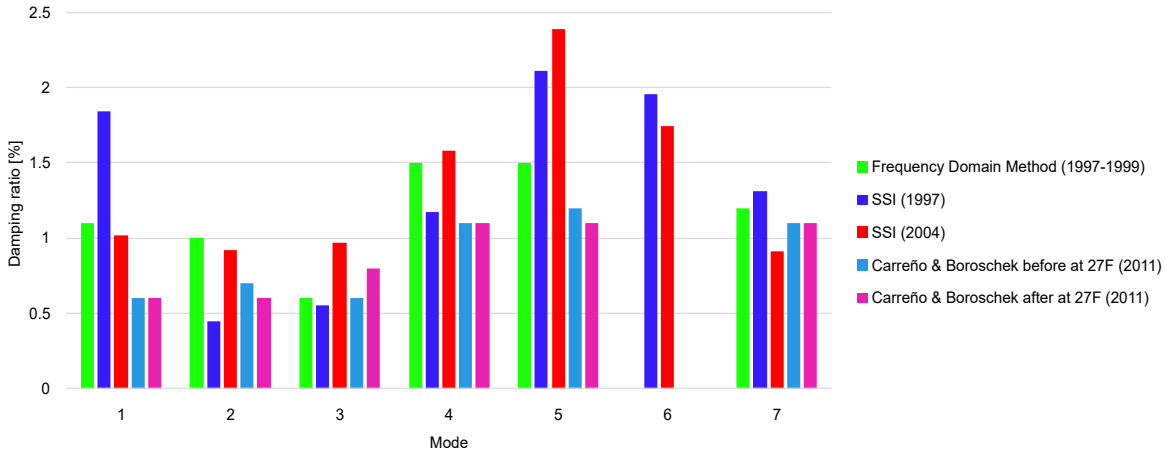

Figure 3.12: CChC Building's damping ratios identified for different conditions.

In general, the frequencies present low variations in their values, except for the frequencies identified after the 27F event, where a strong decrease is observed. On the other hand, the damping ratios show high variations and do not have a clear trend. These parameters will be discussed in more detail in Chapter 4.

Chapter 4

Description of Seismic Events and Chilean Chamber of Construction Building Modal Parameter Identification

This chapter presents the seismic database that will be used on the FE model update algorithm. The main seismic characteristics of each event are summarized and presented. Finally, the seismic records are processed to identify the modal parameters of the building and visualize the periods in which the structure presents changes in its properties, and notify possible structural damages.

4.1. Earthquake's characteristics

The main characteristics of seismic events and the maximum accelerations measured by the instrumentation system are shown below. The complete data of the events can be reviewed in Appendix B of this work.

Figure 4.1 shows the epicenters' location of the seismic events used, which range from Coquimbo (a region with the same name) to Concepción (Bio-Bio region). The epicenter of greatest magnitude is located in the Maule region, corresponding to the event of February 27, 2010, with a magnitude of $M_w = 8.8$. On the other hand, Figure 4.2 shows the depths of the events (hypocenters). Some typical mechanisms of the interaction between South America and the Nazca plate can be appreciated, these include interplate (27F) and intraplate earthquakes [48].

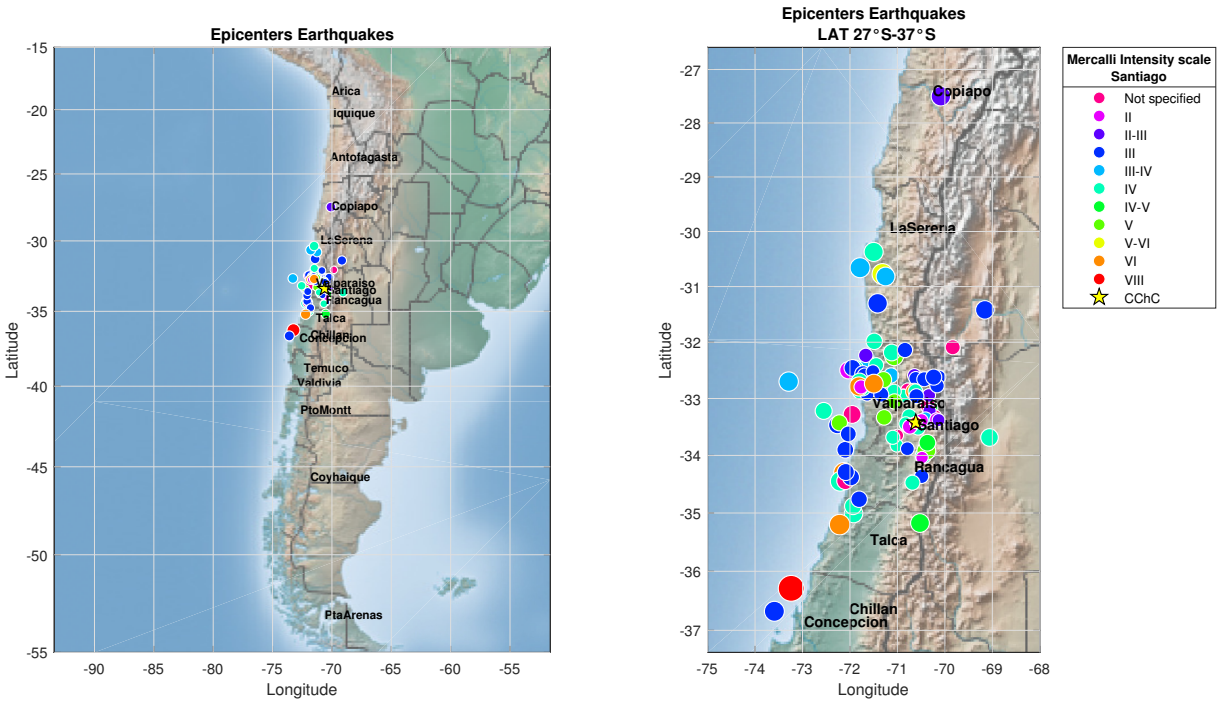

Figure 4.1: Seismic events location. The size of the symbols gives a reference to the magnitude of the event and the color to the Mercalli intensity scale. Map generated with the Mapping Toolbox of MATLAB [38].

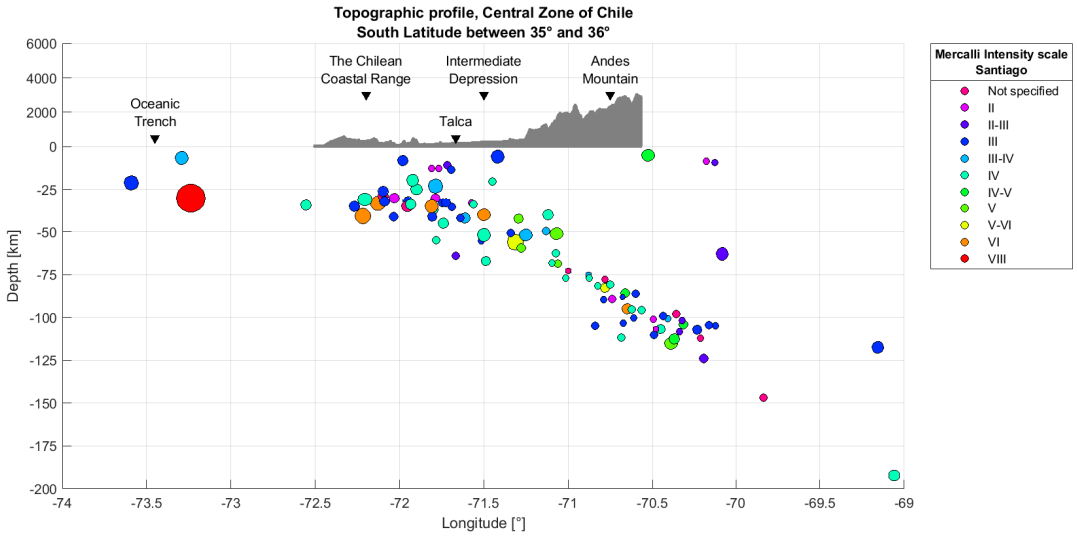

Figure 4.2: Seismic events depth. The size of the symbols gives a reference to the magnitude of the event and the color to the Mercalli intensity scale. Figure adapted from ref. [49].

Additionally, histograms of the distribution of seismic events, according to their magnitude and intensity in Santiago, are shown in Figure 4.3 and Figure 4.4.

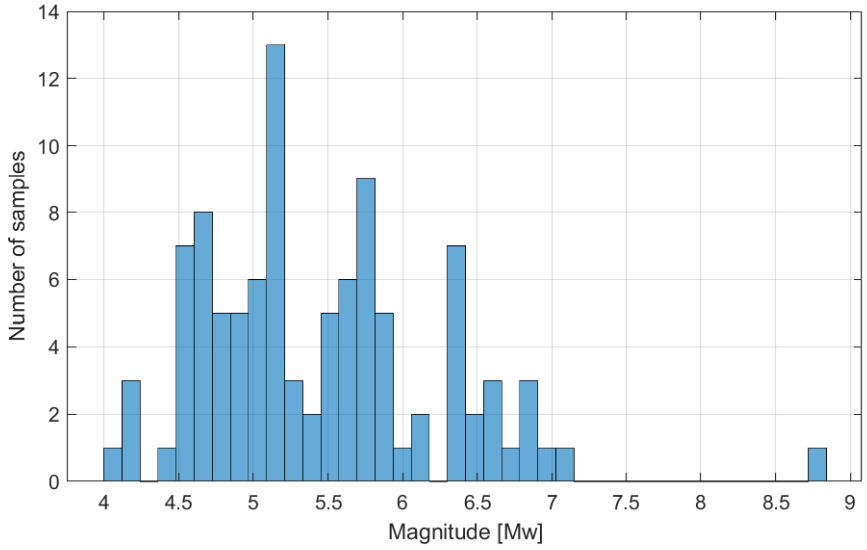

Figure 4.3: Distribution of events according to their magnitude.

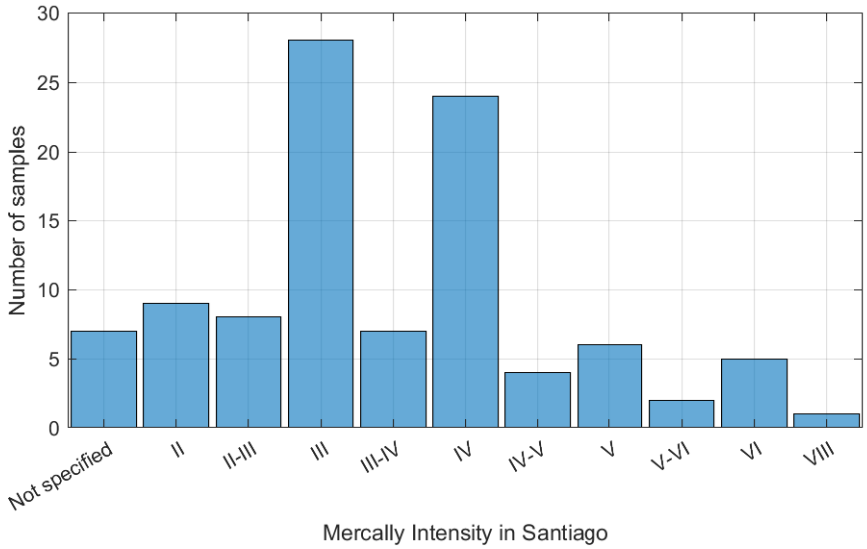

Figure 4.4: Distribution of events according to their intensity in Santiago.

4.2. Distribution of Maximum Accelerations on the Building

This section summarizes the parameters derived from seismic records such as the PGA (Peak Ground Accelerations), Maximum Accelerations on the building, and the Arias' Intensity (1970) [50].

Given the high computation demand required by the Sequential FE model updating algorithm, for their application, each seismic record was resampled from 200 [Hz] to 50 [Hz]. Furthermore, to apply the algorithm, only the "strong phase" of the earthquake was con-

sidered, since it is the one that provides more information about the finite element model parameters to be estimated (this will be discussed in more detail in Chapter 5). The time interval of the strong phase of the accelerations records was obtained through the criterion of "significant duration" defined by Trifunac and Brady [51], which is defined as the time in which 5 % and 95 % of the Arias' Intensity of the seismic record (Equation 4.1). Figure 4.5 shows a seismic record cut by the significant duration criterion.

$$I_A = \frac{\pi}{2g} \int_0^t [a(t)]^2 \mathrm{dt} \tag{4.1}$$

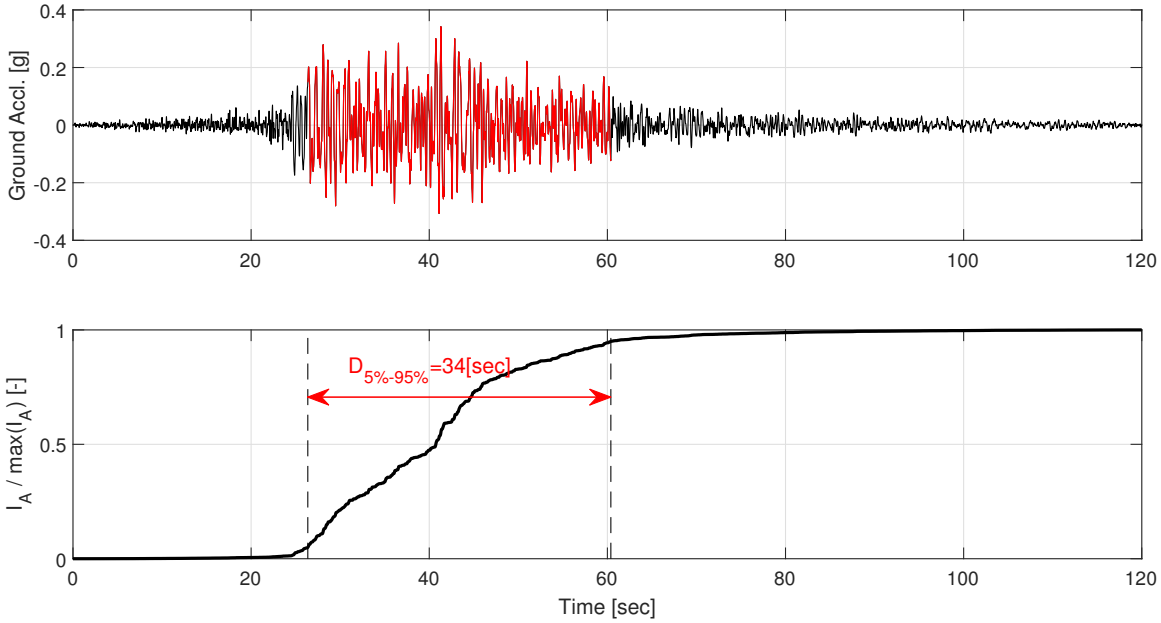

Figure 4.5: Strong phase obtained by the criterion of significant duration.

Figure 4.6 shows the peak ground accelerations (PGA) and the maximum accelerations on the building for each event presented in the previous section. It can be seen that most of the PGAs do not exceed 6 %g, except for the 27F event's PGA. The PGA in the mentioned event reached values near to 10 %g in the E-W and vertical direction, and 14 %g for the N-S direction. On the other hand, the maximum accelerations on the building are concentrated in the range of 0.5-5 %g, and the maximum acceleration was 30 %g for the 27F event. Figure 4.7 shows the distribution of accelerations on the building as a function of height. As can be seen, the 30 % acceleration was reached on the 18$^{\text{th}}$ floor in the N-S direction.

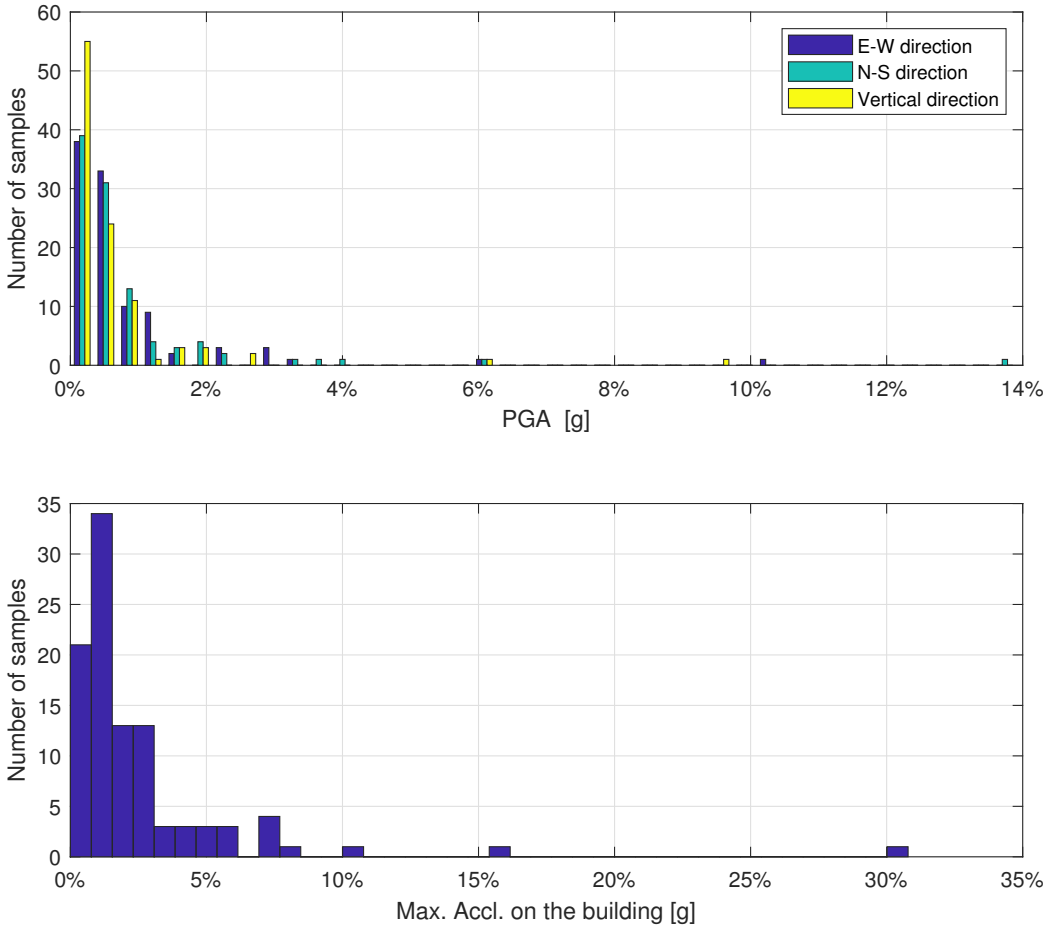

Figure 4.6: Distribution of events according to their PGA and Maximum Accelerations in the CChC Building.

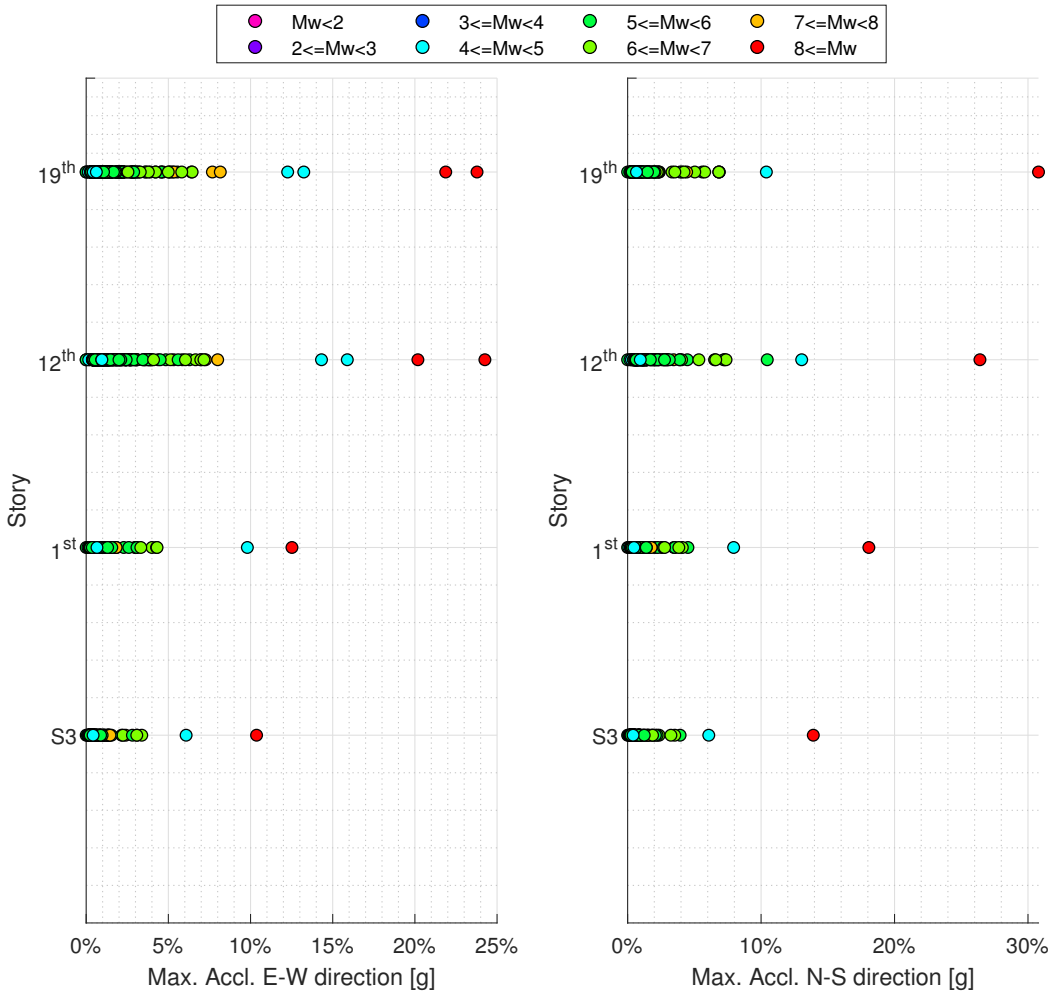

Figure 4.7: Maximum accelerations on the building distributed in height.

4.3. Modal Parameters Identification using Seismic Records

As mentioned in the introduction to this work, a way to evaluate the state of the structure is through monitoring its modal properties, frequencies, mode-shapes, and modal damping ratios. The modal properties were identified using the acceleration records.
To establish the building modal properties two identification techniques are used. The first identification technique is the Spectrogram, a technique that is developed in the domain of time and frequencies [46]. The second is the MOESP (Multi-Output Error State Space) identification technique, which develops in the time domain [33].

4.3.1. Identification method: Spectrogram

The spectrogram is the representation of a signal in the time-frequency domain. To calculate a spectrogram, it is necessary to calculate the Fast Fourier transform of the signal for a defined time window and then shift the time window at a constant step considering the overlap between windows. Channels #11 and #12 were selected for the identification method. These channels have more energy or amplitude, so the building frequencies are more

distinguishable in the spectrogram. Channels #11 and #12 are located on the 18th story of the building (Figure 3.9). The spectrograms of the other channels can be seen in Appendix C.

For spectrograms, the strong phases of the acceleration records with a sample rate of 50 [Hz] were concatenated. The spectrogram looks at the evolution of the building's predominant frequencies for the period under study. For the spectrograms shown in Figures 4.8 to 4.13 a time windows of 15 seconds with an overlap of the 10 % were used.

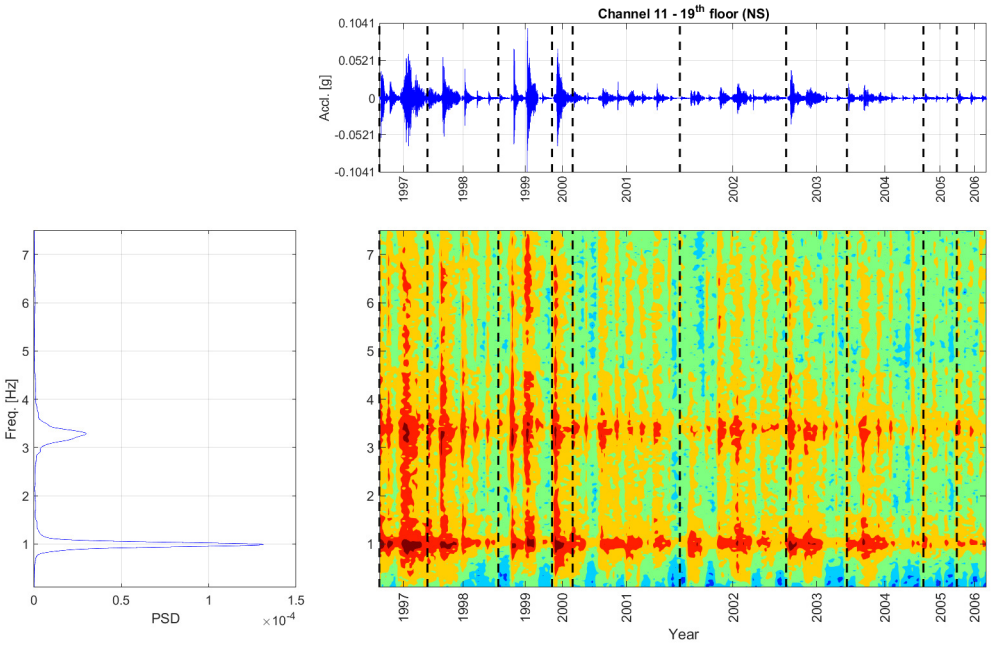

Figure 4.8: Spectrogram for Channel #11 during the periods 1997 to 2006 (the dashed line indicates the separations between years).

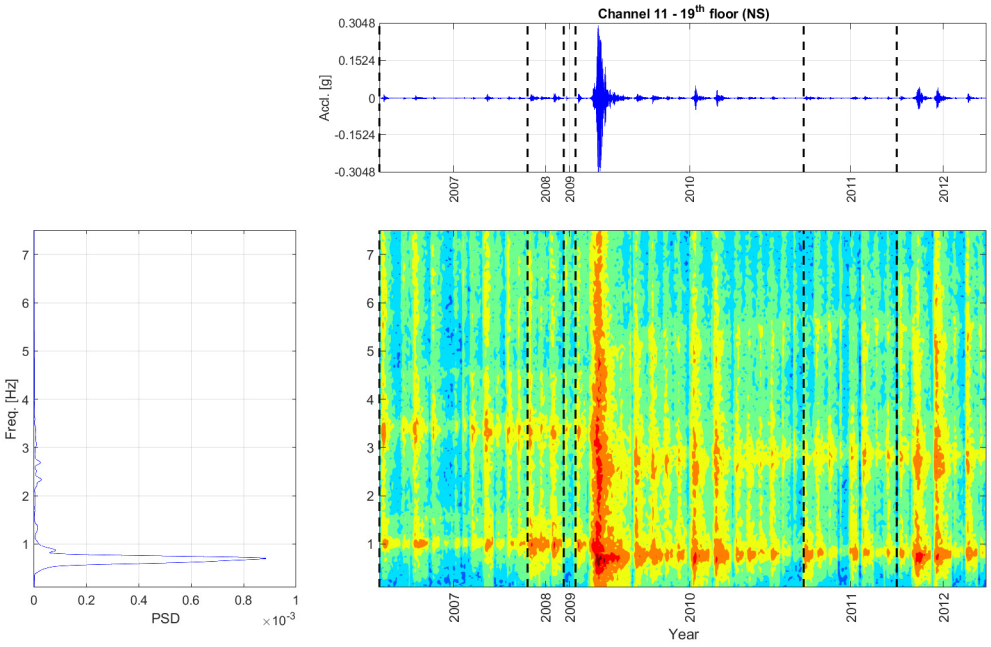

Figure 4.9: Spectrogram for Channel #11 during the periods 2007 to 2012 (the dashed line indicates the separations between years).

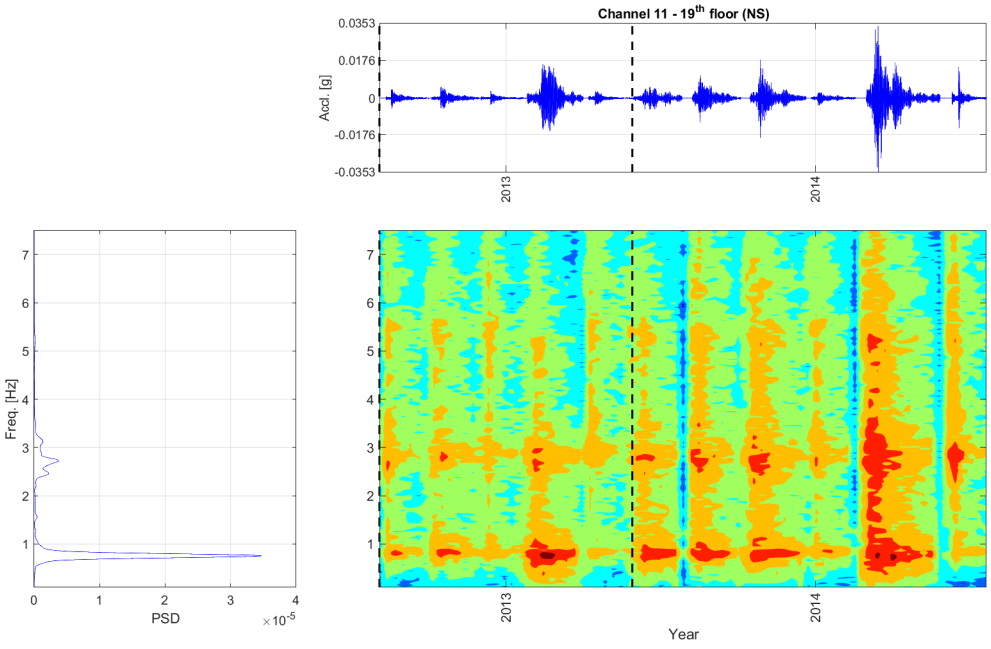

Figure 4.10: Spectrogram for Channel #11 during the periods 2013 to 2014 (the dashed line indicates the separations between years).

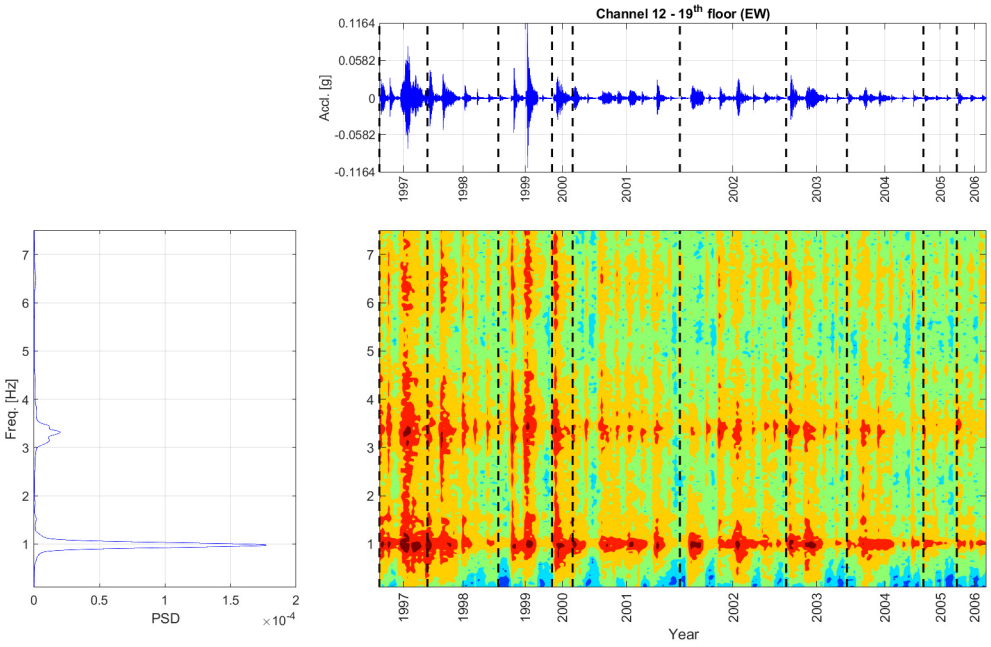

Figure 4.11: Spectrogram for Channel #12 during the periods 1997 to 2006 (the dashed line indicates the separations between years).

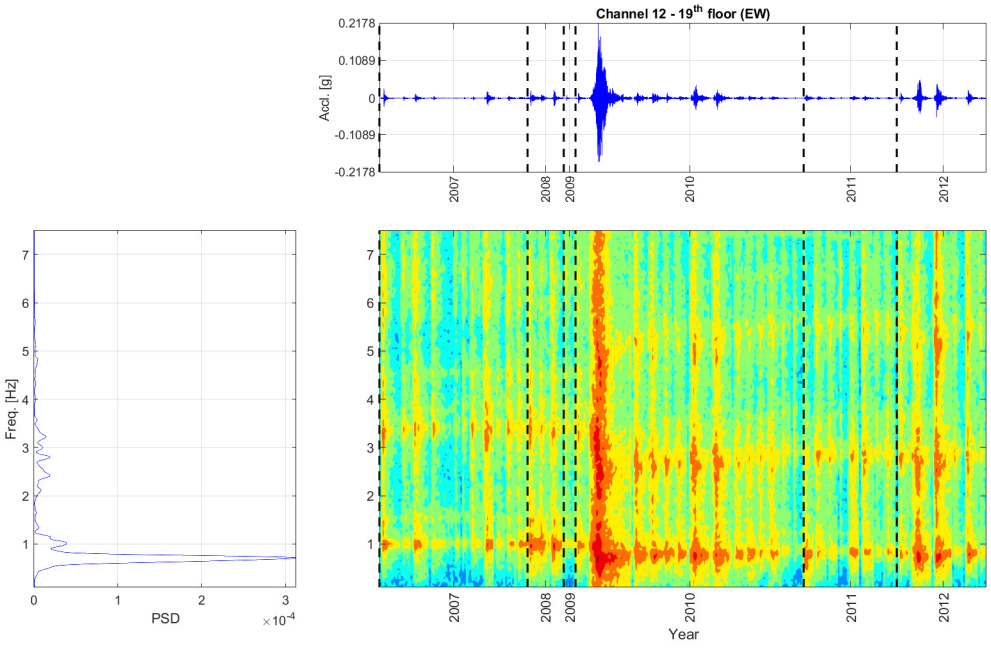

Figure 4.12: Spectrogram for Channel #12 during the periods 2007 to 2012 (the dashed line indicates the separations between years).

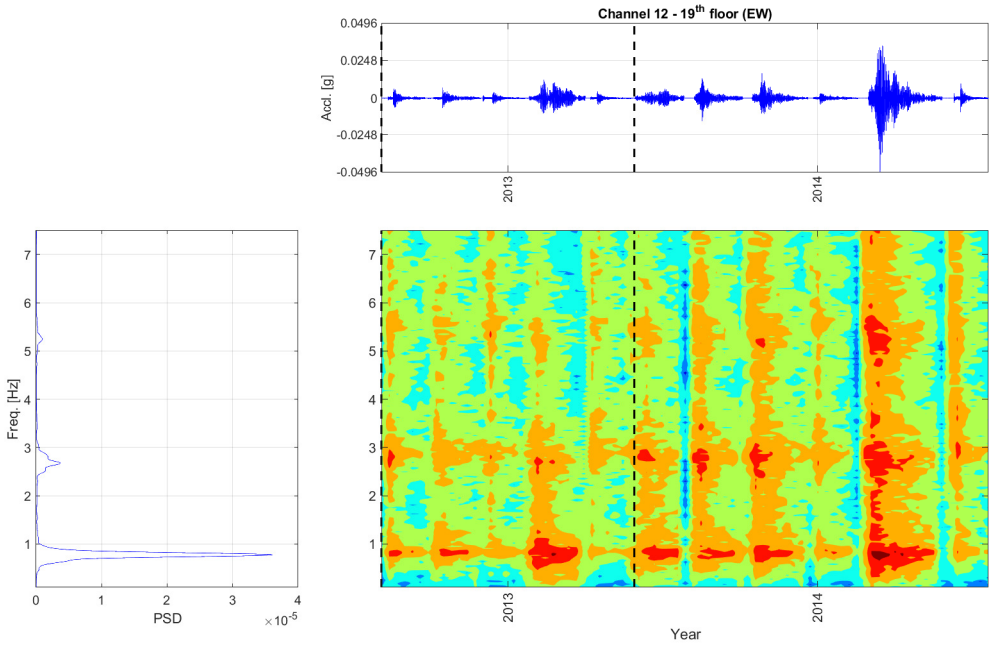

Figure 4.13: Spectrogram for Channel #12 during the periods 2013 to 2014 (the dashed line indicates the separations between years).

As can be seen from the spectrograms, the first modes are around 1 [Hz], but after the 27F event, their frequencies permanently decreased to 0.8 [Hz] as was observed in Carreño & Boroschek [6] with the MIMO identification technique. The same can be observed for modes above 3.5 [Hz].

4.3.2. Identification method: MOESP

The MOESP subspace identification method identifies the modal properties of the system through a linear state-space model [24, 21]. The state-space model at time step i ($i = 1, 2, ..., k$, where k denotes the total number of time steps) is expressed as

$$\boldsymbol{x}_{i+1} = \boldsymbol{A}\boldsymbol{x}_i + \boldsymbol{B}\boldsymbol{u}_i \tag{4.2}$$

$$\boldsymbol{y}_i = \boldsymbol{C}\boldsymbol{x}_i + \boldsymbol{D}\boldsymbol{u}_i \tag{4.3}$$

where Equations 4.2 and 4.3 are the state and output equations, respectively. $\boldsymbol{x} \in \mathbb{R}^{n_{dof} \times 1}$ is the state vector, $\boldsymbol{y} \in \mathbb{R}^{n_y \times 1}$ is the output vector, and $\boldsymbol{u} \in \mathbb{R}^{n_{\ddot{u}g} \times 1}$ is the input vector. The MOESP algorithm is used to get system matrices $\boldsymbol{A}$, $\boldsymbol{B}$, $\boldsymbol{C}$ and $\boldsymbol{D}$ from measured inputs $\boldsymbol{u}$ and outputs $\boldsymbol{y}$ using QR-factorization and singular value decomposition (SVD) operations [33]. The present work will use this method to obtain the dynamic parameters of the CChC Building ($\boldsymbol{A}$ and $\boldsymbol{C}$ matrices of the state-space model) from the data recorded by the accelerometers. For more details about the mathematical development, and application cases, the reader is referred to the works of Yoshimoto, 2005 [33], Villalpando, 2019 [21], and Paredes, 2019 [24]. For this work, the methodology presented by Villalpando, 2019, was used joint with stability diagrams proposed by Bakir, 2011 [52].

For the identification process, identification windows were defined with a duration of 6.0 seconds with an overlap of 80 % between them. An example of the estimation process is presented in Figures 4.14 and 4.17. These figures present the ground accelerations, and the frequencies identified per window. The modal parameters chosen were those that present the highest stability among windows. From these results, it is possible to observe how the frequencies decrease in the strong phase of the earthquake and reach up after the seismic event. These results were observed in Carreño, 2009 [5]. From the mode shapes identified in Figures 4.15 and 4.16, it is observed that modes 1, 2, 4, and 5 belong to translational modes. On the other hand, modes 3 and 6 are associated with torsion.

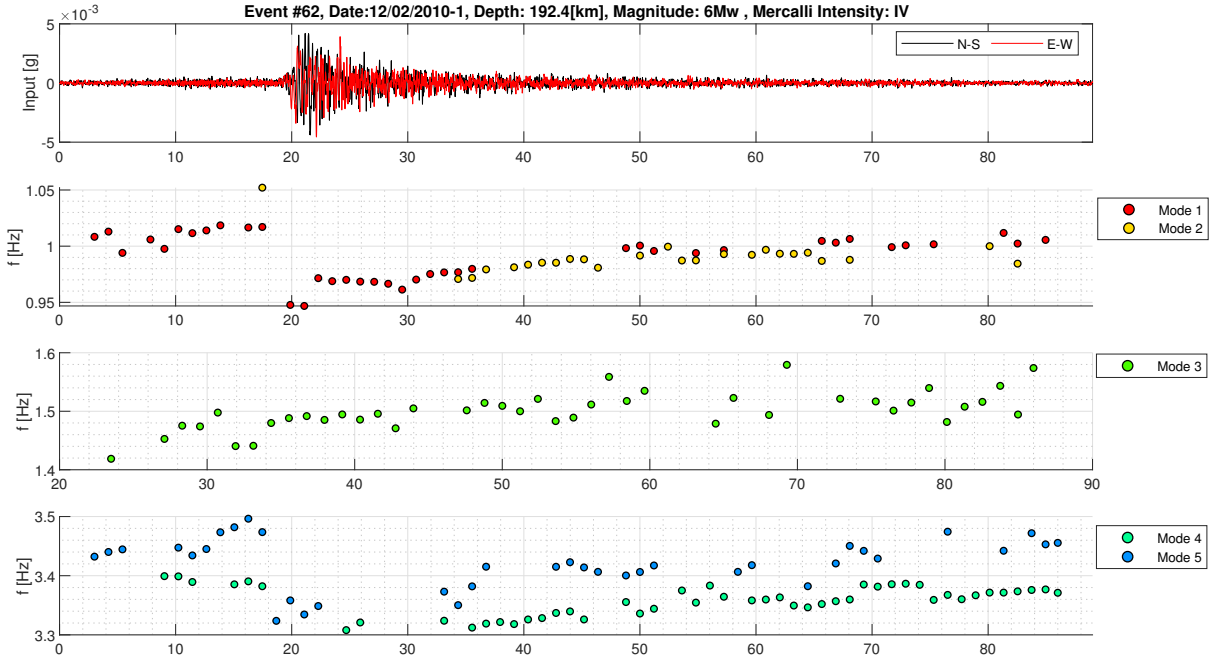

Figure 4.14: Frequencies identified per window with subspace identification method MOESP for seismic event #62.

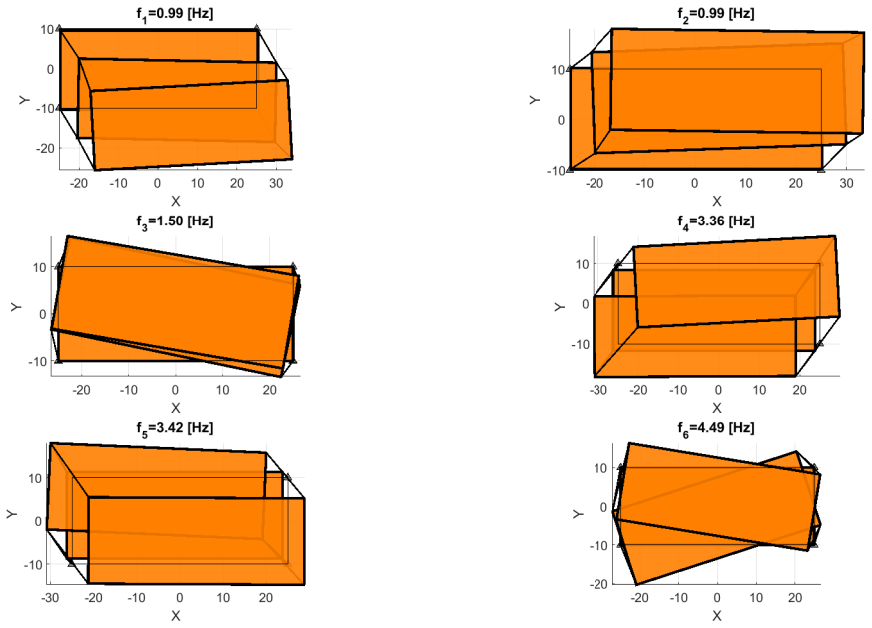

Figure 4.15: Modes-shapes identified by subspace identification method MOESP for seismic event #62, plant view.

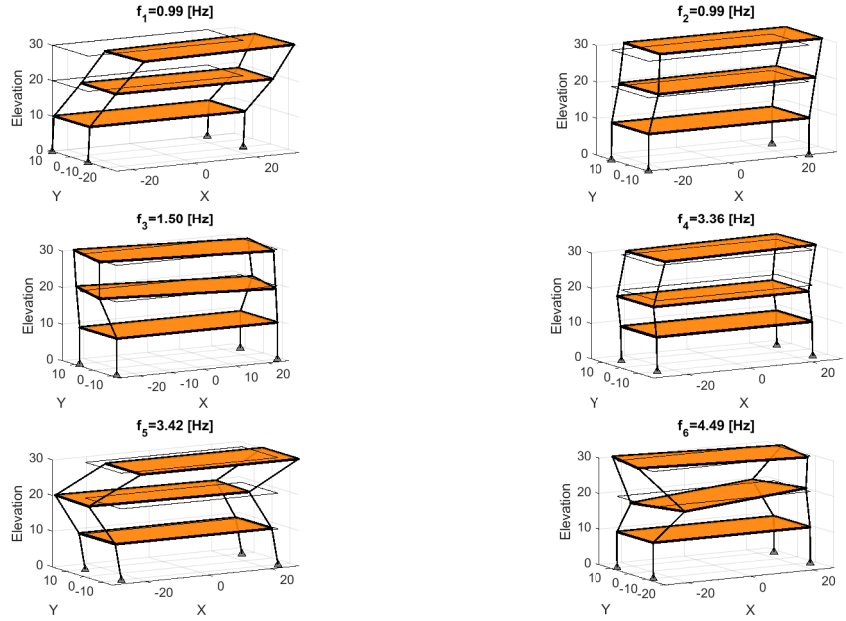

Figure 4.16: Modes-shapes identified by subspace identification method MOESP for seismic event #62, isometric view.

A particular case is presented in Figure 1, where the seismic record #63 associated with the mega-earthquake event is presented. The high resistance demand for the building produces a great reduction on the building frequencies for the first modes. It can be seen at the moment

that the ground motion reaches accelerations near to 5 %g, after the 60 seconds, where the frequencies show a decrease of around 20 % of their initial value for the first six modes one time the seismic event finished.

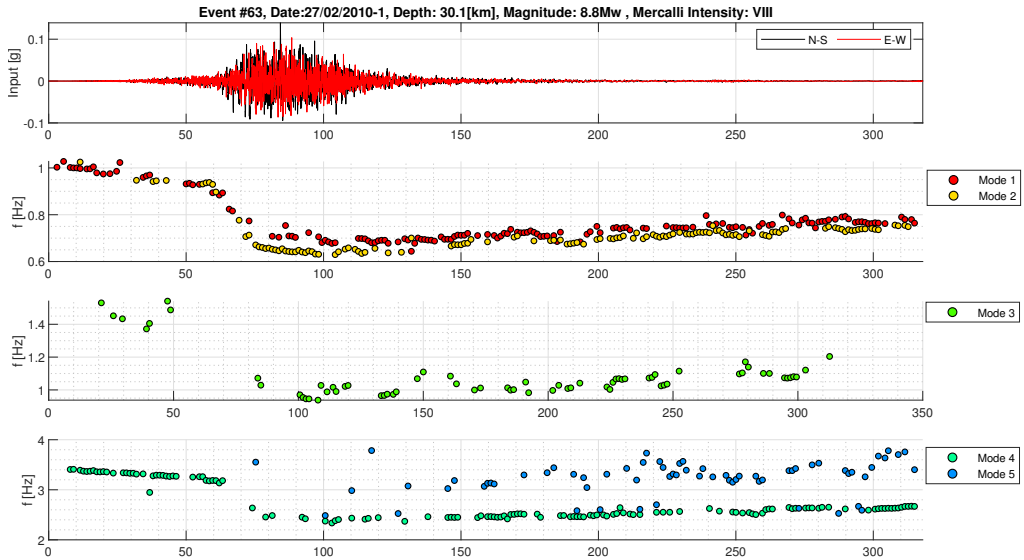

Figure 4.17: Frequencies identified per window with subspace identification method MOESP for seismic event #63.

The evolution of the frequencies and damping ratios over time are shown in Figures 1 and 2. Note the reduction in the frequencies values after 27F, and the slight growth for damping ratios in the aforementioned seismic event.

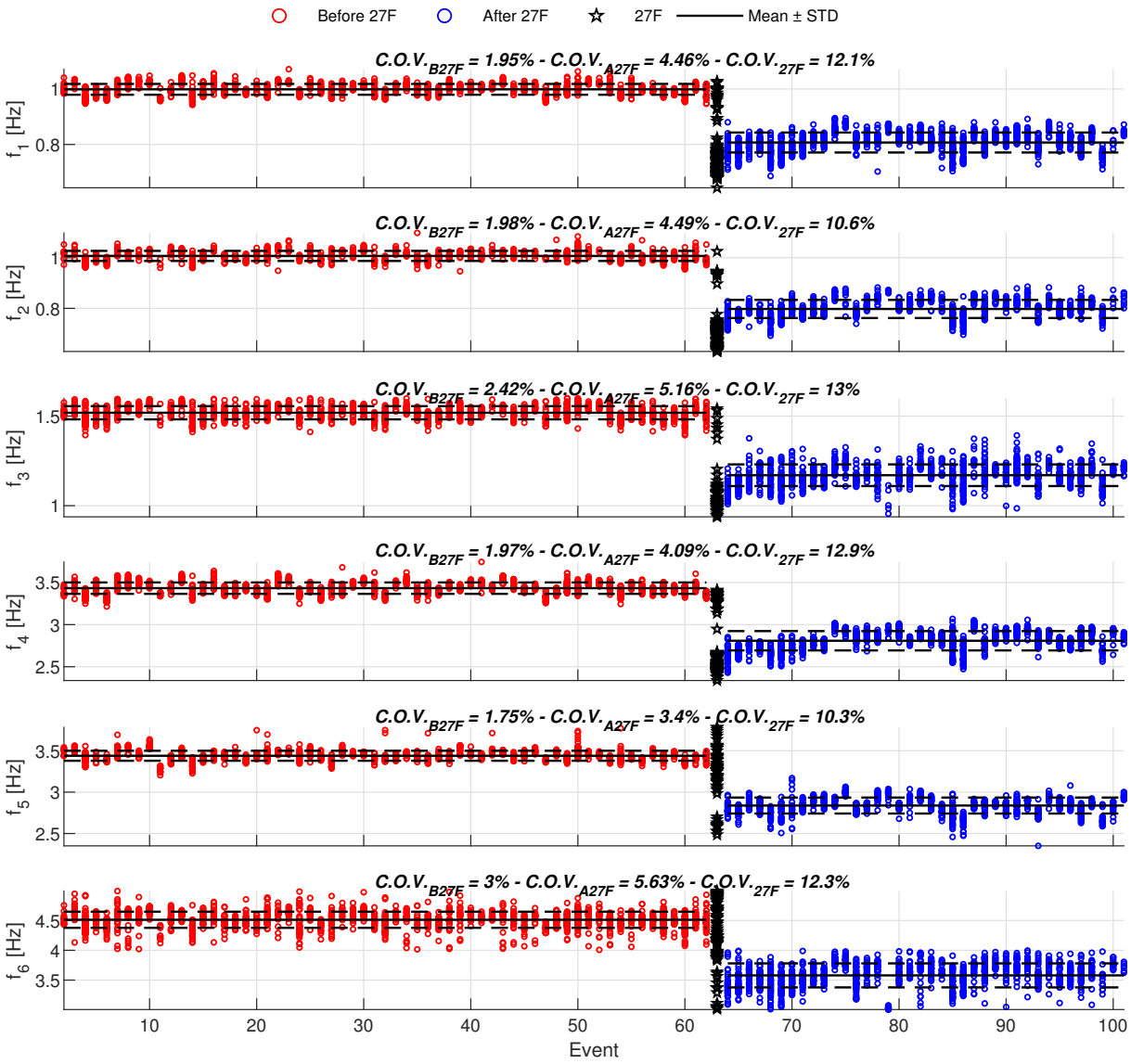

Figure 4.18: Evolution of the frequencies identified for all windows of each event.

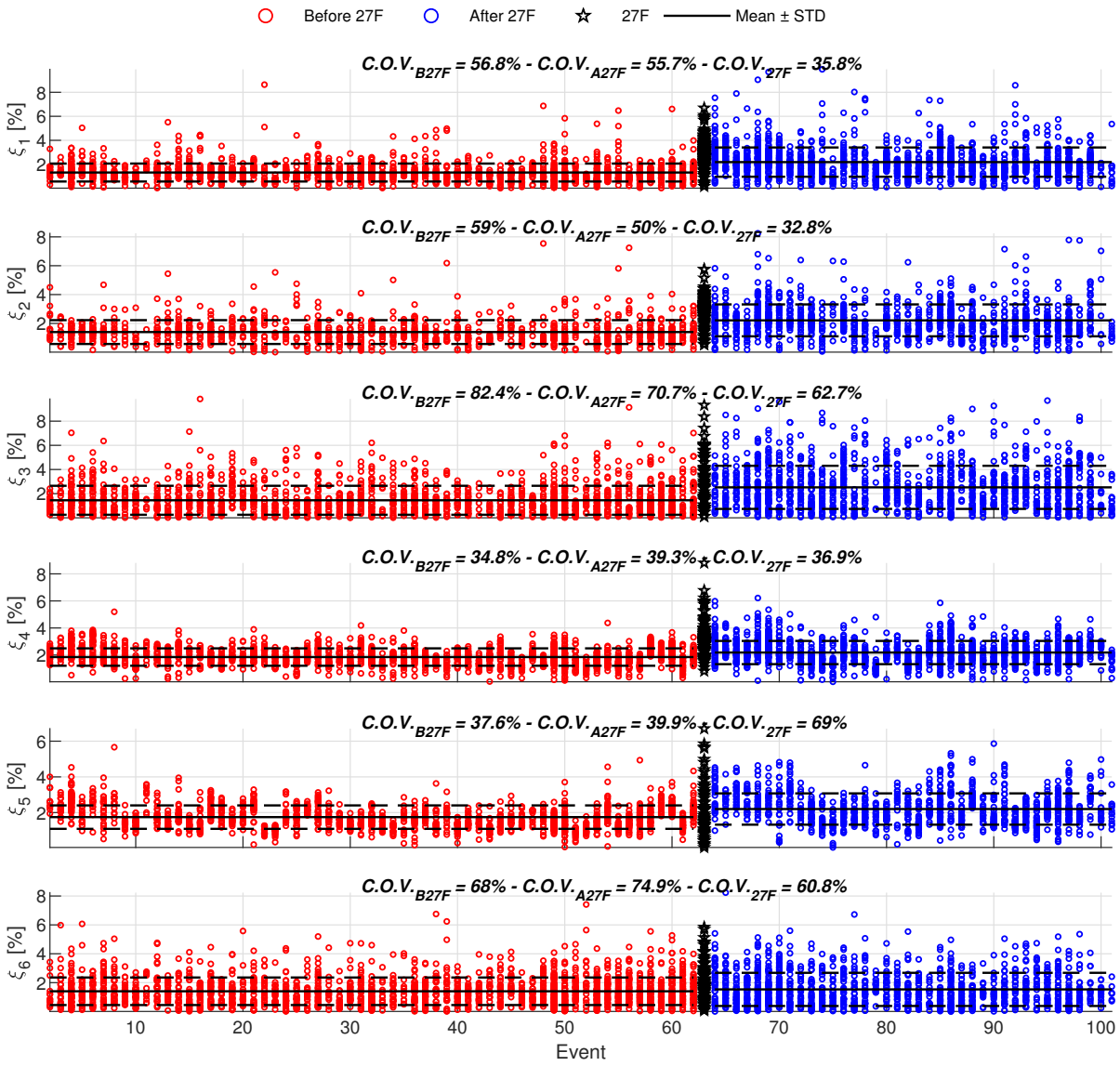

Figure 4.19: Evolution of the damping ratios identified for all windows of each event.

Now, the histograms from modal frequencies and damping ratios are showed for the results got on the identification process for each time window.

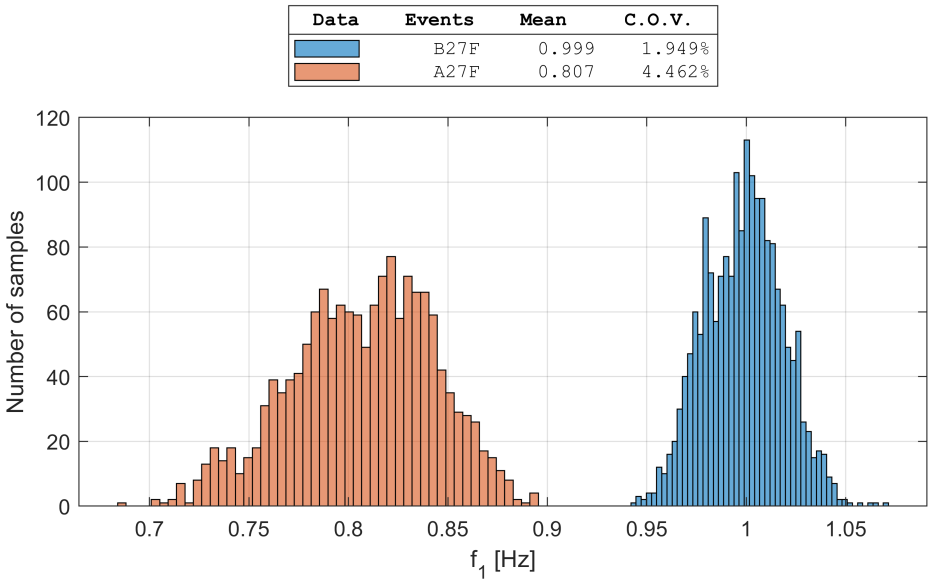

Figure 4.20: Frequencies histograms for Mode 1 for the period under study.

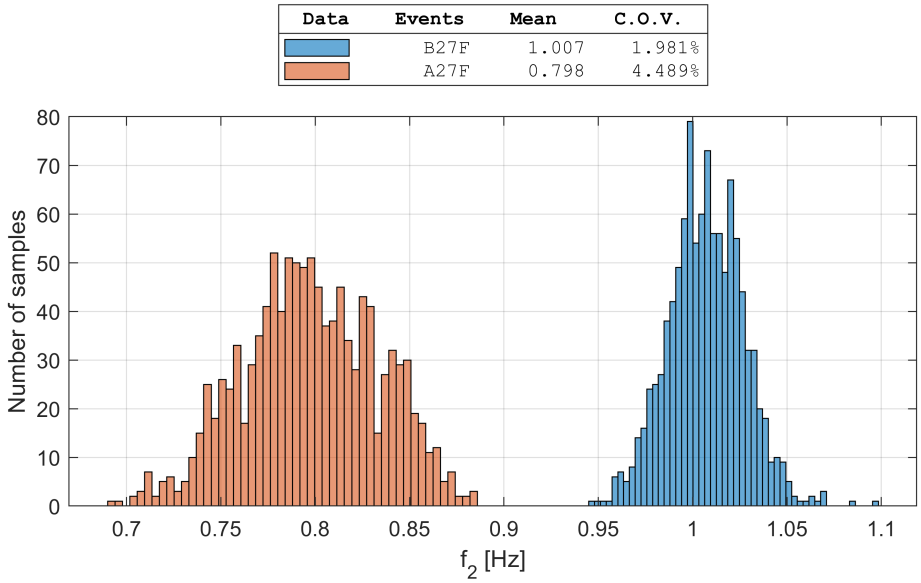

Figure 4.21: Frequencies histograms for Mode 2 for the period under study.

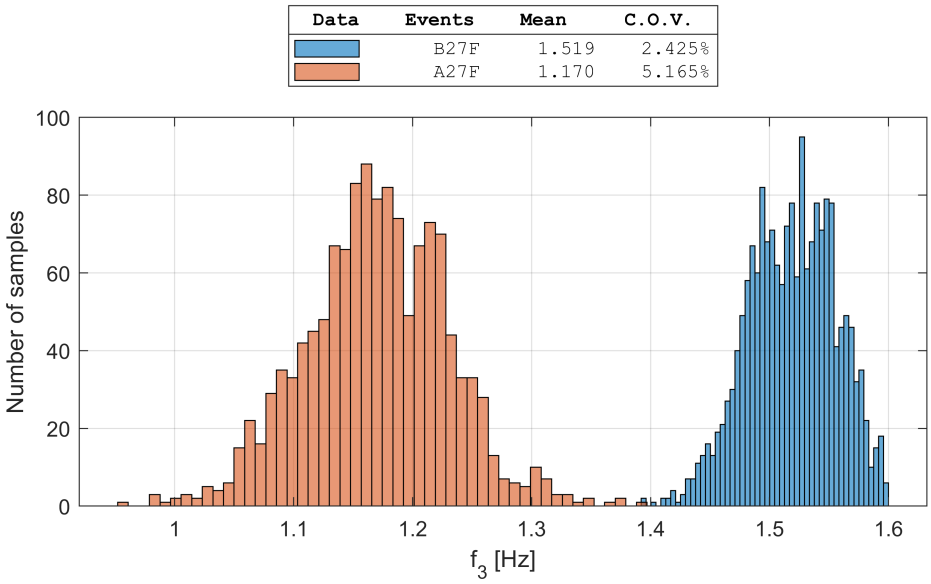

Figure 4.22: Frequencies histograms for Mode 3 for the period under study.

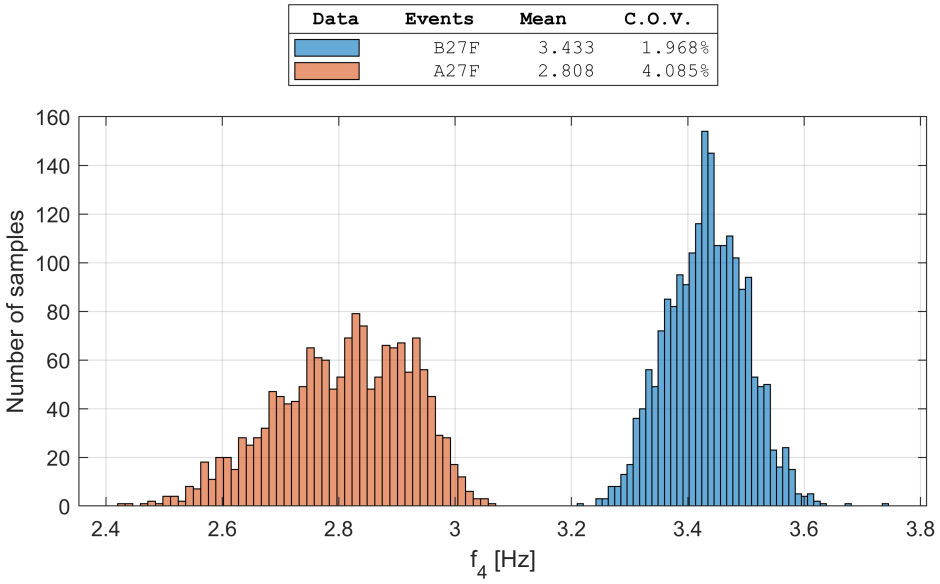

Figure 4.23: Frequencies histograms for Mode 4 for the period under study.

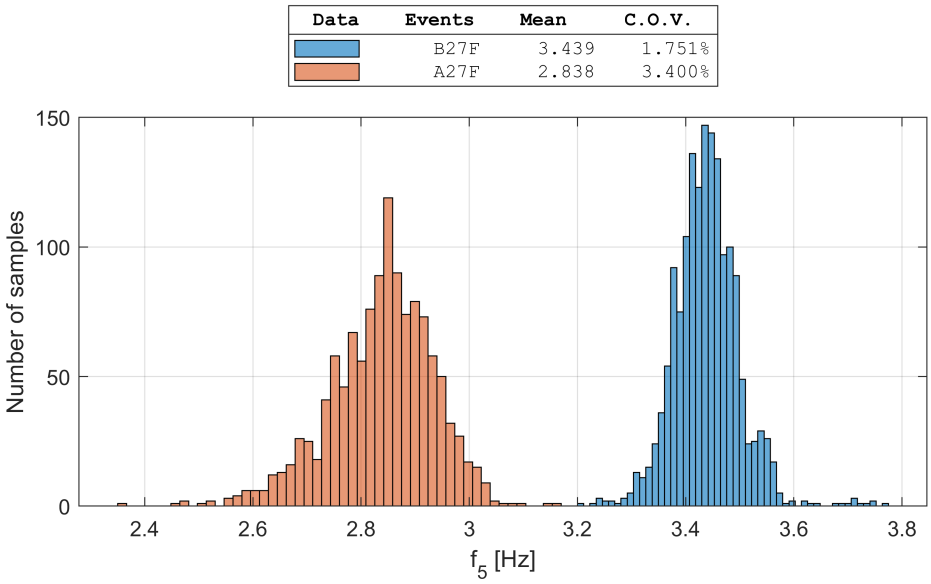

Figure 4.24: Frequencies histograms for Mode 5 for the period under study.

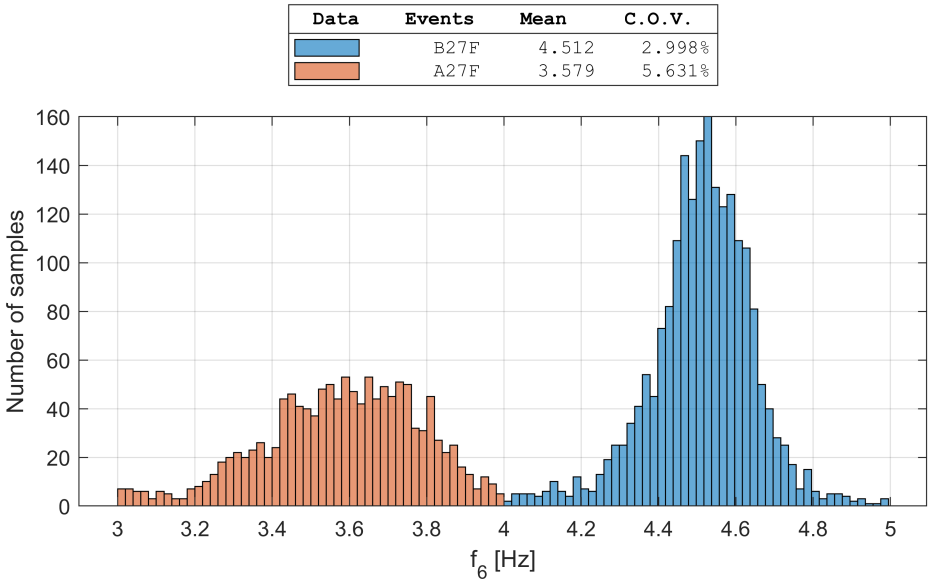

Figure 4.25: Frequencies histograms for Mode 6 for the period under study.

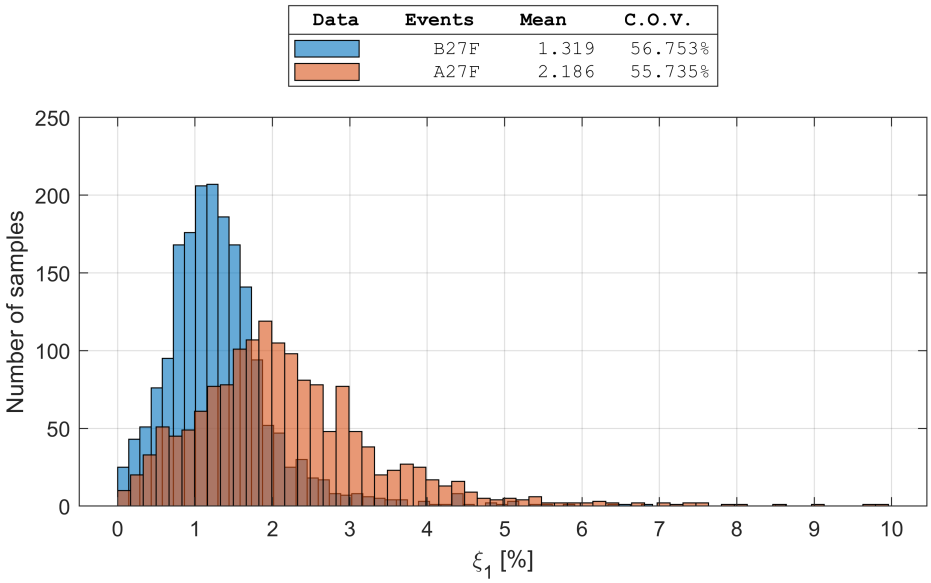

Figure 4.26: Damping ratios histograms for Mode 1 for the period under study.

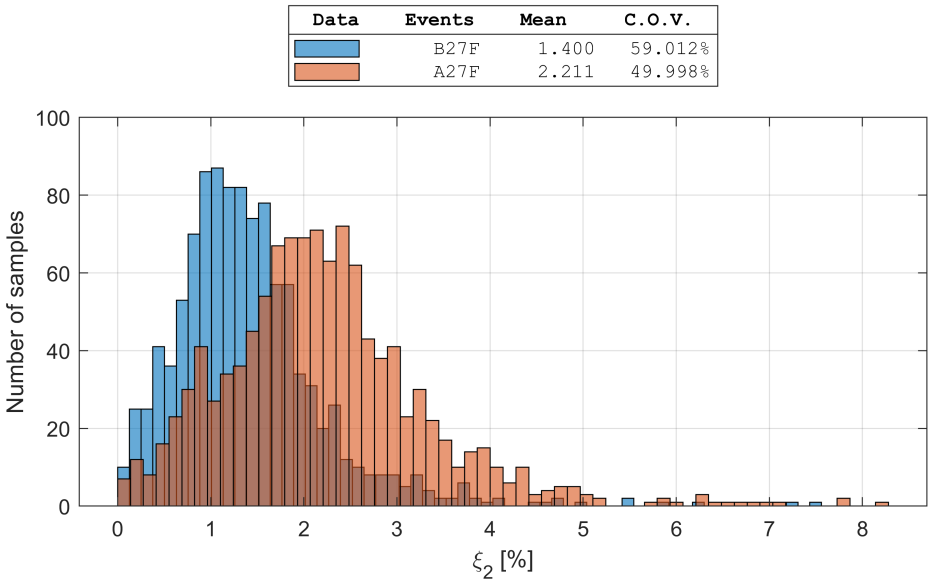

Figure 4.27: Damping ratios histograms for Mode 1 for the period under study.

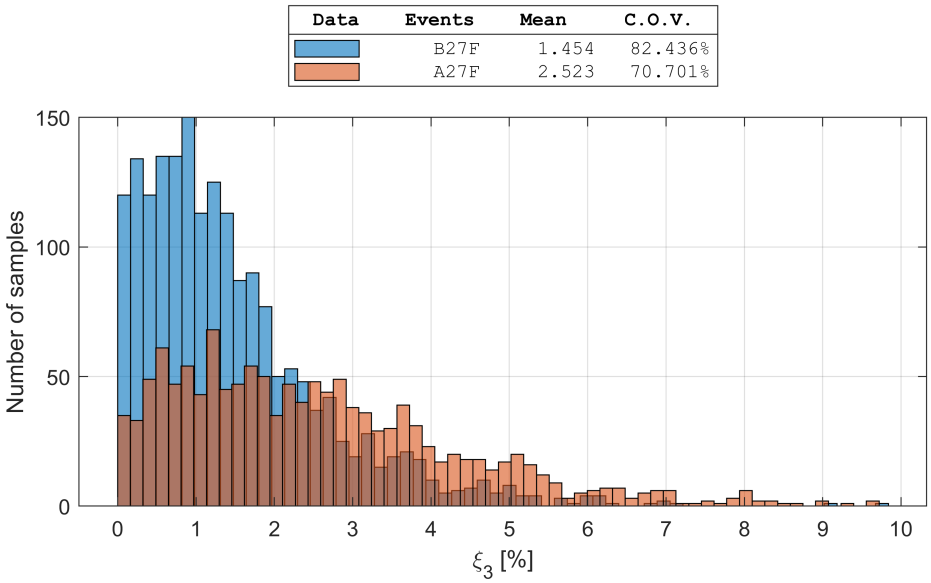

Figure 4.28: Damping ratios histograms for Mode 3 for the period under study.

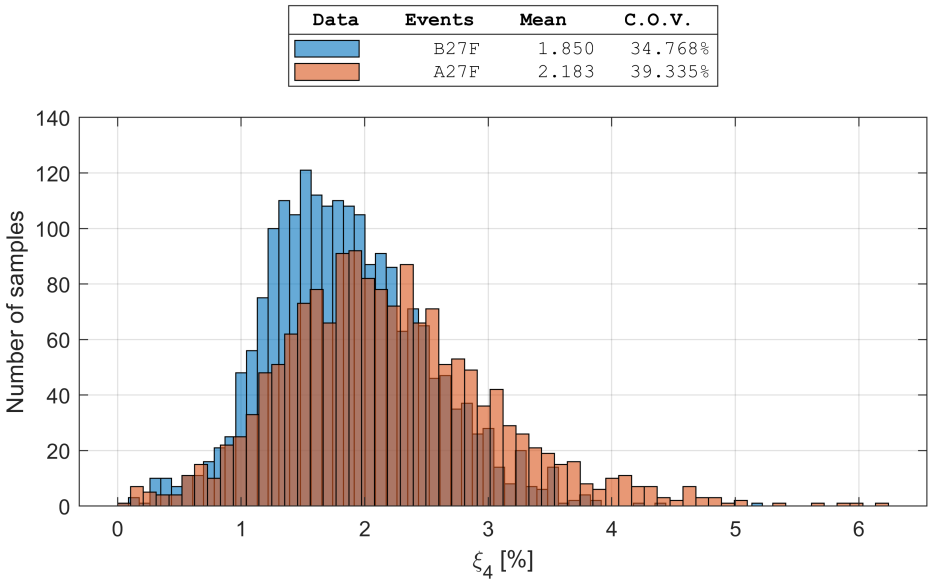

Figure 4.29: Damping ratios histograms for Mode 4 for the period under study.

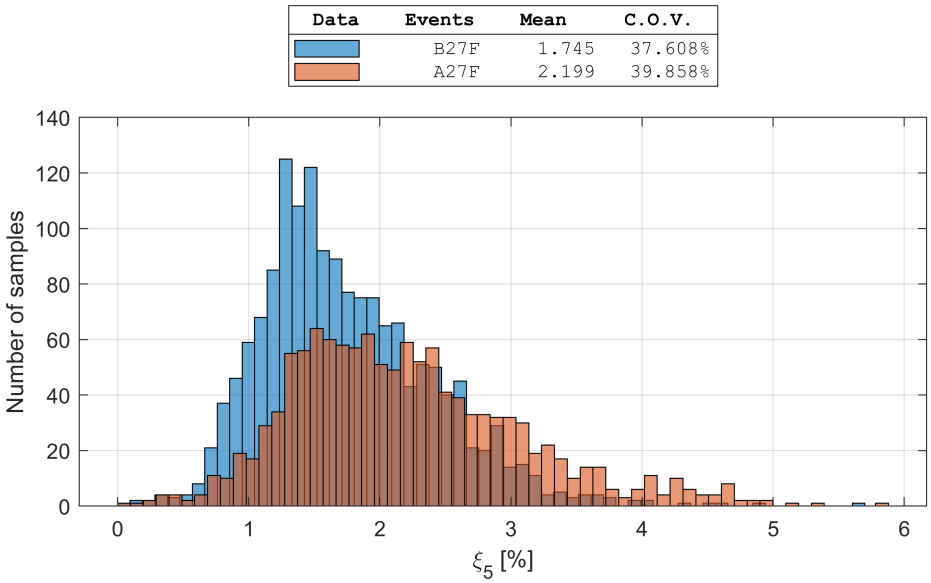

Figure 4.30: Damping ratios histograms for Mode 5 for the period under study.

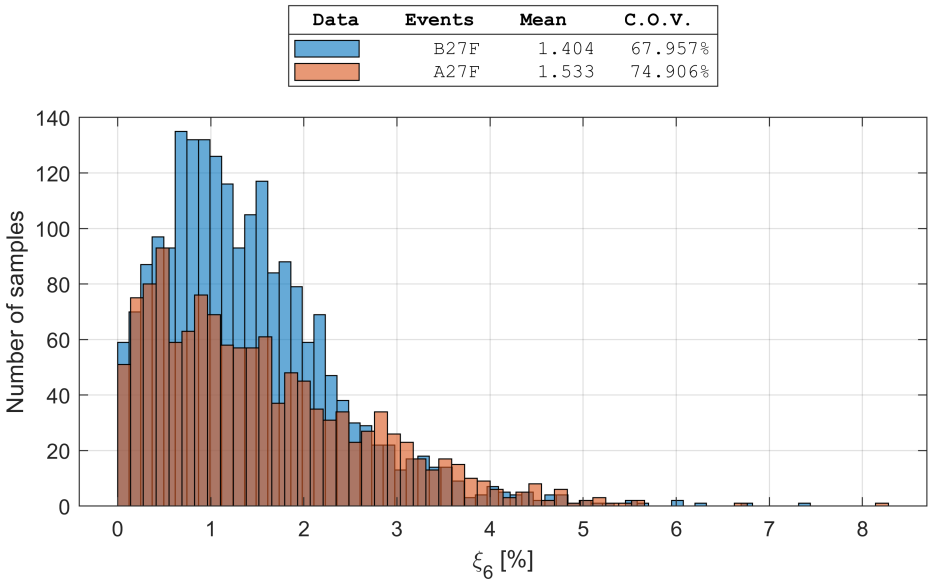

Figure 4.31: Damping ratios histograms for Mode 6 for the period under study.

Table 4.1: Summary of the identified frequencies before and after the mega-earthquake.

	Frequencies before 27F		**Frequencies after 27F**		**Relative difference [%]**
Mode	**Mean [Hz]**	**COV [%]**	**Mean [Hz]**	**COV [%]**	
1	0.999	1.949	0.807	4.462	19.219
2	1.007	1.981	0.798	4.489	20.755
3	1.519	2.425	1.170	5.165	22.976
4	3.433	1.968	2.808	4.085	18.206
5	3.439	1.751	2.838	3.400	17.476
6	4.512	2.998	3.579	5.631	20.678

Table 4.2: Summary of the identified damping ratios before and after the mega-earthquake.

	Damping ratios before 27F		**Damping ratios after 27F**		**Relative difference [%]**
Mode	**Mean [%]**	**COV [%]**	**Mean [%]**	**COV [%]**	
1	1.319	56.753	2.186	55.735	65.732
2	1.400	59.012	2.211	49.998	57.929
3	1.454	82.436	2.523	70.701	73.521
4	1.850	34.768	2.183	39.335	18.000
5	1.745	37.608	2.199	39.858	26.017
6	1.404	67.957	1.533	74.906	9.188

Also, the mode-shapes' components in directions north-south (u_o), east-west (v_o), and torsional (θ_o) were computed referenced to the center of gravity (see Figure 4.32), as follow [30]

$$\begin{aligned} u_1 &= u_o - \theta_o y_1 \\ v_1 &= v_o + \theta_o x_1 \\ v_2 &= v_o + \theta_o x_2 \end{aligned} \tag{4.4}$$

$$\begin{Bmatrix} u_1 \\ v_1 \\ v_2 \end{Bmatrix} = \begin{bmatrix} 1 & 0 & -y_1 \\ 0 & 1 & x_1 \\ 0 & 1 & x_2 \end{bmatrix} \begin{Bmatrix} u_o \\ v_o \\ \theta_o \end{Bmatrix} \tag{4.5}$$

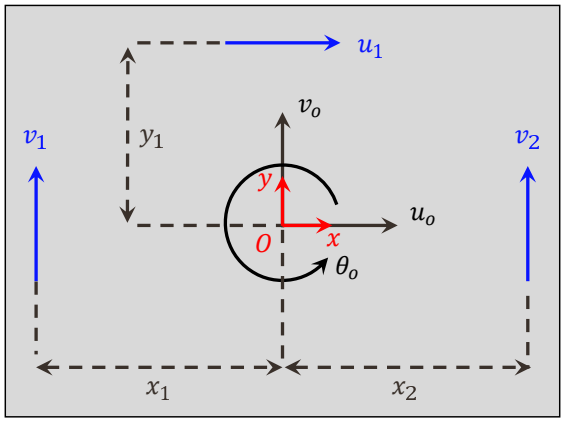

Figure 4.32: Sensors locations for 12$^{\text{th}}$ and 19$^{\text{th}}$ floors. Here, u_o, v_o, and θ_o denote the modal components at the referenced point $O = (0, 0)$, while u_1, v_1, and v_2 denote the modal components refereed to the original position.

The distances x_1, x_2, y_1 were selected according to the ETABS model referred to the center of mass of the floor. The torsional component for the 1$^{\text{st}}$ floor is not computed due to the plant has only one sensor in each horizontal direction (Table 3.2).

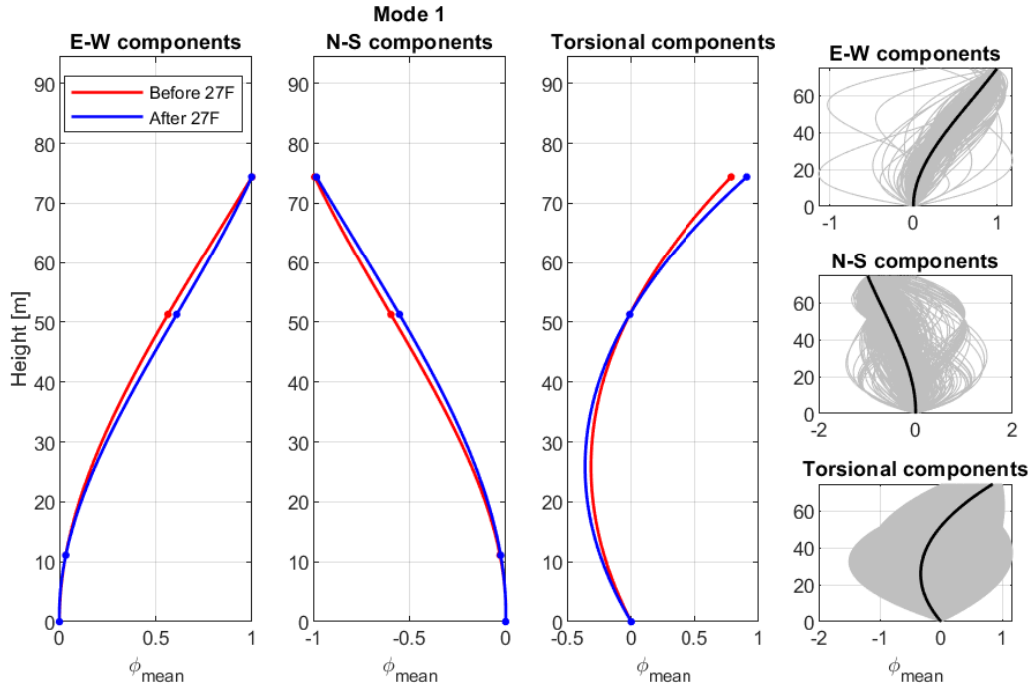

Figure 4.33: The north-south, east-west, and torsional components of the 1$^{\text{st}}$ mode-shape are presented. On the right, the modal forms identified on all events are presented.

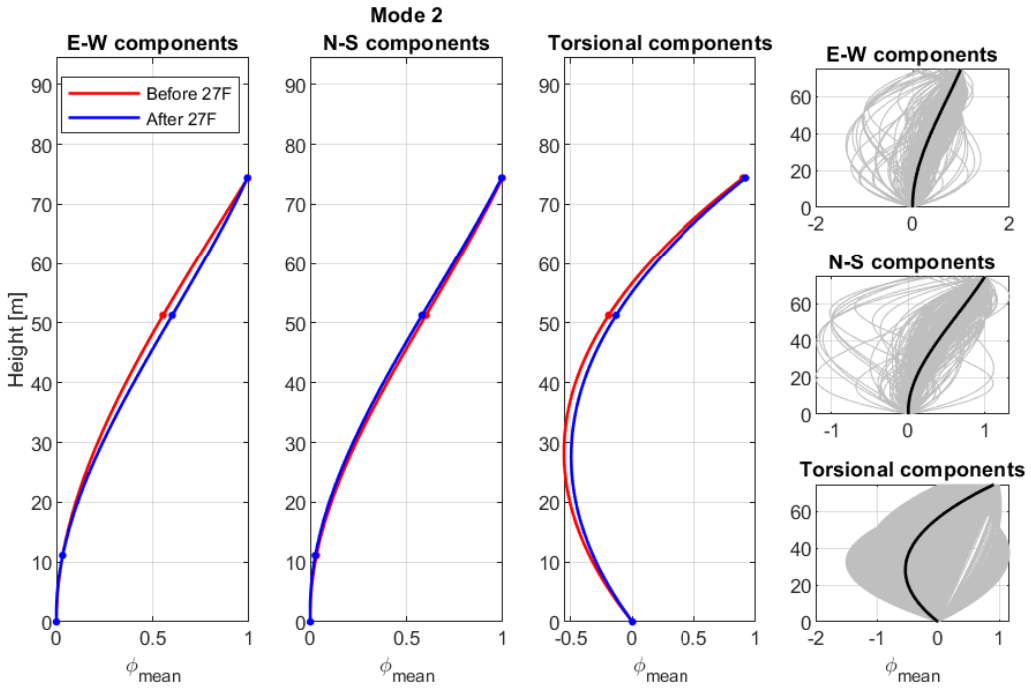

Figure 4.34: The north-south, east-west, and torsional components of the 2nd mode-shape are presented. On the right, the modal forms identified on all events are presented.

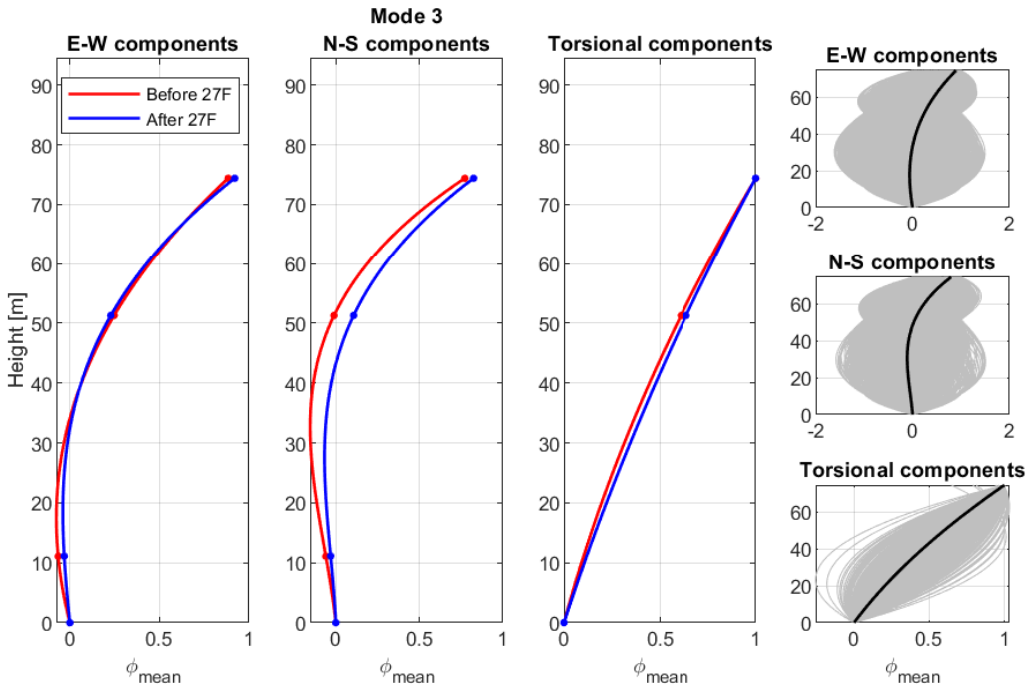

Figure 4.35: The north-south, east-west, and torsional components of the 3rd mode-shape are presented. On the right, the modal forms identified on all events are presented.

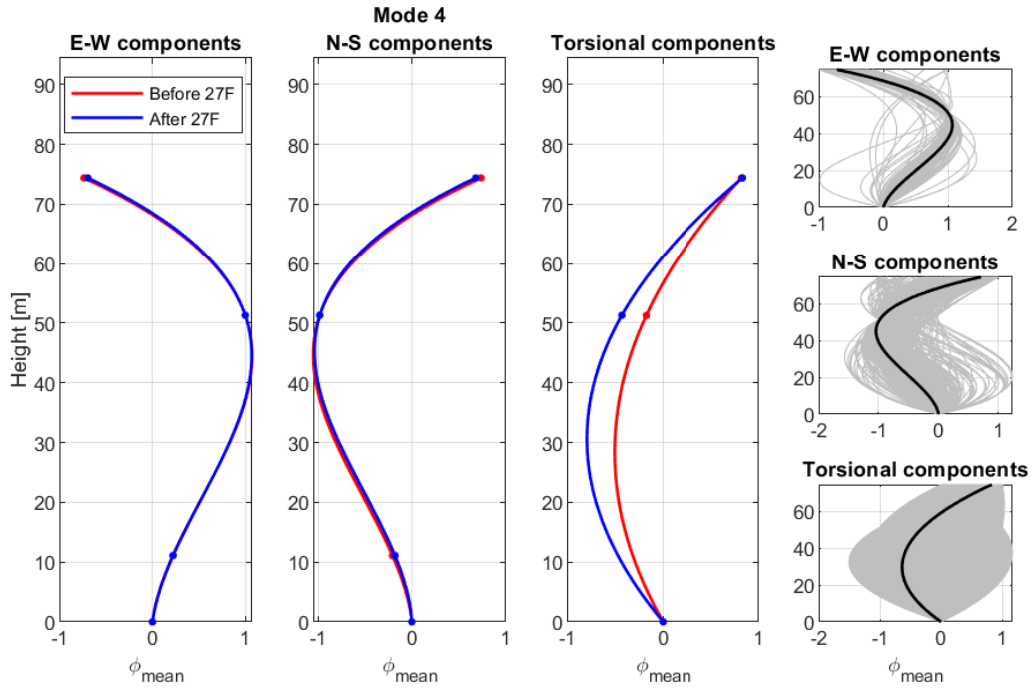

Figure 4.36: The north-south, east-west, and torsional components of the 4^{th} mode-shape are presented. On the right, the modal forms identified on all events are presented.

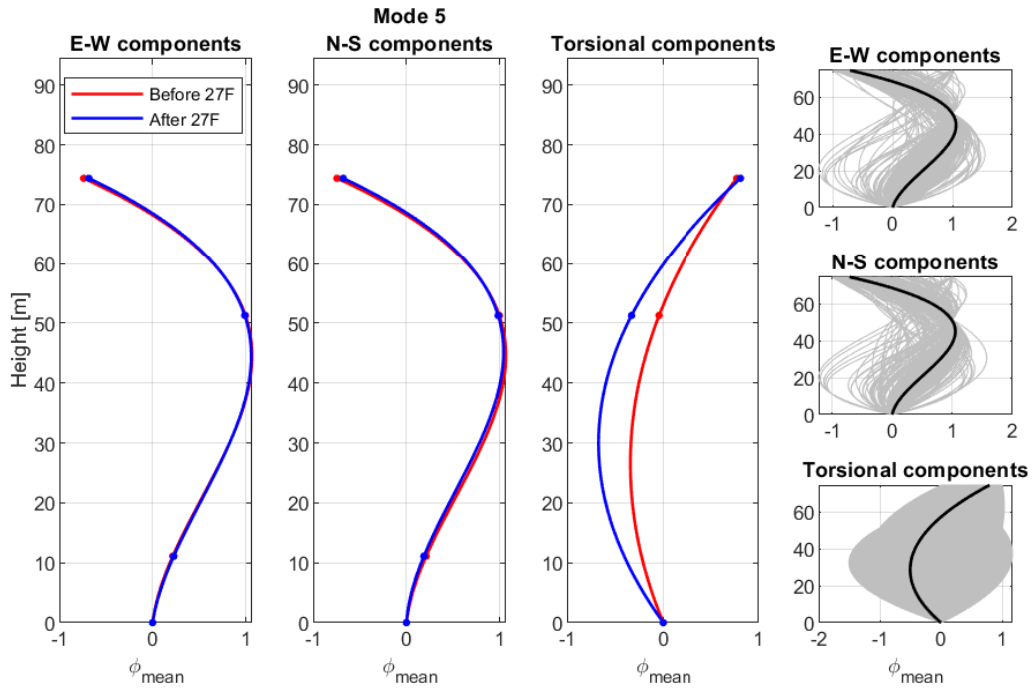

Figure 4.37: The north-south, east-west, and torsional components of the 5^{th} mode-shape are presented. On the right, the modal forms identified on all events are presented.

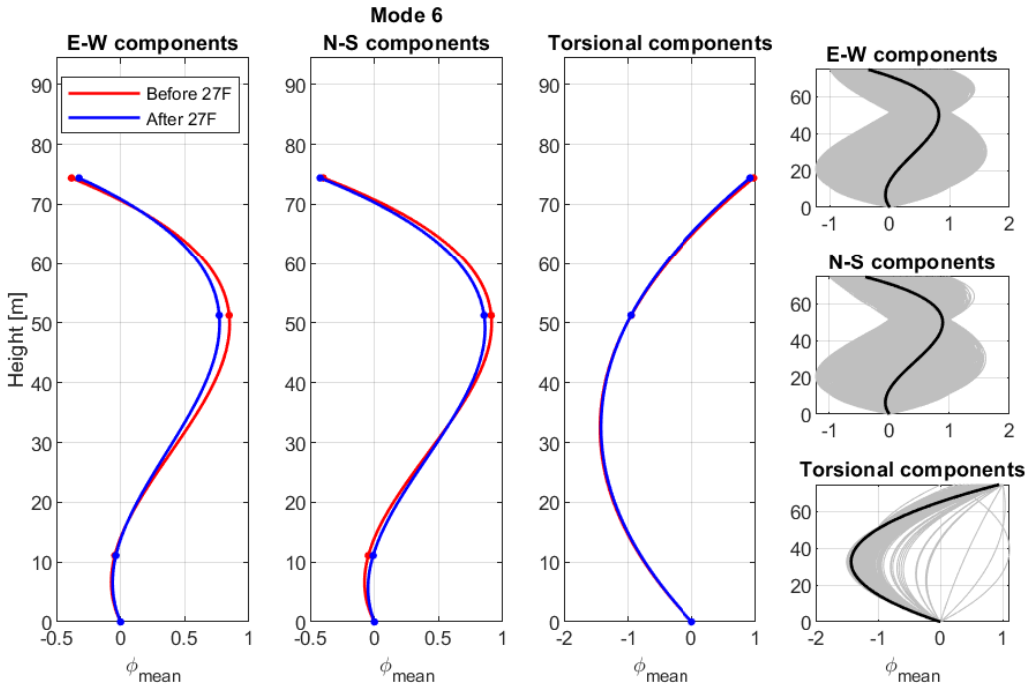

Figure 4.38: The north-south, east-west, and torsional components of the 6^{th} mode-shape are presented. On the right, the modal forms identified on all events are presented.

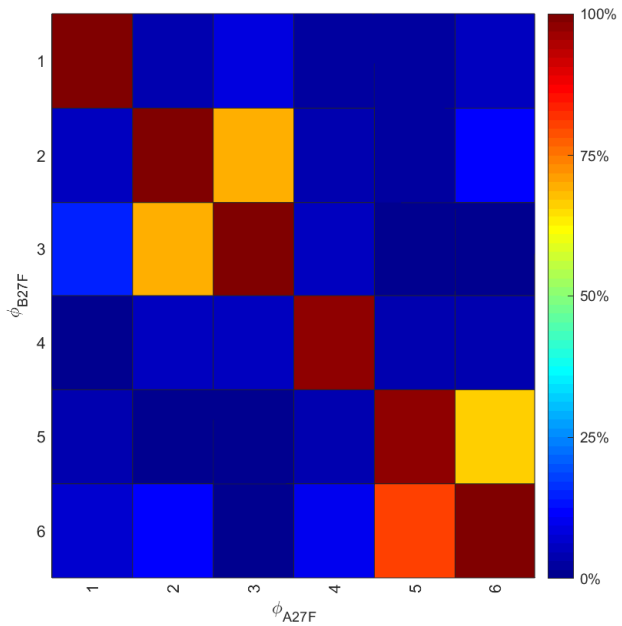

Figure 4.39: MAC between the modes-shapes before damage (B27F) and after damage (A27F).

In addition, replicating the study carried out by Carreño [5], the relationships between the identified frequencies and the demand on the building due to earthquakes are presented. To

quantify the request, the modal amplitude proposed by Carreño & Boroschek [6] was used as a metric.

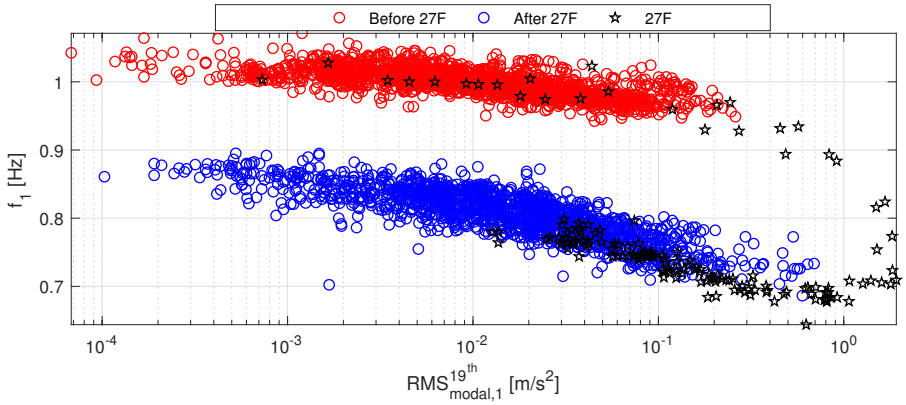

Figure 4.40: Relationship between the identified frequencies of mode 1 and their corresponding modal amplitude.

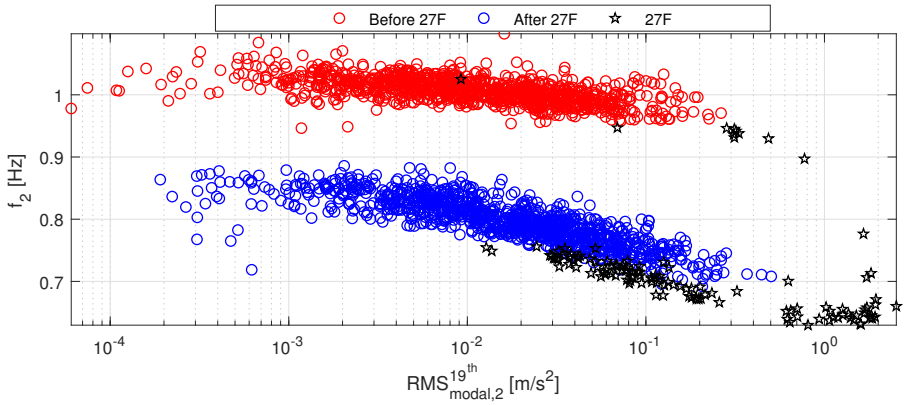

Figure 4.41: Relationship between the identified frequencies of mode 2 and their corresponding modal amplitude.

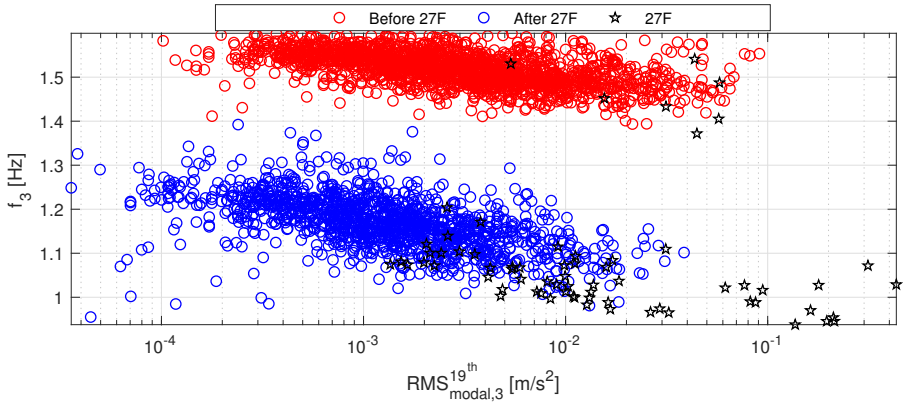

Figure 4.42: Relationship between the identified frequencies of mode 3 and their corresponding modal amplitude.

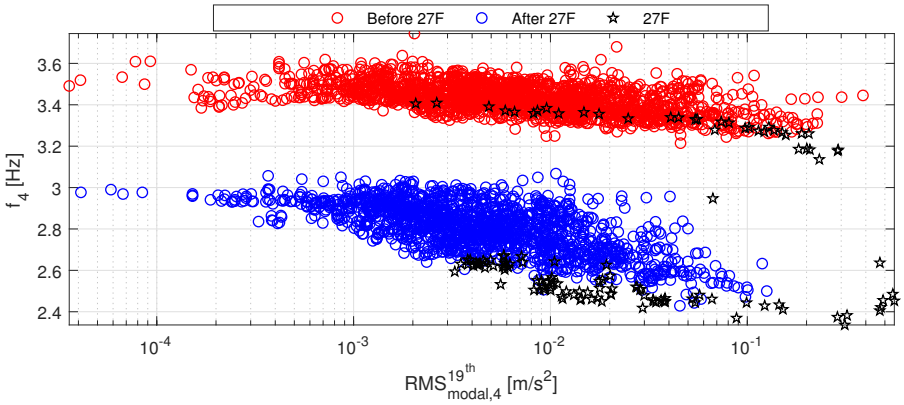

Figure 4.43: Relationship between the identified frequencies of mode 4 and their corresponding modal amplitude.

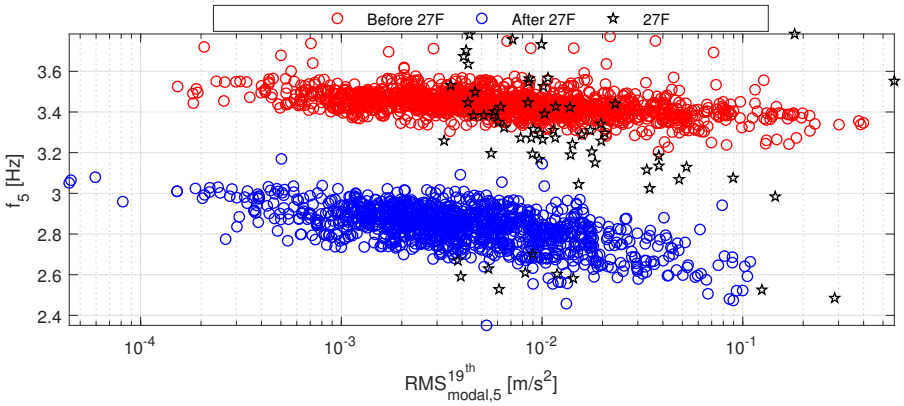

Figure 4.44: Relationship between the identified frequencies of mode 5 and their corresponding modal amplitude.

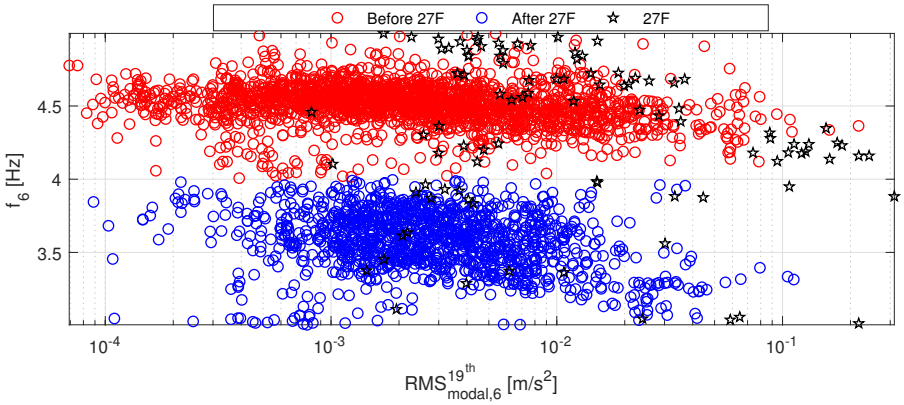

Figure 4.45: Relationship between the identified frequencies of mode 6 and their corresponding modal amplitude.

Regarding the results:

- About the modal parameters identified, the frequencies reduce to around 20 % regarding their initial values, while the damping ratios, show a trend to increase their initial values

after damage. Figure 4.39 shows that mode shapes don't present great changes between the two states of the building (without damage and damaged). Finally, for this system, the mode shapes by themselves are not a well indicator of structural damage.

- The identified frequencies present a coefficient of variation (C.O.V.) under 2 % before the damage and variability under 4.5 % after the damage. This indicates that the results are relatively reliable in comparison to the results observed for the modes-shapes and the damping ratios.

- For the damping ratios, the variability reaches up to 82.5 % for the third mode (before the 27F event), and for the other modes, the variability of the damping ratios is in the range of 30-75 %. Which indicates that this parameter has great uncertainty.

- Observing the north-south, east-west, and torsional components in Figures 4.33 to 4.38, it can be said that the identified modes have torsional components, but the torsional components are predominant in the 3rd and 6th modes. On the other hand, the translational components in the directions N-S and E-W are predominant for the 1st, 2nd, 4th, and 5th modes.

- It is observed that the components of the 1st, 2nd, 4th, and 5th modes are not orthogonal to the X or Y-axis. The 1st and 4th modes move in the second and fourth quadrants of the XY plane, and in the 2nd and 5th modes they move within the first and third quadrants of the same plane. This is because the structural walls located in the core of the building are not parallel to the Y-axis (Figures 3.3, 3.4, 3.5 and 3.6).

- On the relationship between the identified frequencies and the modal amplitude, the elastic nonlinearity present in the response of the system is observed due to the variability of the modal parameters. The variability of the frequencies reach values between 2-3 % before damage, and the dispersion increases to 4-5 % after damage. On the other hand, it is observed for the first 4 modes of translation, the dispersion of the identified frequencies decreases as the accelerations are greater. Regarding the amplitude values, it is observed that for the first two modes, the greatest accelerations occur after the damage. And after damage, the highest accelerations are for the fourth and fifth modes.

Chapter 5

Finite Element Model of the Building

In the current chapter, the finite element (FE) model of the Chilean Chamber of Construction Building is presented, and the assumptions and tools used to execute the numeric model are described. Also, an identifiability evaluation is performed to select the model parameter sets to be estimated with the model updating algorithm.

5.1. The Finite Element Method

In the field of civil engineering, the finite element (FE) method has been widely used for the design of structures. The FE method allows the representation of a continuous structural system in the real world through a discrete matrix equation system. The model matrices represent the inertial, damping, and stiffness properties of the structures.

The method consists of dividing a continuous structural system into a finite number of elements. The mechanical behaviour of each element is characterized by a set of nodes that define the geometry of the element, an interpolation function that defines the displacement fields between the element's nodes, and a constitutive law that determines the material's stress-strain relationship of the involved element. These elements can represent one-dimensional (springs, truss, frames), two-dimensional (membrane, plates), and three-dimensional (soils, fluids) objects present in the real world. Applying the principle of virtual works, compatibility conditions, and constitutive laws, each element's matrices are calculated, to later be assembled in a global matrix of the system [53].

5.2. Analytical Model

A large-scale FE model of the CChC Building initially generated in the ETABS software [54] was presented in Boroschek & Yáñez, 2000 [7]. The ETABS model was then transferred to OpenSees [32] using a MATLAB script [38] in joint with the ETABS application programming interface (API). The OpenSees model used to predict the response of the CChC Building has the following characteristics:

- The model is a linear-elastic 3D frame model, that includes the building's beams, columns, shear walls, and slabs (Figure 5.1).

- For beams and columns were model with linear-elastic Timoshenko beam-column elements. Geometric dimensions were defined using element centerlines. Beams and columns have uncracked section properties.
- For shear walls and slabs were model with quadrilateral shell (DKGQ) elements with linear-elastic (Elastic Membrane Plate) sections [32]. The thickness of slabs and walls was defined considering architectural dimensions and no cracking.
- The modulus of elasticity of reinforcement concrete was determined as $E_C = 1900\sqrt{R_{28}}$ [MPa] (3.29×10^4 [MPa]) for the dynamic analysis, where R_{28} is the cubic concrete strength at 28 days.
- For the dead load, the self-weight using a nominal density of $\rho_{RC} = 2500 \left[\frac{\text{kg}}{\text{m}^3}\right]$ for reinforced concrete elements. Live loads were defined according to NCh1537Of.86 [55]: 5.0 [kPa] for parking areas, 2.5 [kPa] for office use, and 3.5 [kPa] for the auditorium and the dining rooms.
- The seismic-weight was calculated according to NCh433Of.96 [56], 25 % for live loads, and 100 % for the dead load.
- The kinematic interactions between the structure and non-structural components and systems (e.g., partition walls and stairs) are not modeled.
- For the boundary condition at the foundation level, the walls were assigned a fixed support.

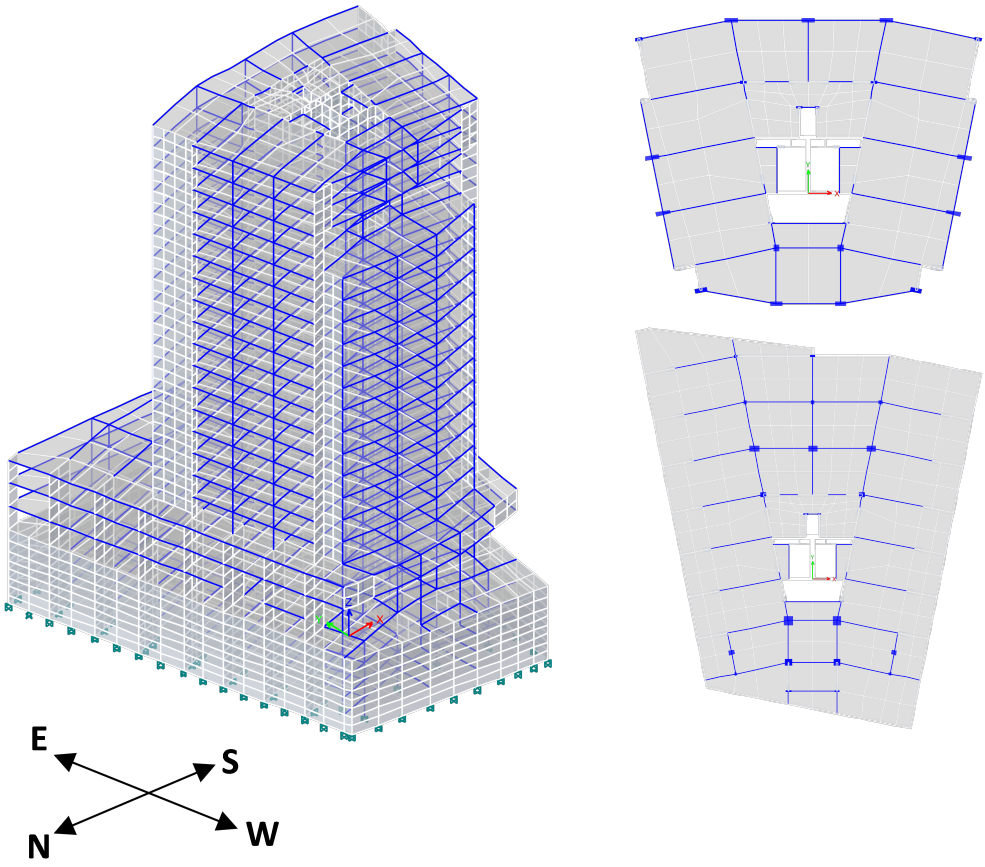

Figure 5.1: FE model of the Chilean Chamber of Construction Building realized in ETABS.

For the above, the periods and modal participating mass ratios of the structural model are as follows.

Table 5.1: Modal periods and modal ratios of participant mass of the structural model to reach 90 % of the mass in X, Y and torsional directions.

Mode	**Period [sec]**	**Effective Modal Mass**			**Cumulative Effective Modal Mass**		
		UX [%]	**UY [%]**	**RZ [%]**	**ΣUX [%]**	**ΣUY [%]**	**ΣRZ [%]**
1	0.9334	1.530	45.520	0.060	1.530	45.520	0.060
2	0.9207	44.640	1.490	0.450	46.170	47.000	0.510
3	0.6900	0.100	0.000	33.290	46.270	47.000	33.800
4	0.2599	1.420	16.470	0.340	47.690	63.470	34.140
5	0.2546	6.970	1.590	6.620	54.660	65.050	40.750
6	0.2514	9.360	0.170	5.630	64.020	65.220	46.380
7	0.1641	1.280	0.010	7.660	65.290	65.230	54.050
8	0.1457	0.130	9.820	0.020	65.430	75.060	54.060
9	0.1354	9.320	0.140	0.130	74.750	75.200	54.190
10	0.1341	0.110	0.000	2.020	74.860	75.200	56.210
11	0.0840	0.090	6.480	0.000	74.950	81.680	56.210
12	0.0830	5.990	0.080	0.030	80.940	81.760	56.240
13	0.0730	0.020	0.001	1.470	80.960	81.770	57.710
14	0.0630	0.150	7.270	0.040	81.110	89.030	57.750
15	0.0620	5.930	0.180	0.130	87.040	89.210	57.880
16	0.0580	0.190	0.002	9.220	87.230	89.210	67.100
17	0.0560	0.100	4.120	0.780	87.330	93.340	67.880
18	0.0550	1.280	0.460	10.850	88.610	93.790	78.730
19	0.0530	3.490	0.040	4.510	92.100	93.830	83.240
20	0.0520	0.010	0.004	2.710	92.100	93.830	85.960
21	0.0510	0.000	0.970	0.002	92.100	94.810	85.960
22	0.0490	1.210	0.010	0.730	93.320	94.820	86.690
23	0.0480	0.130	0.010	4.060	93.450	94.820	90.750
24	0.0480	0.020	0.480	0.190	93.470	95.310	90.940
25	0.0460	0.150	0.140	0.500	93.620	95.450	91.440

In Table 5.1, UX, UY, RZ, indicates the effective modal mass in the X, Y, and torsional directions, respectively. The X and Y-axis correspond to the north-south and east-west directions, respectively, according to the structural planes (Figure 3.3 to Figure 3.6). In addition, the first six mode-shapes of the structure result:

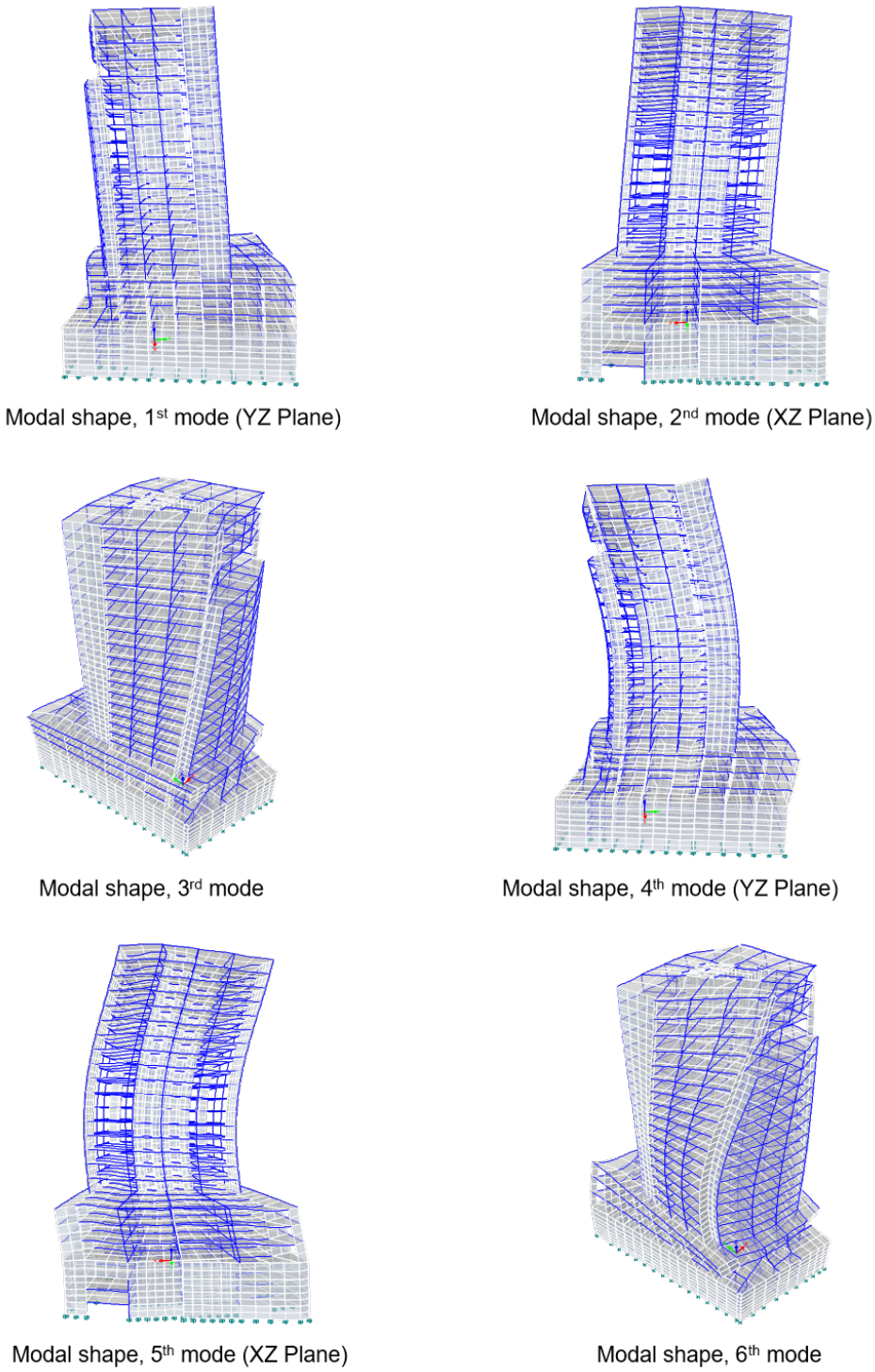

Figure 5.2: Mode-shapes predicted by the finite element model of the CChC Building.

5.2.1. Transfer model to OpenSees (TMOS)

The application of the FE model update algorithm requires updating the parameters in each iteration. Therefore, it is required to work with software that manipulates the model parameters easily. For the last reason, a script called TMOS was developed in MATLAB with

the objective to convert the original ETABS model to OpenSees. The main tasks of TMOS are described below:

- It exports the nodes coordinates, frames-shells elements mechanical properties and the elements-connectivity information of the ETABS model.
- It distributes the nodal masses of the elements to connecting nodes, distributing the structural elements' self-weight. If a slab element is connected with a node, 25 % of the assigned live load is asigned.
- The groups are initially assigned in ETABS, they are exported in TMOS, facilitating the FE model updating task.

For each task described, text files are generated with the FE model's information to be later compiled in OpenSees.

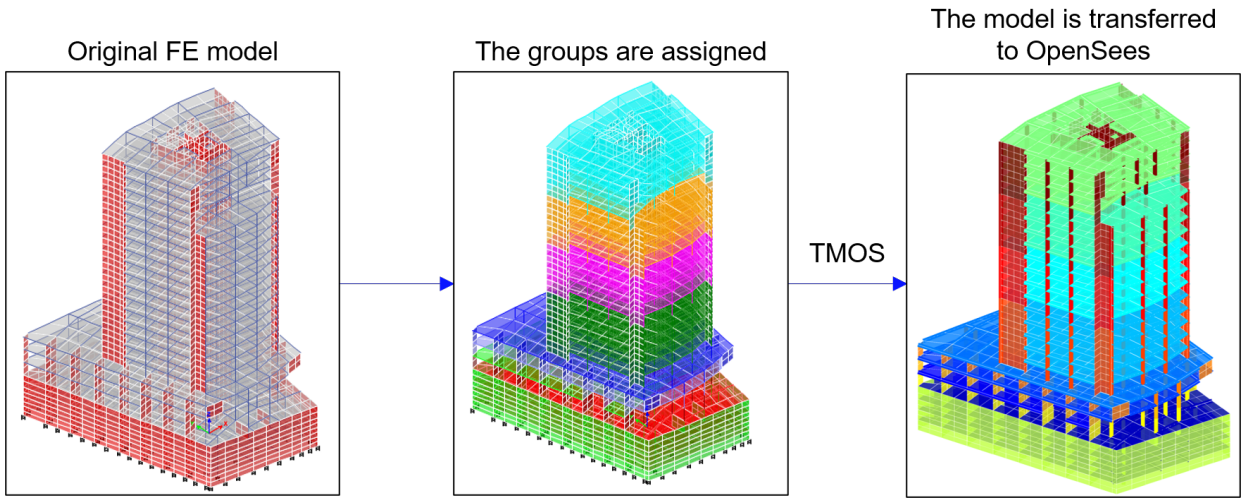

Figure 5.3: Steps used to prepare the FE model before applying the model updating algorithm.

5.2.2. Mesh Analysis

Since OpenSees does not have automatic mesh options, it is necessary to perform a manual meshing that is computationally efficient, therefore, a mesh analysis is carried out. Mesh analysis consists of dividing the shell elements of the initial model and calculating a solution with an FE model with coarse mesh (see Model 1 in Figure 5.7). After computing the solution on the coarse mesh, the process of mesh refinement begins. The mesh refinement process consists to solve the model with successively finer and finer meshes, and comparing the model's results with different mesh densities until the solutions converge with respect to mesh refinement or the number of the system's degrees of freedom [57]. Four models were proposed for this section, which are described below.

- Model 1, the initial model with coarse mesh. It is verified that all the nodes are connected with at least one structural element.

- Model 2, the structural walls above ground level are divided, and it is verified that all the nodes are connected correctly.
- Model 3, the structural walls above ground level and the slabs are divided, and it is verified that all the nodes are connected correctly.
- Model 4, all structural walls are divided (including the basement walls) and the slabs, and it is verified that all the nodes are connected correctly.

It is important to note that the base model was Model 1, which was later subdivided into more elements. For the meshing analysis, the structural periods of the FE model were chosen as the variable to compare.

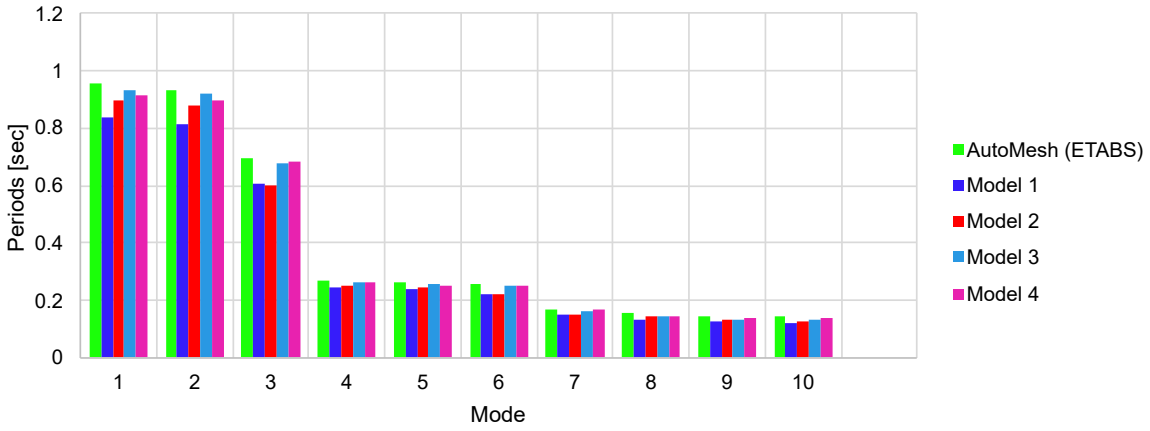

Figure 5.4: The structural periods of the FE models proposed are shown.

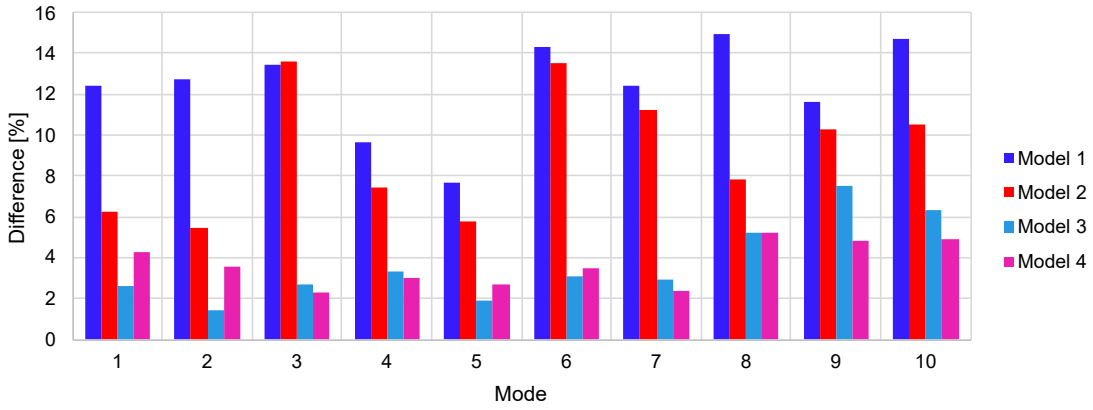

Figure 5.5: The difference between the periods of the proposed FE models and the FE model with automatic meshing is shown.

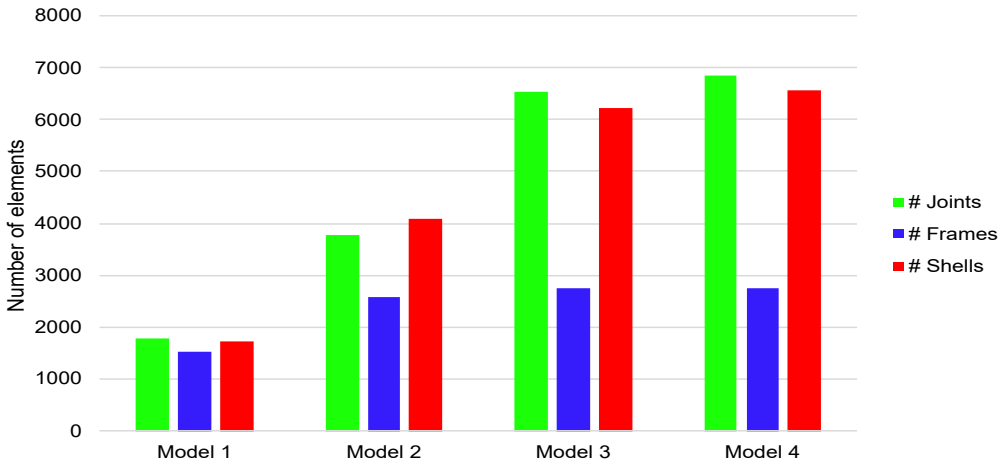

Figure 5.6: The number of elements for each FE model proposed is presented.

It can be observed that Model 3 and Model 4 are the models that present the least difference. On the other hand, it is observed that Model 3 has fewer elements than Model 4. Therefore, it can be concluded that it is computationally less demanding. Consequently, Model 3 is chosen to continue current work. It consists of 2956 frame elements, 7047 shell elements, and 41952 degrees of freedom (see Model 3 in Figure 5.7).

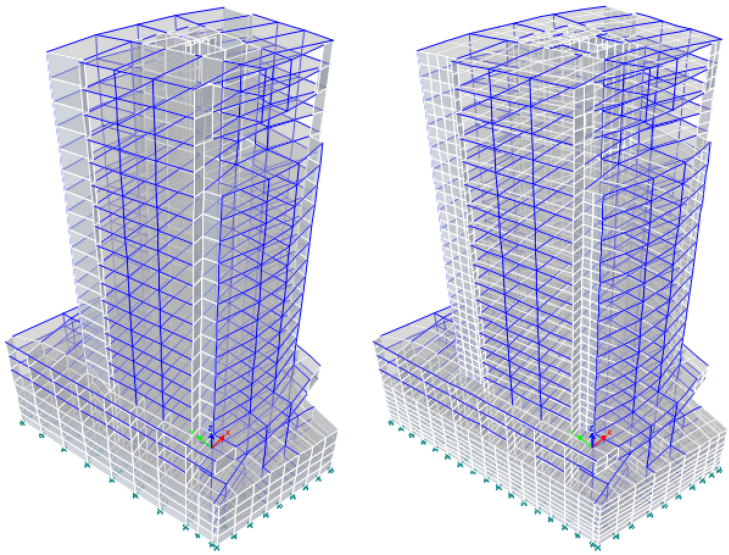

Figure 5.7: Model 1 (left) and Model 3 (right) described in the current section are presented.

5.2.3. OpenSees model validation

The OpenSees model is validated, comparing the periods and mode shapes with the ETABS model predictions. For the OpenSees model, the concrete elastic modulus was adjusted by amplifying its by 1.15 times its initial value. By doing the above, the vibration periods of OpenSees coincide well with those of the ETABS periods. The results are presented below.

Table 5.2: Periods of the ETABS and OpenSees FE models.

Mode	ETABS periods [sec]	OpenSees periods [sec]	Difference [%]
1	0.9334	0.9338	0.0429
2	0.9207	0.8977	2.4981
3	0.6900	0.7126	3.2754
4	0.2599	0.2611	0.4617
5	0.2546	0.2594	1.8853
6	0.2514	0.2474	1.5911
7	0.1641	0.1662	1.2797
8	0.1457	0.1488	2.1277
9	0.1354	0.1445	6.7208
10	0.1341	0.1394	3.9523

The modal forms are compared through the MAC criterion, calculated as follows [46].

$$MAC = \frac{|\phi_{A,i}^T \phi_{B,j}|^2}{\left(\phi_{A,i}^T \phi_{A,i}\right)\left(\phi_{B,j}^T \phi_{B,j}\right)} \tag{5.1}$$

$\phi_{A,i} \in \mathbb{R}^{n_y \times 1}$ is the i^{th} mode shape of the OpenSees model, $\phi_{B,j} \in \mathbb{R}^{n_y \times 1}$ is the j^{th} mode shape of the ETABS model, and n_y is the number of sensors available on the structure. A value of zero for MAC indicates that the modes are not correlated, while a value of one for MAC indicates that both modes are perfectly correlated. An advantage of the MAC is that the correlation does not depend on the scale of the modes, but only on the shape of the modes. For this case, the MAC was calculated using the sensors available in the building (Table 3.2).

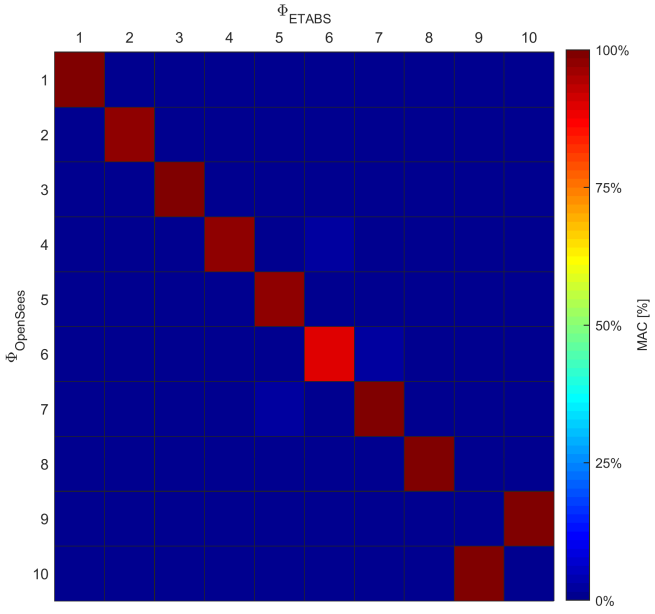

Figure 5.8: MAC' values matrix.

The MAC matrix shows that the modal forms of both models are correctly correlated. The

9^{th} and 10^{th} modes are cross-correlated because the eigenvalues of these modes have close values (Table 5.2).

As mentioned previously, the structure's seismic weight was calculated, taking 100 % of the dead weight plus 25 % of the live loads. The values are presented in Table 5.3.

Table 5.3: Seismic weight predicted by the ETABS and OpenSees FE model.

	Seismic Weight [kN]
ETABS	289620.93
OpenSees	289620.94
Difference [%]	3.251×10^{-6}

5.2.4. Time-history Analysis and Parallel Computing

Once the model was validated, a series of studies were carried out to evaluate the computational demand when performing time-history analysis in OpenSees. Newmark's constant acceleration method was defined as an integrating algorithm, with a constant time step of $\Delta t = 0.02$ [sec]. As mentioned in Chapter 4, all measured acceleration response time histories were re-sampled at 50 [Hz] (or $\Delta t = 0.02$ [sec]). For viscous forces, was considered a Rayleigh [35]. For the stiffness-proportional Rayleigh damping, the initial stiffness matrix was used, since it meant a great computational saving (see Figure 5.9). To calculate the Rayleigh proportional coefficients, the damping for the first and fifth modes was fixed, using the mean values of the modal parameters identified (after damage) in Chapter 4, 1.319 % and 1.745 % for the first and fifth modes, respectively (see Tables 4.2 and 4.1).

Table 5.4: Rayleigh damping coefficients for the time-history analysis.

Mode	**Frequency [Hz]**	**Angular Frequency [rad/sec]**	**Damping ratio [%]**
1	0.999	6.276	1.319
5	3.439	21.570	1.745
Mass-proportional Rayleigh damping coefficient			0.111
Stiffness-proportional Rayleigh damping coefficient			1.376×10^{-3}

One of the main difficulties when applying the algorithm is the high computational demand involved in calculating the sensitivity matrix with the Finite Difference Method. If it is necessary to estimate n_θ parameters, the model must be run $(n_\theta + 1)$ times before calculating the sensitivity matrix.

Given the above, parallel computing was implemented in OpenSees through the interpreter OpenSeesSP [39]. The idea of this tool is that large problems can be divided into smaller ones, which are then solved simultaneously (in parallel). To study the efficiency of this tool, a cost study was carried out for time-history analysis with 1000-time steps with the analysis characteristics described above. The results of the time cost analysis are presented in Figure 5.9.

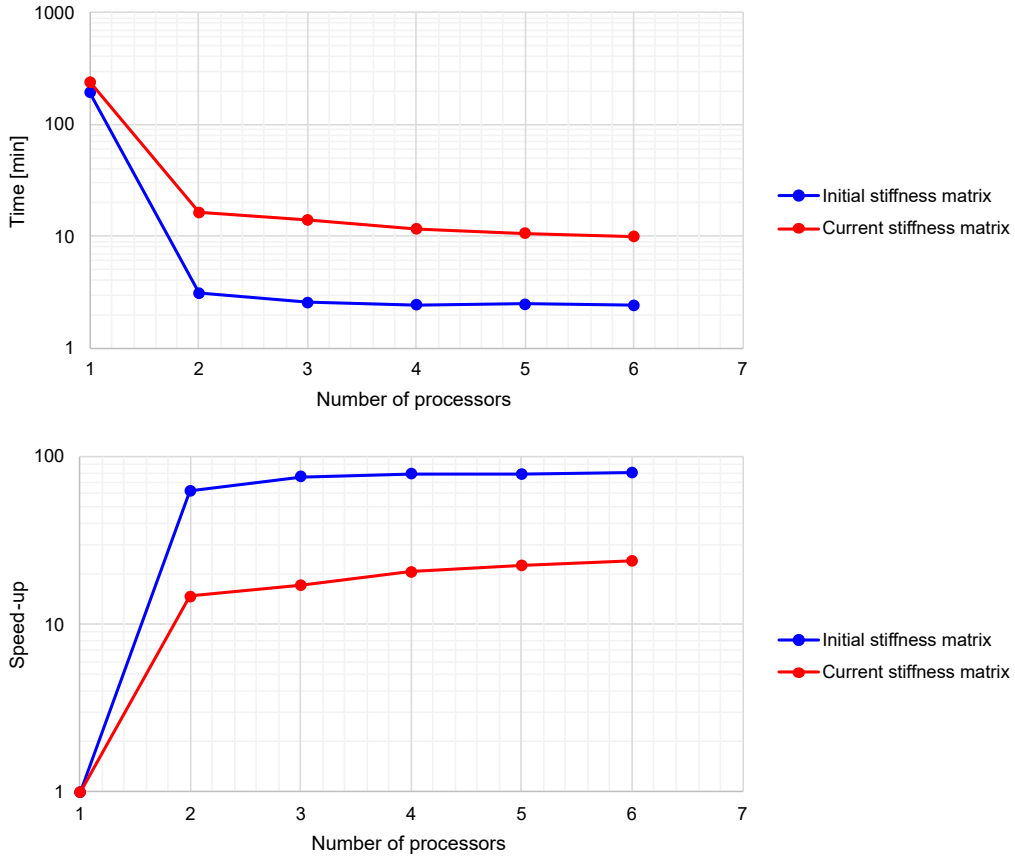

Figure 5.9: Time cost analysis for 1000 time-steps (the current stiffness matrix is also called the tangent stiffness matrix [32]).

In general, it is observed that when applying this tool, the calculation times are reduced from 3 hours to almost 2 minutes, thus obtaining a model that runs 80 times faster.

5.3. Identifiability Assessment of the FE Model Parameters

The measures contain information about the linear and non-linear response of the structure. The amount of information depends on the number and type of sensor. For example, if it is required to determine the local response of a structural column, the sensor that provides more information would be a strain-gauge located at the base of the column. On the other hand, if it is required to obtain information on the global response of the structure, an array of accelerometers set is the best alternative, since the latter can measure signals in a wide frequency range and are sensitive to low amplitudes.

As mentioned, the CChC Building is instrumented with 12 uni-directional accelerometers, 4 sensors are located in the basement, and 8 sensors measure the global response of the structure. Before selecting the model parameters to be estimated with the model updating technique, it is necessary to estimate how much information for the model parameters we can obtain with the limited number of sensors.

5.3.1. Identifiability Assessment Based on Information Entropy and Mutual Information

In the current section, an identifiability assessment of the FE model parameters is realized following the methodology proposed by Ebrahimian *et al.* (2019) [34]. The methodology first selects a set of estimation parameters as candidates and then uses the available measurement data set, to subsequently calculate the entropy gain of each candidate parameter. Entropy gain is a quantitative metric for measuring the information that each model parameter receives from the available measurement data [34]. Assuming a Gaussian a priori distribution for the FE model parameter vector, i.e., $\boldsymbol{\theta}^{pri} \sim \boldsymbol{N}(\boldsymbol{\theta}_0, \boldsymbol{P}_0)$, the entropy gain for the θ_j parameter can be estimated as follows [34]

$$\Delta H(\theta_j) = \frac{1}{2} \ln \left(I(\theta_j)\, p_j + 1 \right) \tag{5.2}$$

$$I(\theta_j) = \sum_{i=1}^{k} \left(\frac{\partial \hat{\boldsymbol{y}}_i(\boldsymbol{\theta})}{\partial \theta_j} \right)^T (\boldsymbol{R})^{-1} \left(\frac{\partial \hat{\boldsymbol{y}}_i(\boldsymbol{\theta})}{\partial \theta_j} \right) \tag{5.3}$$

Where p_j is the a priori variance of the θ_j parameter, $\boldsymbol{R} \in \mathbb{R}^{n_y \times n_y}$ is the simulation error covariance matrix. As can be seen, the entropy gain of parameter θ_j depends largely on the sensitivity of the response when the parameter θ_j is disturbed. Once the entropy gain is calculated, this metric is compared between the estimation parameters to assess their relative identifiability. Furthermore, to evaluate the mutual dependence of the candidate estimation parameters, the mutual entropy gain (mutual gain) is calculated as follows [34]

$$\Delta M(\theta_i, \theta_j) = \frac{1}{2} \ln \left(\frac{\left(I(\theta_i) + p_i^{-1} \right) \left(I(\theta_j) + p_j^{-1} \right)}{|\boldsymbol{I}(\theta_i, \theta_j) + \boldsymbol{P}_{0,ij}^{-1}|} \right) \tag{5.4}$$

The parameters p_i and p_j are the a priori variance of the i^{th} and j^{th} model parameters θ_i and θ_j, respectively; $P_{0,ij}$ is the a priori covariance matrix of θ_i and θ_j, which is a diagonal matrix with p_i and p_j as diagonal entries. In this case, $\boldsymbol{I}(\theta_i, \theta_j)$ is the two-by-two marginalized Fisher Information matrix for parameters θ_i and θ_j. If the pairwise dependencies are high, and if the parameters have physical meaningful the author suggests to joint the parameters in the model updating process, in otherwise, to put aside one of the parameters.

5.3.2. Parameter Selection Stage

For the given input ground motion (only translational components were considered), the entropy gain is calculated with the prior estimates of the candidate parameters. Candidate parameters are initially selected based on their potential contribution to structural response. These should characterize the properties of the materials, furthermore inertia plus damping of the system. These parameters and their nominal value are described below.

For the updating process, groups of stories distributed throughout the building are defined. The groups are characterized by three parameters, these parameters are: the elastic modulus of the floor system (slabs and beams), the elastic modulus of the set of columns-walls, and the distributed floor live loads (the distributed floor mass associated remains implicit in the

live loads).
The groups assigned are shown in Figure 5.10 and described in Table 5.5. The results presented below were calculated with seismic event #2 (see Appendix B.1) and a 10 % coefficient of variation was assumed for all parameters to derive the a priori covariance matrix. Given that the damage occurs only for the 27F mega-earthquake, it is assumed that the behaviour of the structure will be linear-elastic for all seismic events except for the aforementioned event. It assumes that the results of the identifiability evaluation should not have significant changes for different records.

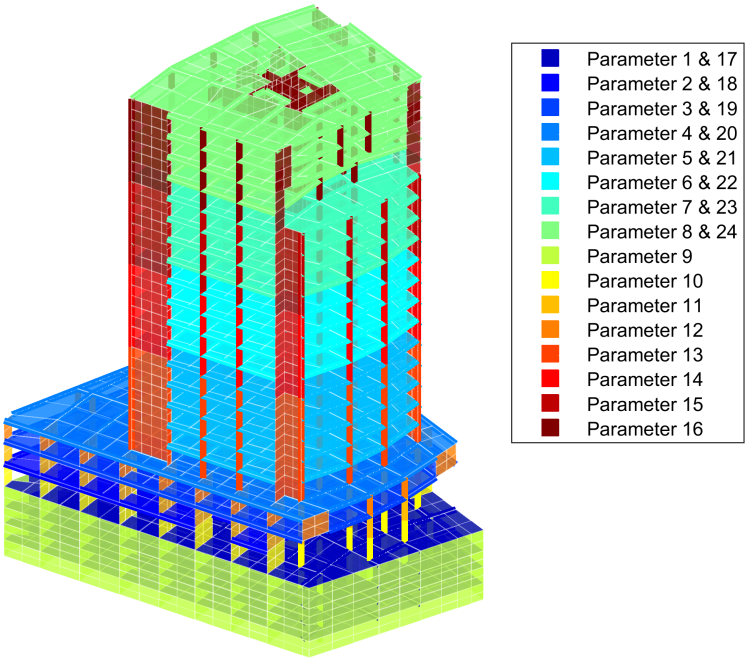

Figure 5.10: Candidate parameters distribution throughout the building (see, Table 5.5 for parameter IDs).

Figure 5.11 displays the relative entropy gain of the twenty-six candidates estimation parameters. Entropy gains are relative, which means that the entropy gain values are scaled with respect to the largest value. A low entropy gain value indicates that the parameters are likely to be unidentifiable (e.g., parameters #17 to #20). The results indicate that the parameters that control the structural response are those associated with the lateral stiffness of the building (columns and walls' elastic modulus). On the other hand, the parameters associated with the elastic modulus of the floor system (parameters #1 to #8) and the distributed live loads (parameters #17 to #20), provide lower information and are therefore difficult to identify. While the entropy gain of these parameters is small, they are considered as unknown parameters to estimate; however, large uncertainties and inaccuracies are expected in the estimation process. The same applies to proportional Rayleigh damping coefficients. Since low information is available for live loads distributed per floor (parameters #17 to #24), these parameters are merged for the validation stage. In case the algorithm has a poor performance for the validation stage, these parameters must be discarte, i.e., are defined as constant in the updating process. As mentioned above, considering parameters with low entropy gain can make it difficult to converge the mentioned parameters.

Figure 5.12 shows the relative mutual entropy gain between parameter pairs. The strong mutual gain between parameters #9 and #10 suggests merging these couple of parameters. This action is physically meaningful since these parameters characterize the lateral stiffness of the building's first stories. It is also the case of parameters #13, #14, and #15. Given the low entropy gain of parameter #16, it will be merged with parameters #13, #14, and #15, this will increase the information of this group from the measurement data. Also, parameters #11 and #12 are merged to enhance the algorithm performance. As a result of the described identifiability assessment process, 7 parameters are selected to estimate. The final parameters are listed in Table 5.6.

Table 5.5: Twenty-six model parameters used for prior model identifiability assessment.

Parameter ID	**Description**	**Value**
1	Elastic modulus of beam and slab concrete at S1, S2, S3 and Z floors	32.9 [GPa]
2	Elastic modulus of beam and slab concrete at 1^{st} floor	32.9 [GPa]
3	Elastic modulus of beam and slab concrete at 2^{nd} floor	32.9 [GPa]
4	Elastic modulus of beam and slab concrete at 3^{rd} floor	32.9 [GPa]
5	Elastic modulus of beam and slab concrete at 4^{th}, 5^{th}, 6^{th}, 7^{th} and 8^{th} floors	32.9 [GPa]
6	Elastic modulus of beam and slab concrete at 9^{th}, 10^{th}, 11^{th} and 12^{th} floors	32.9 [GPa]
7	Elastic modulus of beam and slab concrete at 13^{th}, 14^{th}, 15^{th}, and 16^{th} floors	32.9 [GPa]
8	Elastic modulus of beam and slab concrete at 17^{th}, 18^{th}, 19^{th}, and 20^{th} floors	32.9 [GPa]
9	Elastic modulus of column and wall concrete at S1, S2, S3 and Z stories	32.9 [GPa]
10	Elastic modulus of column and wall concrete at 1^{st} story	32.9 [GPa]
11	Elastic modulus of column and wall concrete at 2^{nd} story	32.9 [GPa]
12	Elastic modulus of column and wall concrete at 3^{rd} story	32.9 [GPa]
13	Elastic modulus of column and wall concrete at 4^{th}, 5^{th}, 6^{th}, 7^{th} and 8^{th} stories	32.9 [GPa]
14	Elastic modulus of column and wall concrete at 9^{th}, 10^{th}, 11^{th} and 12^{th} stories	32.9 [GPa]
15	Elastic modulus of column and wall concrete at 13^{th}, 14^{th}, 15^{th}, and 16^{th} stories	32.9 [GPa]
16	Elastic modulus of column and wall concrete at 17^{th}, 18^{th}, 19^{th}, and 20^{th} stories	32.9 [GPa]
17	Distributed floor live loads on S1, S2, S3 and Z floors	5.0 [kPa]
18	Distributed floor live loads on 1^{st} floor	3.5 [kPa]
19	Distributed floor live loads on 2^{nd} floor	3.5 [kPa]
20	Distributed floor live loads on 3^{rd} floor	3.5 [kPa]
21	Distributed floor live loads on 4^{th}, 5^{th}, 6^{th}, 7^{th} and 8^{th} floors	2.5 [kPa]
22	Distributed floor live loads on 9^{th}, 10^{th}, 11^{th} and 12^{th} floors	2.5 [kPa]
23	Distributed floor live loads on 13^{th}, 14^{th}, 15^{th}, and 16^{th} floors	2.5 [kPa]
24	Distributed floor live loads on 17^{th}, 18^{th}, 19^{th}, and 20^{th} floors	2.5 [kPa]
25	Mass-proportional Rayleigh damping coefficient	0.111
26	Stiffness-proportional Rayleigh damping coefficient	1.376×10^{-3}

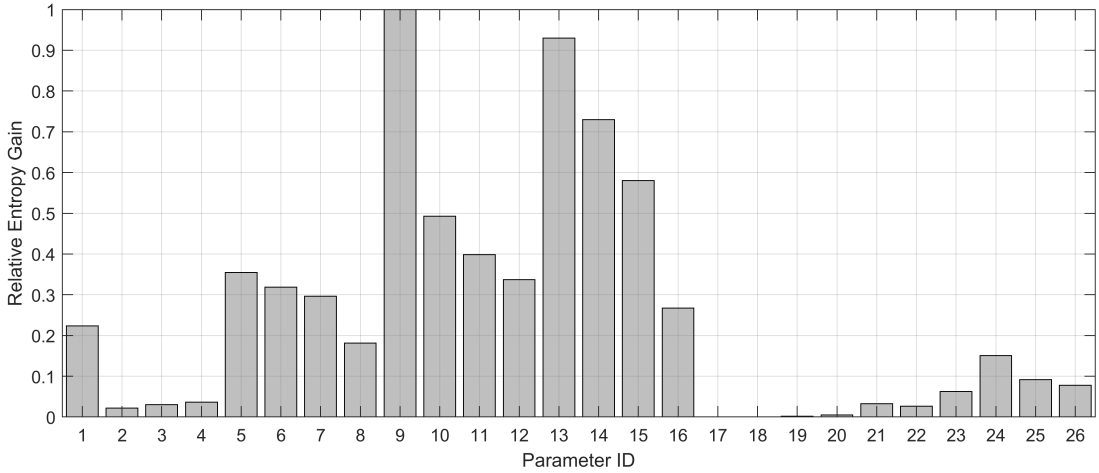

Figure 5.11: Relative entropy gain of the candidate parameters to estimate (see Table 5.5 for parameter IDs).

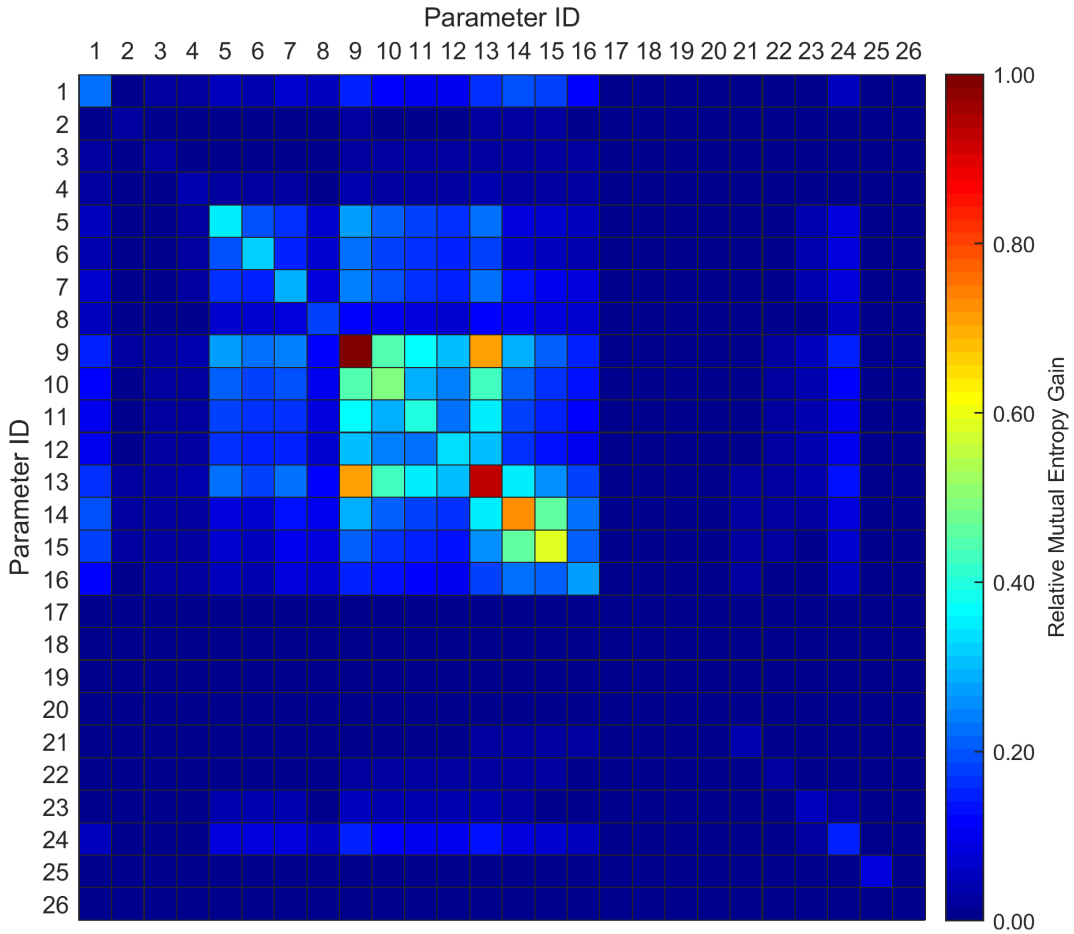

Figure 5.12: Relative mutual entropy gain between the candidate parameters pairs to estimate.

Table 5.6: Final selected model parameters for identifiability assessment stage.

Parameter ID	Description	Value
1	Elastic modulus of beam and slab concrete at S1 to 20$^{\text{th}}$ floors (E_{floor})	32.9 [GPa]
2	Elastic modulus of column and wall concrete at S1, S2, S3, Z and 1$^{\text{st}}$ stories ($E_{C\&W}^{S3\text{ to }P1}$)	32.9 [GPa]
3	Elastic modulus of column and wall concrete at 2$^{\text{nd}}$ and 3$^{\text{rd}}$ stories ($E_{C\&W}^{P2\text{ to }P3}$)	32.9 [GPa]
4	Elastic modulus of column and wall concrete at 4$^{\text{th}}$ to 20$^{\text{th}}$ stories ($E_{C\&W}^{P4\text{ to }P20}$)	32.9 [GPa]
5	Distributed floor live loads on S1 to 20$^{\text{th}}$ floors (Q_{floor})	2.5 [kPa]
6	Mass-proportional Rayleigh damping coefficient (α)	0.111
7	Stiffness-proportional Rayleigh damping coefficient (β)	1.376×10^{-3}

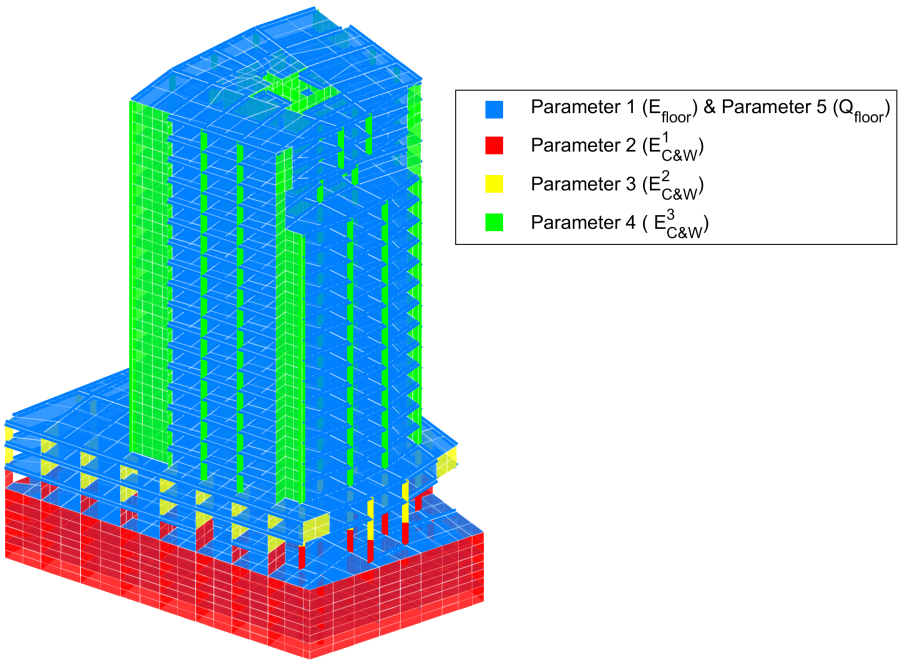

Figure 5.13: Final parameters distribution throughout the building (see Table 5.6 for parameter IDs).

Chapter 6

Finite Element Model Updating

In Chapter 6, the sequential FE model updating algorithm is applied to real data measured to improve the FE model prediction. First, a simulation case is performed to show the expected results. After that, the estimation results for a seismic record with real measures are presented and last, a summary of the results of the model updating process is presented.

6.1. Simulation Case

A numeric simulation case is carried out to validate the parameters selected in the identifiability assessment stage. If the algorithm can not find a true value of a parameter, this parameter must be put aside in the model updating process.

For the simulation case, the initial estimates are selected as $\hat{\boldsymbol{\theta}}_0 = 0.80\boldsymbol{\theta}^{true}$, and their initial coefficient of variation is selected as 10 %. The estimation constraints for the model parameters are selected as $0.1\hat{\boldsymbol{\theta}}_0 \leq \boldsymbol{\theta} \leq 6.0\hat{\boldsymbol{\theta}}_0$. The tolerance (for parameters) was selected as 0.02 and with a maximum of 15 iterations per estimation window. For the strong phase of the earthquake, the estimation window was defined with a length equal to 2.0 seconds for the first 5.0 seconds, with an overlap of 50 % with subsequent windows. For the rest of the updating process, the estimation windows have a length of 5.0 seconds with an overlapping of 20 % between windows. The process noise covariance matrix $\boldsymbol{Q}$ was selected as $(q\hat{\theta}_i)^2$, where $q = 1 \times 10^{-3}$, and $\hat{\theta}_i$ is the mean estimate of the i^{th} model parameter, and is time-invariant diagonal matrix. Finally, the simulation error covariance matrix $\boldsymbol{R}$ was also selected as a time-invariant diagonal matrix, whose diagonal entries are selected as $(0.01\text{g})^2$. This matrix represents the measurement noise variances, and the amplitude noise was estimated as 1 %g RMS Gaussian white noise. For the present analysis, seismic record #62 of the catalogue (see Appendix B) was used. The input ground motion was considered deterministic. The simulation duration was one hour and ten minutes.

Table 6.1: Comparison of finite element model parameter estimation results for simulation case.

Parameter ID	**Final estimates of FE model parameters** $(\hat{\boldsymbol{\theta}}/\boldsymbol{\theta}^{true})$	**Final estimates of coefficient of variation (%)** $(C.O.V.(\hat{\boldsymbol{\theta}}))$
E_{floor}	0.986	0.573
$E_{C\&W}^{S3\text{ to }P1}$	0.985	0.917
$E_{C\&W}^{P2\text{ to }P3}$	0.995	1.498
$E_{C\&W}^{P4\text{ to }P20}$	0.989	0.323
Q_{floor}	0.807	4.526
α	0.996	1.203
β	0.996	1.006

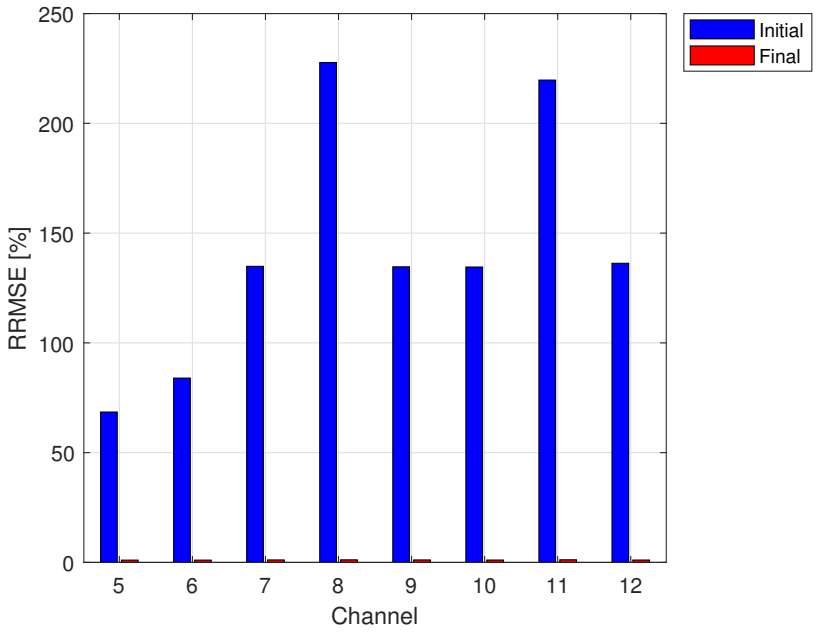

Figure 6.1: Relative root mean square error (RRMSE) of the FE predicted structural responses using the initial and final-updated FE models for simulation case.

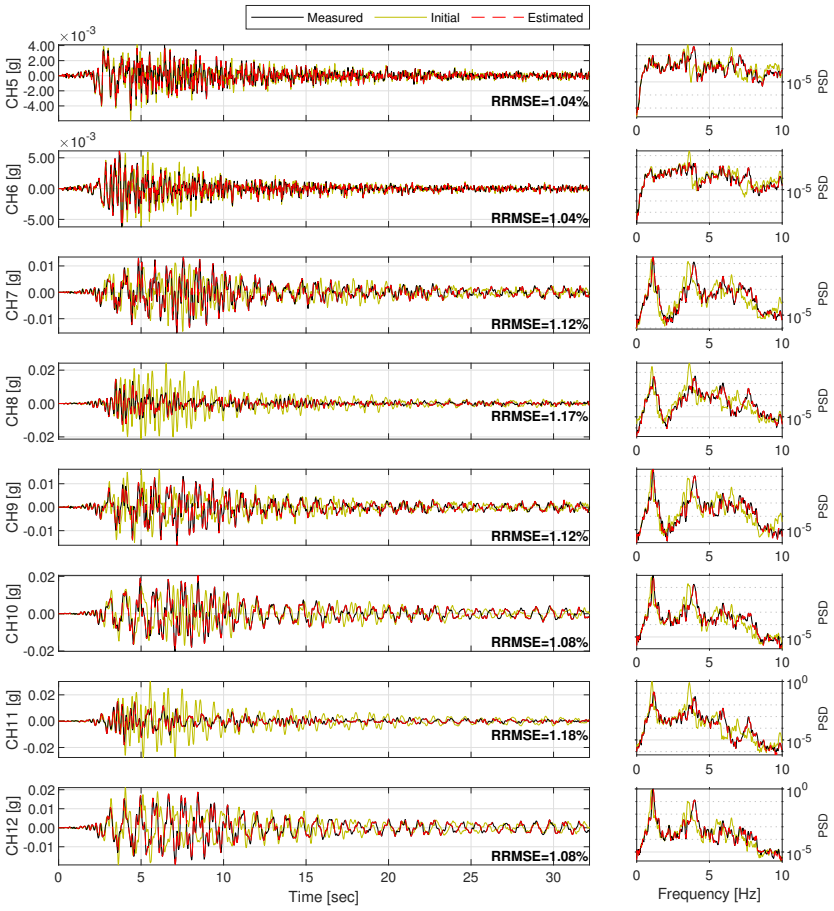

Figure 6.2: Comparison of the measured structural responses with the structural responses predicted using the initial and final-updated FE models for simulation case.

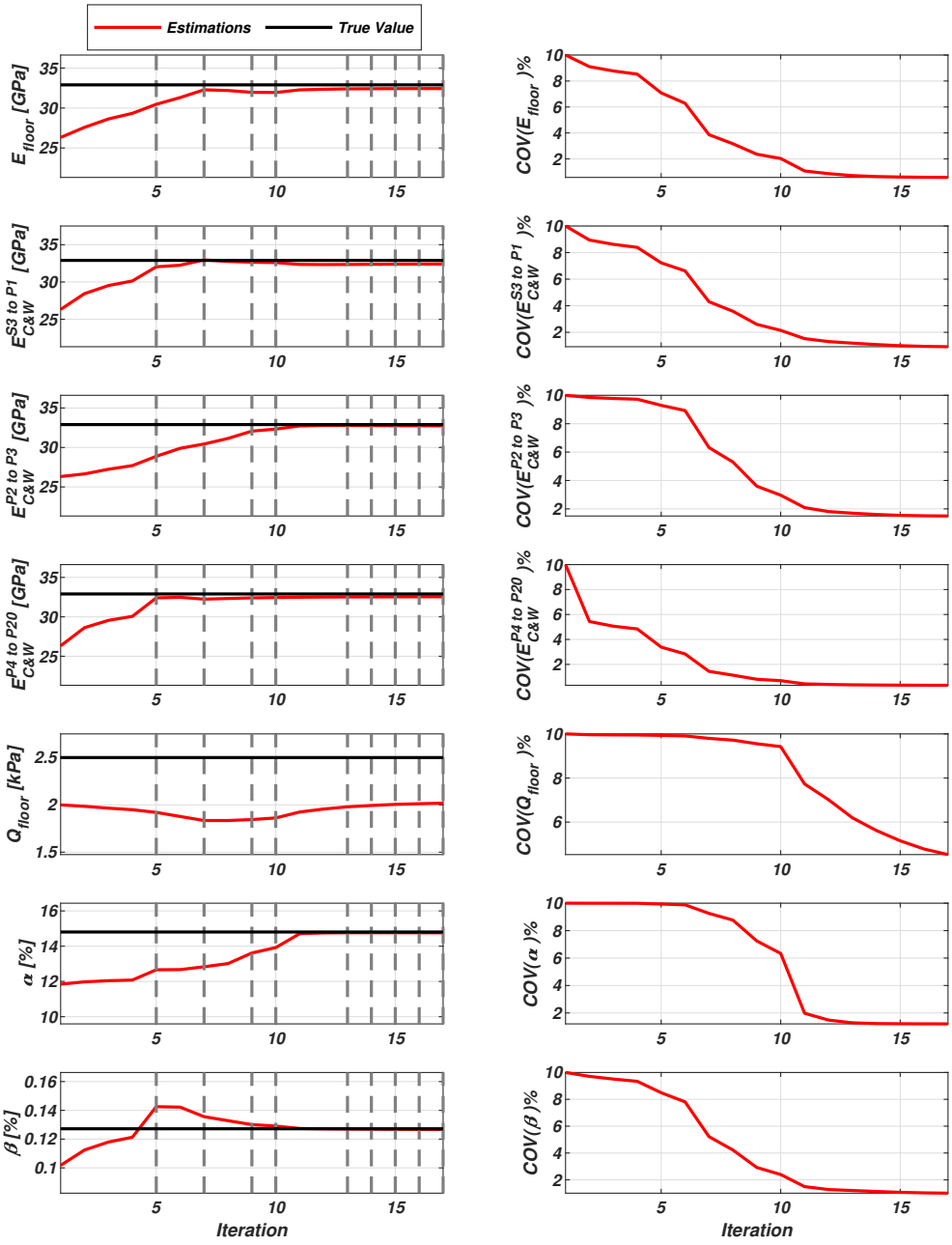

Figure 6.3: Time histories of the posterior mean (left) and coefficient of variation (COV) (right) of the model parameters estimated from the seismic event #62 for the simulation case. The vertical dashed lines (left) indicate that the iterations have converged for the corresponding estimation window.

Figure 6.3 show the posterior mean (left) and C.O.V. (right) of the FE model parameters. It is observed that all the model parameters are iteratively updated to reach the true value except for the parameter Q_{floor}. The rest of the parameters are converged closely to the corresponding true values, with reasonable accuracy and small C.O.V. The vertical dashed lines in the sub-figures of Figure 6.3 indicate that the iteration limit has been reached for each estimation window. As discussed in Chapter 5, grouping the parameters, associated with the modulus of elasticity of the floor system improved the convergence of the algorithm. A different case is the distributed floor live loads, where due to a small entropy gain (low

sensitivity in structural response), the parameter estimation has a poor performance. Finally, the distributed floor live loads are fixed with their initial values (see Table 5.5).

Table 6.2: Final selected model parameters for model updating stage.

Parameter ID	Description	Value
1	Elastic modulus of beam and slab concrete at S1 to 20$^{\text{th}}$ floors (E_{floor})	32.9 [GPa]
2	Elastic modulus of column and wall concrete at S1, S2, S3, Z and 1$^{\text{st}}$ stories ($E_{C\&W}^{S3\text{ to }P1}$)	32.9 [GPa]
3	Elastic modulus of column and wall concrete at 2$^{\text{nd}}$ and 3$^{\text{rd}}$ stories ($E_{C\&W}^{P2\text{ to }P3}$)	32.9 [GPa]
4	Elastic modulus of column and wall concrete at 4$^{\text{th}}$ to 20$^{\text{th}}$ stories ($E_{C\&W}^{P4\text{ to }P20}$)	32.9 [GPa]
5	Mass-proportional Rayleigh damping coefficient (α)	0.111
6	Stiffness-proportional Rayleigh damping coefficient (β)	1.376×10^{-3}

6.2. Model Updating using the real data measured

The CChC Building FE model was improved through the sequential Bayesian FE model updating technique for each seismic event presented in Chapter 4. The process noise ($\boldsymbol{Q}$) and simulation error ($\boldsymbol{R}$) covariances matrices were selected equal to values used on the simulation case.

6.2.1. Results for real data measured before damage to the building

The improved FE model predictions for seismic record #62 are presented below.

Table 6.3: Comparison of finite element model parameter estimation results for seismic event #62.

Parameter ID	Final estimates of FE model parameters ($\hat{\boldsymbol{\theta}}/\boldsymbol{\theta}^{initial}$)	Final estimates of coefficient of variation (%) ($C.O.V.(\hat{\boldsymbol{\theta}})$)
E_{floor}	0.779	0.190
$E_{C\&W}^{S3\text{ to }P1}$	0.863	0.184
$E_{C\&W}^{S2\text{ to }P3}$	2.852	0.549
$E_{C\&W}^{P4\text{ to }P20}$	0.843	0.069
α	1.068	0.586
β	3.112	0.715

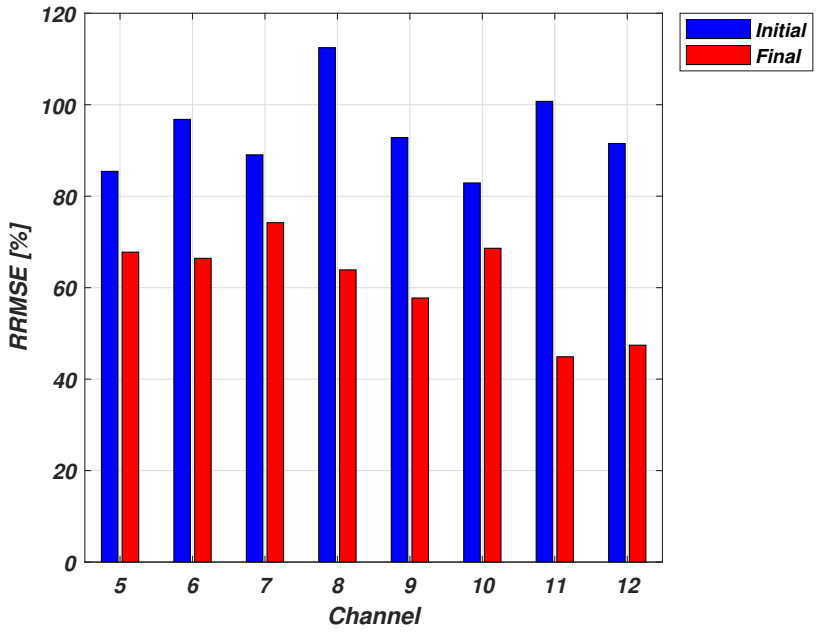

Figure 6.4: Relative root mean square error (RRMSE) of the FE predicted structural responses using the initial and final-updated FE models for seismic event #62.

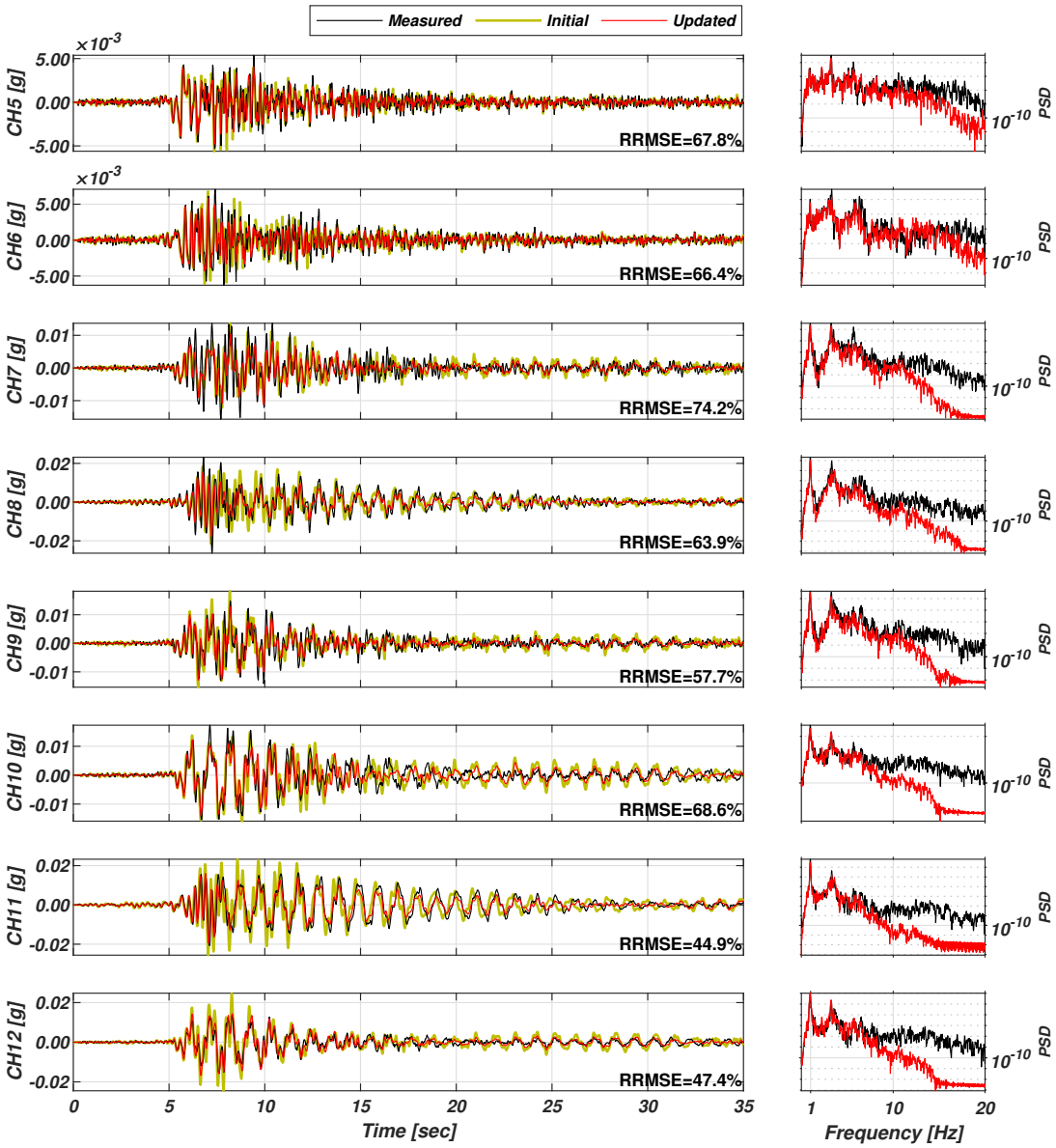

Figure 6.5: Comparison of the measured structural responses with the structural responses predicted using the final-updated FE model for seismic event #62.

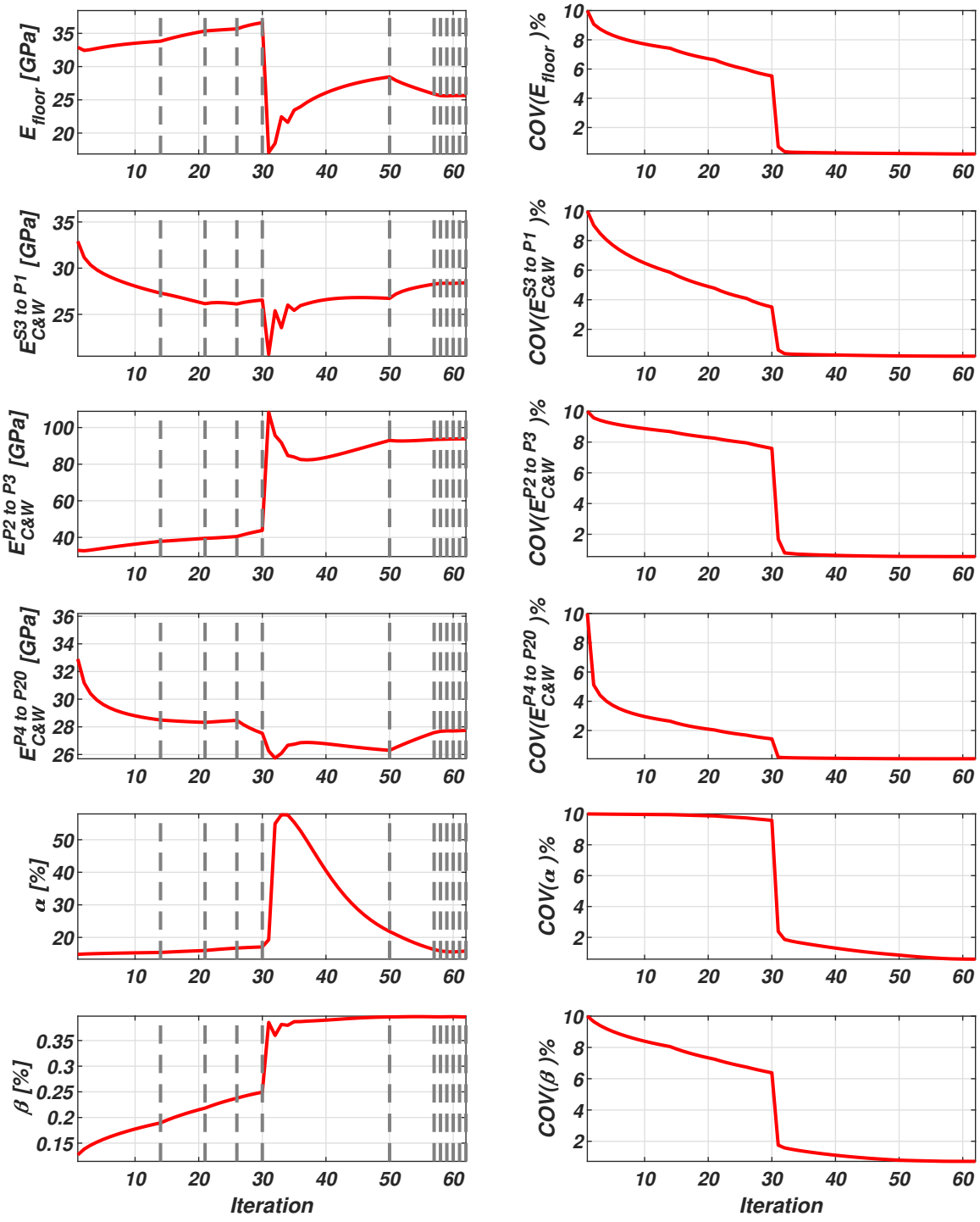

Figure 6.6: Time-histories of the posterior mean (left) and coefficient of variation (COV) (right) of the model parameters estimated from the seismic event #62.

Figure 6.4 indicates the algorithm reduces the misfit between real data measured and FE model prediction using the final estimates. The C.O.V. values indicate the algorithm converges correctly, and the estimates are unbiased given the small uncertainties. The misfits between the real measured and structural responses of the FE model are due to the limitations of the numeric model. That can improve considering the simulation of other physical phenomena, such as the soil stiffness in the basement stories and the rotational and torsional components

of the ground motion. These elements provide a better fidelity of the real-world response. Another point to observe is the content of frequencies in the FE model response, these PSD decay after 10 [Hz]. This is different on the PSD of the real-data measured. This effect occurs when the vertical mass is considered in the eigen-analysis of the CChC Building FE model, the structural frequencies of higher modes converge.

6.2.2. Results for real data measured after damage to the building

Due to the mega-earthquake, of 2010 (seismic record #63), the properties of the structure changed permanently. This section demonstrates the sequential Bayesian FE model updating algorithm is a powerful technique for tracking the structure's material properties. For the above, the improved FE model predictions for seismic record #64 are presented below.

Table 6.4: Comparison of finite element model parameter estimation results for seismic event #64.

Parameter ID	**Final estimates of FE model parameters** $(\hat{\boldsymbol{\theta}}/\boldsymbol{\theta}^{initial})$	**Final estimates of coefficient of variation (%)** $(C.O.V.(\hat{\boldsymbol{\theta}}))$
E_{floor}	0.428	0.326
$E_{C\&W}^{S3\text{ to }P1}$	0.818	0.422
$E_{C\&W}^{P2\text{ to }P3}$	0.504	0.322
$E_{C\&W}^{P4\text{ to }P20}$	0.606	0.214
α	2.202	1.006
β	4.386	1.561

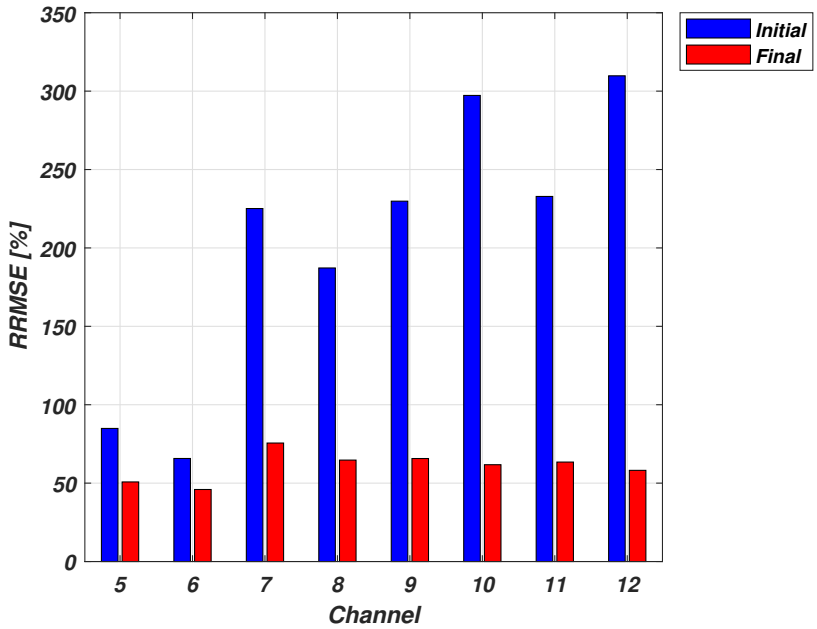

Figure 6.7: Relative root mean square error (RRMSE) of the FE predicted structural responses using the initial and final-updated FE models for seismic event #64.

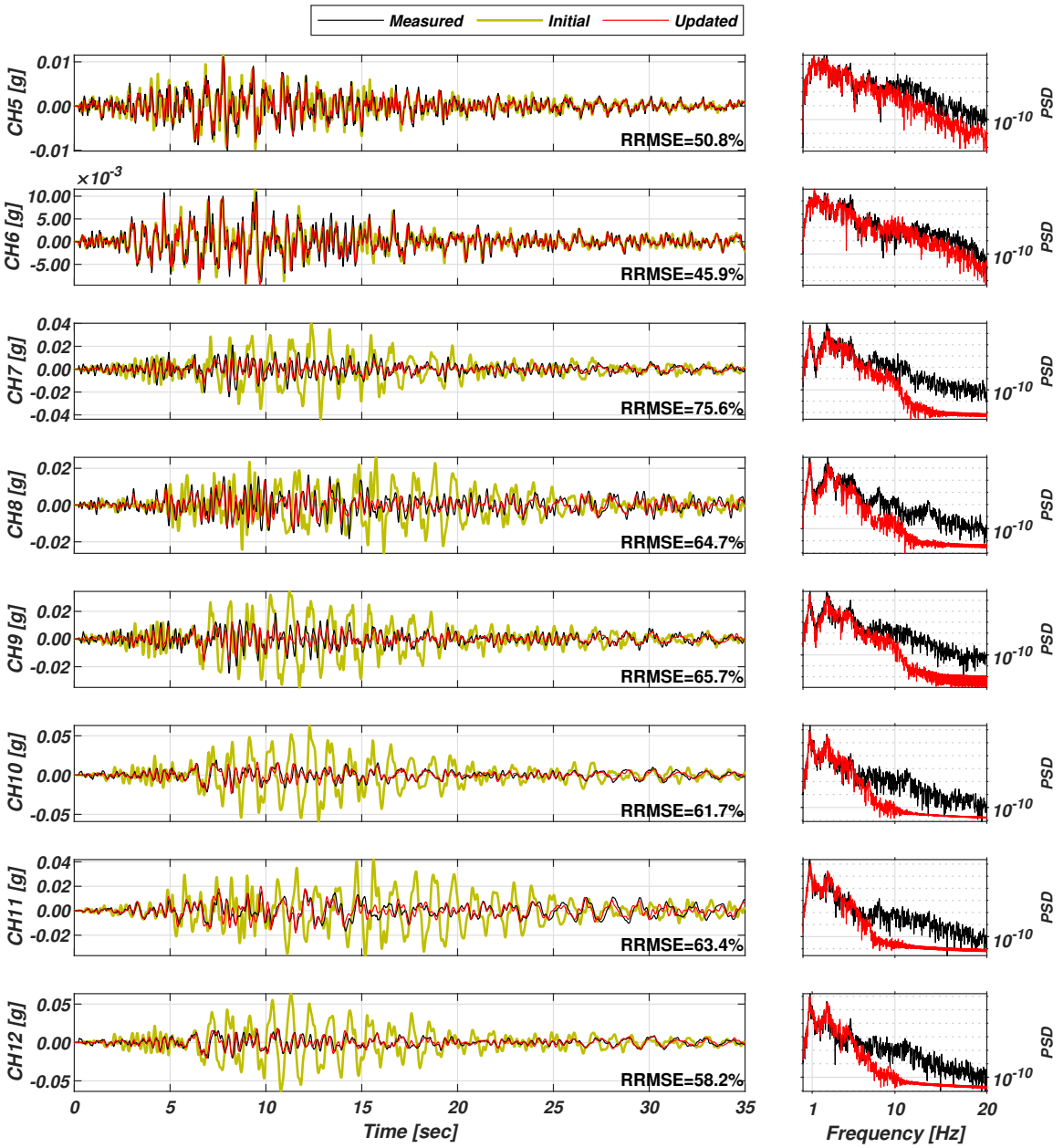

Figure 6.8: Comparison of the measured structural responses with the structural responses predicted using the final-updated FE model for seismic event #64.

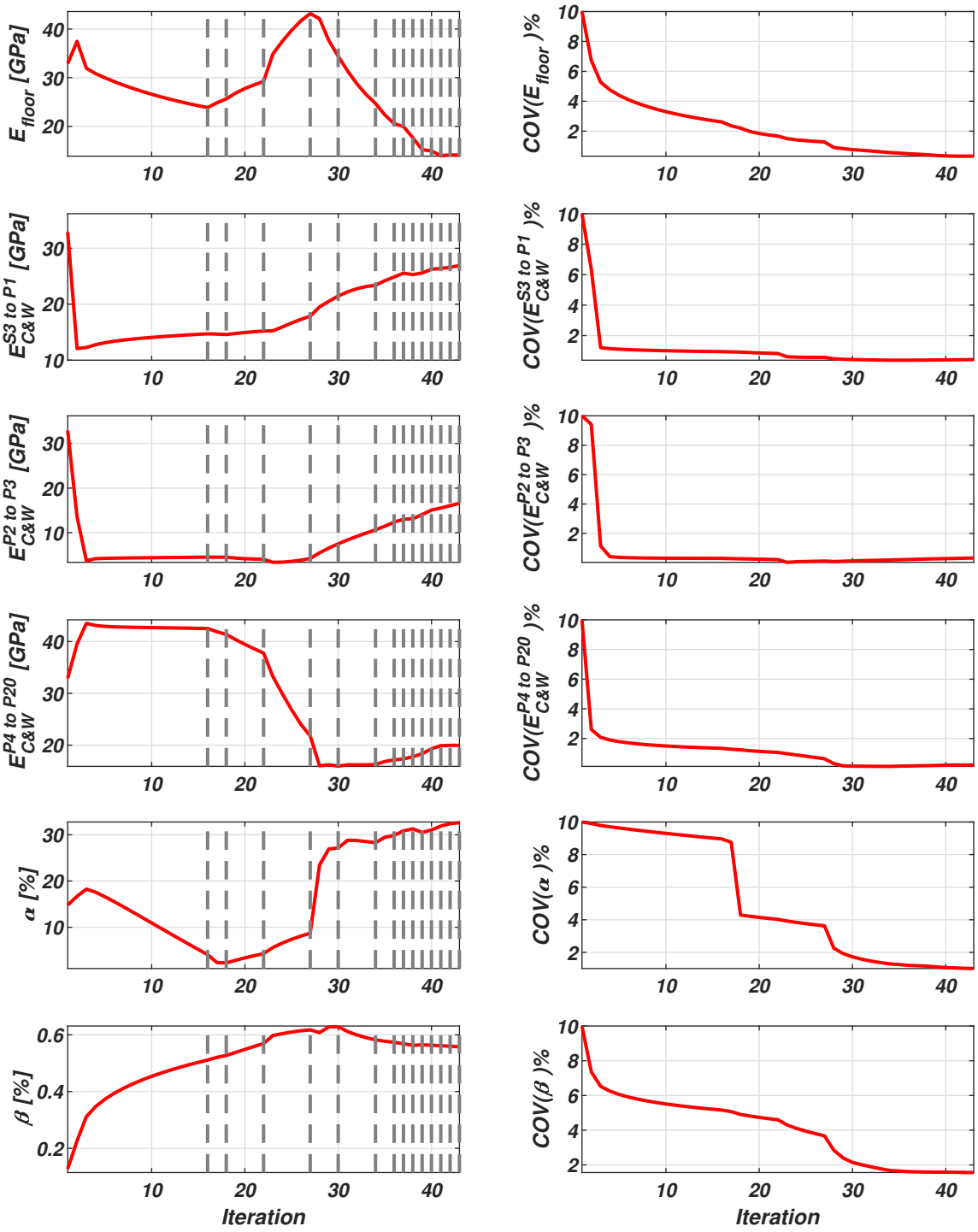

Figure 6.9: Time-histories of the posterior mean (left) and coefficient of variation (COV) (right) of the model parameters estimated from the seismic event #64.

As measured by the relative root mean square error values, the algorithm reduces the discrepancy between real data measured and the finite element model prediction (Figure 6.7). However, there is still a physical phenomenon that the numeric model does not consider since an average RRMSE remains around 50 % between seismic events #62 and #64.

Table 6.5 presents the final parameters estimates for the two cases presented. The lateral

stiffness of the system has been reduced, presenting a principal decay for the columns & walls elastic modulus of stories P2 to P3. The Rayleigh damping coefficients increase, which means that the damping of the system increases after damage, validating the results obtained by MOESP in Chapter 4.

Table 6.5: Parameters final estimates for seismic events #62 and #64.

	Final Estimate		**Percentage**
Parameter ID	**Seismic event #62**	**Seismic event #64**	**variation [%]**
E_{floor}	25.645	14.110	-44.98
$E_{C\&W}^{S3\text{ to }P1}$	28.423	26.928	-5.258
$E_{C\&W}^{P2\text{ to }P3}$	93.857	16.600	-82.313
$E_{C\&W}^{P4\text{ to }P20}$	27.744	19.951	-28.089
α	15.822	32.613	106.120
β	0.395	0.557	40.917

6.3. Summary of results for each event.

The maximum a posteriori estimation problem (Equation 2.6) was solved for each seismic record presented, and the algorithm performance was measured through the RRMSE metric. The evolution of the parameters for each event is presented in Figures 6.10 to 6.15, and Figures 6.16 to 6.21 display the histograms for each parameter before and after damage. Given that the algorithm did not perform well for all records, the final estimates with RRMSE mean greater than 75 % are denoted by black crosses. The means presented in Figures 6.10 to 6.15 and the histograms (Figures 6.16 to 6.21), only considered the final estimates with RRMSE mean minor to 75 %. The factors that led to poor algorithm performance are discussed in the following sections.

6.3.1. Final Parameters Estimates

Table 6.6: The mean and the coefficient of variation of the parameter estimates obtained before the damage are presented.

Parameter	$\boldsymbol{\theta}_{mean}$	$C.O.V.(\boldsymbol{\theta})[\%]$
E_{floor} [GPa]	31.203	25.638
$E_{C\&W}^{S3\text{ to }P1}$ [GPa]	26.728	22.834
$E_{C\&W}^{P2\text{ to }P3}$ [GPa]	149.140	36.630
$E_{C\&W}^{P4\text{ to }P20}$ [GPa]	27.824	14.873
α [%]	9.602	65.902
β [%]	0.384	26.469

Table 6.7: The mean and the coefficient of variation of the parameter estimates obtained after the damage are presented.

Parameter	$\boldsymbol{\theta}_{mean}$	$C.O.V.(\boldsymbol{\theta})[\%]$
E_{floor} [GPa]	23.600	55.527
$E_{C\&W}^{S3\,\text{to}\,P1}$ [GPa]	20.132	29.003
$E_{C\&W}^{P2\,\text{to}\,P3}$ [GPa]	49.404	111.970
$E_{C\&W}^{P4\,\text{to}\,P20}$ [GPa]	24.409	38.067
α [%]	24.827	32.197
β [%]	0.587	21.675

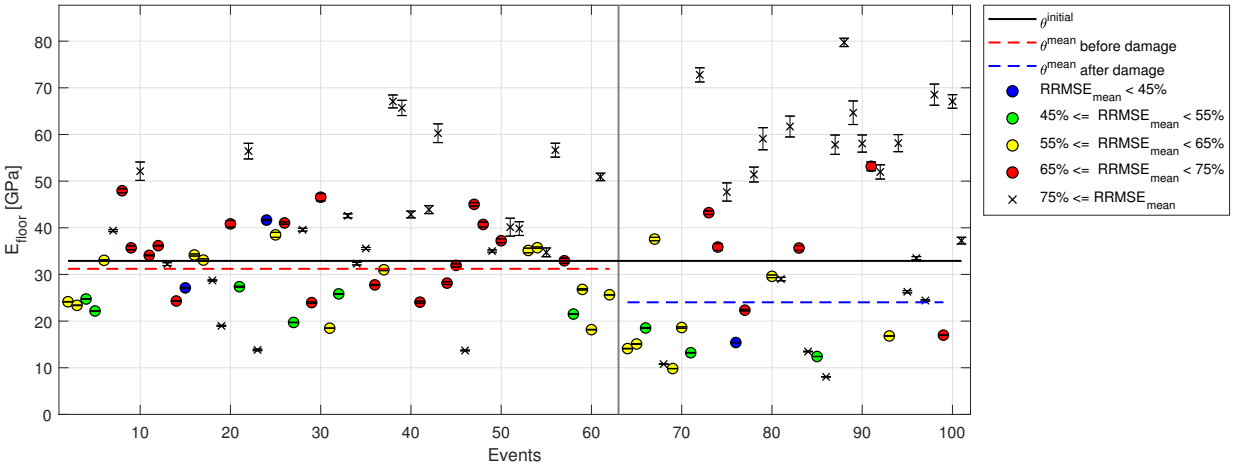

Figure 6.10: Parameter estimate E_{floor} for all seismic events and the standard deviations per estimate (the estimates mean does not consider the black cross estimates).

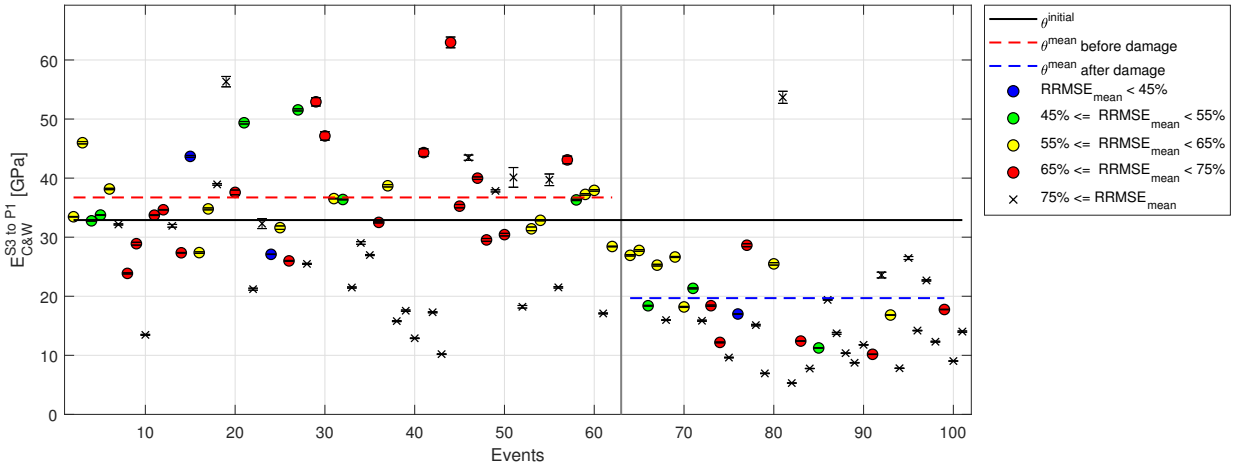

Figure 6.11: Parameter estimate $E_{C\&W}^{S3\,\text{to}\,P1}$ for all seismic events and the standard deviations per estimate (the estimates mean does not consider the black cross estimates).

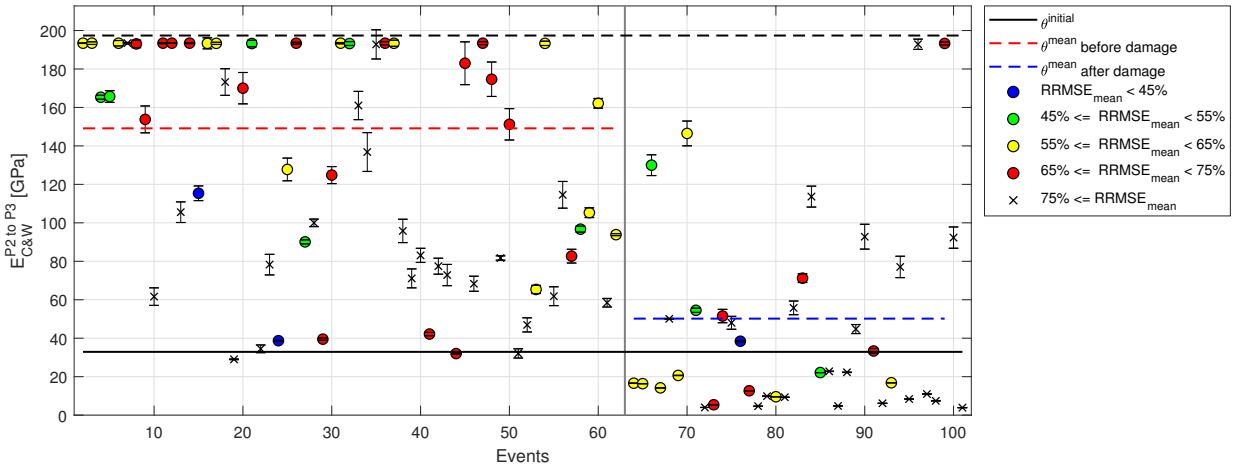

Figure 6.12: Parameter estimate $E^{P2\,\text{to}\,P3}_{C\&W}$ for all seismic events and the standard deviations per estimate (the estimates mean does not consider the black cross estimates). The black dash line represent upper edge constraint.

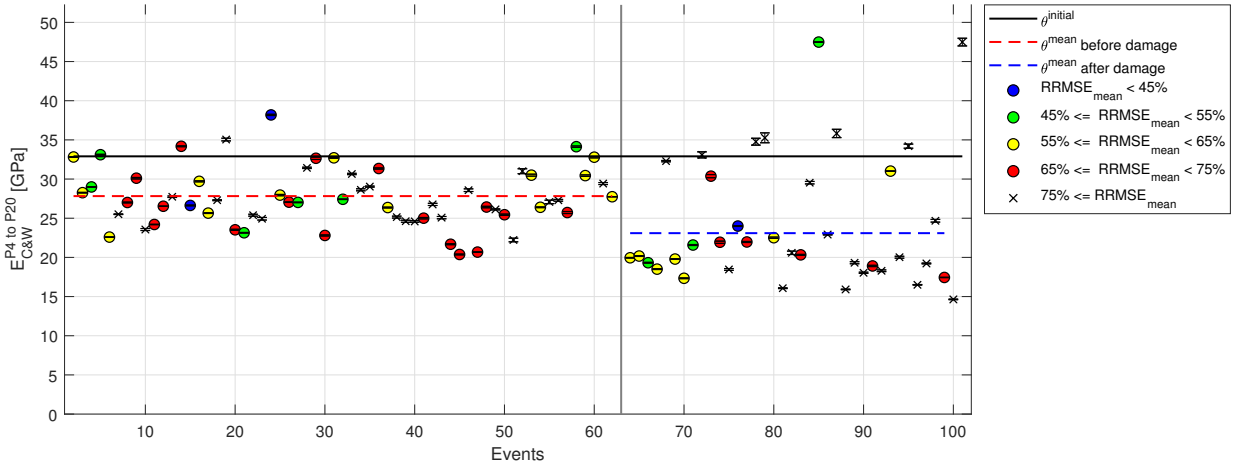

Figure 6.13: Parameter estimate $E^{P4\,\text{to}\,P20}_{C\&W}$ for all seismic events and the standard deviations per estimate (the estimates mean does not consider the black cross estimates).

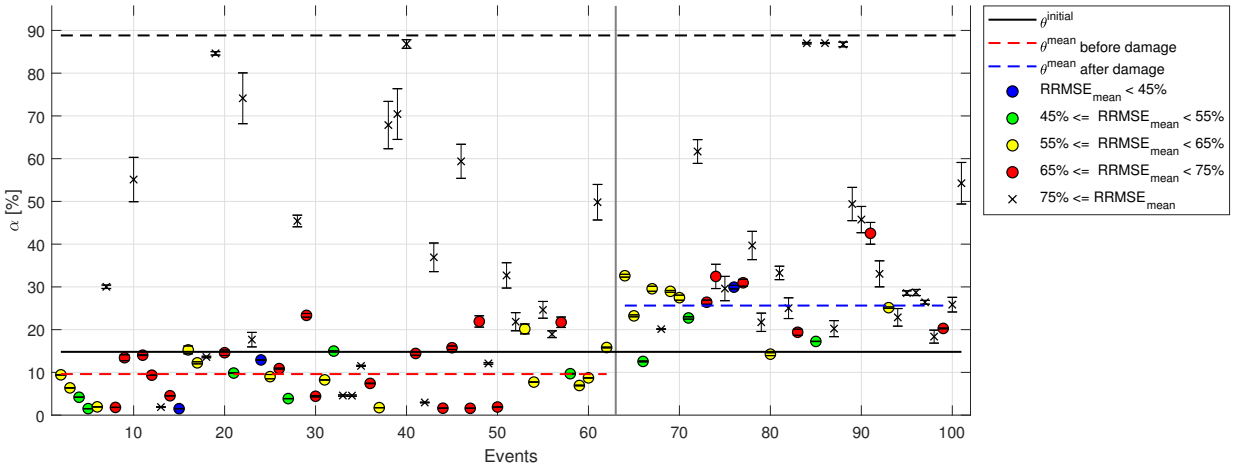

Figure 6.14: Parameter estimate α for all seismic events and the standard deviations per estimate (the estimates mean does not consider the black cross estimates). The black dash line represent upper edge constraint.

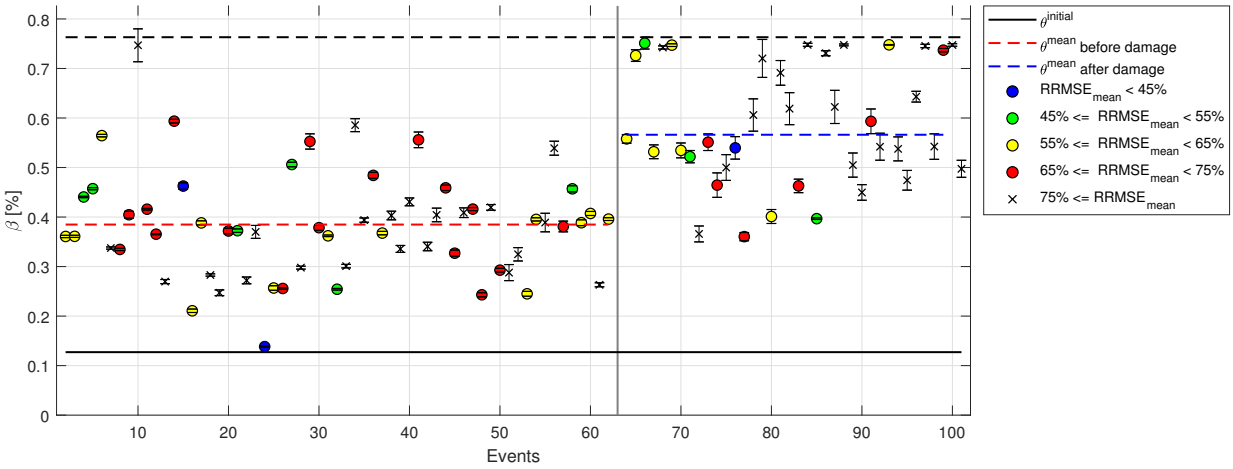

Figure 6.15: Parameter estimate β for all seismic events and the standard deviations per estimate (the estimates mean does not consider the black cross estimates). The black dash line represent upper edge constraint.

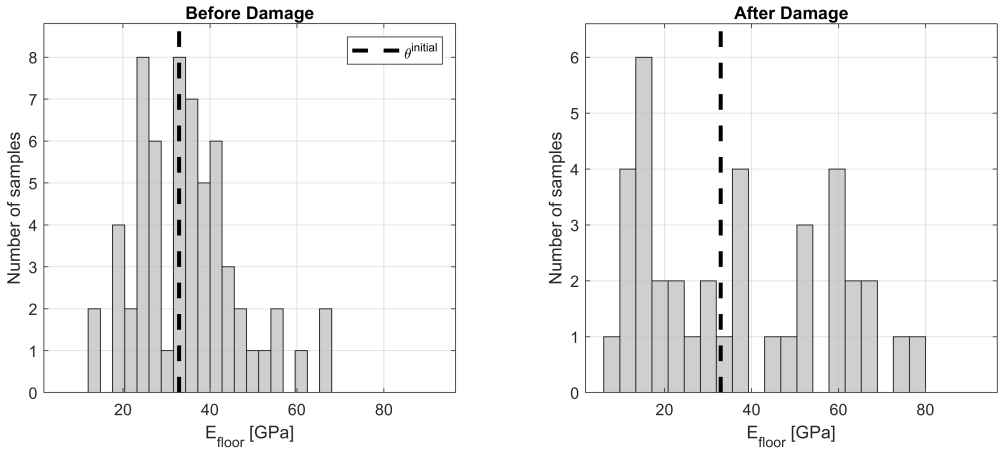

Figure 6.16: Histograms of parameter E_{floor} for all seismic events (the histograms do not consider the black cross estimates).

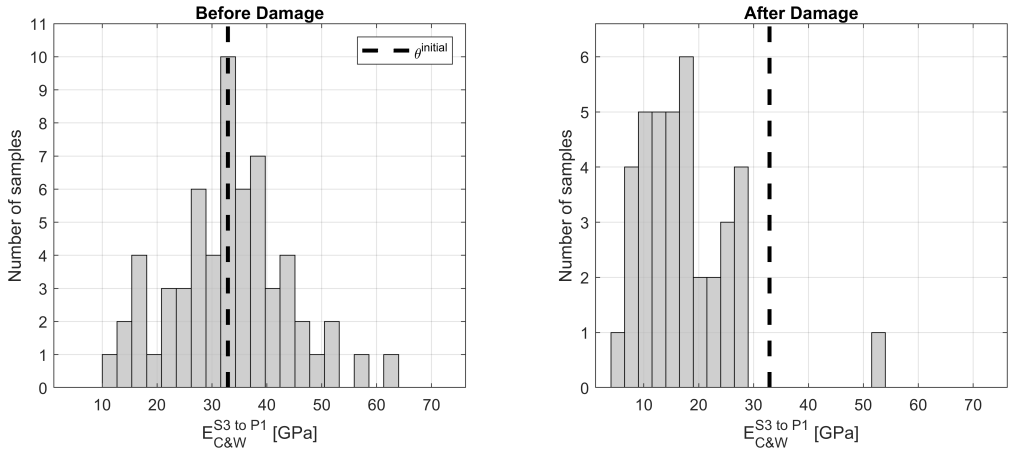

Figure 6.17: Histograms of parameter $E_{C\&W}^{S3\,\text{to}\,P1}$ for all seismic events (the histograms do not consider the black cross estimates).

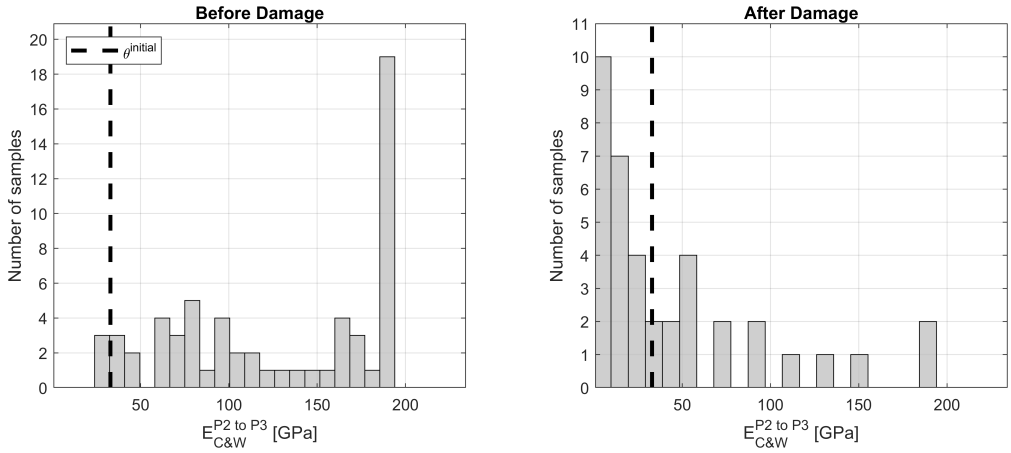

Figure 6.18: Histograms of parameter $E_{C\&W}^{P2\,\text{to}\,P3}$ for all seismic events (the histograms not consider the black cross estimates).

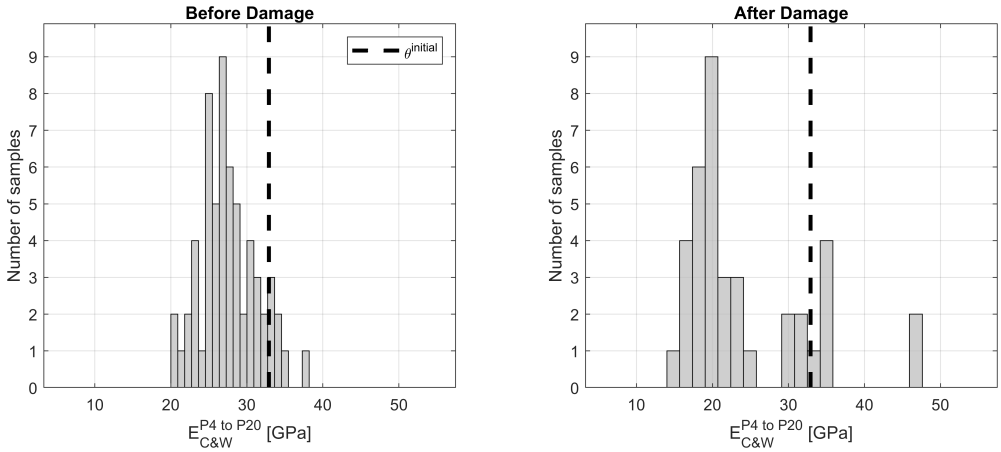

Figure 6.19: Histograms of parameter $E_{C\&W}^{P4\,\text{to}\,P20}$ for all seismic events (the histograms do not consider the black cross estimates).

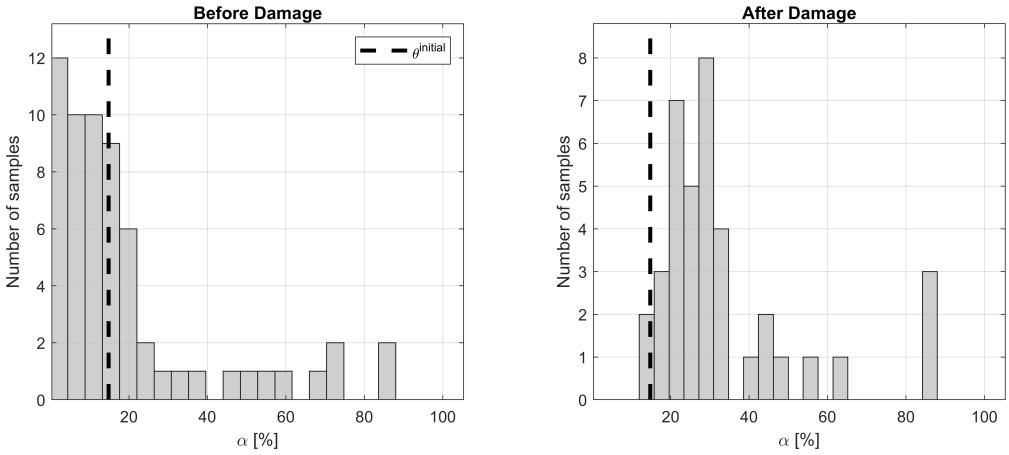

Figure 6.20: Histograms of parameter α for all seismic events (the histograms do not consider the black cross estimates).

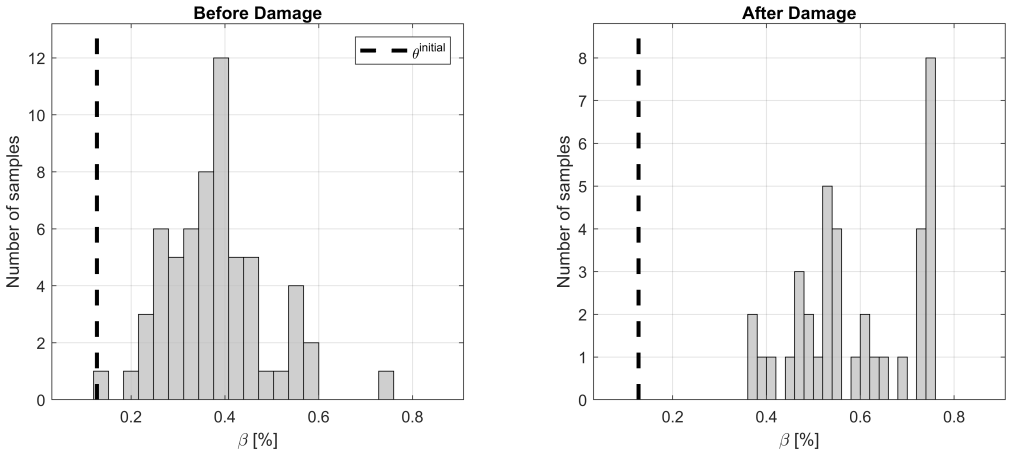

Figure 6.21: Histograms of parameter β for all seismic events (the histograms do not consider the black cross estimates).

Below are the damping ratios and frequencies identified by MOESP and the set by the Rayleigh damping model curves.

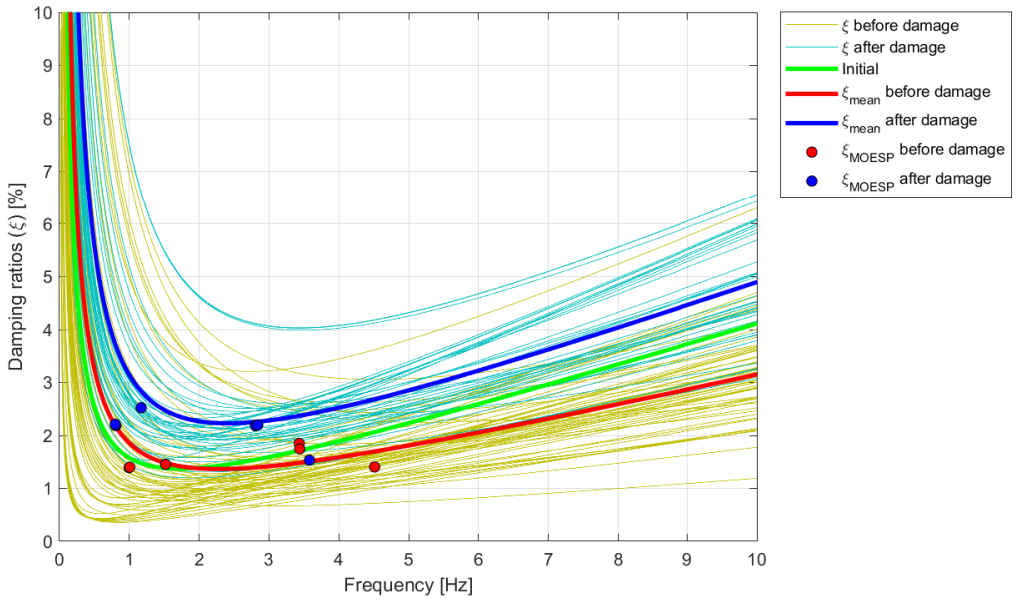

Figure 6.22: The Rayleigh damping ratio as a function frequency for the initial, and updated FE models.

The parameter estimates have large variability, presenting high values for the variation coefficients in the case of the parameters E_{floor}, $E_{C\&W}^{P2\,\text{to}\,P3}$, and α. From figures 6.10 to 6.15, a gray line is established to mark the event associated with the mega-earthquake (event 27F) and separate the estimates before and after the damage to the building.

Figure 6.10 shows the evolution of the elastic modulus of the floor system (E_{floor}). These estimates do not show a clear tendency, what was expected was a reduction of these estimates given the damage report localized in the perimeter beams [6].
Figure 6.11 shows the elastic modulus of the basement stories ($E_{C\&W}^{S3\,\text{to}\,P1}$). Before the damage, the estimates indicate these stories trend to increment the stiffness regarding the initial value. On the other hand, these values present a clear tendency to stiffness reduction after damage. The histogram presented in Figure 6.17 indicates that before the damage, the parameter estimates show a normal Gaussian distribution, but after damage, this distribution shifts to the left of the initial value.

The parameter $E_{C\&W}^{P2\,\text{to}\,P3}$ presents the highest variability among the parameters (6.12) with the lowest entropy gain (Figure 6.27). If more floors are included in this group to increase the entropy gain, the variability must be reduced. On the other hand, before building damage, this parameter increases its value, even reaching the upper edge constraint, equal to 197.4 [GPa]. If the estimates mean are compared between the two states of the building (without damage and with damage), the stiffness loss is clear. The great variability of the estimates can be seen in the histogram of this parameter (Figure 6.18).

The estimates of $E_{C\&W}^{P4\,\text{to}\,P20}$ indicate a similar distribution to parameter $E_{C\&W}^{S3\,\text{to}\,P1}$, but a minor

factor stiffness is seen before and after damage. Same case for histograms, where before damage a Gaussian distribution is visible in Figure 6.19, but not for distributions after damage. The loss of stiffness is visible before damage in Figure 6.13.

Rayleigh damping coefficients show great variability for α (Tables 6.6 and 6.7). It occurs since this parameter has a low entropy gain (Figure 5.11). The reduction of the structural response for the building in its damaged state, explains the increment in the proportional Rayleigh coefficients (α and β). Figure 6.22 shows the damping ratios as a function of frequency calculated from proportional Rayleigh' coefficients (α and β). The incorrect match between the MOESP damping ratios occurs due to the high variability of these values in the identification process (Table 4.2).

6.3.2. Algorithm Performance

Figure 6.23 shows the relative root mean square error for each seismic event. The algorithm reduces the discrepancy between the FE predictions and real data measured response after the model updating, except for the seismic events #13 and #24, where some channels show the opposite. The increment in the RRMSE metric for events in the right of the gray line is due to the fact the initial model was updated considering initial parameters without deterioration by damage.

Table 6.8 shows the summary of the RRMSE values. This table indicates the RRMSE mean not change between two states of structure (damaged and un-damaged). We can conclude remaining error is due to model uncertainties (input force, boundary conditions, among others).

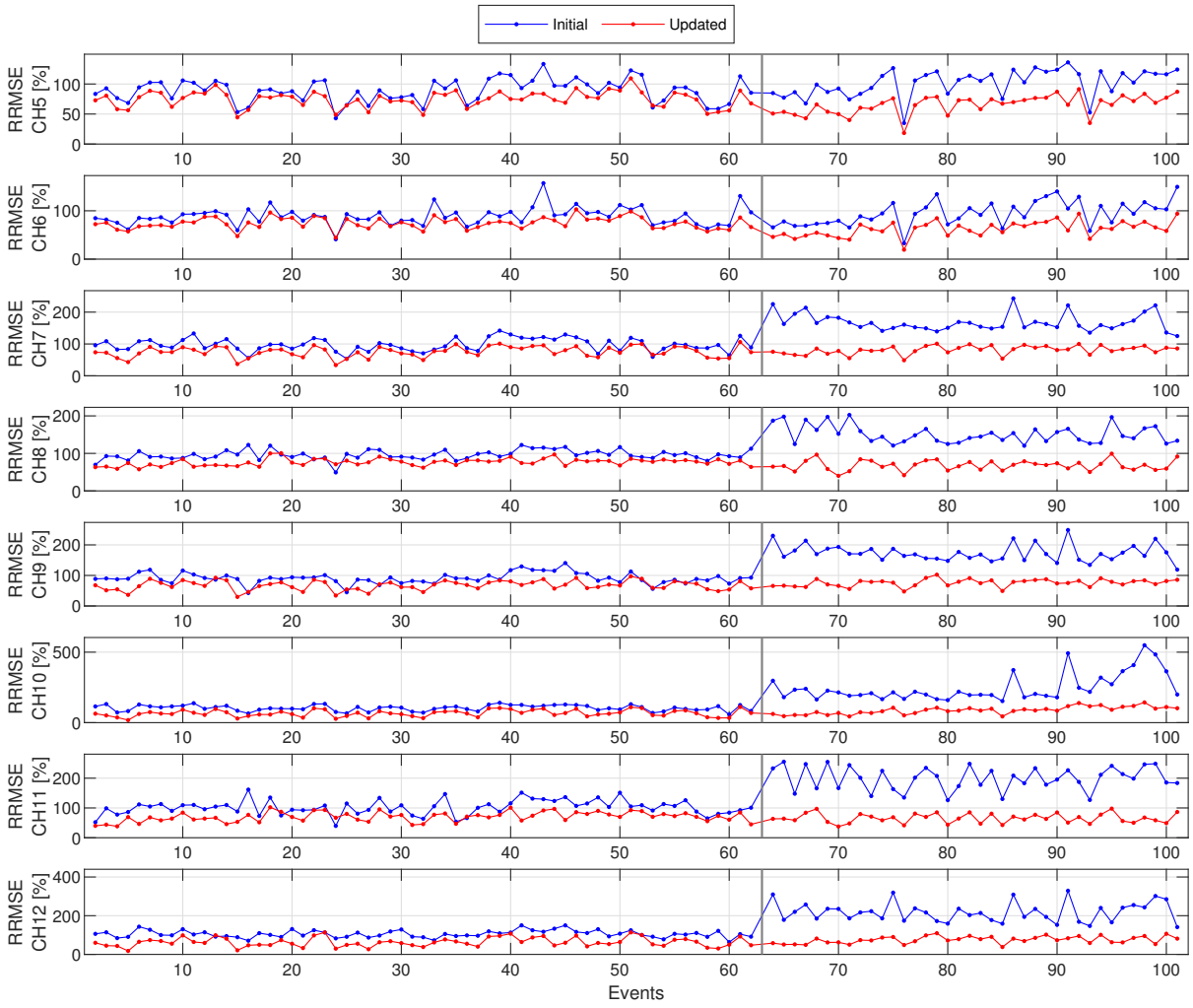

Figure 6.23: RRMSE for each seismic event for the initial and updated FE models.

Table 6.8: The means and coefficients of variation for the RRMSE for the updated model are shown.

	Before damage		After damage	
Channel	**RRMSE [%]**	**C.O.V.(RRMSE) [%]**	**RRMSE [%]**	**C.O.V.(RRMSE) [%]**
5	68.255	17.385	52.314	23.665
6	69.117	15.070	50.012	20.539
7	65.703	19.666	70.678	15.967
8	73.261	11.743	60.577	19.911
9	58.977	20.599	66.299	15.497
10	51.823	28.842	69.339	30.723
11	63.438	21.696	57.174	25.466
12	49.805	28.545	61.488	22.909

Figure 6.24 shows the mean of the RRMSE's values of each seismic event. The colors scale selected is equal to that which is presented in Figures 6.10 to 6.15. The results indicate the algorithm's poor performance is not necessarily due to the presence of non-linearities in the structural response, except for seismic event #12, where the building reached accelerations

around 15 %g. For this case, the RRMSE remain within the average. Figure 6.25 show the relation between the RRMSEs and the accelerations experimented by CChC Building for each channel. On the other side, the final C.O.V.s of each parameter and the maximum accelerations on the building are displayed in Figure 6.26. The C.O.V.s have a clear tendency to reduce while acceleration increases are experienced.

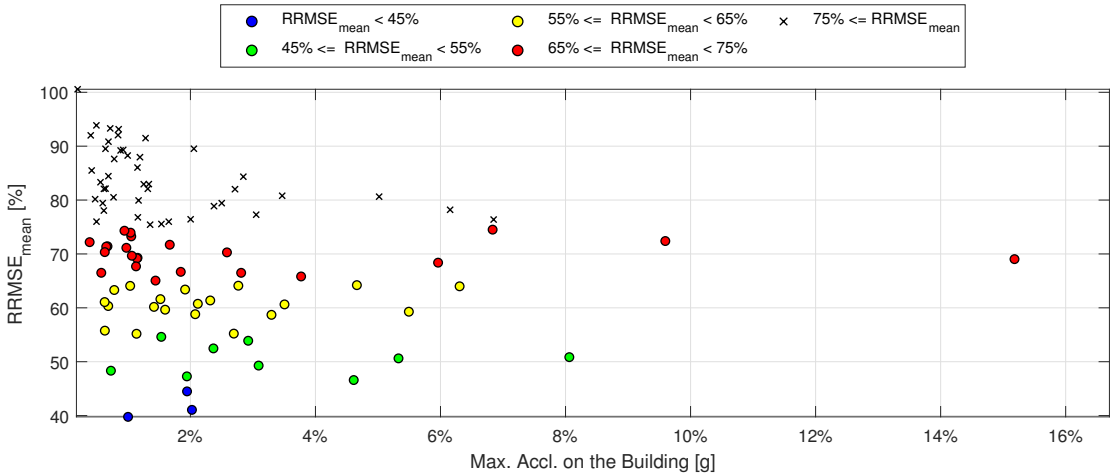

Figure 6.24: The mean of RRMSE's values for each seismic event versus Maximum Accelerations on the building.

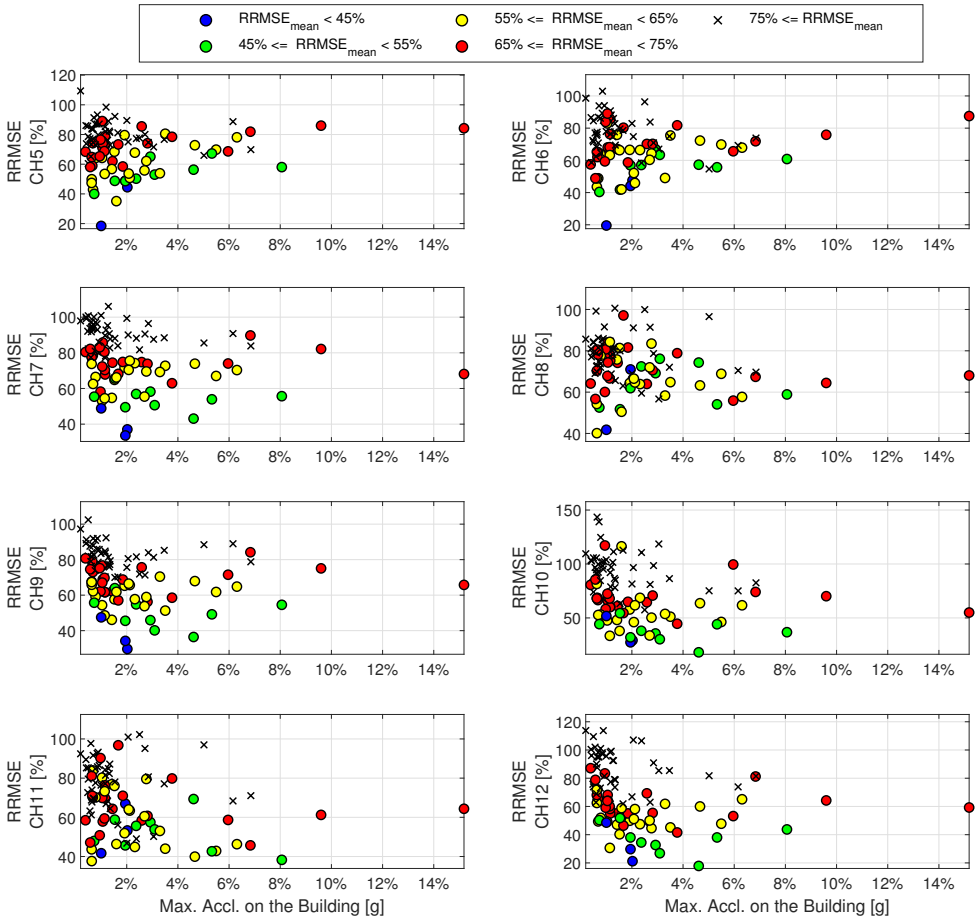

Figure 6.25: RRMSE for each seismic event versus Maximum Accelerations on the building.

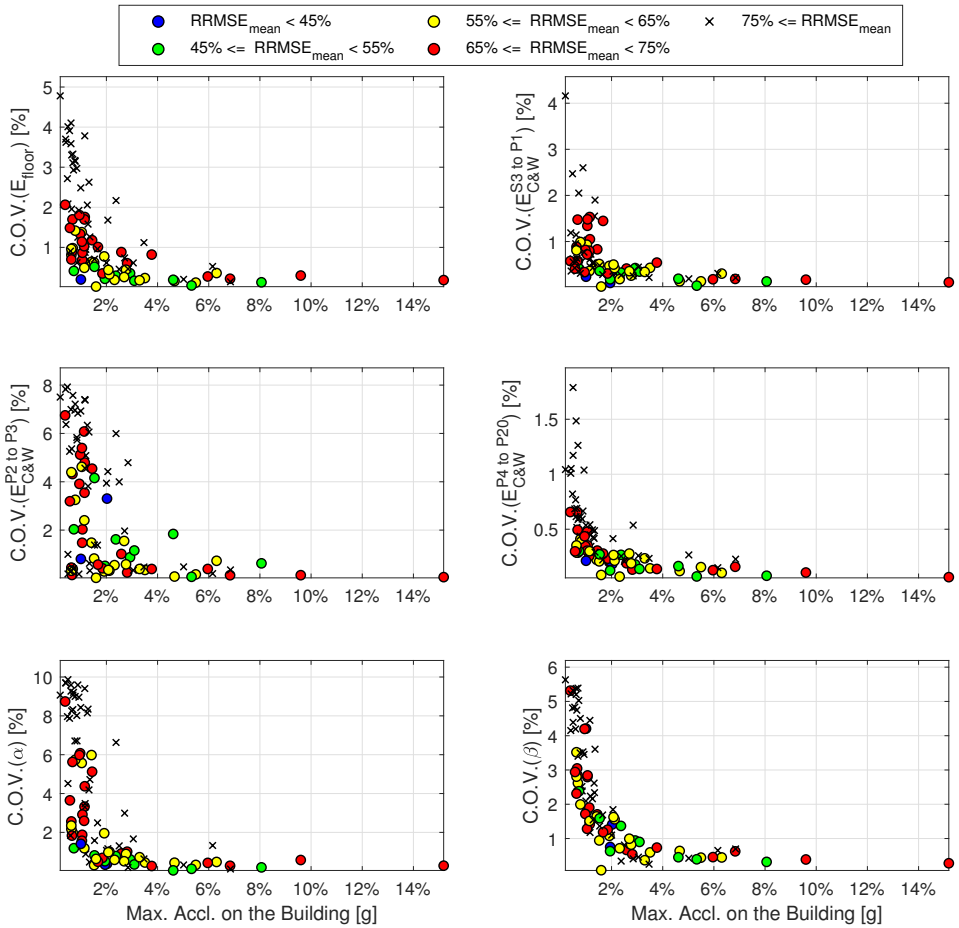

Figure 6.26: Final C.O.V.s for each seismic event versus Maximum Accelerations on the building.

Another indicator used in this work is the entropy gain of each parameter. These quantify the amount of information that can be measured in each parameter given the available sensors. The importance of this parameter was seen in the identifiability evaluation section for the selection of parameters (Chapter 5). Figure 6.27 presents the evolution of the entropy gain for each parameter. The entropy gain values from Figure 6.27 were calculated with the initial estimates (Table 6.2). As expected, the parameters that presented more information were those associated with the stiffness of the system, especially that of the columns and walls of the basement stories, and the lateral stiffness of 4^{th} to 20^{th} stories. It can be concluded that the aforementioned parameters control the structural response. On the other hand, it is important to mention that the parameters that presented the greatest variability (Table 6.6 and 6.7), are those with the lowest entropy. As mentioned above, to increase the entropy gain values, different groups of parameters must be joined, as long as they have the same physical meaning.

Regarding the entropy gain and RRMSE values, Figure 6.28 shows that estimates with poor algorithm performance trend to grouping in the area where there are low values of entropy gain. A similar case shows Figure 6.29, where the final estimates and entropy gain values are presented. For parameters that control structural response (E_{floor} and $E_{C\&W}^{P4\text{ to }P20}$), the estimates trend to be grouped in a zone but do not show a clear tendency.

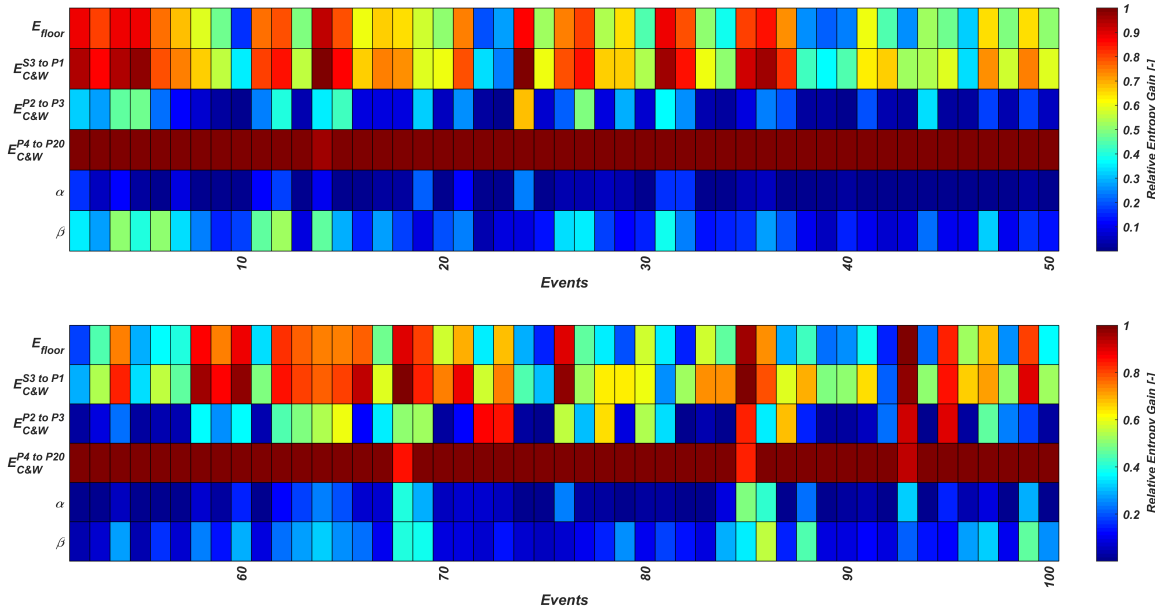

Figure 6.27: Entropy Gain evolution for each seismic event

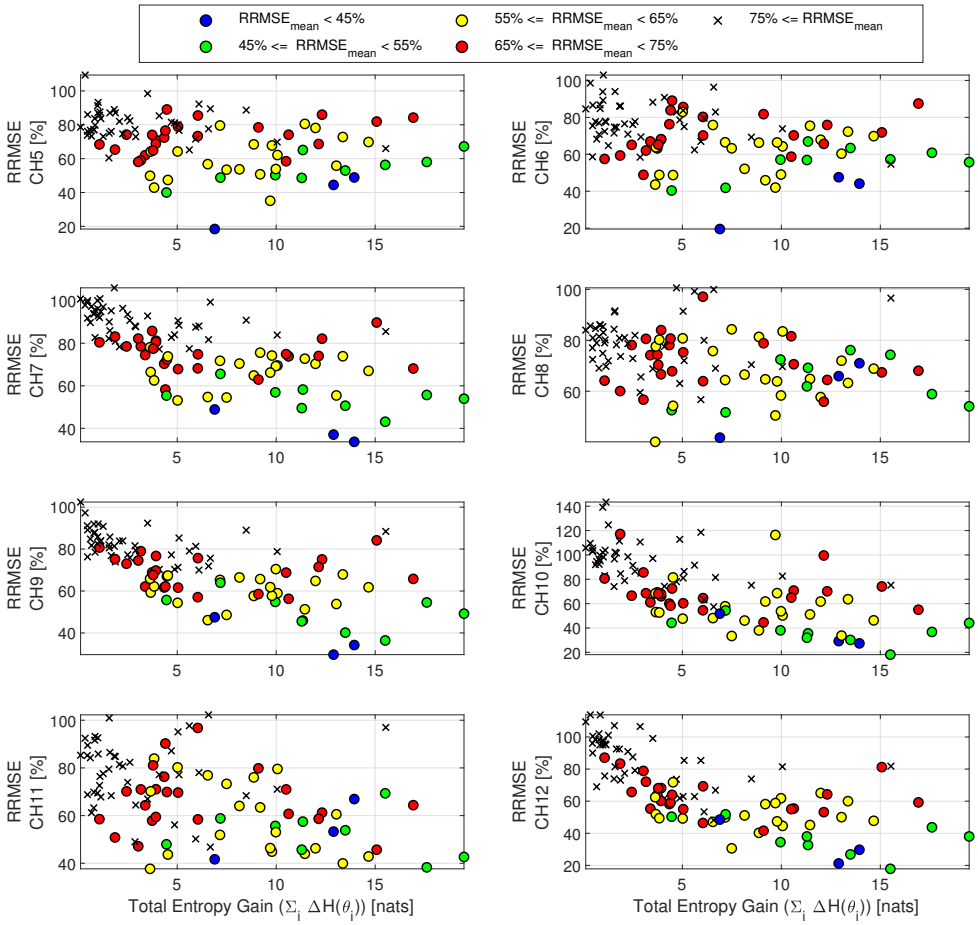

Figure 6.28: RRMSE for each seismic event versus Total Entropy Gain ($\Sigma_i \Delta H(\theta_i)$).

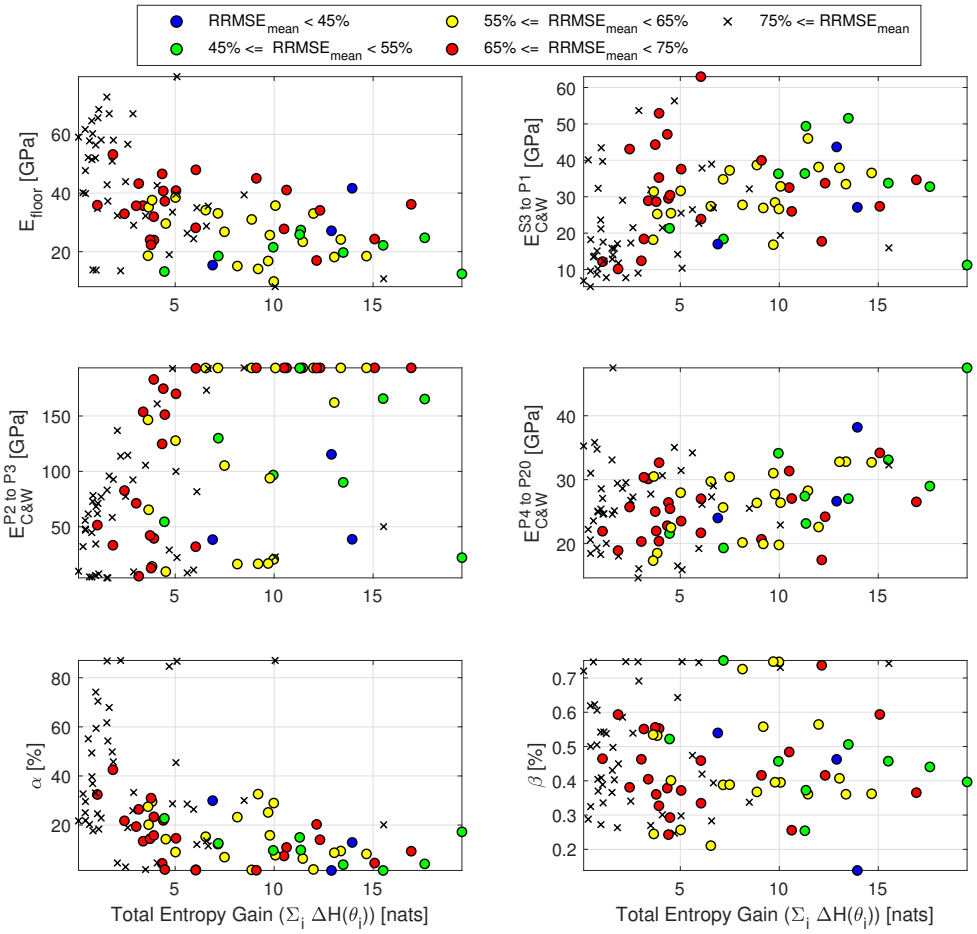

Figure 6.29: Final parameter estimates for each seismic event versus Total Entropy Gain ($\Sigma_i \Delta H(\theta_i)$).

Chapter 7

Conclusions

This study uses a model updating algorithm based on Bayesian inferences to improve the Chilean Chamber of Construction Building finite element model predictions for different accelerations records due to seismic events. For that purpose, the algorithm updates the probability distribution function (PDF) of the model parameters to minimize the misfit between the CChC Building response and the numerical prediction of the model. The principal advantage of the Sequential Bayesian FE model updating is to estimate the time history response of the building using data real measured and an FE model. That tracks the model parameters and gives an idea of how the behavior is during seismic events. In addition, the uncertainties of the model parameters are estimated. This chapter summarizes and discusses the results and gives recommendations to continue with the present investigation.

7.1. Summary of research work performed

The work presented in this dissertation improved the predictions of a large-scale model using data measured on the CChC Building and the Sequential Bayesian finite element model updating technique. The building under study is the Chilean Chamber of Construction Building (CChC Building).

The three parts of this work are:

- Building state evaluation.
- Finite element model preparation.
- Finite element model update.

In chapters 3 to 4, for the evaluation of the state of the building, the studies carried out by Boroschek *et al.* [7, 6, 4, 47] were read in-depth. In addition, an FE model was developed using the structural plans of the CChC Building. Due to damage reports in Boroschek & Soto, 2012 ([47]), an identification stage was carried out to track the modal parameters of the building with Spectrogram and MOESP identification methods. The results indicate the first translational modes frequencies were reduced around 20 % after the mega-earthquake of 27 February 2010 (27F event). Consequently, the defined assumption was that the FE model of the CChC Building has a linear-elastic behaviour for all seismic events, except for event 27F, due to the modal parameters not changing over 5 %. As an additional study, the study

carried out by Carreño & Boroschek [6] was complemented, which compares the amplitude of the movement with the identified frequencies. It was determined that at a low amplitude of motion, the frequencies have a large dispersion, and as the amplitude increases, the frequencies tend to converge to a value. It is concluded that the structure has a non-linear elastic behaviour for seismic forces.

The second part of the research which is covered in Chapter 5, was focused on the FE model preparation. A graphic-user interface of ETABS software [54] was used to develop the initial geometry of the model. The ETABS model was then transferred to OpenSees [32] using a custom-developed MATLAB [38] script based on the ETABS application programming interface (API). The ETABS and OpenSees model were compared through static (dead loads), periods, and mode-shapes. The validation stage was completed successfully. As a secondary step, the OpenSeesSP [39] was implemented, and time-saving analysis evaluated the performance of the parallel computation. It was concluded the parallel computation is 80 times faster than simple solvers. Finally, the identifiability assessment stage was performed to select the model parameters that be updated to improve the FE model predictions. The identifiability assessment stage is based on Information Entropy theory.

Finally, Chapter 2 reviews the theory behind the sequential Bayesian finite element model updating technique for joint estimation of parameters and input forces. In addition, the correction by constraints method for the estimated parameters and an adaptive scaling method for improving the algorithm performance was described. The above, uses as a guideline the works carried out by Ebrahimian *et al.* [2, 1, 34]. Chapter 6 shows the results after apply the algorithm using real data measured on the building. The final parameters estimates for each seismic event are presented. Moreover, the algorithm performance is compared with the parameters uncertainties and information available (through the coefficient of variation, and entropy gain, respectively). The relative root means square error (RRMSE) metric was selected to evaluate the algorithm performance.

7.2. Limitations of the research work and summary of major findings

In the first stage of the current work, the modal parameters of the building were identified how they evolved during a seismic record was observed. It was observed that during the strong phase of the earthquake, the building's frequencies decrease. The modal parameters were identified for each window for all seismic records. When comparing the frequencies with the modal amplitude defined by Carreño & Boroschek, 2011 [6], it was observed that at low modal amplitude values, the frequencies have great variability, and the frequencies tend to converge as the modal amplitude increases. Carreño carried out this process for the seismic records from 1997 to 2010. In this work, records were included within the period from 2010 to 2014. On the other hand, if the mode shapes for a record before and after the damage are compared (records #62 and #64 of the catalogue Table B.1) it is observed that the mode shapes do not show great changes between a damaged and undamaged state. The damping of the system tends to increase for registers when the building is in its damaged state. However, the high variability of this parameter makes it difficult to describe the damping behaviour of the system. To conclude this stage, the MOESP subspace stochastic identification method

proves to be a great tool to identify the modal parameters of the system during earthquakes. Given the limited arrangement of sensors in the superstructure, it is not possible to determine a change in the state of the building through the mode-shapes. However, the variability of the structure's frequencies is sufficient to assess the structure's health, but with this parameter alone it is not possible to locate the damage. The last can be complemented with studies of environmental vibrations or model updating techniques that update the model using modal parameters as input.

About the FE model updating, the results show that the procedure carried out did not identify the building parameters correctly. The high variability of estimates indicates that the model updating problem is a bad conditioned problem. A change in the parameters of the problem can change the results. In this case, from different seismic events, the parameter estimates present high variability. Occasionally, in some cases the parameters estimates track a trend, for example, the parameter $E_{C\&W}^{P4\,\text{to}\,P20}$ (Figure 6.13). Nevertheless, the algorithm reduces the misfit between the real data measured and the FE model predictions. The algorithm can successfully match the dynamic response of the building and the responses of the FE model for signals that are in a frequency range between 0.5 and 10 hertz. That means that the first six vibration modes of the structure are captured correctly. In general, in some cases, the signals do not show a coincidence for amplitude. In these cases, the torsional and rocking ground motions components could influence the structural response. The influence of the ground rotational components falls outside the scope of this work.

In the context of the response spectrum [35], the structures subject to damage suffer a lengthening of the period. Consequently, the demand for response tends to decrease. The reduction in earthquake demand can be seen in the acceleration time series of the dynamic response for the damaged structure when compared to the response of the non-updating finite element model. The algorithm manages to properly match the response of the FE model with the response of the damaged structure after the update process, looking at a coincidence in amplitude and frequency. Given the above, the algorithm identifies the reduction in the structure's stiffness with the parameter estimates associated with the elastic modulus before and after damage. In order not to get unrealistic estimates, constraints were defined. In addition, the constraints allow that the periods of the finite element model match with those identified by MOESP. The unreal values for the modulus of elasticity are due to the fact that the stiffness also depends on the geometric properties of the sections (moment of inertia, area, shear factor, among others). By representing the stiffness of the system through the moduli of elasticity, this error is incurred.

Considering the non-linear elastic behaviour of the structure observed on the modal parameters identification stage, a way to improve the estimations is to consider materials and elements that can model this physic phenomenon. A non-linear model requires a great computational demand. Future investigations can consider using GPU-solvers as CUDA, applied by Lu *et al.* [58], where the time calculus for a time-history analysis for a big-scale model (Shanghai Tower) was compared with other CPU-parallel solvers, and the studies showed that GPU-solvers were 15 times faster in comparison to normal parallel solvers.

Recognizing that limitations of this study were the hardware used, the limited number of parameters selected, and the low values of entropy gain obtained given the small number of

sensors, the algorithm matches the signals in the frequencies domain to find the reduction of stiffness of the system after damage. The trend of estimates could be a good indicator of damage, but with the high variability, it is not possible to conclude without uncertainties in the process. Given the above, the parameter estimates can be complemented with the estimates given for other model updating algorithms, based on environmental vibrations, or techniques based on response function in the frequency domain.

The landmarks made in this work are mentioned below:

- The first part of this work focused on ordering and characterizing the seismic records according to their PGAs, maximum accelerations in the building, and identifying its modal properties using the MOESP subspace method. The results validate the research carried out by Carreño & Boroschek, 2011 [6]. Based on this, it was possible to identify the records that were highly non-linear, corresponding to seismic event #63 of catalogue B.

- A routine was generated that allows converting a model from ETABS to OpenSees in addition to validating the model by performing gravitational load analysis, eigenvalues and eigenvectors analysis, and static analysis. It also allows assigning groups of parameters, to later be updated with some finite element model update algorithm. In addition, a parallel CPU solver was implemented, which shows the great advantage over using a simple solver. The results show the parallel solver is 80 times faster than a simple solver for time-history analysis with 1000 time-steps.

- A code was implemented that allows calculating the entropy gain and mutual entropy to evaluate the amount of information contained in the measurement dataset about each FE model parameter for the selection of parameters.

- The sequential finite element model update algorithm was applied for parameter estimation for 100 different seismic records. The results were summarized, and conclusions were made about the distribution of the estimates, and factors that affect the performance of the algorithm.

7.3. Recommendations for future research work

1. To enhance the algorithm, it is recommended to extend the investigation to the estimation of the rocking and torsional ground motion components and evaluate their influence on the structural response. With the above, validate the recommendations in the field of soil-structure interaction. On the other hand, it is also recommended to include other sources of uncertainty in the finite element model as the correct modelling of energy dissipation mechanisms, in terms of boundary conditions, include the flexibility of the foundations, soil-structure interaction, among others. Given that the building is located on a gravel floor (with good performance), it is recommended to include a spring system to model the confinement of the floor to the basement floors. On the other hand, given the fact that the building has large stiffness, the periods and modal shapes of the initial model coincide in a good way with those identified by the MOESP method, so it is not recommended to include non-structural elements such as stairs in the model, dividing walls, among other elements.

2. The Rayleigh damping coefficients for the updated FE model can estimate the damping increment for periods in which the structure is damaged, validating the trend to increase the damping ratios identified by MOESP. A further study could include the modal damping ratios in the model updating problem, using modal damping for identifiable modes, and complemented with the Rayleigh damping for upper modes. The uncertainties propagation in the modal damping ratios could give indicators of the behaviour of the viscous forces in the structures for seismic events.

3. Finite element model updating techniques require running the model several times, which does not allow a quick response to detecting damage given the time it takes. For the above, it is recommended to implement parallel solvers that use the GPU. The mentioned solvers have been validated in other software such as Abaqus, Ansys, among other numerical modelling programs. Currently, the solver Cusp is available in OpenSees, having as a requirement an NVIDIA's GPU's with the CUDA^{TM} architecture.

4. Given the low number of sensors, it is recommended to validate the parameter estimates with other FE model updating techniques that use other types of input, such as environmental vibrations, in order to assess the uncertainty of the estimates. On the other hand, the sequential FE model updating technique proves to be a powerful technique when estimating the non-linear properties of structures. It is recommended to extend the present investigation to a non-linear model of the CChC building, specifically for record #63 of the catalogue, which was omitted in the present investigation. Complement the previous study, with an evaluation of the identifiability of parameters to verify the hypothesis that the structure has a linear behaviour for the other earthquakes except for the mega-earthquake. The above should indicate a low entropy for the parameters that model the non-linearity of the materials, and a high entropy gain for the parameters that model the elastic behaviour of the building.

Bibliography

[1] H. Ebrahimian, R. Astroza, J. P. Conte, and C. Papadimitriou, "Bayesian Optimal Estimation for Output - Only Nonlinear System and Damage Identification of Civil Structures," *Structural Control and Health Monitoring*, vol. 25, no. 4, pp. 1–32, 2018.

[2] H. Ebrahimian, R. Astroza, and J. P. Conte, "Extended Kalman Filter for Material Parameter Estimation in Nonlinear Structural Finite Element Models using Direct Differentiation Method," *Earthquake Engineering & Structural Dynamics*, vol. 44, no. 10, pp. 1495–1522, 2015.

[3] P. Lazcano, "Variación de los Parámetros Modales del Edificio de la Cámara Chilena de la Construcción a partir de Registros Ambientales y Sísmicos," *Memoria para optar al título de Ingeniero Civil. Universidad de Chile.*, 2008.

[4] R. Boroschek and P. Lazcano, "Non-damage Modal Parameter Variations on a 22 Story Reinforced Concrete Building International Modal Analysis Conference," *International Modal Analysis Conference, IMAC XXVI, Orlando Paper*, vol. 255, 2008.

[5] R. Carreño, "Variación de Propiedades Dinámicas del Edificio de la Cámara Chilena de la Construcción: Caso Sísmico," *Memoria para optar al título de Ingeniero Civil. Universidad de Chile.*, 2009.

[6] R. Carreño and R. Boroschek, "Modal parameter variations due to earthquakes of different intensities," in *Civil Engineering Topics*, vol. 4, pp. 321–333, Springer, 2011.

[7] R. Boroschek and F. Yáñez, "Experimental verification of basic analytical assumptions used in the analysis of structural wall buildings," *Engineering Structures*, vol. 22, no. 6, pp. 657–669, 2000.

[8] R. Boroschek, E. Peña, P. Villalpando, and N. Novoa, "Evaluación de las Propiedades Modales en Puertos bajo Condiciones Sísmicas y Operacionales," *XII Congreso Chileno de Sismología e Ingeniería Sísmica, ACHISINA*, 2019.

[9] M. Moroni, R. Boroschek, and M. Sarrazin, "Dynamic Characteristics of Chilean Bridges with Seismic Protection," *Journal of Bridge Engineering*, vol. 10, no. 2, pp. 124–132, 2005.

[10] M. Moroni, M. Sarrazin, and P. Soto, "Behavior of Instrumented Base-Isolated Structures during the 27 February 2010 Chile Earthquake," *Earthquake Spectra*, vol. 28, pp. 407–424, 2012.

[11] R. Boroschek, P. Soto, and R. Leon, "Registros del Terremoto del Maule Mw=8.8 de 27 de Febrero de 2010," *Informe RENADIC 10/05 Rev.2, Departamento de Ingeniería Civil. Universidad de Chile*, 2010.

[12] M. Astroza, S. Ruiz, and R. Astroza, "Damage Assessment and Seismic Intensity Analysis of the 2010 (Mw 8.8) Maule Earthquake," *Earthquake Spectra*, vol. 28, no. S1, pp. 145–164, 2012.

[13] M. Astroza, F. Cabezas, M. Moroni, L. Massone, S. Ruiz, E. Parra, F. Cordero, and A. Mottadelli, "Intensidades Sismicas en el area de daños del Terremoto del 27 de Febrero," *Reporte técnico, Departamento de Ingeniería Civil, Universidad de Chile.*, 2010.

[14] Earthquake Engineering Research Institute, "The Mw 8.8 Chile Earthquake of February 27, 2010," *EERI Special Earthquake Report*, no. June, 2010.

[15] K. Worden, C. Farrar, G. Manson, and G. Park, "The Fundamental Axioms of Structural Health Monitoring," *Proceedings of the Royal Society A: Mathematical, Physical and Engineering Sciences*, vol. 463, pp. 1639–1664, 2007.

[16] S. Doebling, C. Farrar, M. Prime, and D. Shevitz, "Damage Identification and Health Monitoring of Structural and Mechanical Systems from Changes in their Vibration Characteristics: A literature review," *Report LA-13070-MS, Los Alamos, New Mexico.*, 1996.

[17] F. Hemez and S. Doebling, "Review and Assessment of Model Updating for Non-linear, Transient Dynamics," *Mechanical Systems and Signal Processing*, vol. 15, no. 1, pp. 45–74, 2001.

[18] E. Carden and P. Fanning, "Vibration Based Condition Monitoring: A review," *Structural Health Monitoring: An International Journal*, vol. 3, no. 4, pp. 355–377, 2004.

[19] Y. J. Yan, L. Cheng, Z. Y. Wu, and L. H. Yam, "Development in Vibration-Based Structural Damage Detection Technique," *Mechanical Systems and Signal Processing*, vol. 21, no. 5, pp. 2198–2211, 2007.

[20] J. Caroca, "Desarrollo e Implementación de un Sistema de Detección de Daño Estructural," *Tesis para optar al grado de magíster en Ciencias, mención Ingeniería Sísmica. Universidad de Chile*, 2012.

[21] P. Villalpando, "Identificacion Experimental de Daño en Estructuras a través del Principio de Máxima Entropía e Información Mutua," *Tesis para optar al grado de magíster en Ciencias, mención Ingeniería Sísmica. Universidad de Chile*, 2019.

[22] T. Núñez, "Variación Debido a Cambios de Masa y una Estructura en Proceso Constructivo," *Tesis para optar al grado de magíster en Ciencias, mención Ingeniería Sísmica. Memoria para optar al título de Ingeniero Civil. Universidad de Chile.*, 2009.

[23] P. León, "Variación de Propiedades Dinámicas de la Torre Central debido a Factores Sísmicos," *Memoria para optar al título de Ingeniero Civil. Universidad de Chile.*, 2013.

[24] A. Paredes, "Identificación de Sistemas con Aislación Sísmica," *Tesis para optar al grado de magíster en Ciencias, mención Ingeniería Sísmica. Memoria para optar al título de Ingeniero Civil. Universidad de Chile.*, 2019.

[25] N. F. Alkayem, M. Cao, Y. Zhang, M. Bayat, and Z. Su, "Structural damage detection using finite element model updating with evolutionary algorithms: a survey," *Neural Computing and Applications*, vol. 30, no. 2, pp. 389–411, 2018.

[26] D. Simon, *Optimal State Estimation Kalman, H-Infinity, and Nonlinear Approaches*. John Wiley & Sons, 2006.

[27] S. Särkkä, *Bayesian Filtering and Smoothing.* Cambridge University Press, 2013.

[28] L. Xie, Z. Zhou, L. Zhao, C. Wan, H. Tang, and S. Xue, "Parameter identification for structural health monitoring with extended Kalman filter considering integration and noise effect," *Applied Sciences (Switzerland)*, vol. 8, no. 12, 2018.

[29] Z. Xie and J. Feng, "Real-time nonlinear structural system identification via iterated unscented Kalman filter," *Mechanical Systems and Signal Processing*, vol. 28, no. 20100480049, pp. 309–322, 2012.

[30] H. Sun, A. Mordret, G. A. Prieto, and M. N. Toksöz, "Bayesian characterization of buildings using seismic interferometry on ambient vibrations," *Mechanical Systems and Signal Processing*, vol. 85, pp. 468–486, 2017.

[31] H. A. Nasrellah and C. S. Manohar, "Finite element method based Monte Carlo filters for structural system identification," *Probabilistic Engineering Mechanics*, vol. 26, no. 2, pp. 294–307, 2011.

[32] Pacific Earthquake Engineering Research Center, "Open System for Earthquake Engineering Simulation (OpenSees) [online], Accesed: 31.03.2021," *Available: https://opensees.berkeley.edu/*, 2006.

[33] R. Yoshimoto, A. Mita, and K. Okada, "Damage detection of base-isolated buildings using multi-input multi-output subspace identification," *Earthquake Engineering and Structural Dynamics*, vol. 34, no. 3, pp. 307–324, 2005.

[34] H. Ebrahimian, R. Astroza, J. Conte, and R. Bitmead, "Information-Theoretic Approach for Identifiability Assessment of Nonlinear Structural Finite-Element Models," *Journal of Engineering Mechanics*, vol. 145, no. 7, 2019.

[35] A. K. Chopra, *Dynamics of structures: Theory and applications to earthquake engineering.* Englewood Cliffs: Prentice Hall, fourth edi ed., 1995.

[36] J. Beck and L. Katafygiotis, "Updating Models and Their Uncertainties. Part I: Bayesian Statistical Framework," *Journal of Engineering Mechanics*, no. April, pp. 455–461, 1998.

[37] J. Beck, "Bayesian System Identification based on Probability Logic," *Structural Control and Health Monitoring*, no. September, pp. 825–847, 2010.

[38] The MathWorks Inc., "MATLAB," 2012.

[39] F. Mckenna and G. L. Fenves, "Using the OpenSees interpreter on parallel computers," *Network for earthquake engineering simulations*, pp. 1–15, 2008.

[40] H. Ebrahimian, "Bayesian Filters Notes, Professor Ebrahimian," *Webpage: https://www.hamedebrahimian.com/*, 2020.

[41] D. Simon and D. L. Simon, "Constrained Kalman filtering via density function truncation for turbofan engine health estimation," *International Journal of Systems Science*, vol. 41(2), pp. 159–171, 2009.

[42] H. Ebrahimian, M. Kohler, A. Massari, and D. Asimaki, "Parametric Estimation of Dispersive Viscoelastic Layered Media with application to Structural Health Monitoring," *Soil Dynamics and Earthquake Engineering*, vol. 105, pp. 204–223, 2018.

[43] H. Ebrahimian, R. Astroza, J. P. Conte, and R. A. de Callafon, "Nonlinear finite ele-

ment model updating for damage identification of civil structures using batch Bayesian estimation," *Mechanical Systems and Signal Processing*, vol. 84, pp. 194–222, 2017.

[44] S. L. Wood, "Performance of Reinforced Concrete Buildings during the 1985 Chile Earthquake: Implications for the Design of Structural Walls," 1991.

[45] Instituto Nacional de Normalización, "NCh433 Of.72, Earthquake resisting design of buildings," 1972.

[46] R. Boroschek, "Advance Dynamic of Structures, Course Notes," *Universidad de Chile*, 2014.

[47] R. Boroschek and P. Soto, "Respuesta Sísmica de Edificios Instrumentados," in *Mw=8.8 Terremoto en Chile 27 de febrero de 2010*, ch. 7, Santiago, Chile: Facultad de Ciencias Físicas y Matemáticas, Universidad de Chile, 2012.

[48] Centro Sismológico Nacional, "Sismicidad y Terremotos en Chile," *Universidad de Chile*, p. 4, 2013.

[49] IGM, "Mapa del perfil topográfico de la Zona Central," *Curriculum Nacional*, 2012.

[50] A. Arias, "Measure of Earthquake Intensity," *Massachusetts Inst. of Tech., Cambridge. Univ. of Chile, Santiago de Chile*, pp. 438–83, 1970.

[51] M. D. Trifunac and A. G. Brady, "A study on the duration of strong earthquake ground motion," *Bulletin of the Seismological Society of America.*, vol. 65, no. 3, pp. 581–626, 1975.

[52] P. G. Bakir, "Automation of the stabilization diagrams for subspace based system identification," *Expert Systems with Applications*, vol. 38, no. 12, pp. 14390–14397, 2011.

[53] K. J. Bathe, "Finite Element Procedures," 1996.

[54] Computers & Structures Inc., "Computers and Structures, Inc. official website," 2011.

[55] Instituto Nacional de Normalización, "NCh1537 Of.86, Structural design of building - Dead and live loads," 1986.

[56] Instituto Nacional de Normalización, "NCh433 Of.96, Mod.2012, Earthquake resisting design of buildings," 1996.

[57] C. Multiphysics, "Comsol multiphysics cyclopedia, [online], Accessed: 31.03.2021," *Available: https://www.comsol.com/multiphysics*, 1998.

[58] Y. Tian, L. Xie, Z. Xu, and X. Lu, "GPU-Powered High-Performance Computing for the Analysis of Large-Scale Structures Based on Opensees," *Congress on Computing in Civil Engineering, Proceedings*, vol. 2015-Janua, no. January, pp. 411–418, 2015.

Appendix A

Input Sensitivity in LTI Systems

Consider the differential equation of a single-degree-of-freedom (SDOF) system with a unit mass subject to a unit impulse load of amplitude $p_o = 1/\tau$, with a time duration τ starting at the instant of time $t = \tau$.

$$\ddot{u} + 2\xi\omega_n\dot{u} + \omega_n^2 u = \frac{p_o(t)}{m} \tag{A.1}$$

Subject to the initial conditions

$$u(0) = 0 \quad \dot{u}(0) = 0 \tag{A.2}$$

Where ω_n and ξ are the natural frequency and damping ratio of the system, respectively. The impulse response function (IRF) is defined as follows [35]

$$h(t-\tau) = \frac{1}{\omega_n\sqrt{1-\xi^2}} e^{-\xi\omega_n(t-\tau)} \sin\omega_n\sqrt{1-\xi^2}(t-\tau), \quad t \geq \tau \tag{A.3}$$

Given an arbitrary ground motion $\ddot{u}_g(t)$, the total response at time t of the linear time-invariant (LTI) system defined in Equation A.1 can be calculated through the Duhamel's integral (or the convolution integral), that is

$$u(t) = \int_0^t \ddot{u}_g(\tau)\, h(t-\tau)\mathrm{d}\tau, \quad t \geq \tau \tag{A.4}$$

$$u(t) = (\ddot{u}_g * h)(t), \quad t \geq \tau \tag{A.5}$$

This result is restricted to linear systems because it is based on the principle of superposition [35]. Given the above, the output $y(t)$ for a discrete LTI system subject to a basal excitation $\ddot{u}_g(t)$ is

$$y(t) = (\ddot{u}_g * h)(t), \quad t \geq \tau \tag{A.6}$$

$$y(t) = \sum_{\tau=0}^{t} \ddot{u}_g(\tau) h(t-\tau), \quad t \geq \tau \tag{A.7}$$

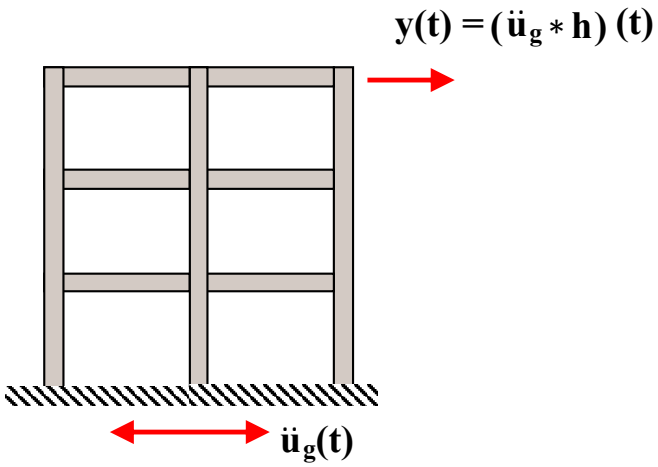

Figure A.1: Scheme for obtaining the response of a LTI system through IRF.

Taking Equation A.7, the derivate of $y(t)$ with respect to $\ddot{u}_g(\tau)$ is equal to system's IRF.

$$\frac{\partial y(t)}{\partial \ddot{u}_g(\tau)} = h(t-\tau) \tag{A.8}$$

From the above expression, the sensitivity of the output concerning the input is equal to IRF shifted a time step τ. Using the finite difference method (FDM) for the input sensitivity computation, the equation A.8 for the time-steps $\tau = 0, 1, ..., t$ is approximate as follows

$$\begin{aligned}
\frac{\partial y(t)}{\partial \ddot{u}_g(0)} &\approx \frac{\Delta y(t)}{\Delta \ddot{u}_g(0)} = h(t) \\
\frac{\partial y(t)}{\partial \ddot{u}_g(1)} &\approx \frac{\Delta y(t)}{\Delta \ddot{u}_g(1)} = h(t-1) \\
&\cdots \\
\frac{\partial y(t)}{\partial \ddot{u}_g(t)} &\approx \frac{\Delta y(t)}{\Delta \ddot{u}_g(t)} = h(0)
\end{aligned} \tag{A.9}$$

With $\Delta\ddot{u}_g(\tau)$ defined as a small number. Equation A.9 indicates the input sensitivity is equal to ratio between the structural response due to a unit impulse and $\Delta\ddot{u}_g(\tau)$.

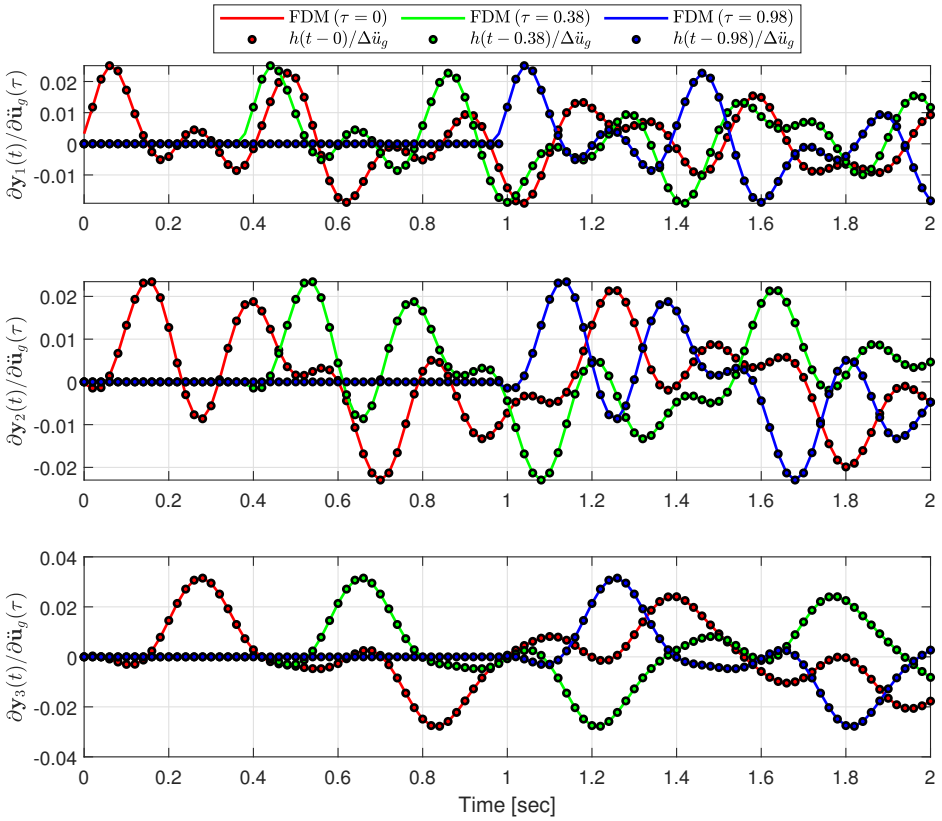

Figure A.2: Input response sensitivities for the validation problem of Chapter 2 using the FDM and the IRF in LTI systems.

Since it is required to calculate the response of a LTI system for the case of multiple inputs is only necessary to apply the superposition principle, that means

$$y(t) = \sum_{\tau=0}^{t} \ddot{u}_{g,1}(\tau)\, h_1(t-\tau) + ... + \sum_{\tau=0}^{t} \ddot{u}_{g,n}(\tau)\, h_n(t-\tau), \quad t \geq \tau \tag{A.10}$$

And the sensitivity for the i^{th} input component is calculated as below

$$\frac{\Delta y(t)}{\Delta \ddot{u}_{g,i}(\tau)} = h_i(t-\tau) \tag{A.11}$$

Appendix B

Earthquakes' Database

The table presented below summarizes the main properties of each seismic event to be used for the study. Among them are the date of the event, the local time, the location of the epicenter, the depth, magnitude, and Intensity scale for the city of Santiago.

Table B.1: Summary characteristic values of each seismic event.

Event Code	**Date**	**Local hour**	**Latitude [°]**	**Longitude [°]**	**Depth [km]**	**Magnitude**	**Mercalli Intensity**
2	20-04-1997	15:53:18	-34.001	-70.452	106.7	5.6 Mw	IV
3	19-06-1997	8:21:04	-33.166	-70.316	104.3	5.4 Mw	IV-V
4	14-10-1997	22:03:31	-30.773	-71.315	56.1	7.1 Mw	V-VI
5	12-01-1998	7:14:13	-31.302	-71.417	5.9	6.6 Mw	III
6	29-07-1998	3:14:24	-32.251	-71.069	51.0	6.4 Mw	V
7	29-10-1998	16:55:57	-32.868	-70.662	85.8	5.3 Mw	IV-V
8	09-11-1998	18:01:45	-33.385	-70.198	124.1	5.3 Mc	II-III
9	27-11-1998	7:27:03	-32.090	-69.835	147.0	5.1 Mw	Not specified
10	04-04-1999	17:04:26	-33.650	-71.000	73.0	4.2 Mw	Not specified
11	01-08-1999	21:06:39	-33.130	-70.358	98.0	5.1 Mw	Not specified
12	03-08-1999	12:24:44	-32.852	-70.783	78.0	4.8 Mw	Not specified
13	01-09-1999	22:37:19	-33.315	-70.215	112.0	4.6 Mw	Not specified
14	16-06-2000	3:55:36	-33.918	-70.391	115.2	6.4 Mw	V
15	07-01-2001	7:18:22	-33.468	-72.267	35.0	5.9 Mw	III
16	01-02-2001	14:30:32	-32.946	-70.339	108.4	4.6 Mb	II-III
17	15-03-2001	9:02:44	-32.404	-71.614	41.9	5.9 Mw	III-IV
18	05-04-2001	1:16:58	-34.364	-70.491	110.4	4.9 Mb	III
19	09-04-2001	5:00:54	-32.701	-73.292	6.5	6.6 Mw	III-IV
20	06-05-2001	1:59:49	-32.592	-71.133	49.7	5.2 Mw	III-IV
21	24-07-2001	13:42:41	-32.878	-71.785	54.8	5.2 Mw	IV
22	13-12-2001	10:38:28	-33.220	-70.324	102.0	4.5 Mb	II-III
23	19-02-2002	4:07:10	-32.235	-71.667	64.0	4.9 Mb	II-III
24	18-04-2002	2:08:35	-27.502	-70.084	63.0	6.6 Mw	II-III
25	10-05-2002	5:21:35	-33.361	-70.409	100.8	4.8 Mb	III-IV
26	23-05-2002	20:23:19	-32.183	-71.119	40.0	5.7 Mw	IV
27	18-06-2002	9:56:25	-30.818	-71.250	52.0	6.4 Mw	III-IV
28	19-07-2002	2:55:47	-33.313	-70.752	81.0	5 Mc	IV

Table B.1 continued from previous page.

29	23-09-2002	23:57:21	-31.420	-69.158	117.3	6.3 Mw	III
30	13-10-2002	20:52:34	-32.618	-71.574	33.3	4.7 Mc	II
31	06-01-2003	21:54:52	-33.778	-70.369	112.4	5.7 Mw	IV-V
32	20-06-2003	9:30:41	-30.659	-71.788	23.1	6.8 Mw	III-IV
33	18-07-2003	6:17:57	-33.826	-71.015	77.1	4.5 Mb	IV
34	31-12-2003	15:53:28	-32.941	-70.878	75.3	4.2 Mc	III-IV
35	30-04-2004	6:03:45	-33.516	-70.566	95.8	5 Mw	IV
36	28-08-2004	9:41:26	-35.173	-70.525	5.0	6.4 Mw	IV-V
37	27-09-2004	9:41:27	-32.688	-71.743	32.9	5.5 Mw	III
38	29-09-2004	7:25:00	-33.371	-70.179	8.6	4.6 Mb	II
39	29-09-2004	10:50:00	-33.380	-70.132	9.1	4.4 Ml	II-III
40	11-12-2004	6:34:44	-32.956	-70.874	77.1	4.6 Mb	IV
41	13-03-2005	16:39:01	-32.731	-71.718	10.8	5.2 Mw	II-III
42	14-05-2005	13:08:21	-32.593	-70.642	95.7	4.7 Mb	II-III
43	12-08-2005	4:59:19	-33.462	-70.676	88.0	4.1 Mb	III
44	10-02-2006	14:51:54	-32.599	-71.561	33.8	5.2 Mw	IV
45	19-06-2006	22:14:07	-32.919	-71.638	42.0	4.9 Mb	III
46	09-09-2006	13:31:10	-32.644	-70.613	100.4	4.7 Mb	III
47	22-04-2007	6:22:02	-32.408	-71.448	20.2	5.1 Mw	IV
48	10-05-2007	12:57:37	-32.621	-70.125	105.0	4.7 Mb	III
49	28-06-2007	15:25:20	-31.984	-71.489	67.0	5.6 Mw	IV
50	11-07-2007	11:12:22	-32.660	-70.435	99.3	5.1 Mw	III
51	29-09-2007	0:11:29	-34.037	-70.481	106.9	4.2 Mb	II
52	30-09-2007	14:41:05	-33.884	-70.791	89.6	4.7 Mb	III
53	08-10-2007	12:30:18	-32.673	-71.689	35.4	4.9 Ml	III
54	15-12-2007	15:22:27	-32.803	-71.740	45.0	5.9 Mw	IV
55	17-12-2007	3:29:51	-32.709	-71.812	12.8	4.8 Mb	II
56	17-12-2007	6:26:34	-32.877	-71.074	62.5	5 Mb	IV
57	20-12-2007	0:06:56	-32.713	-71.788	30.1	5.5 Mw	II

Table B.1 continued from previous page.

58	18-12-2008	18:19:28	-32.476	-71.900	24.8	6.1 Mw	IV
59	18-12-2008	18:50:28	-32.499	-72.033	30.2	5.9 Mw	II
60	19-12-2008	6:36:04	-32.458	-71.949	32.2	5.7 Mw	III
61	30-06-2009	10:17:00	-33.444	-70.825	81.5	4.7 Ml	IV
62	12-02-2010	9:03:00	-33.686	-69.060	192.4	6 Ml	IV
63	27-02-2010	3:34:00	-36.290	-73.239	30.1	8.8 Mw	VIII
64	27-02-2010	7:30:00	-33.281	-71.955	35.0	6.1 Ml	Not specified
65	28-02-2010	8:25:00	-35.010	-71.924	19.4	6.3 Mw	IV
66	03-03-2010	16:58:00	-33.429	-72.223	38.9	5.5 Ml	V
67	03-03-2010	22:59:44	-33.219	-72.554	34.5	5.8 Ml	IV
68	11-03-2010	11:39:41	-34.301	-72.130	33.1	6.9 Mw	VI
69	11-03-2010	11:55:27	-34.451	-72.206	31.0	6.7 Mw	IV
70	11-03-2010	12:05:58	-34.444	-72.096	28.6	5.9 Ml	Not specified
71	11-03-2010	17:11:20	-34.381	-71.979	8.0	5.8 Ml	III
72	29-03-2010	4:35:06	-34.881	-71.935	34.1	5.8 Ml	IV
73	02-05-2010	10:52:39	-34.290	-72.088	32.1	5.8 Ml	III
74	25-11-2010	0:27:29	-32.139	-70.841	105.0	5.2 Ml	III
75	27-11-2010	15:08:34	-33.390	-70.496	101.2	4.7 Ml	II
76	11-02-2011	17:05:26	-36.679	-73.593	20.9	6.8 Mw	III
77	16-03-2011	19:36:16	-32.564	-71.726	32.7	5.6 Ml	III
78	17-03-2011	8:14:24	-32.590	-71.692	13.3	5 Ml	III
79	07-05-2011	15:39:59	-33.452	-70.674	103.3	4.5 Ml	III
80	15-07-2011	20:26:11	-33.901	-72.099	26.0	5.7 Ml	III
81	14-09-2011	4:03:51	-32.696	-71.797	37.0	5.6 Ml	IV
82	16-10-2011	7:39:47	-32.525	-71.516	55.5	4.7 Ml	III
83	22-11-2011	4:41:32	-34.762	-71.807	41.4	5.6 Ml	III
84	24-03-2012	4:28:33	-33.052	-71.063	68.8	5.2 Ml	V
85	25-03-2012	19:37:06	-35.200	-72.217	40.7	7 Mw	VI
86	17-04-2012	0:50:13	-32.787	-71.812	35.0	6.5 Mw	VI

Table B.1 continued from previous page.

87	13-05-2012	8:42:49	-32.796	-71.767	12.7	4.8 Ml	II
88	11-10-2012	14:22:10	-32.879	-70.651	95.0	5.7 Mw	VI
89	25-10-2012	2:37:58	-32.773	-70.165	104.7	4.9 Ml	III
90	30-04-2013	6:57:07	-33.498	-70.739	89.4	5 Ml	II
91	19-06-2013	17:29:11	-32.621	-70.236	107.1	5.5 Ml	III
92	30-08-2013	6:48:13	-34.475	-70.684	111.7	5.1 Ml	IV
93	31-10-2013	20:03:58	-30.372	-71.501	52.0	6.5 Ml	IV
94	21-12-2013	22:53:29	-32.872	-70.621	95.3	5 Ml	IV
95	04-03-2014	7:51:15	-33.624	-72.035	41.4	5.4 Ml	III
96	06-03-2014	1:37:05	-33.333	-71.280	59.7	5.3 Ml	V
97	04-04-2014	23:22:29	-32.669	-71.295	42.3	5.6 Mw	V
98	12-07-2014	23:16:52	-32.930	-71.340	50.7	5.1 Mw	III
99	23-08-2014	18:32:23	-32.737	-71.498	40.1	6.4 Mw	VI
100	16-11-2014	21:33:46	-32.959	-70.600	86.2	5.1 Ml	III

Appendix C

Spectrograms of Seismic Records

In this section, the spectrograms of the missing channels in Chapter 4 for the periods under study are shown. It is observed that the spectrograms associated with the vibrations of the ground provide information on the ground motion, in general, it is observed that these vibrations come in wave packets of 0.1 to 7 [Hz] (for the ground motion spectrograms was defined a frequency limit of 10 [Hz]). On the other hand, the predominant frequencies obtained by the MOESP method are observed in each channel for the channels present on the upper floors. For Channels #8, #9 and #10, a reduction on frequencies is view for the periods 2007 to 2012.

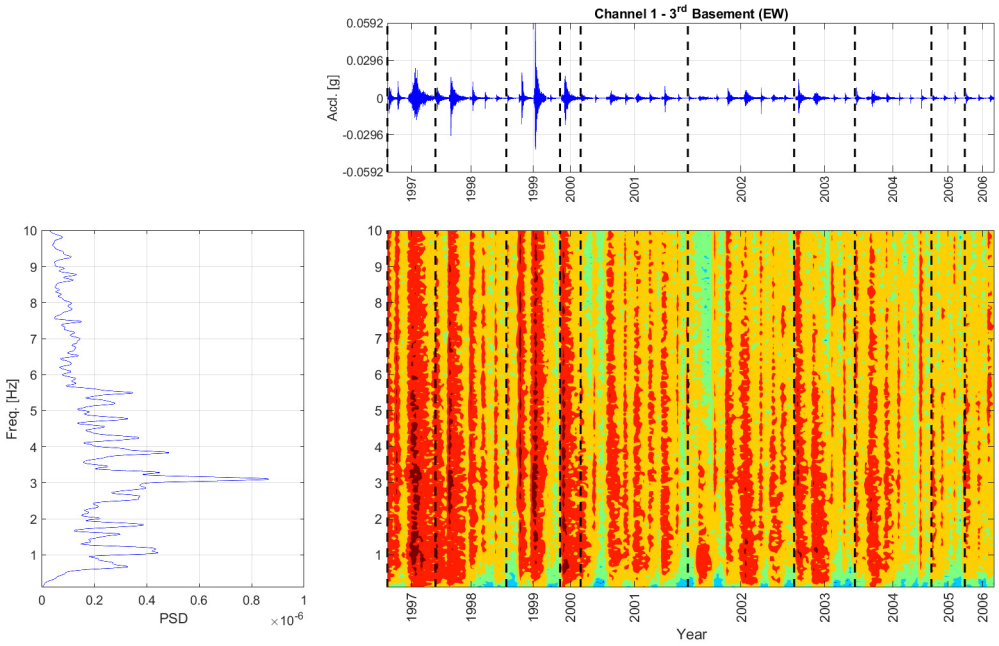

Figure C.1: Channel #1 spectrogram for the periods 1997 to 2006 (the dash line indicates the years separations).

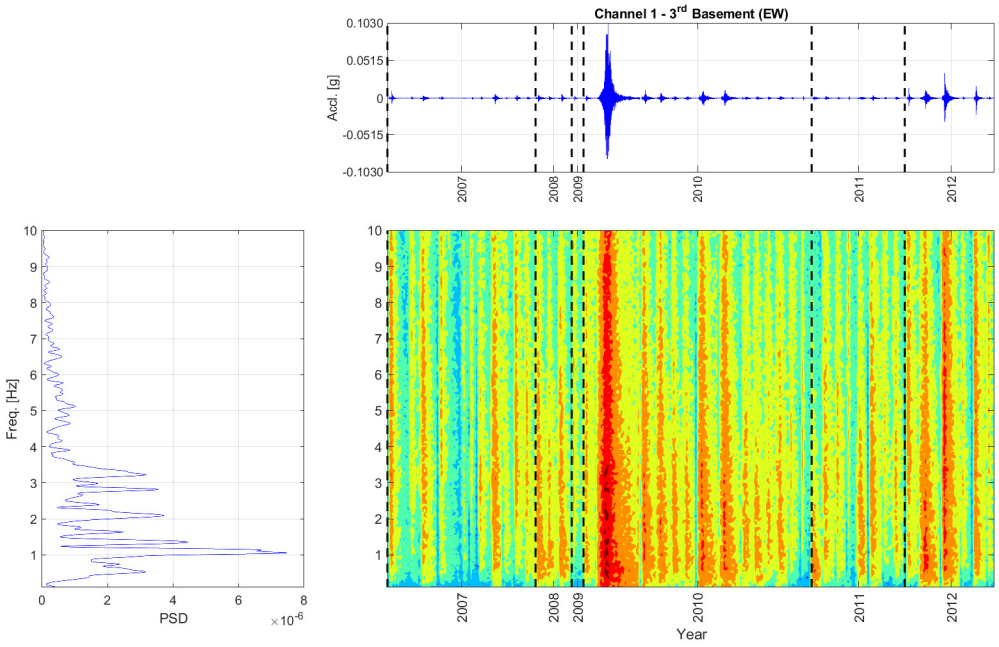

Figure C.2: Channel #1 spectrogram for the periods 2007 to 2012 (the dashed line indicates the separations between years).

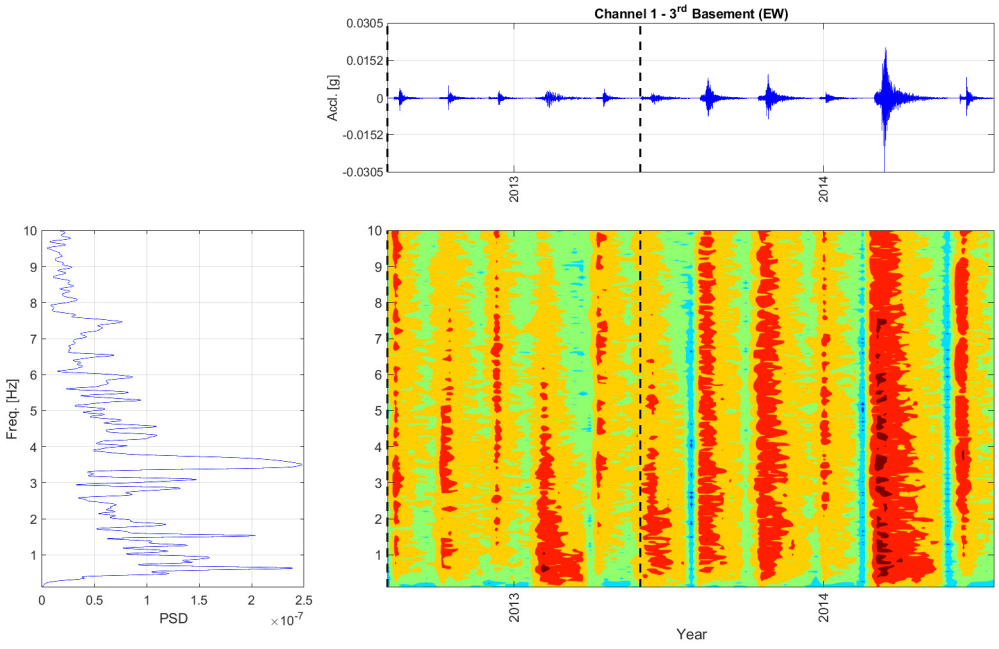

Figure C.3: Channel #1 spectrogram for the periods 2013 to 2014 (the dashed line indicates the separations between years).

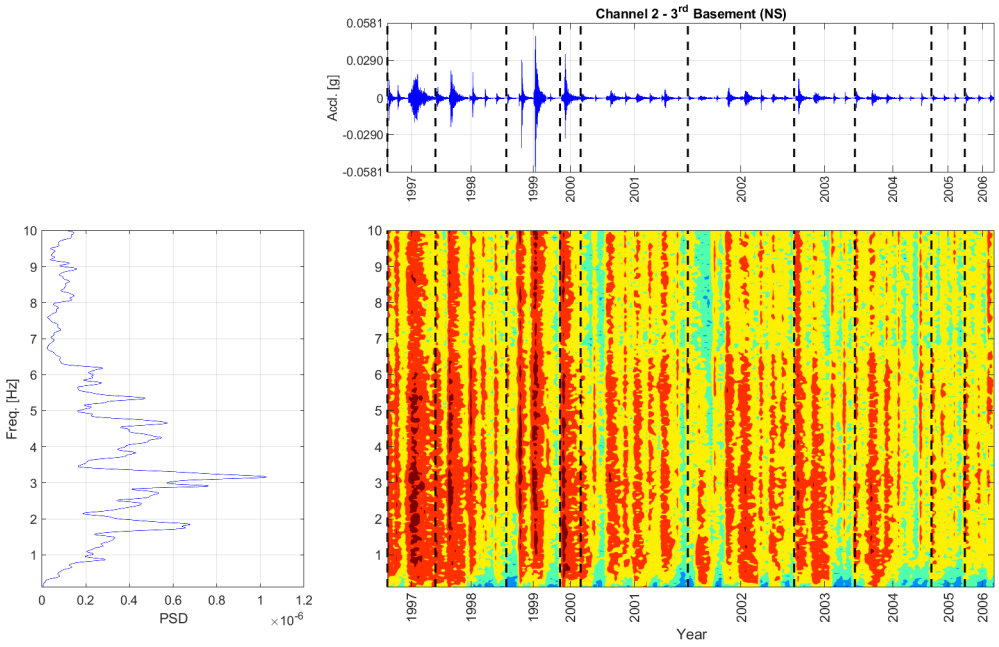

Figure C.4: Channel #2 spectrogram for the periods 1997 to 2006 (the dashed line indicates the separations between years).

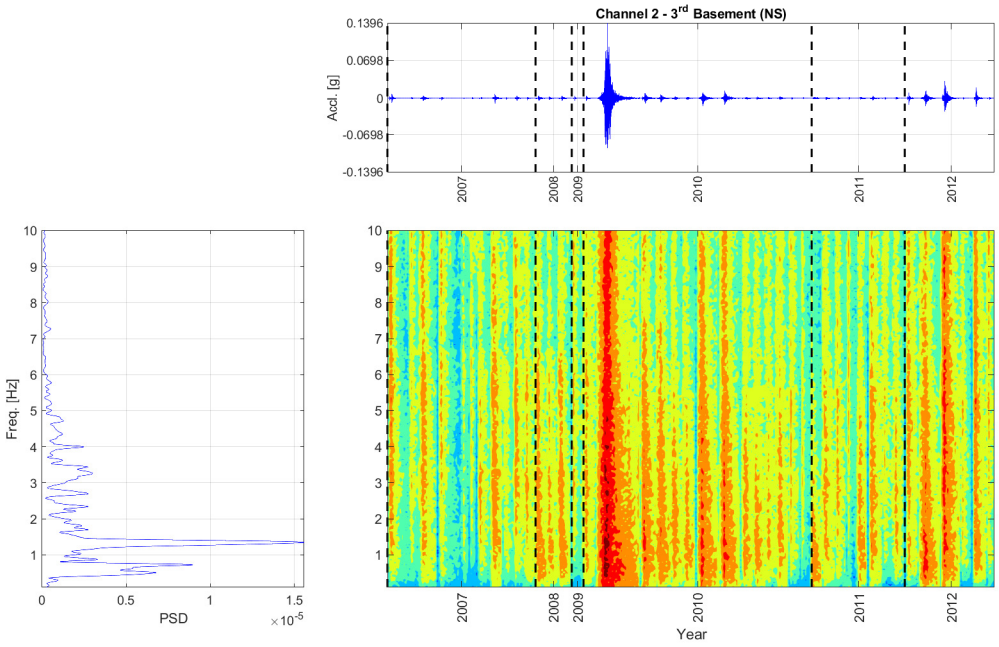

Figure C.5: Channel #2 spectrogram for the periods 2007 to 2012 (the dashed line indicates the separations between years).

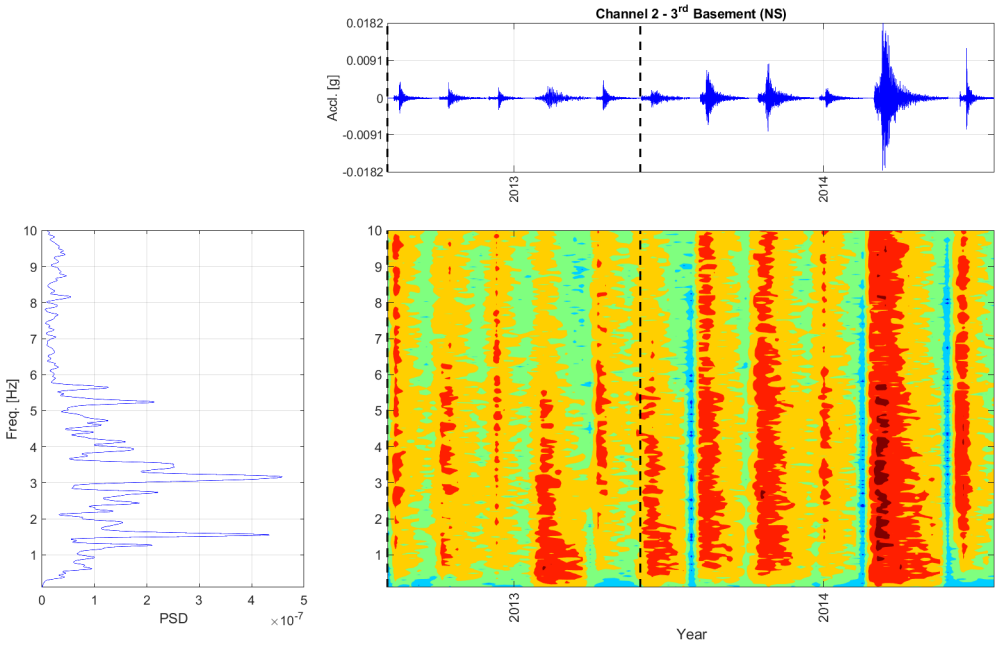

Figure C.6: Channel #2 spectrogram for the periods 2013 to 2014 (the dashed line indicates the separations between years).

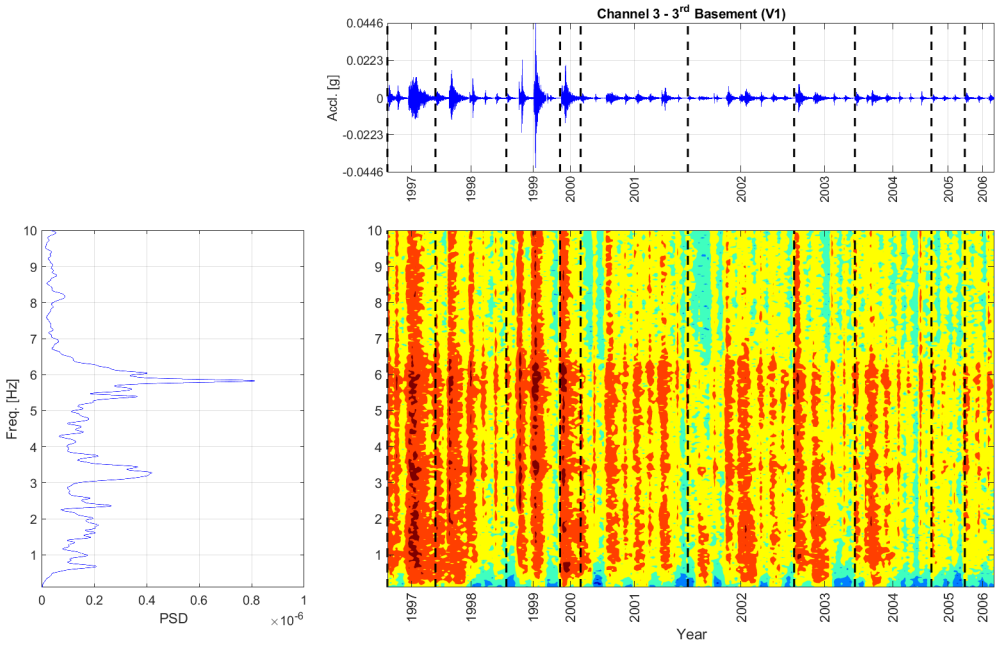

Figure C.7: Channel #3 spectrogram for the periods 1997 to 2006 (the dashed line indicates the separations between years).

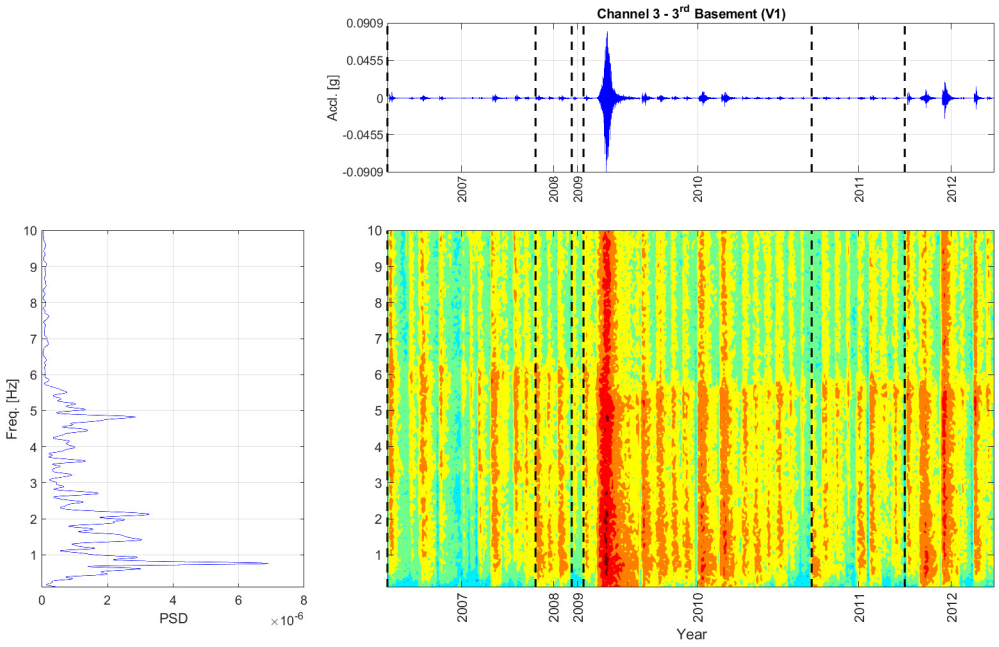

Figure C.8: Channel #3 spectrogram for the periods 2007 to 2012 (the dashed line indicates the separations between years).

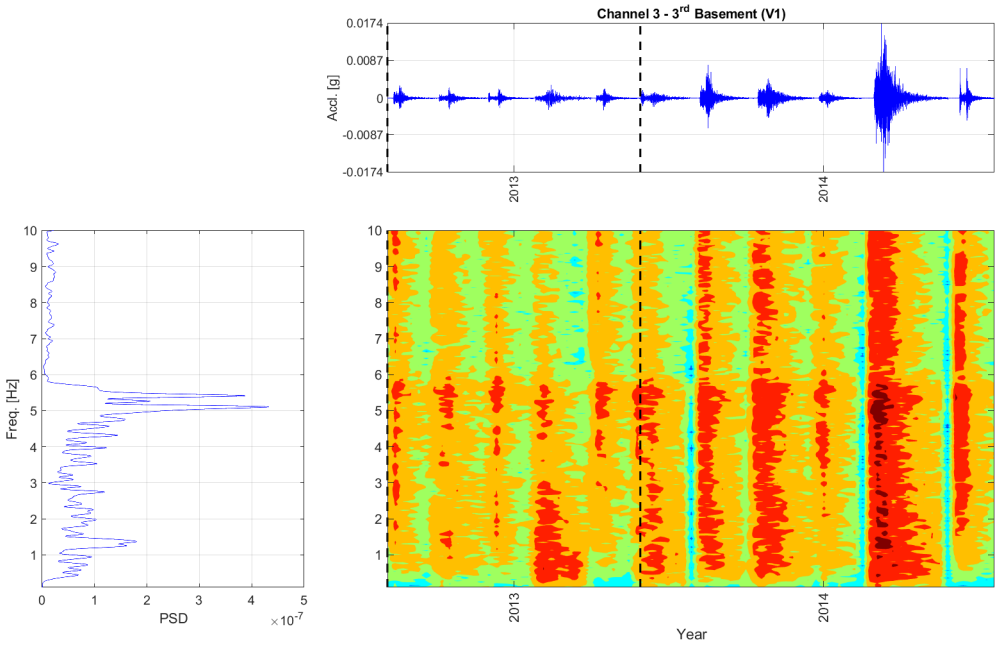

Figure C.9: Channel #3 spectrogram for the periods 2013 to 2014 (the dashed line indicates the separations between years).

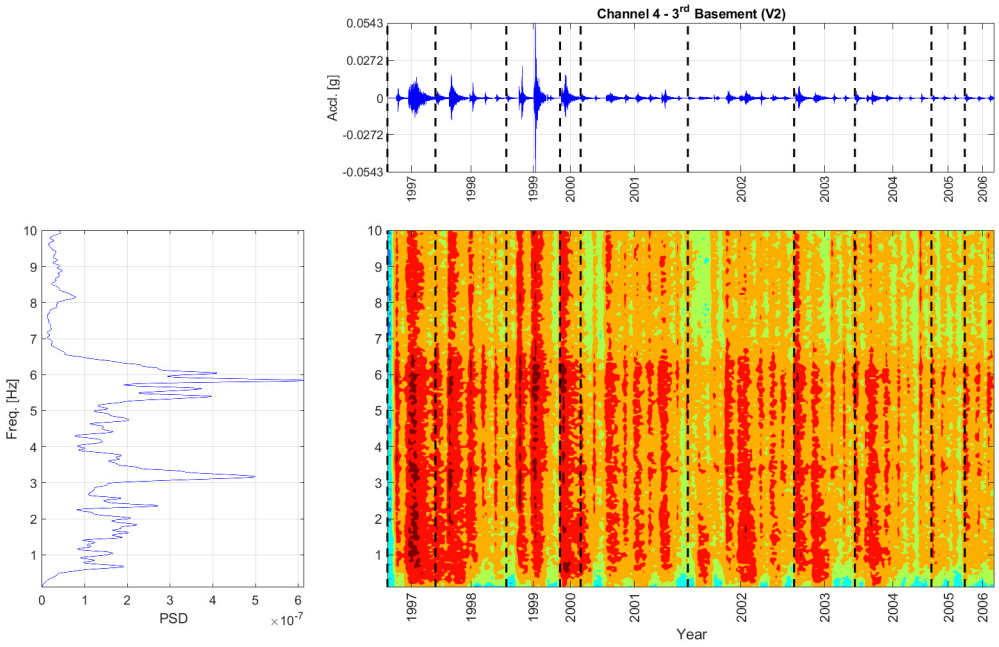

Figure C.10: Channel #4 spectrogram for the periods 1997 to 2006 (the dashed line indicates the separations between years).

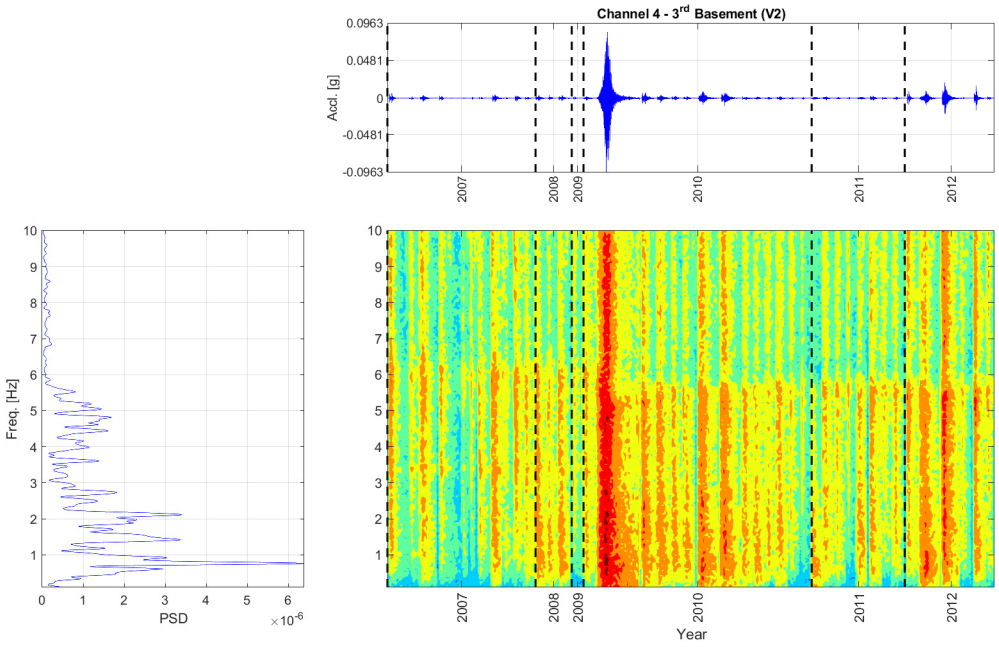

Figure C.11: Channel #4 spectrogram for the periods 2007 to 2012 (the dashed line indicates the separations between years).

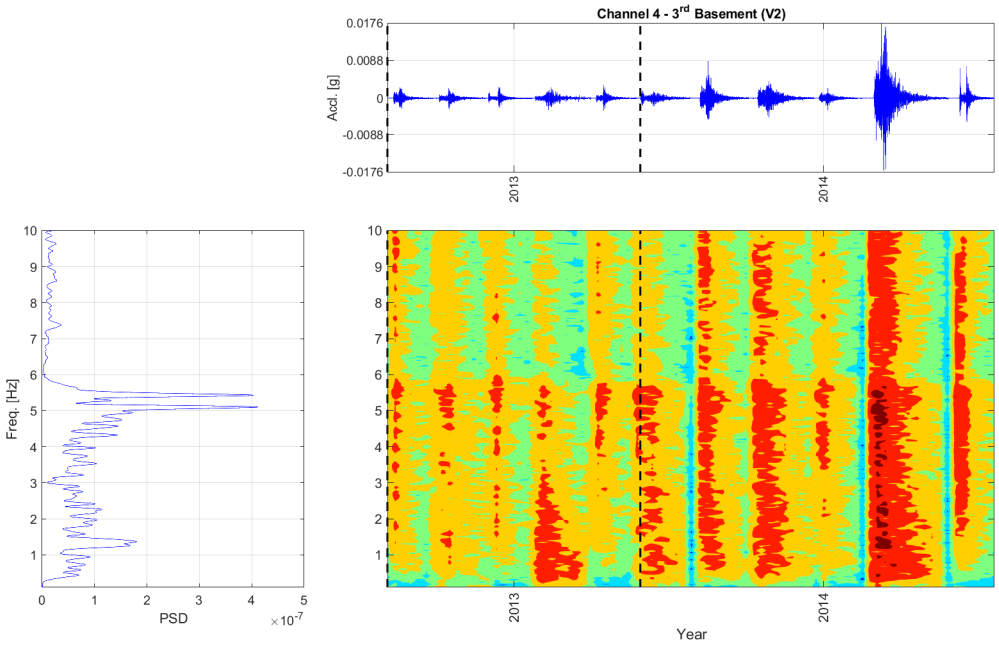

Figure C.12: Channel #4 spectrogram for the periods 2013 to 2014 (the dashed line indicates the separations between years).

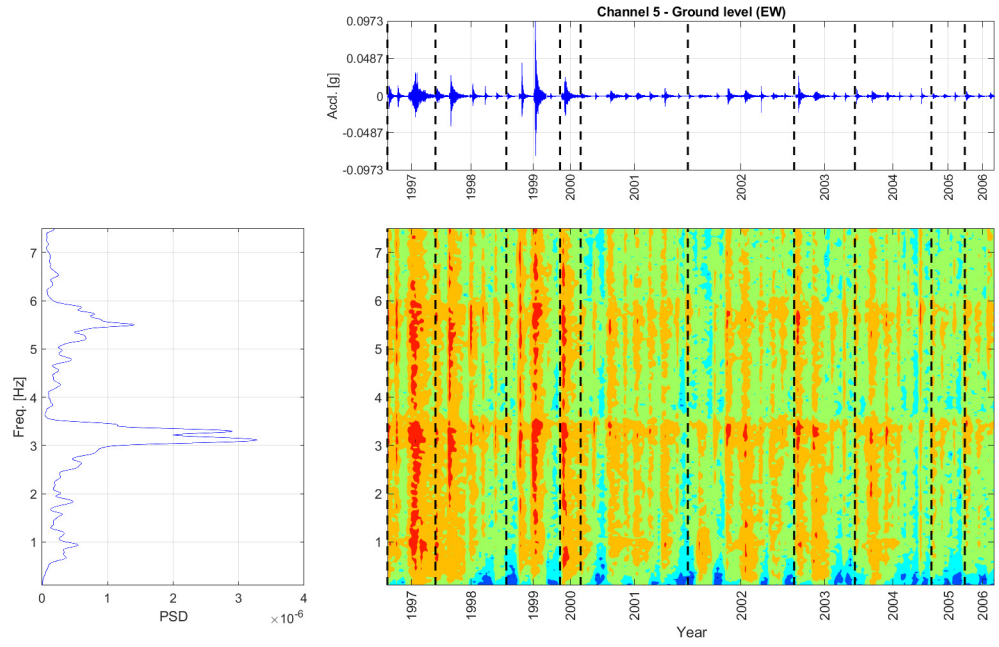

Figure C.13: Channel #5 spectrogram for the periods 1997 to 2006 (the dashed line indicates the separations between years).

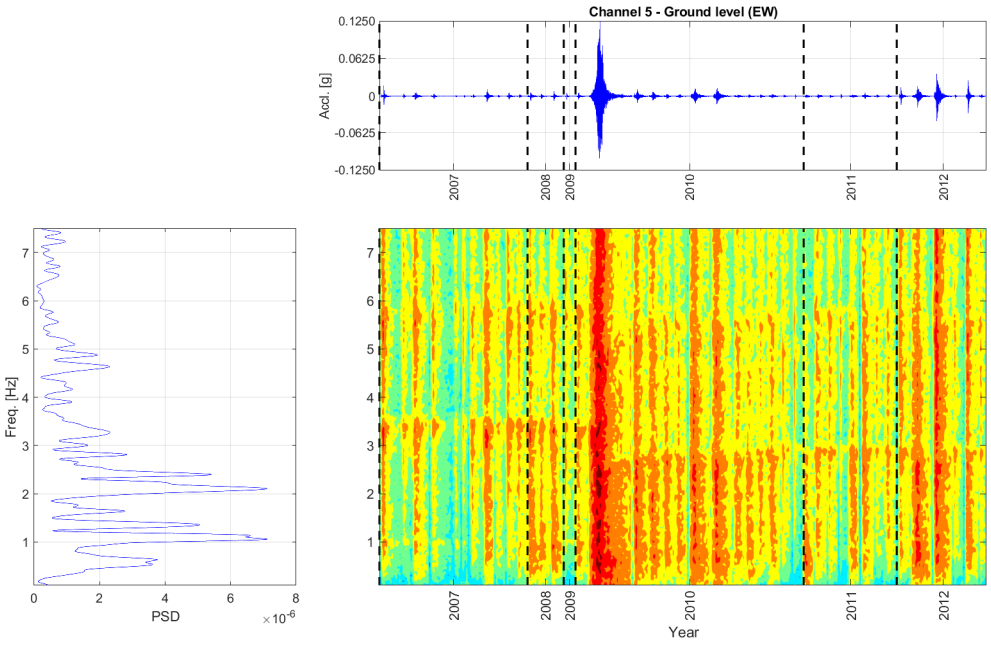

Figure C.14: Channel #5 spectrogram for the periods 2007 to 2012 (the dashed line indicates the separations between years).

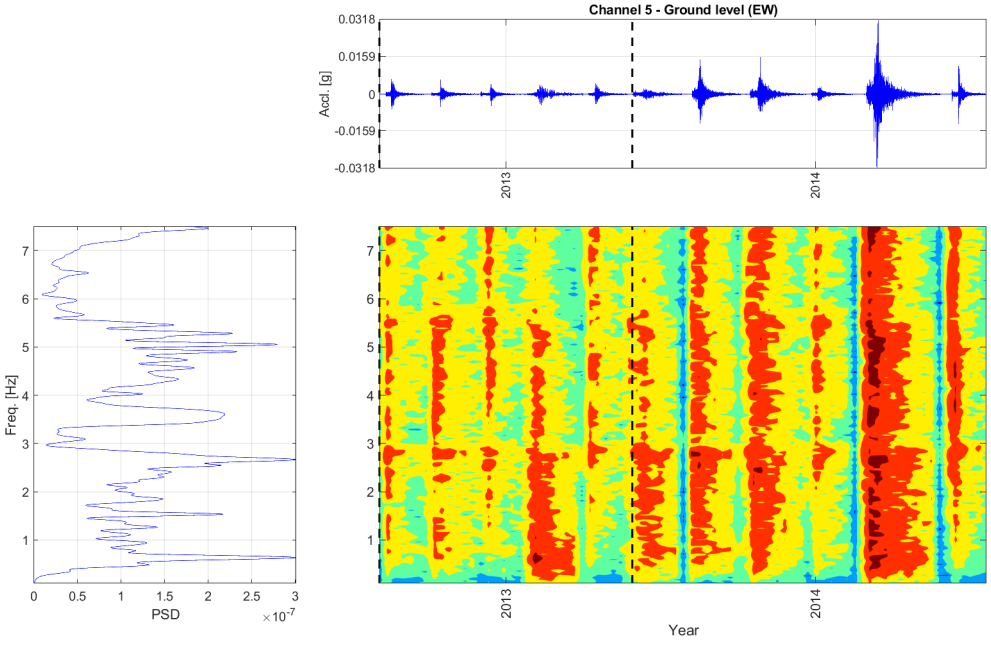

Figure C.15: Channel #5 spectrogram for the periods 2013 to 2014 (the dashed line indicates the separations between years).

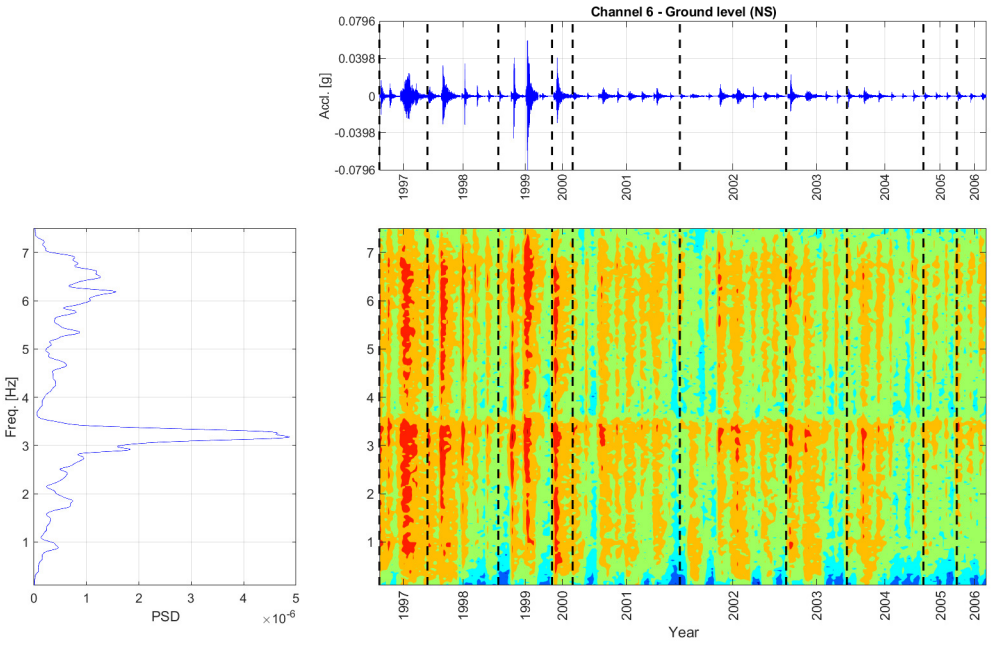

Figure C.16: Channel #6 spectrogram for the periods 1997 to 2006 (the dashed line indicates the separations between years).

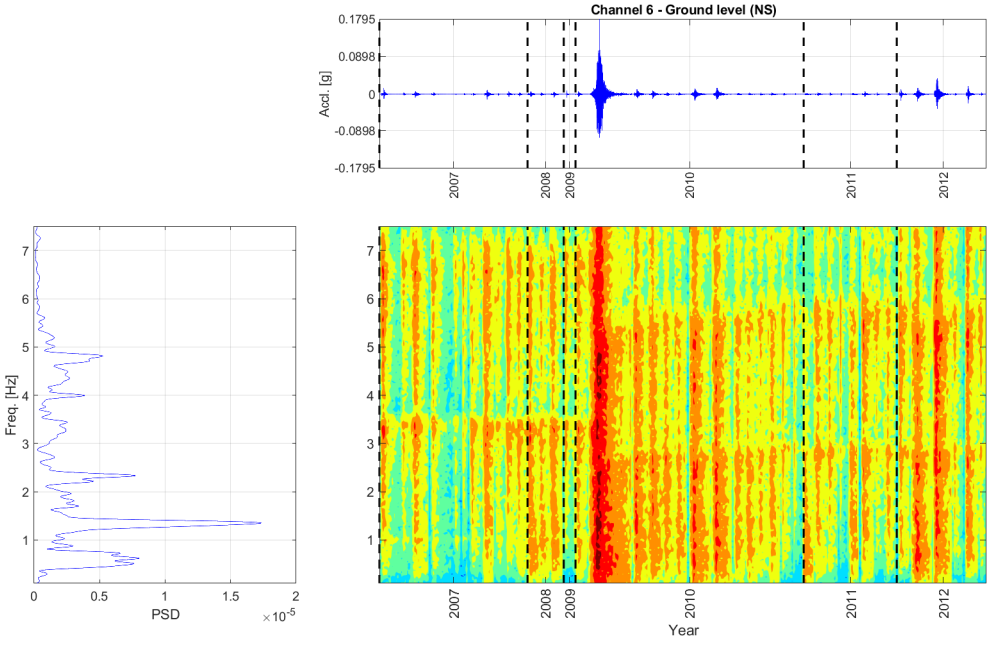

Figure C.17: Channel #6 spectrogram for the periods 2007 to 2012 (the dashed line indicates the separations between years).

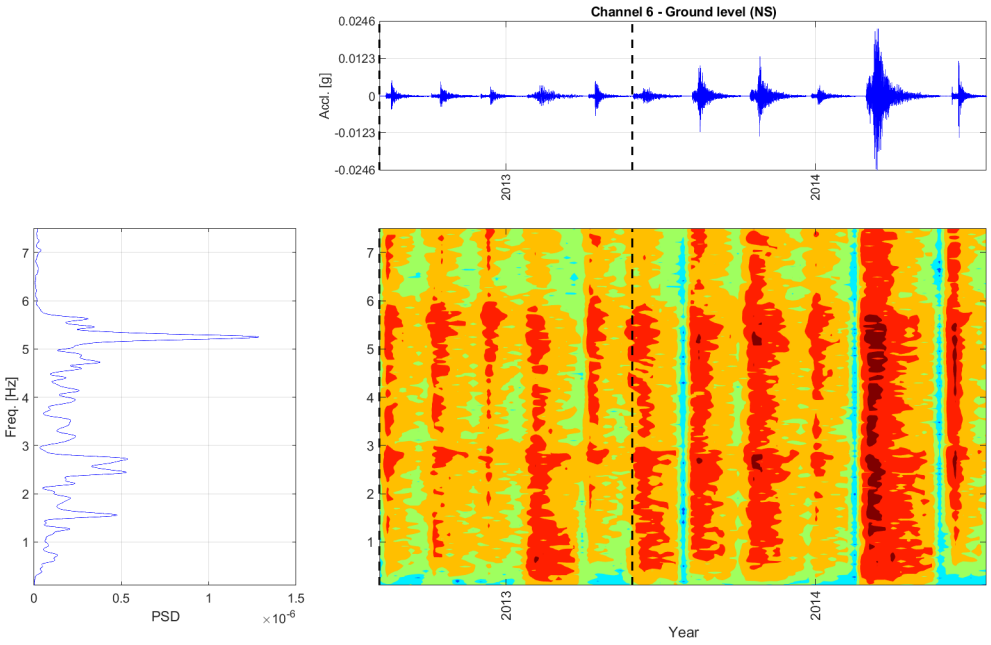

Figure C.18: Channel #6 spectrogram for the periods 2013 to 2014 (the dashed line indicates the separations between years).

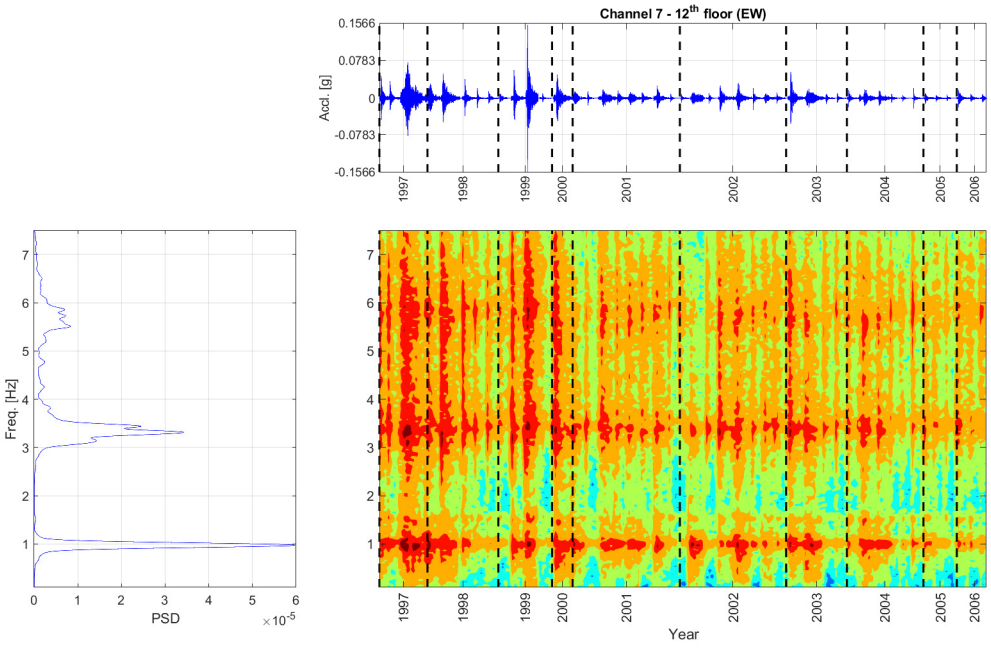

Figure C.19: Channel #7 spectrogram for the periods 1997 to 2006 (the dashed line indicates the separations between years).

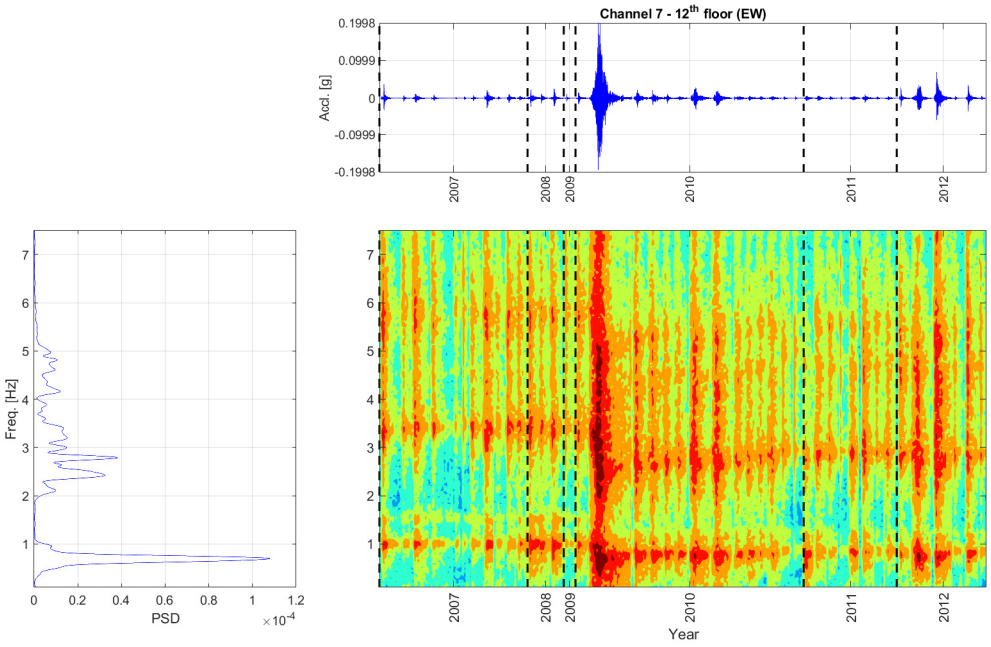

Figure C.20: Channel #7 spectrogram for the periods 2007 to 2012 (the dashed line indicates the separations between years).

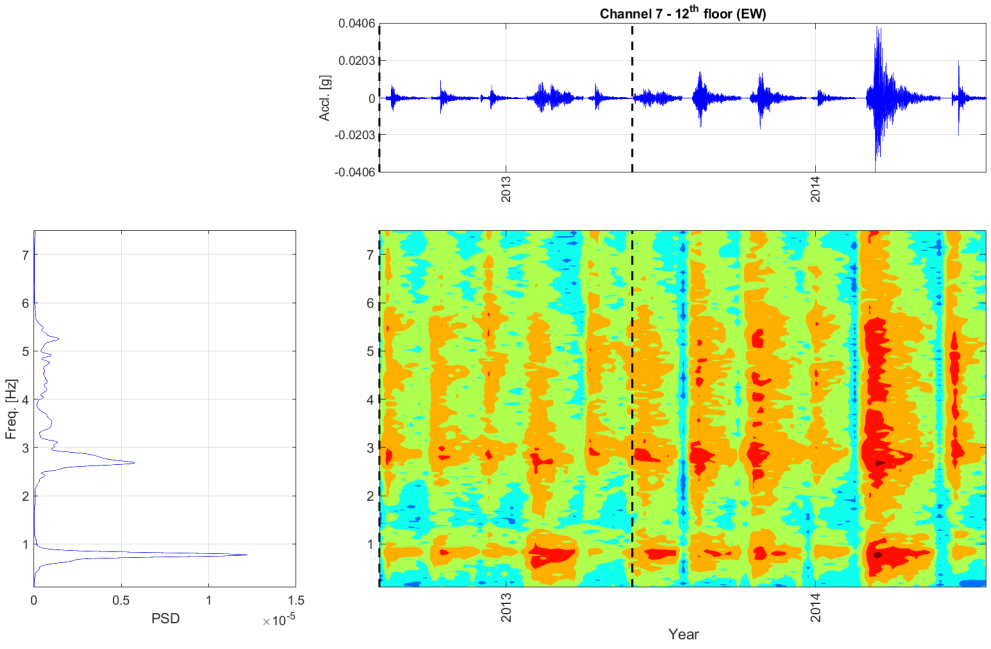

Figure C.21: Channel #7 spectrogram for the periods 2013 to 2014 (the dashed line indicates the separations between years).

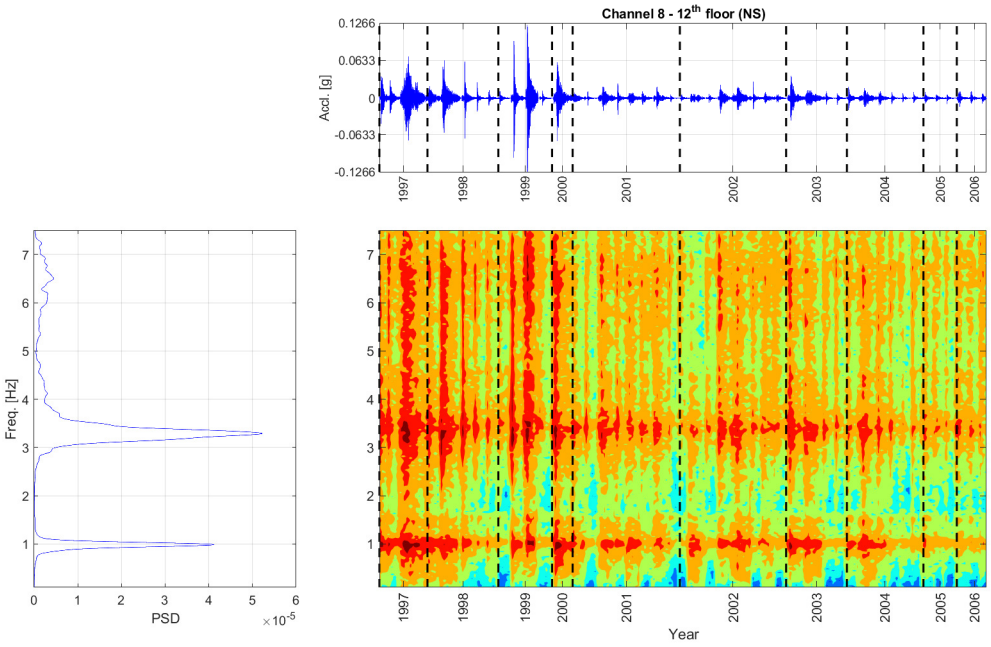

Figure C.22: Channel #8 spectrogram for the periods 1997 to 2006 (the dashed line indicates the separations between years).

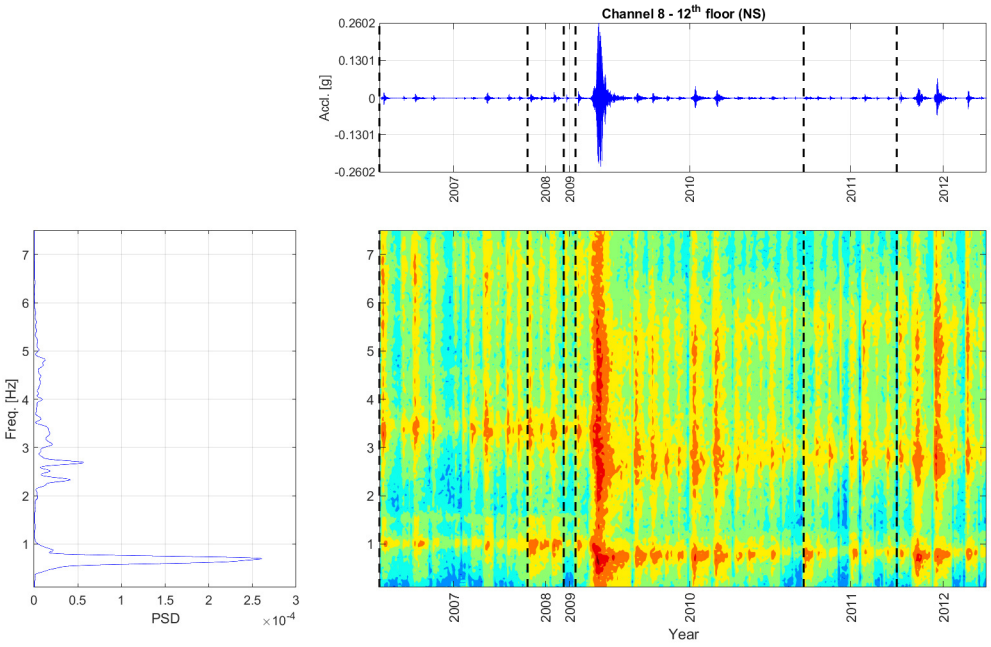

Figure C.23: Channel #8 spectrogram for the periods 2007 to 2012 (the dashed line indicates the separations between years).

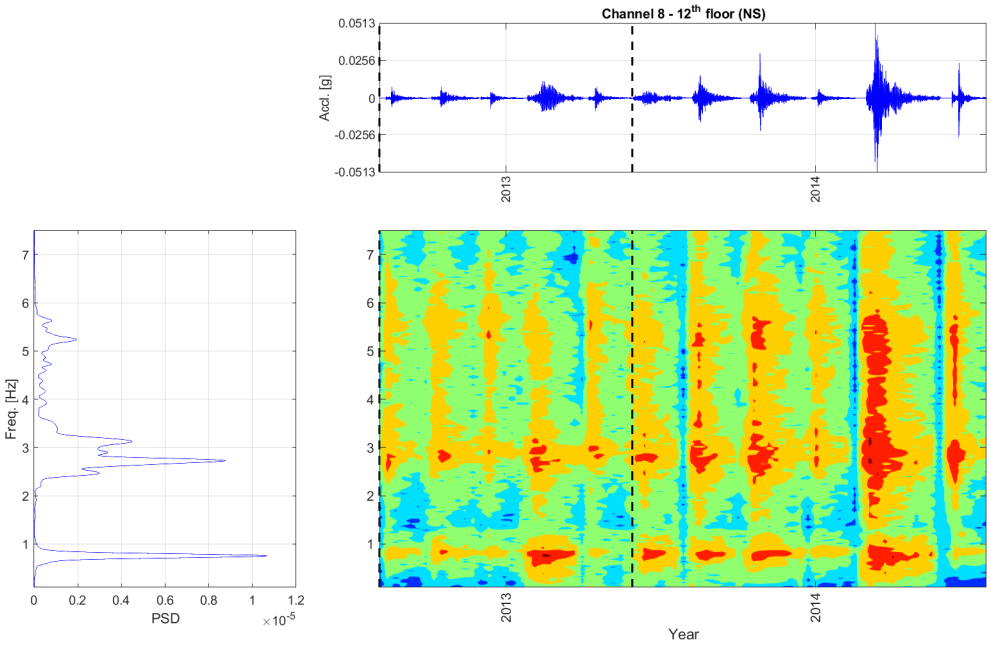

Figure C.24: Channel #8 spectrogram for the periods 2013 to 2014 (the dashed line indicates the separations between years).

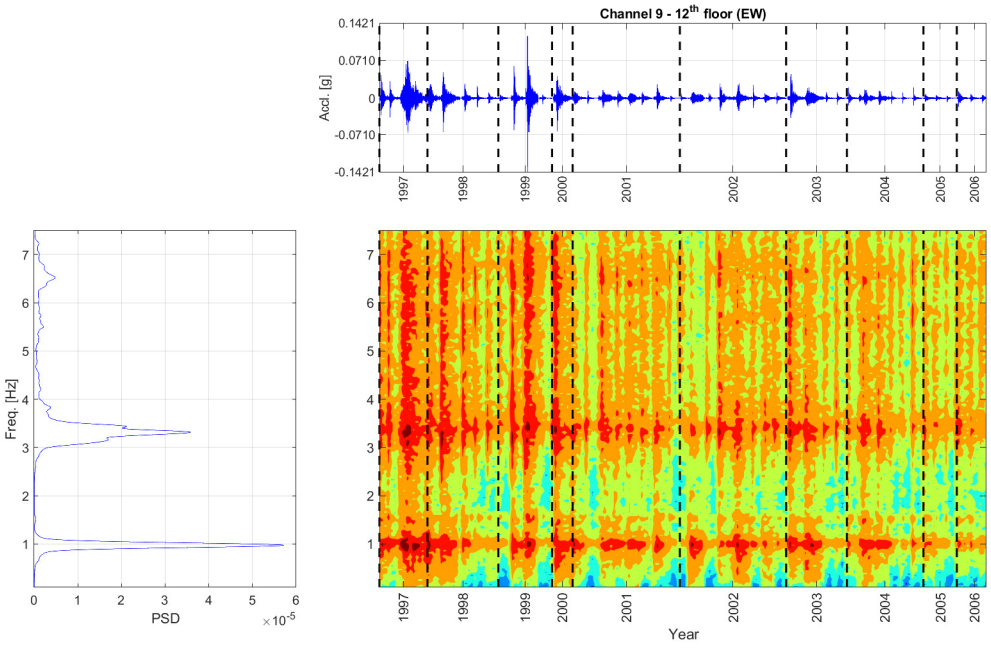

Figure C.25: Channel #9 spectrogram for the periods 1997 to 2006 (the dashed line indicates the separations between years).

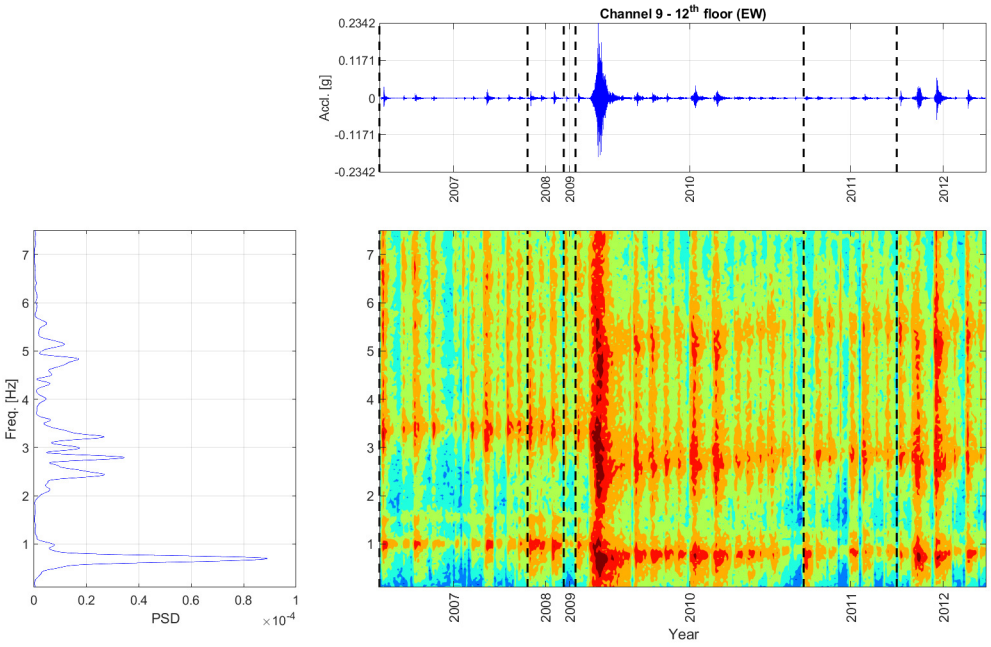

Figure C.26: Channel #9 spectrogram for the periods 2007 to 2012 (the dashed line indicates the separations between years).

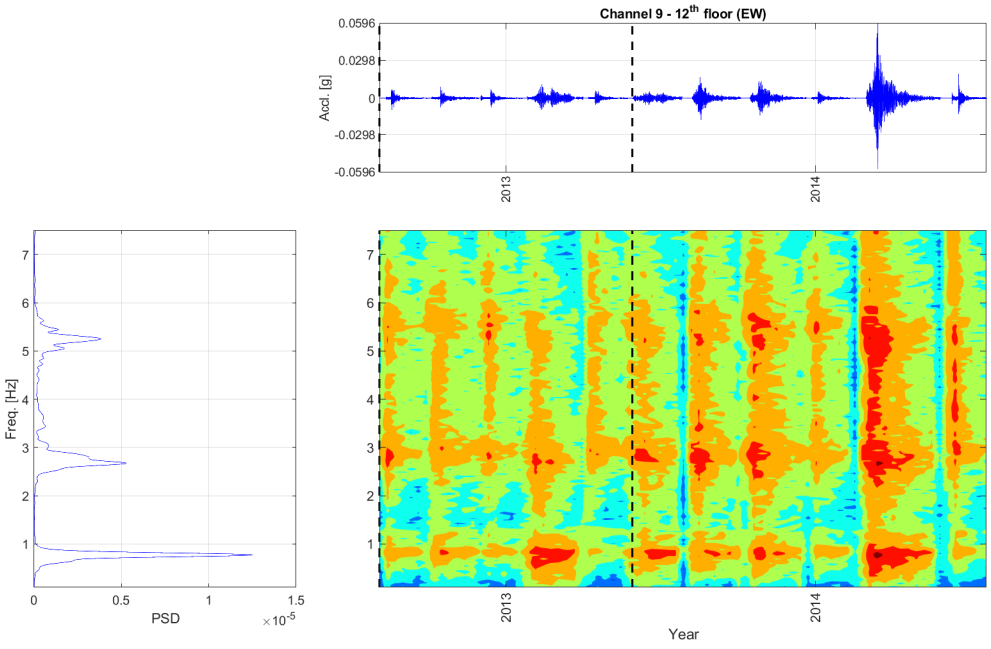

Figure C.27: Channel #9 spectrogram for the periods 2013 to 2014 (the dashed line indicates the separations between years).

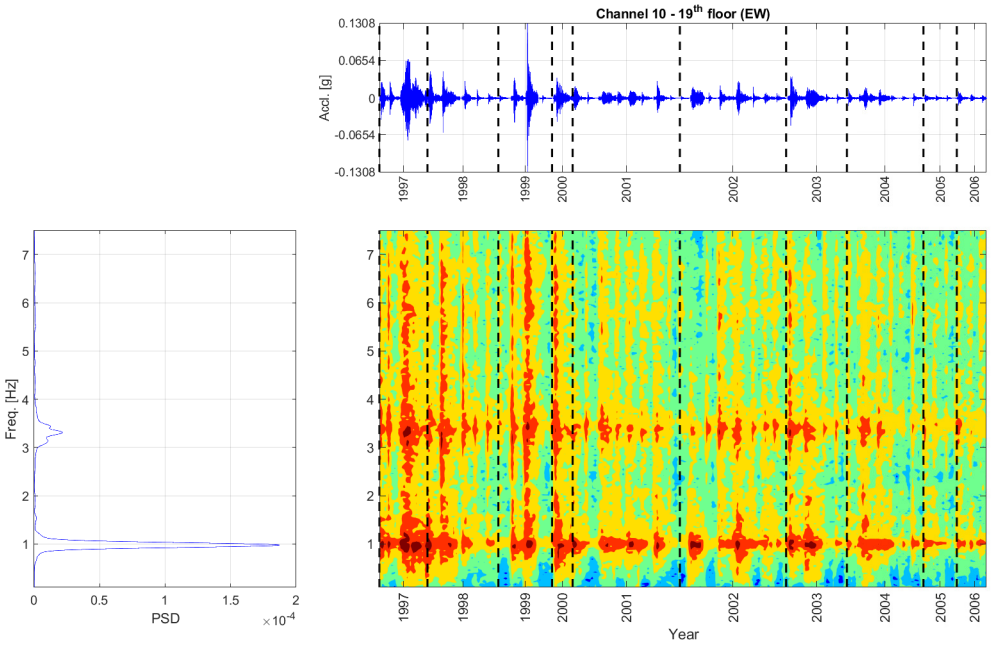

Figure C.28: Channel #10 spectrogram for the periods 1997 to 2006 (the dashed line indicates the separations between years).

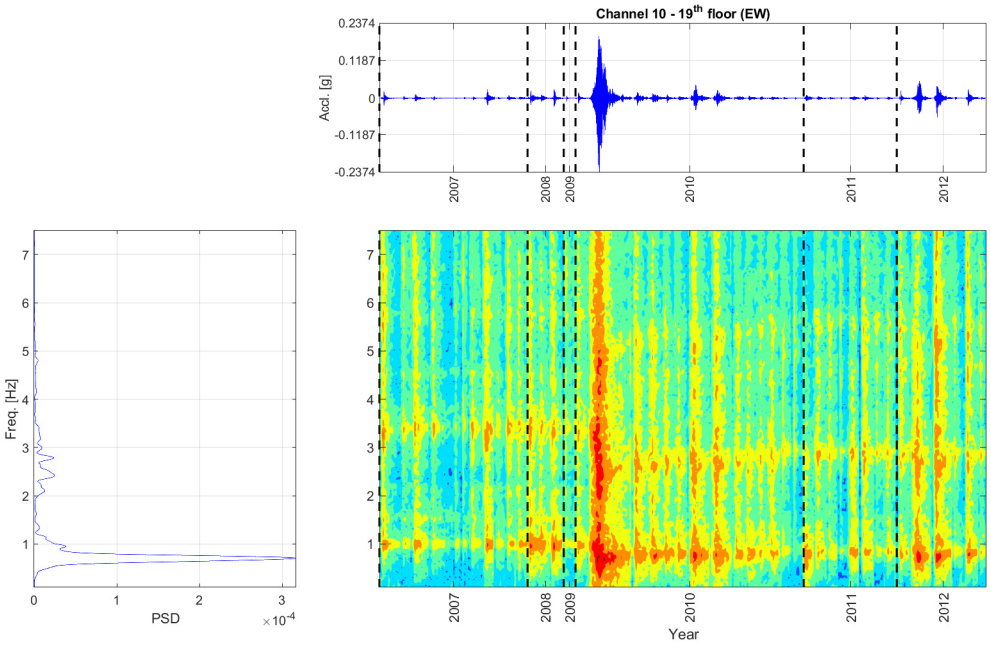

Figure C.29: Channel #10 spectrogram for the periods 2007 to 2012 (the dashed line indicates the separations between years).

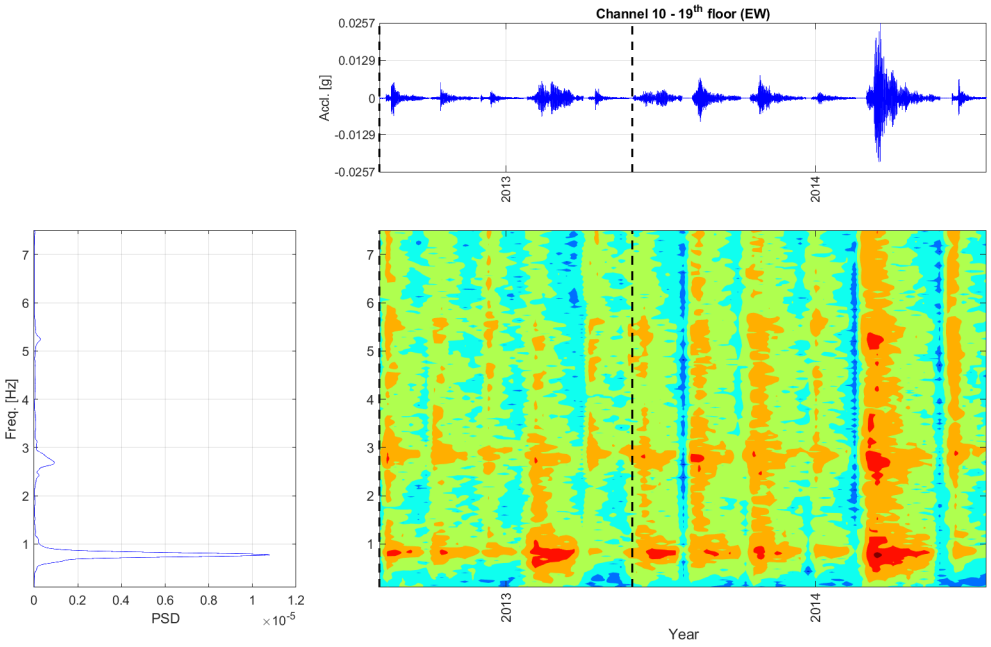

Figure C.30: Channel #10 spectrogram for the periods 2013 to 2014 (the dashed line indicates the separations between years).

Appendix D

Structural responses predicted using final-updated FE model

The time series of the real structural response measured, and that predicted by the initial and updated model, are presented.

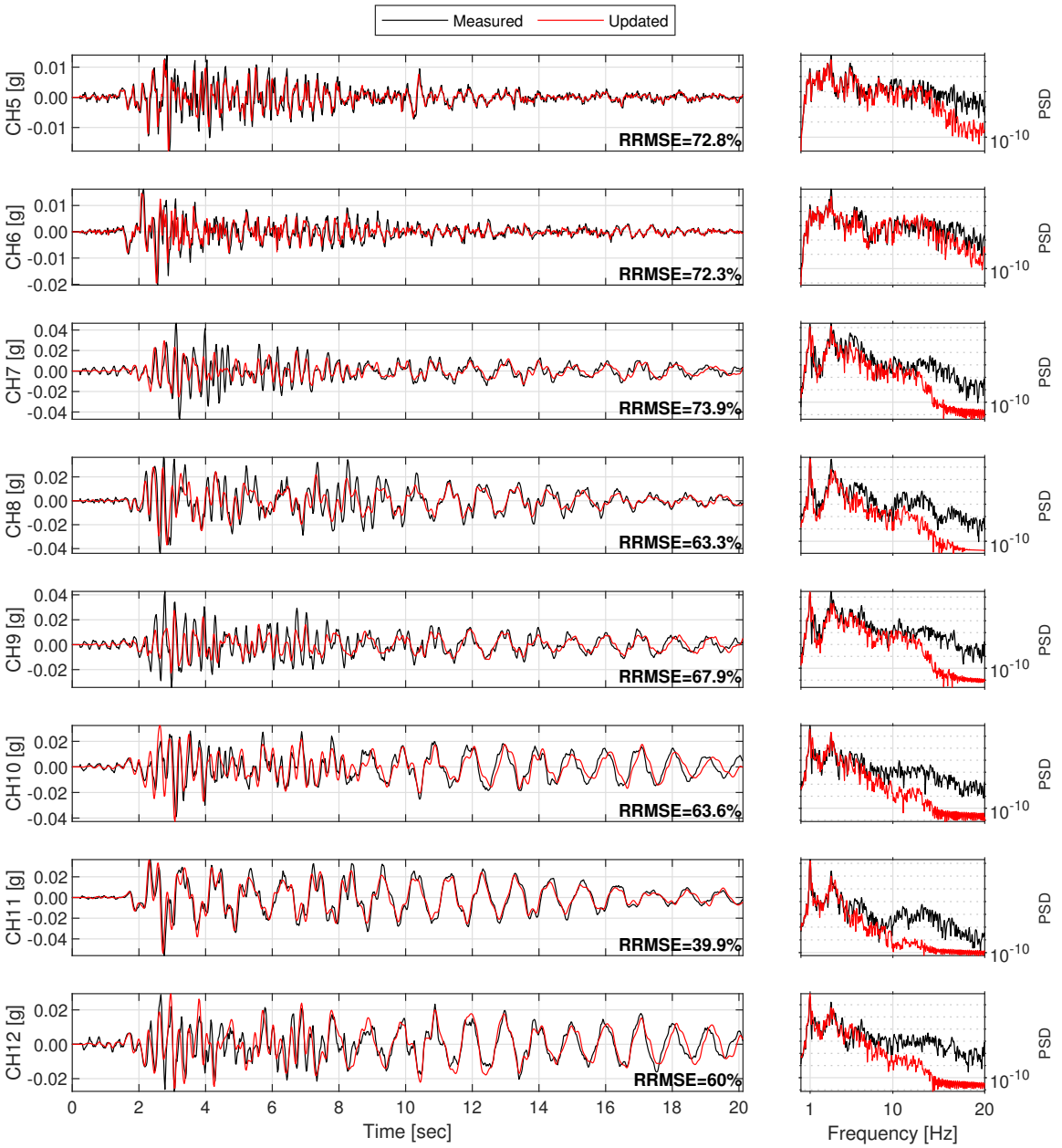

Figure D.1: Structural response comparison for seismic event #2.

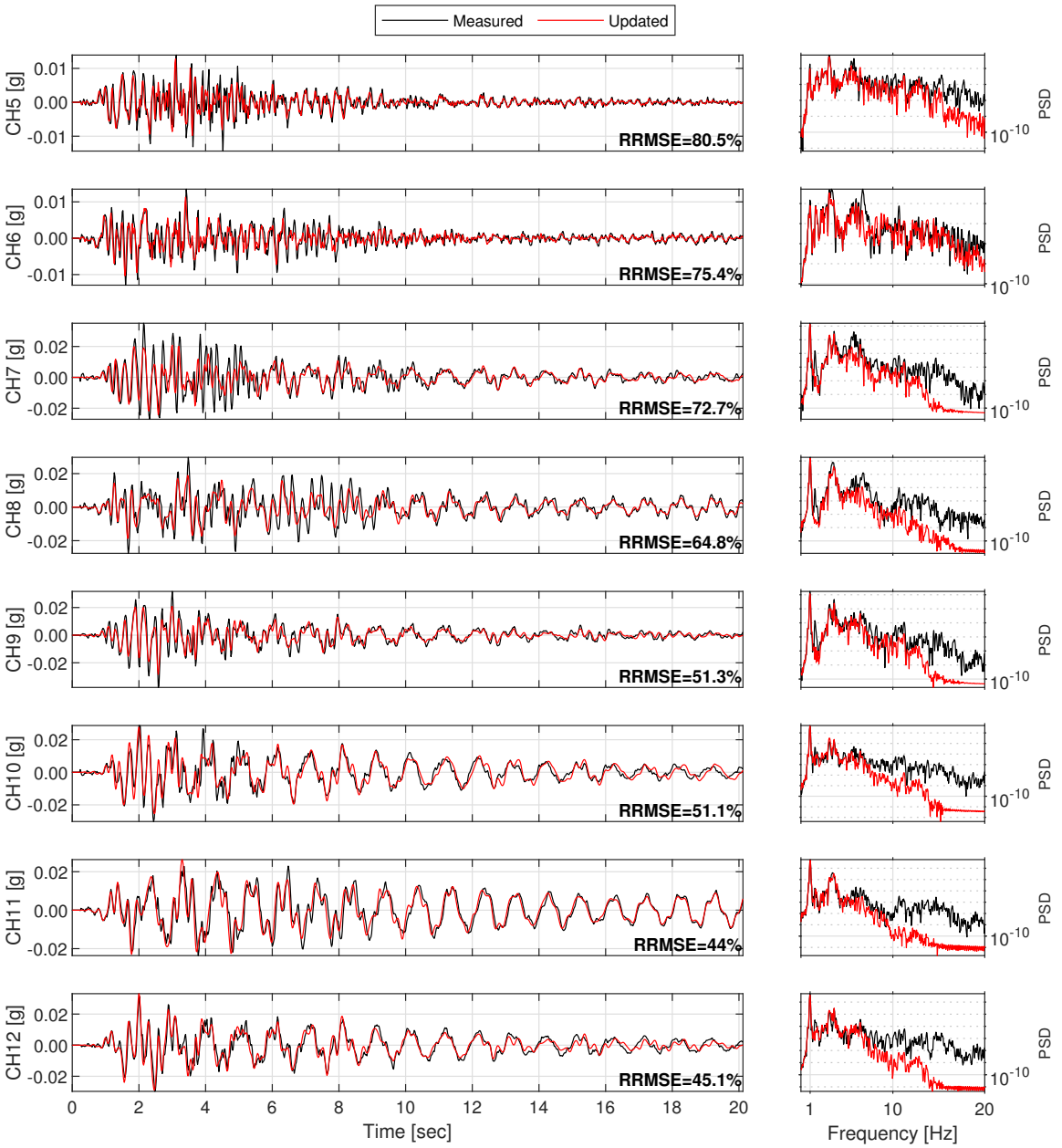

Figure D.2: Structural response comparison for seismic event #3.

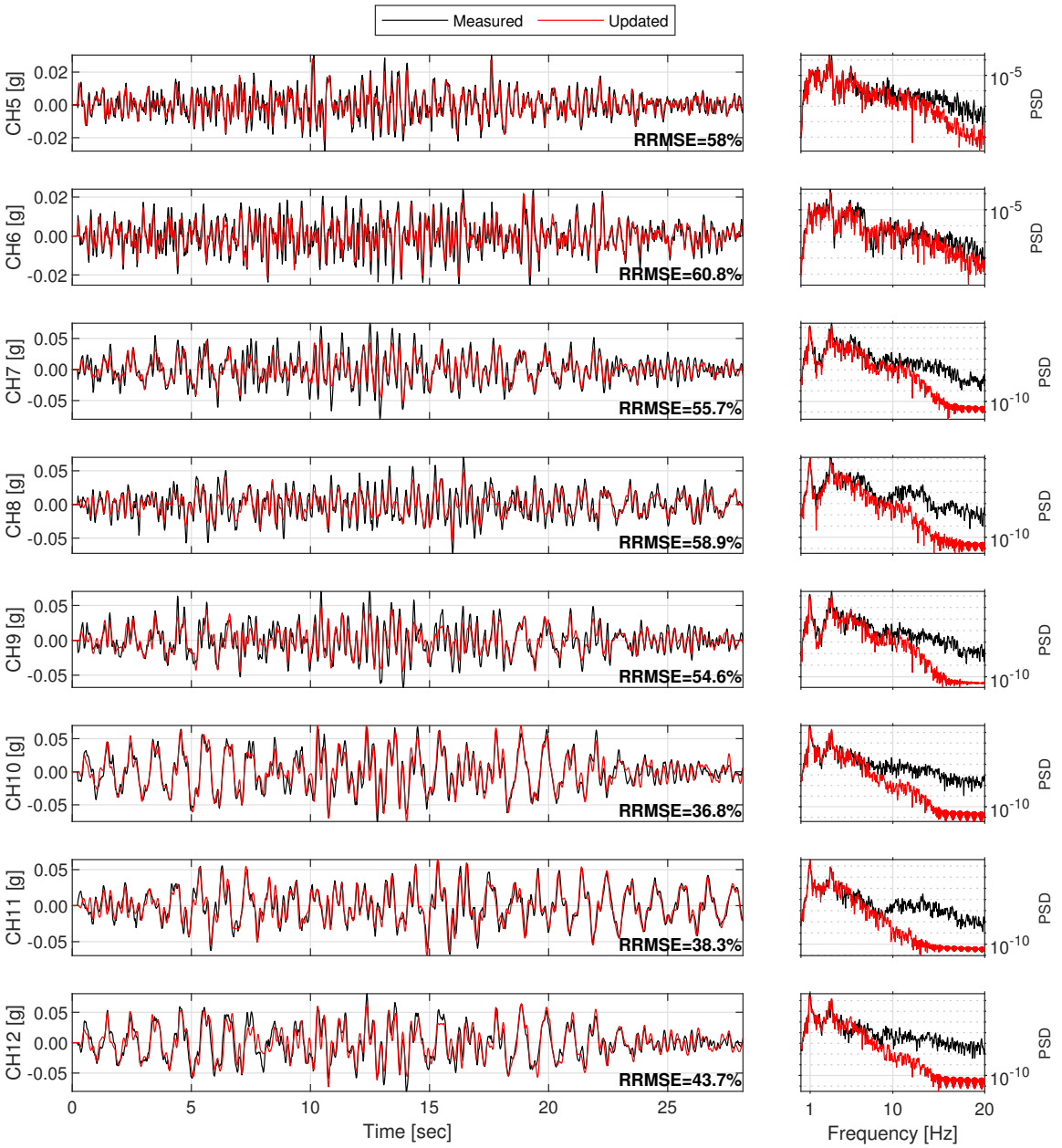

Figure D.3: Structural response comparison for seismic event #4.

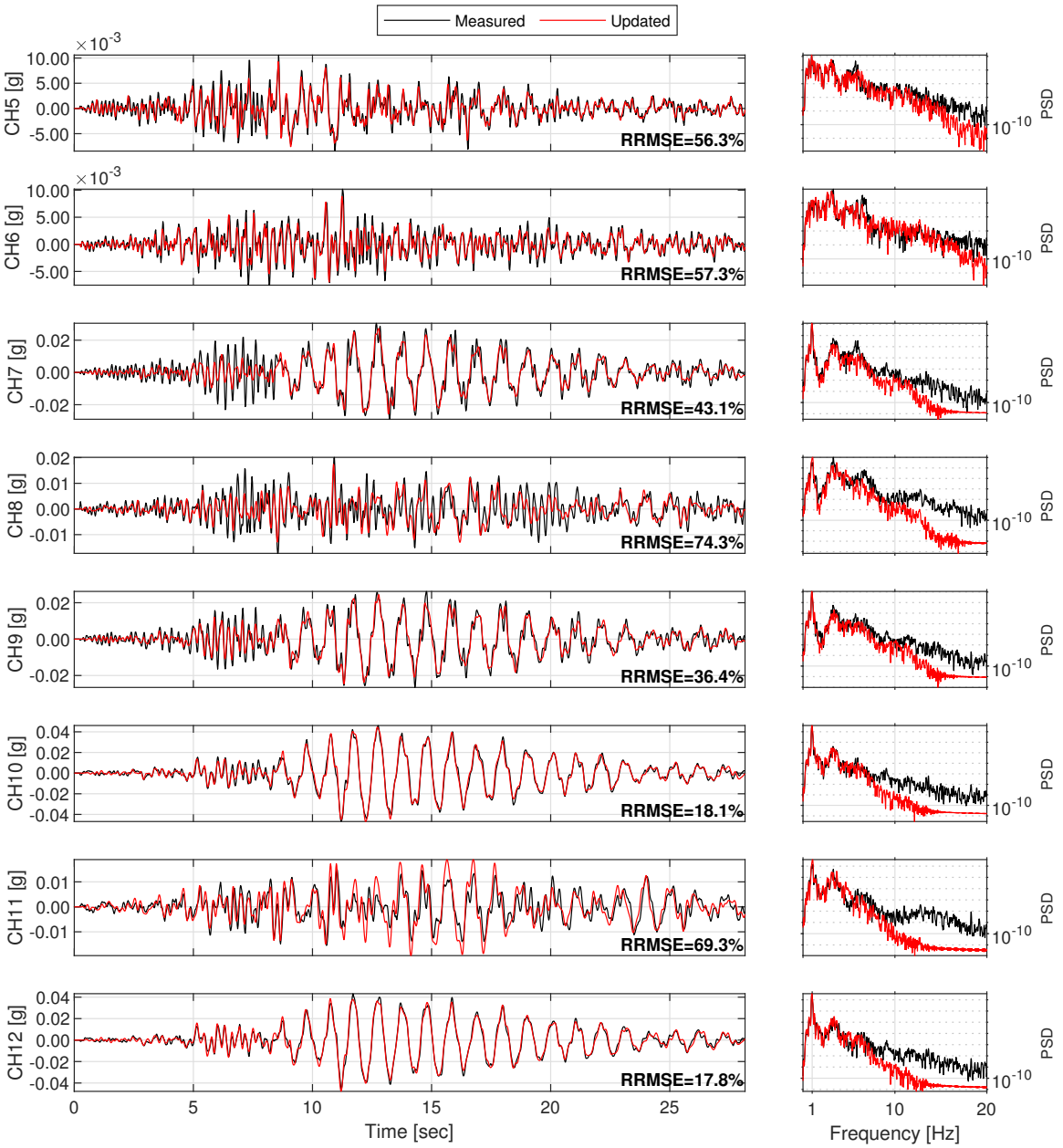

Figure D.4: Structural response comparison for seismic event #5.

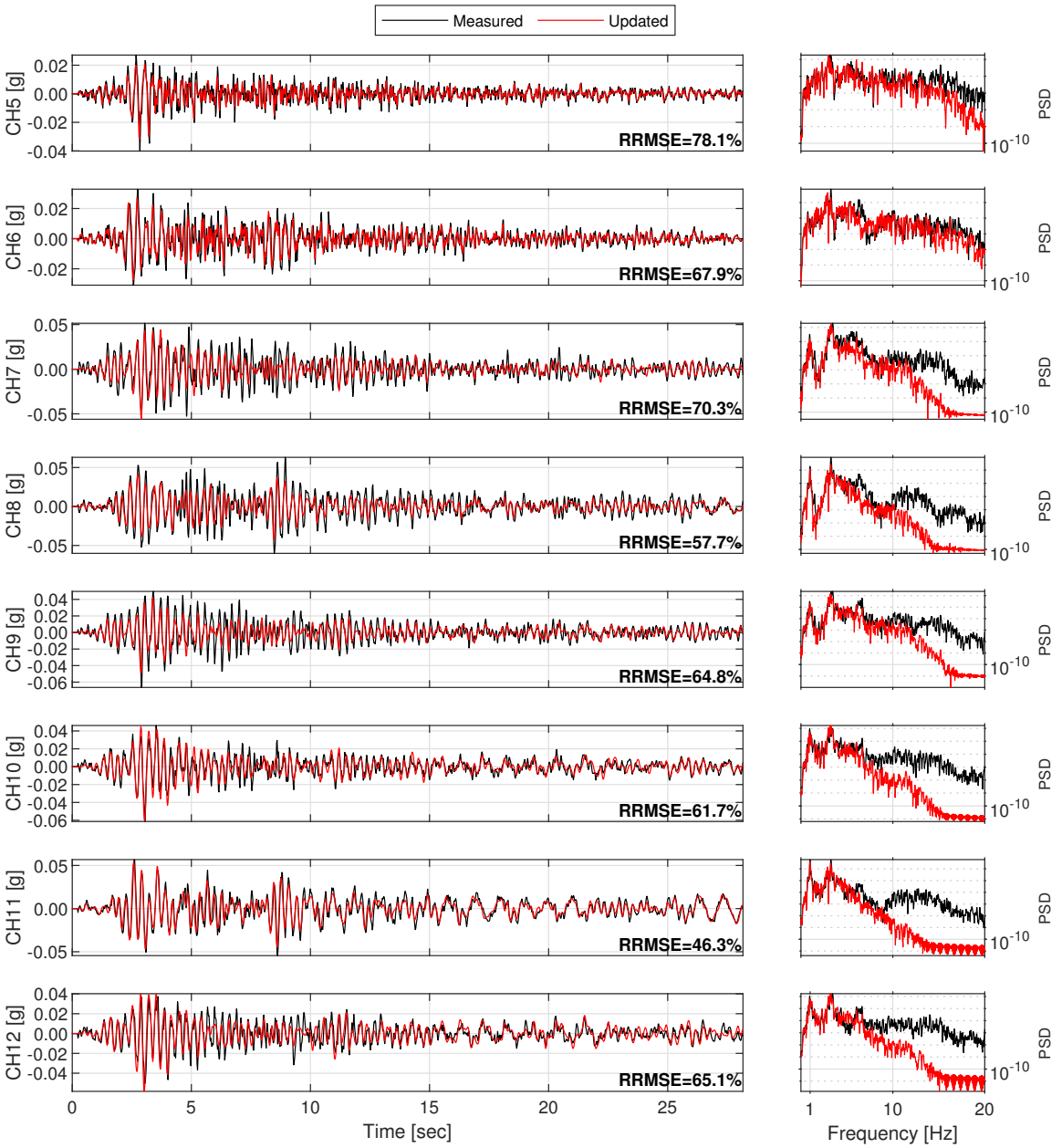

Figure D.5: Structural response comparison for seismic event #6.

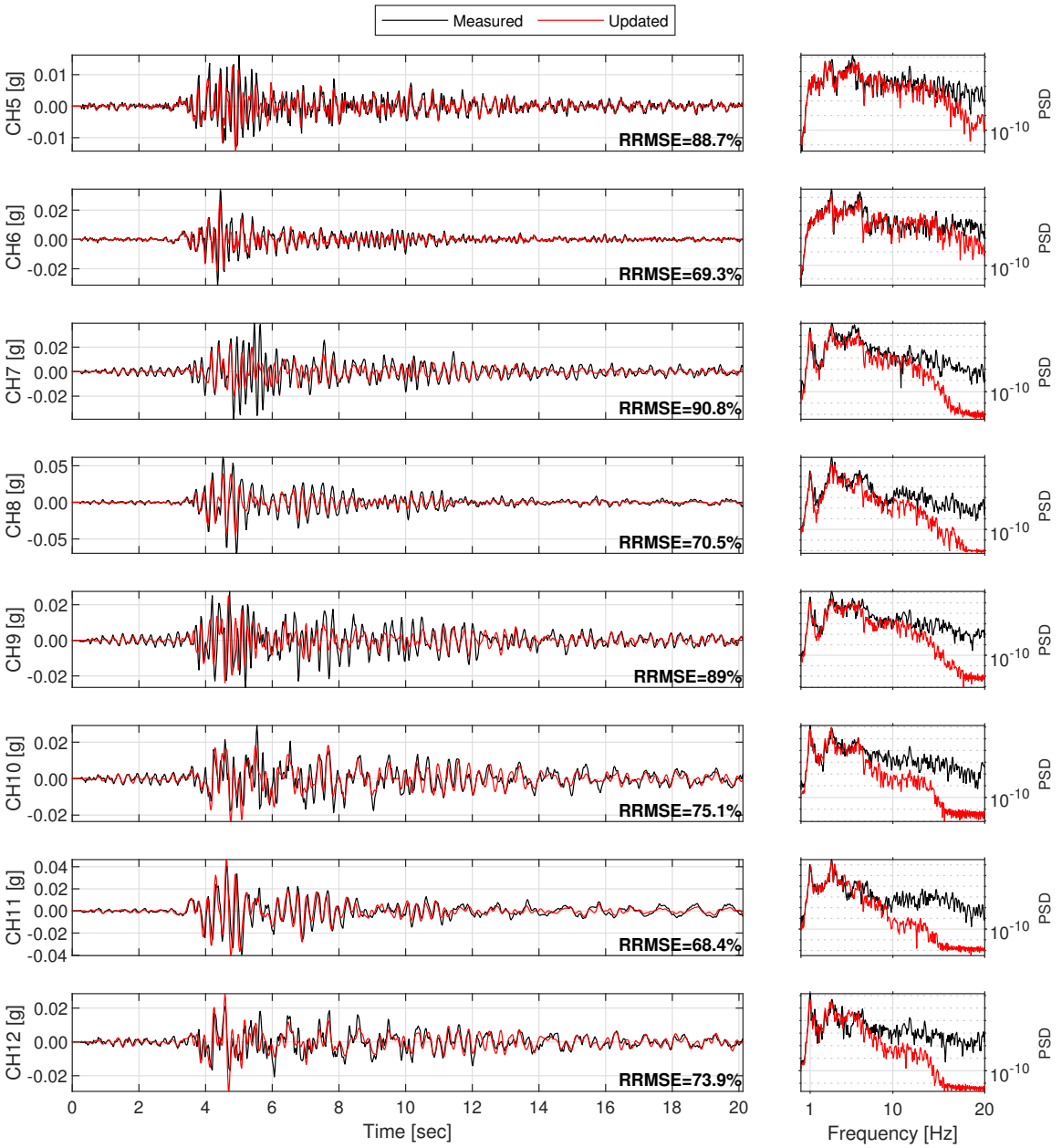

Figure D.6: Structural response comparison for seismic event #7.

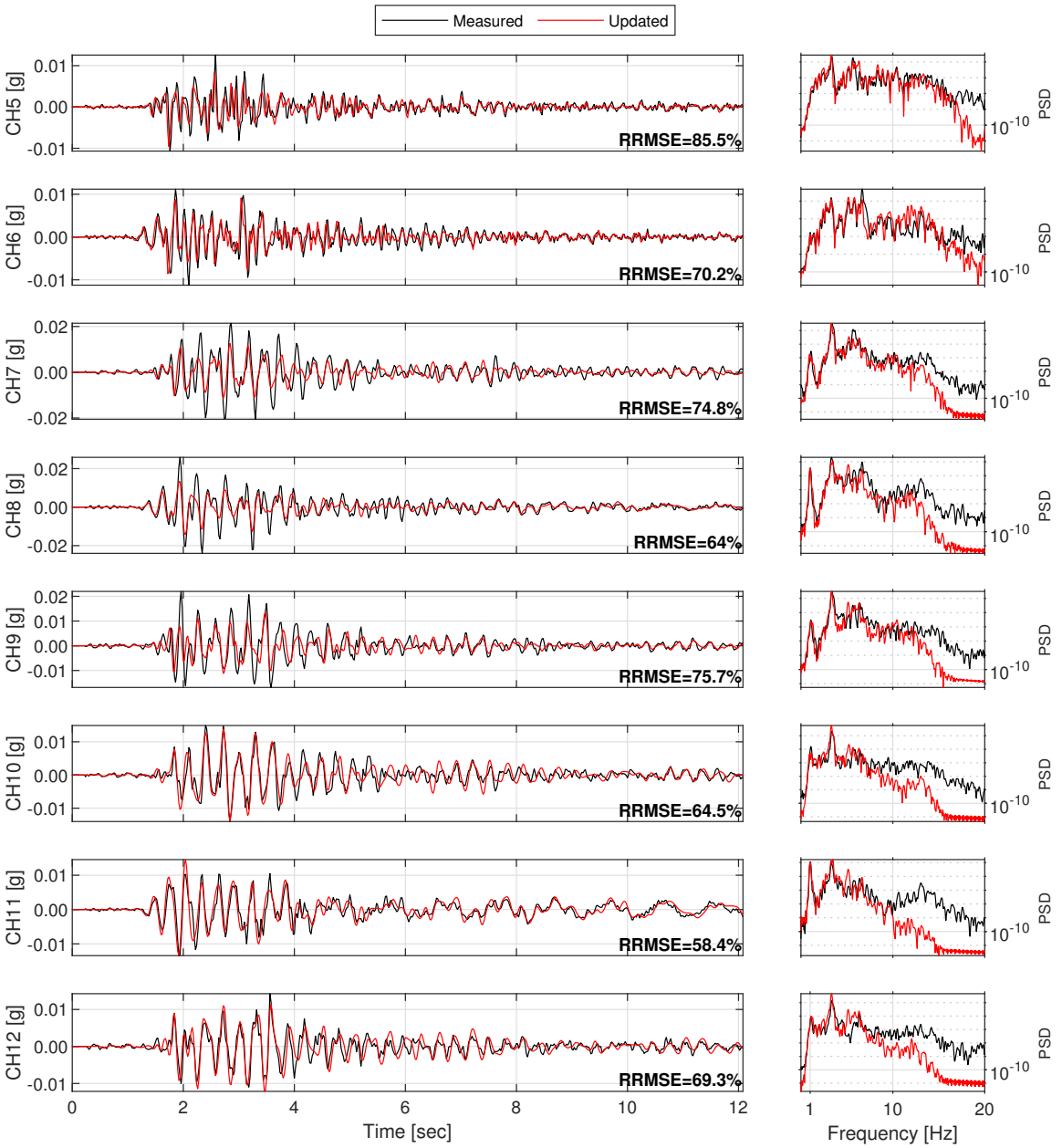

Figure D.7: Structural response comparison for seismic event #8.

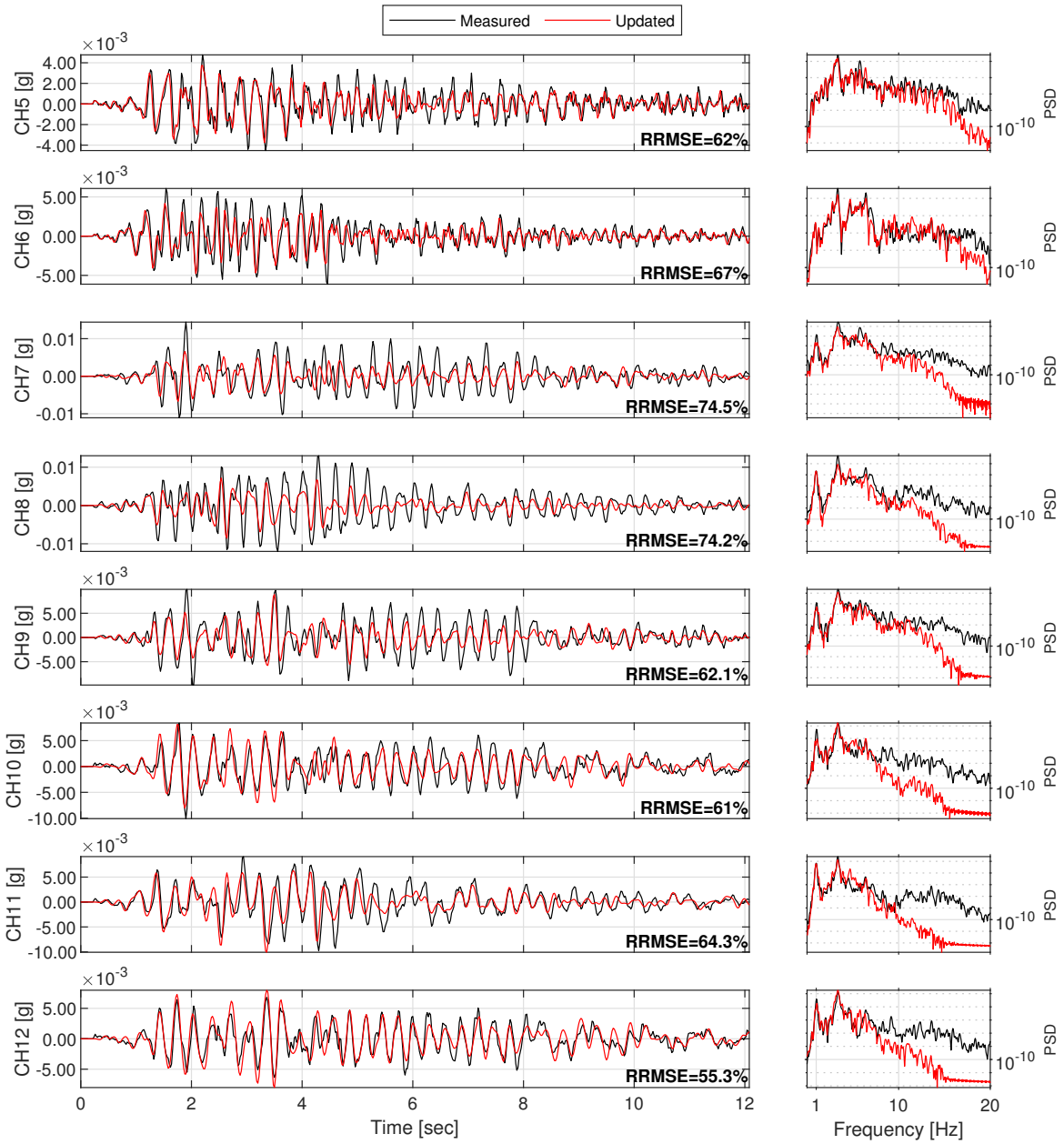

Figure D.8: Structural response comparison for seismic event #9.

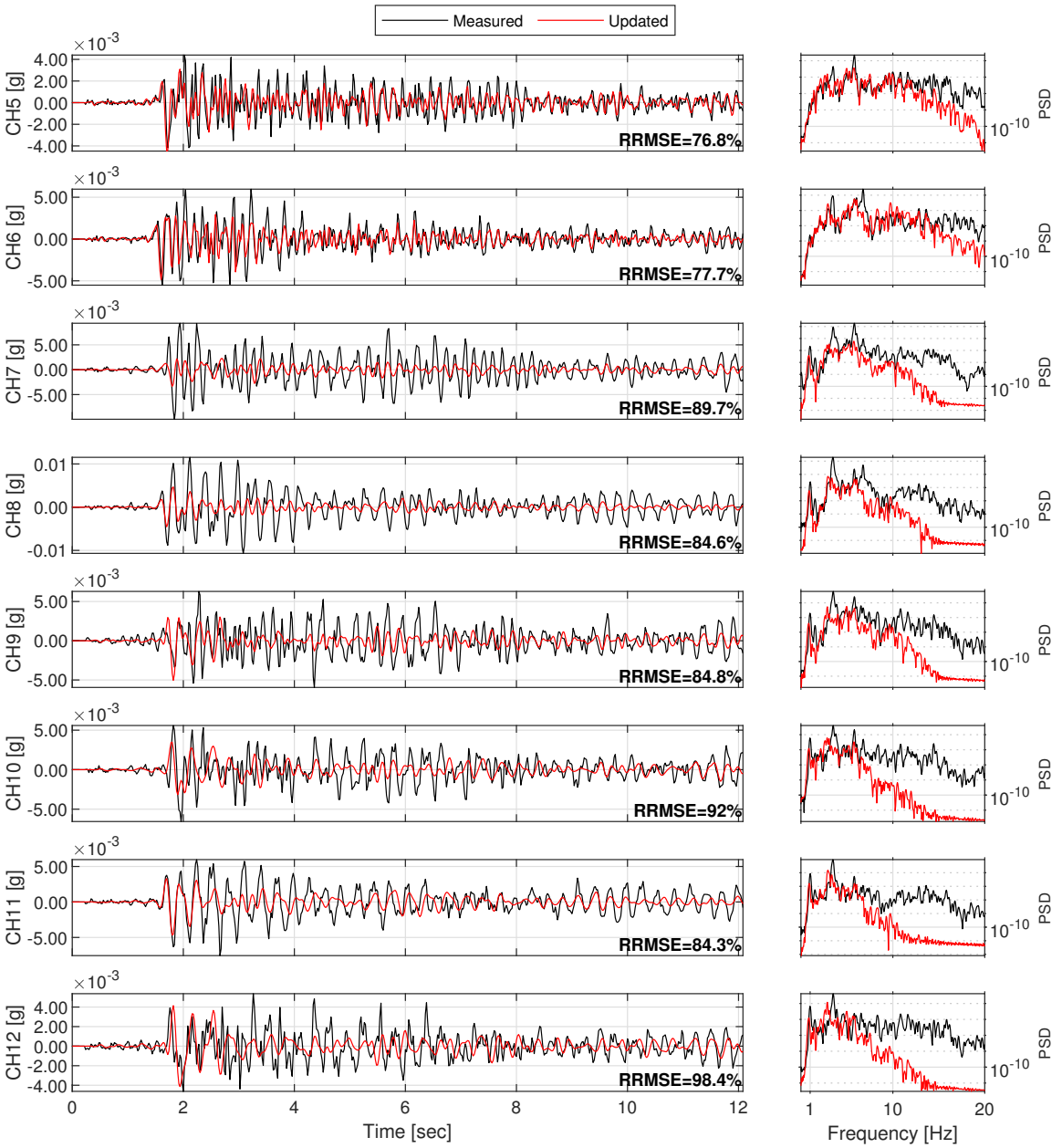

Figure D.9: Structural response comparison for seismic event #10.

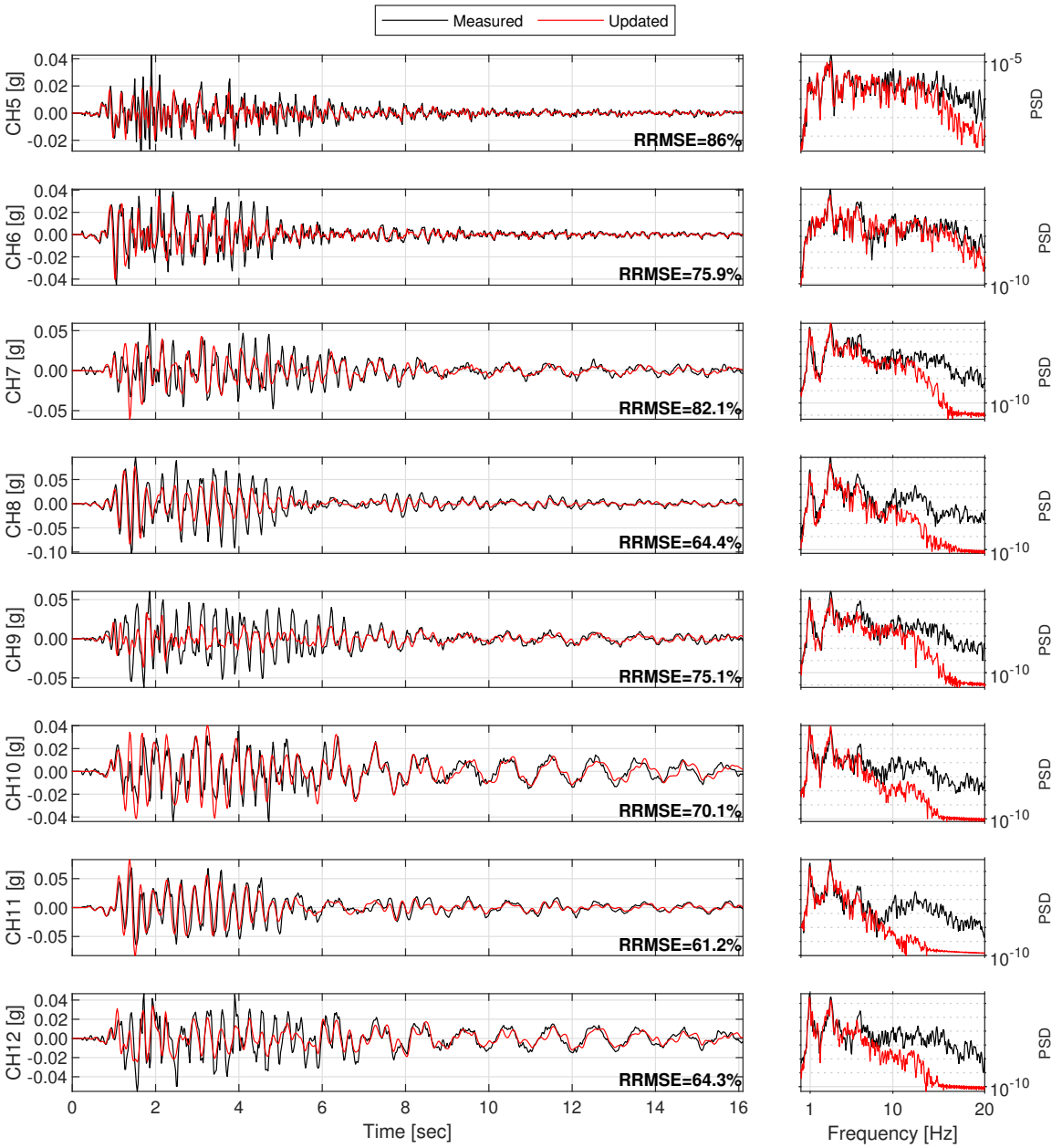

Figure D.10: Structural response comparison for seismic event #11.

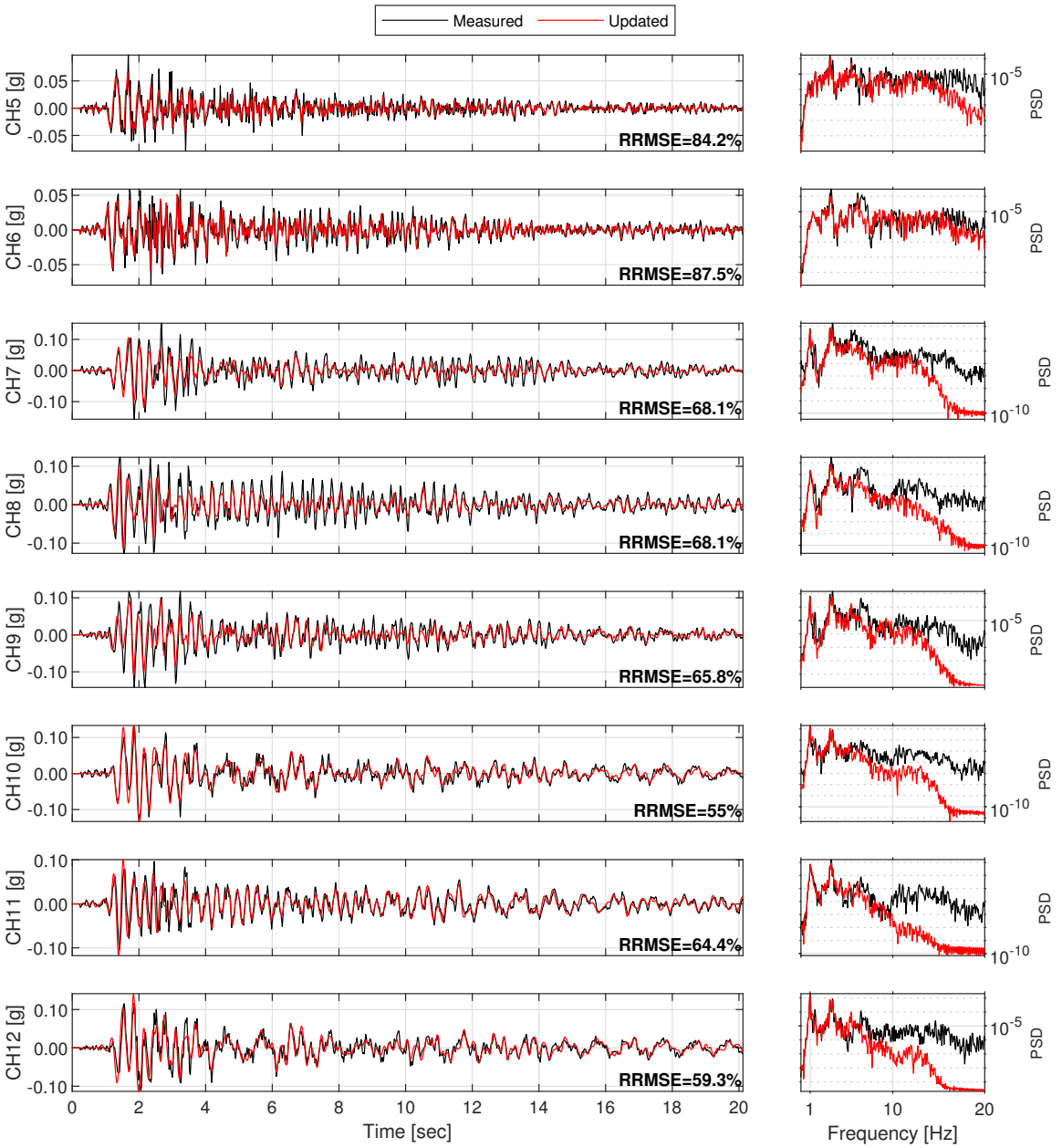

Figure D.11: Structural response comparison for seismic event #12.

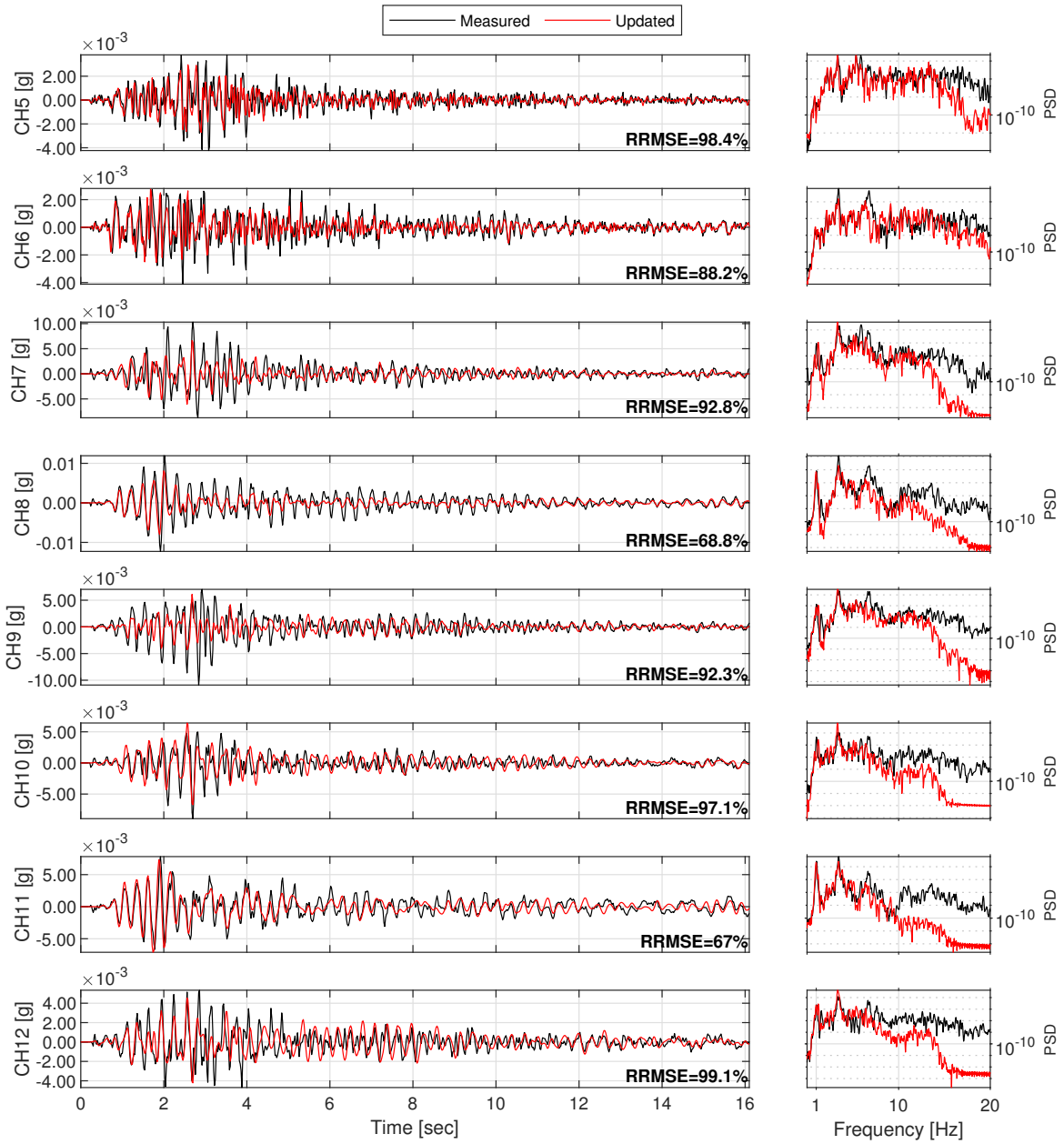

Figure D.12: Structural response comparison for seismic event #13.

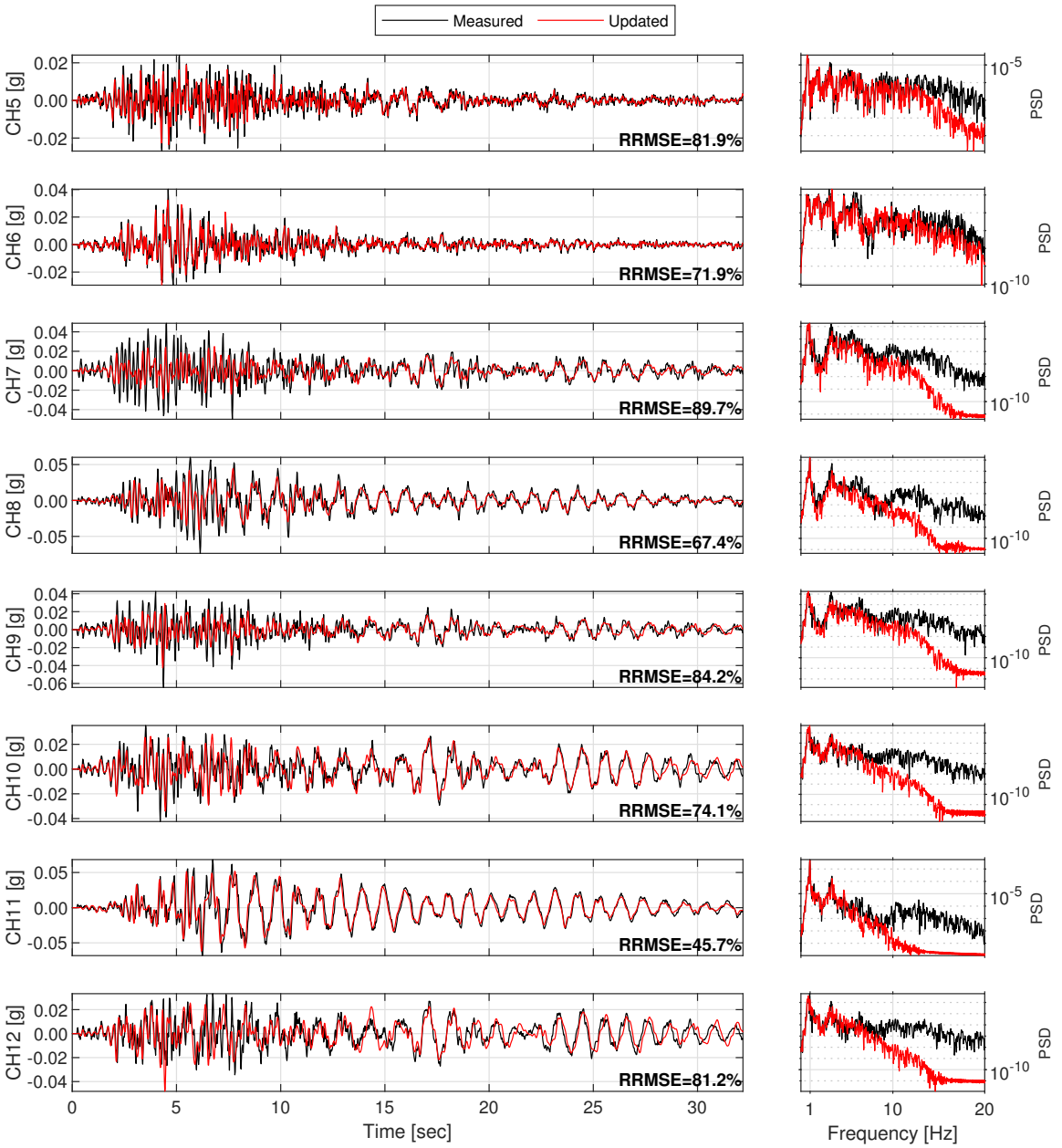

Figure D.13: Structural response comparison for seismic event #14.

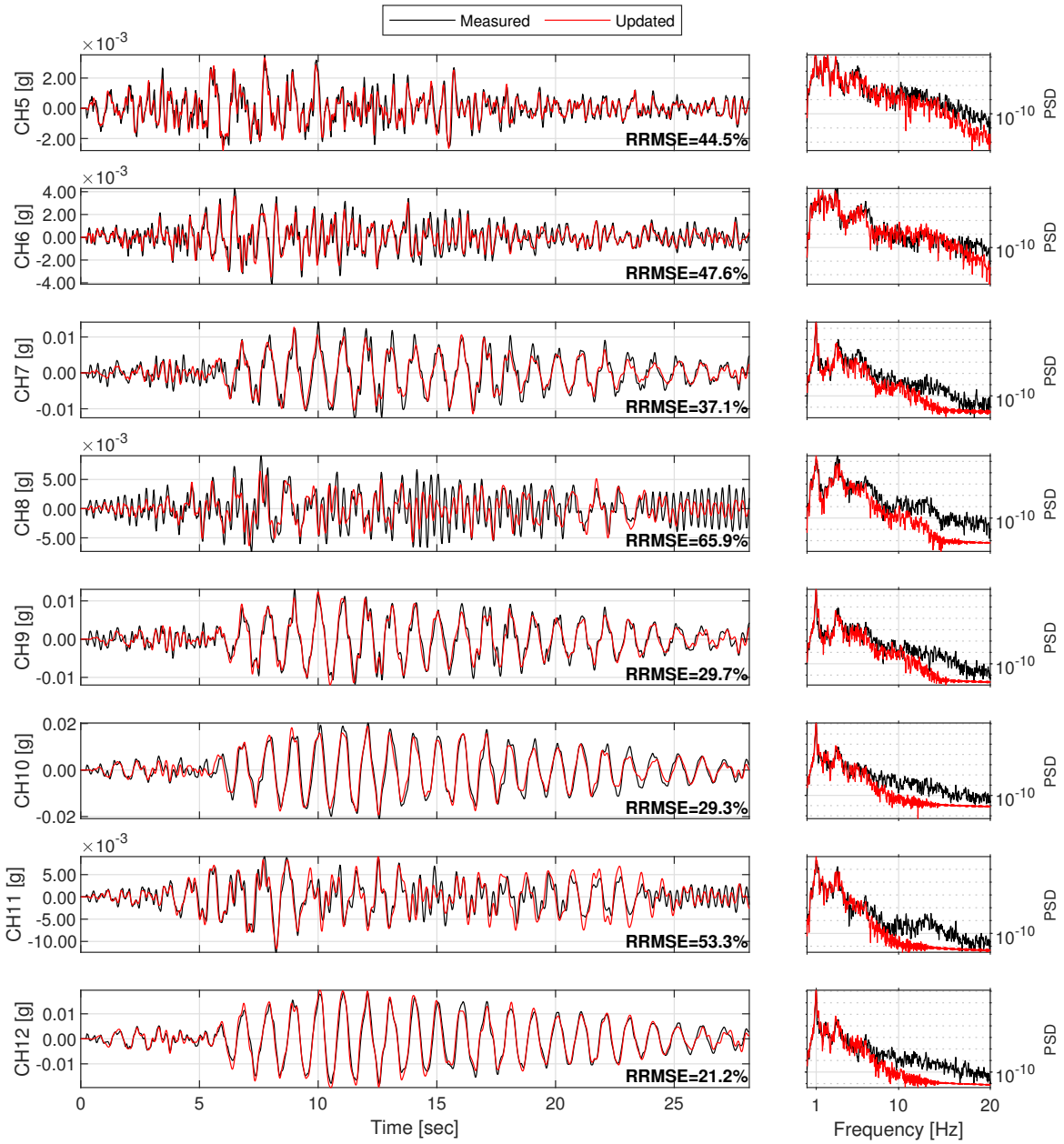

Figure D.14: Structural response comparison for seismic event #15.

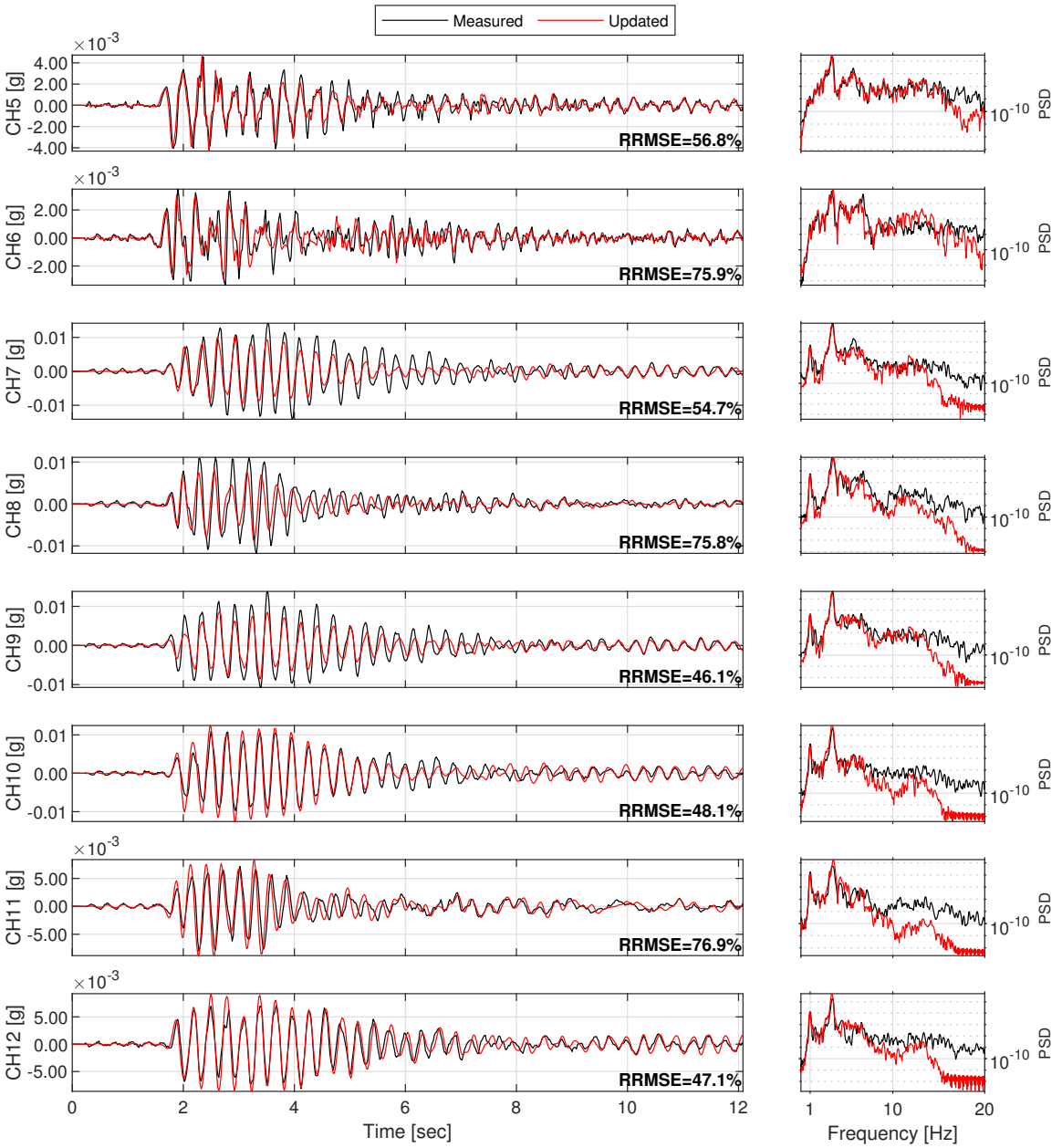

Figure D.15: Structural response comparison for seismic event #16.

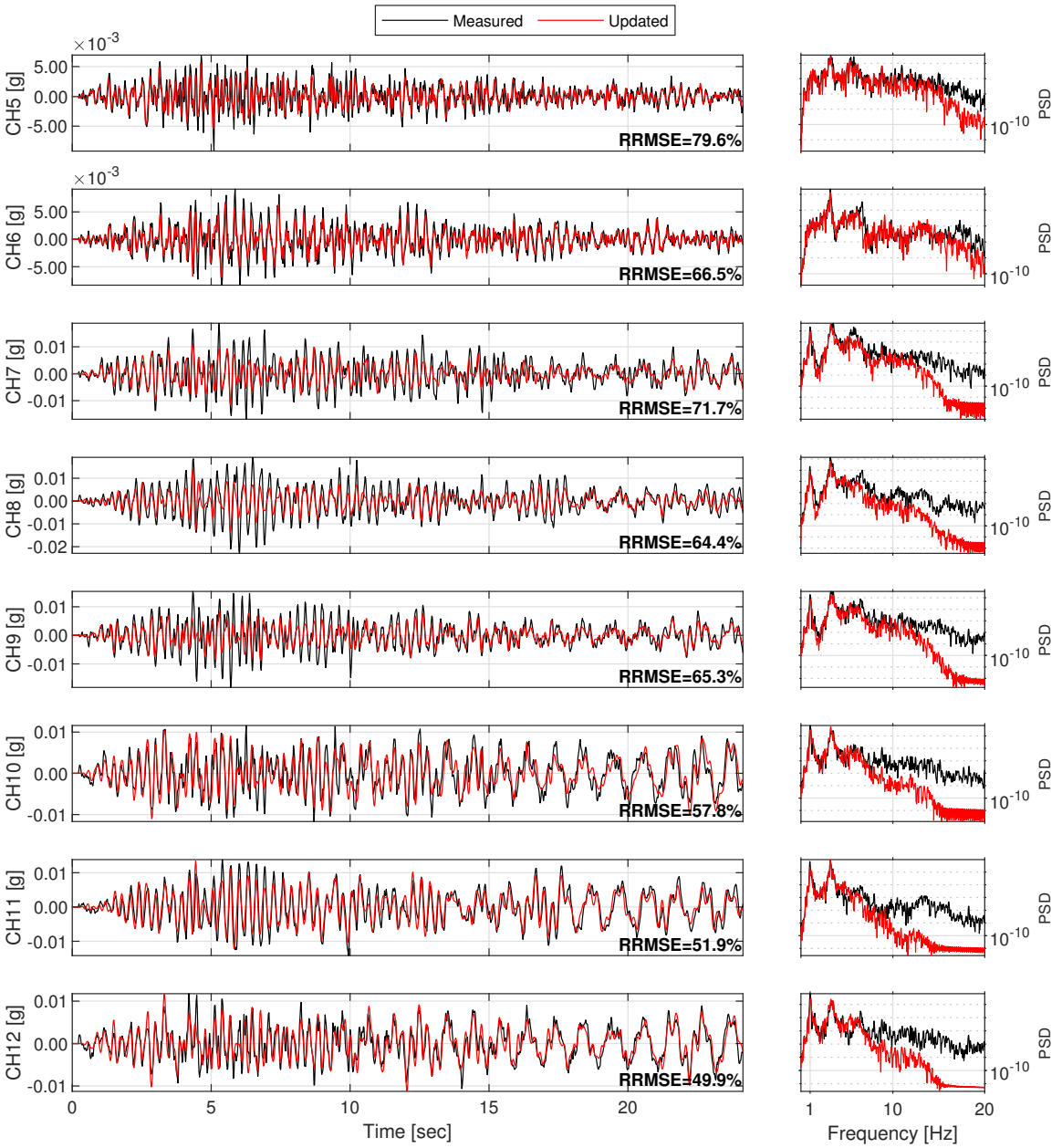

Figure D.16: Structural response comparison for seismic event #17.

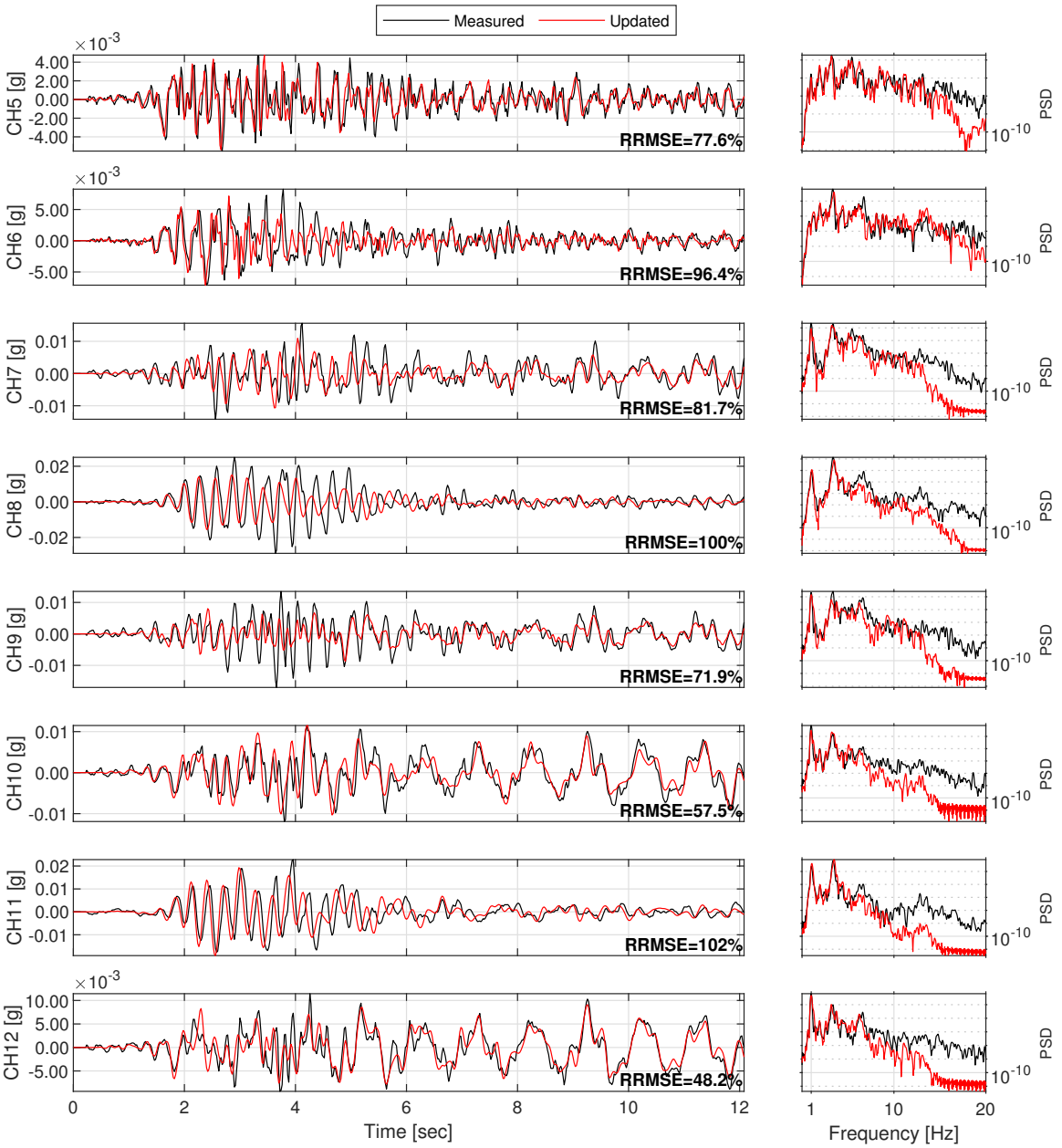

Figure D.17: Structural response comparison for seismic event #18.

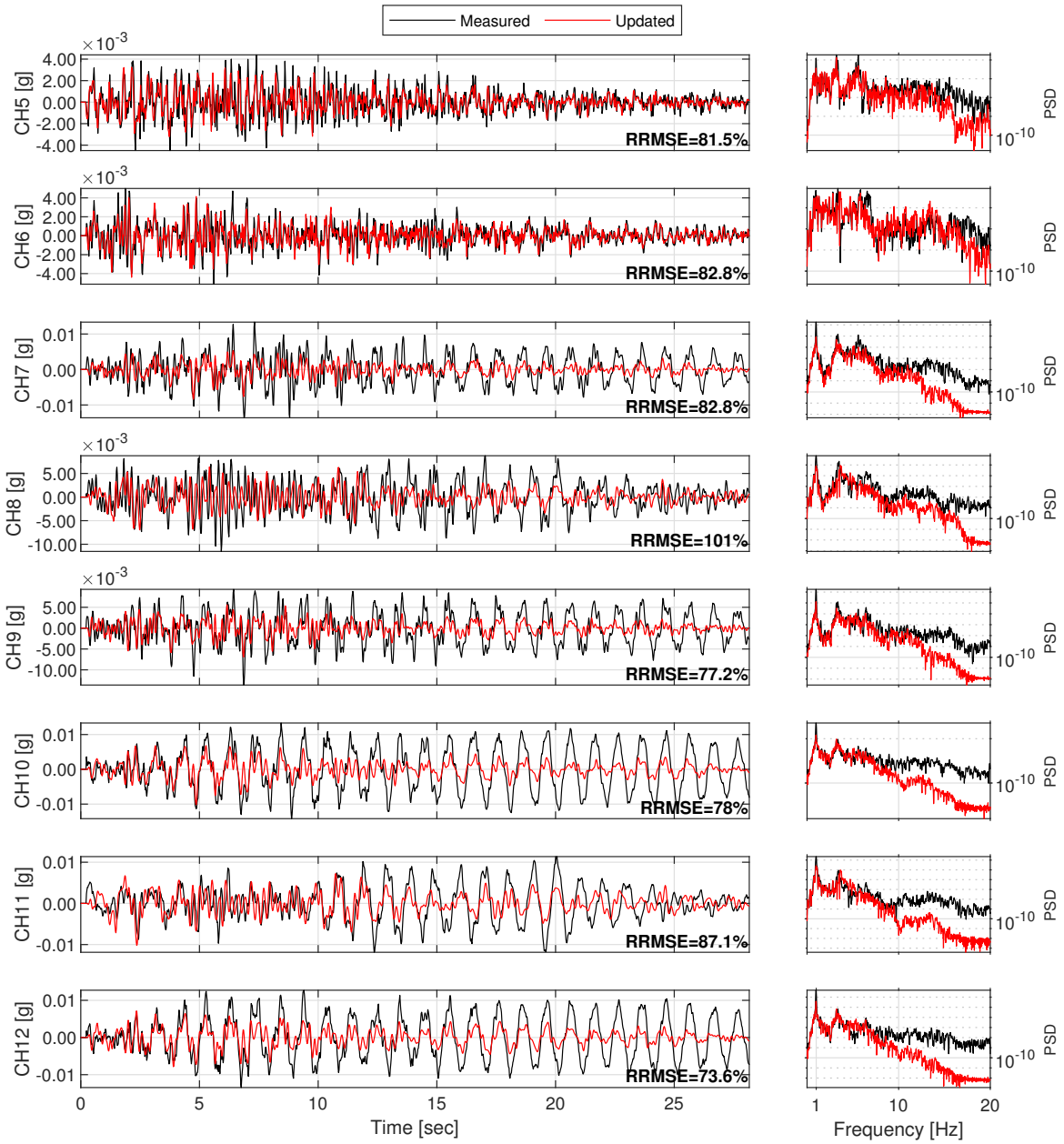

Figure D.18: Structural response comparison for seismic event #19.

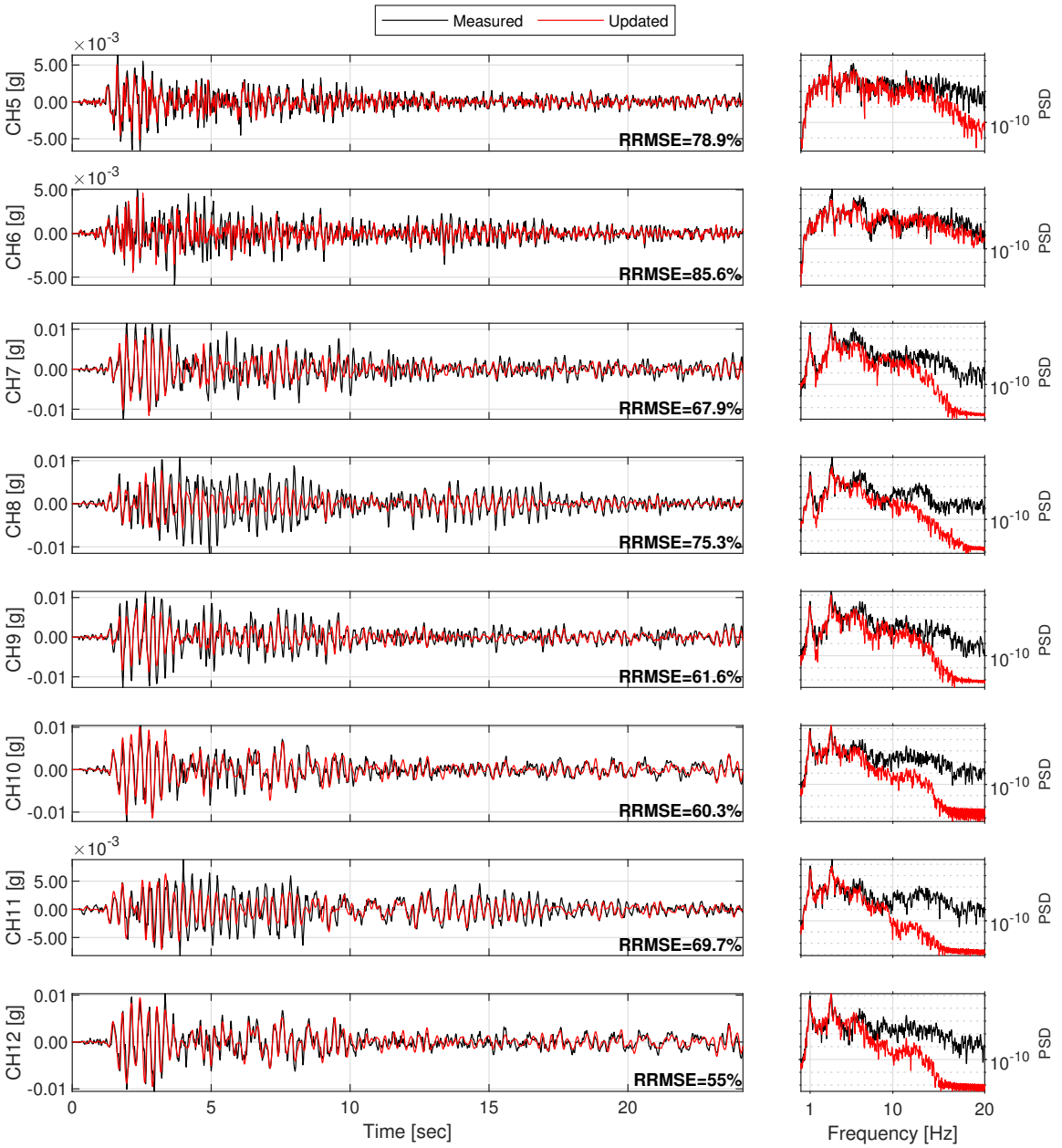

Figure D.19: Structural response comparison for seismic event #20.

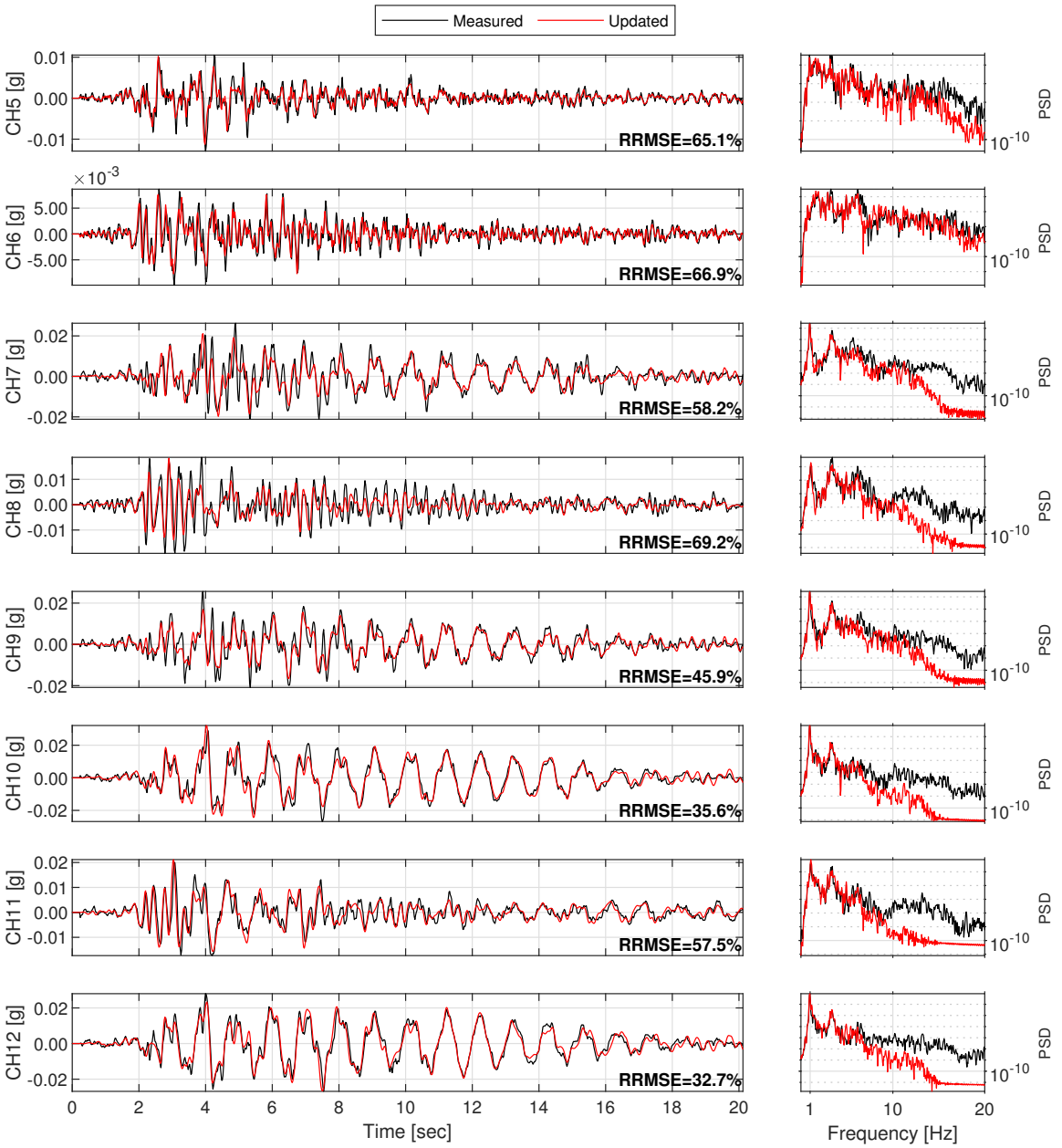

Figure D.20: Structural response comparison for seismic event #21.

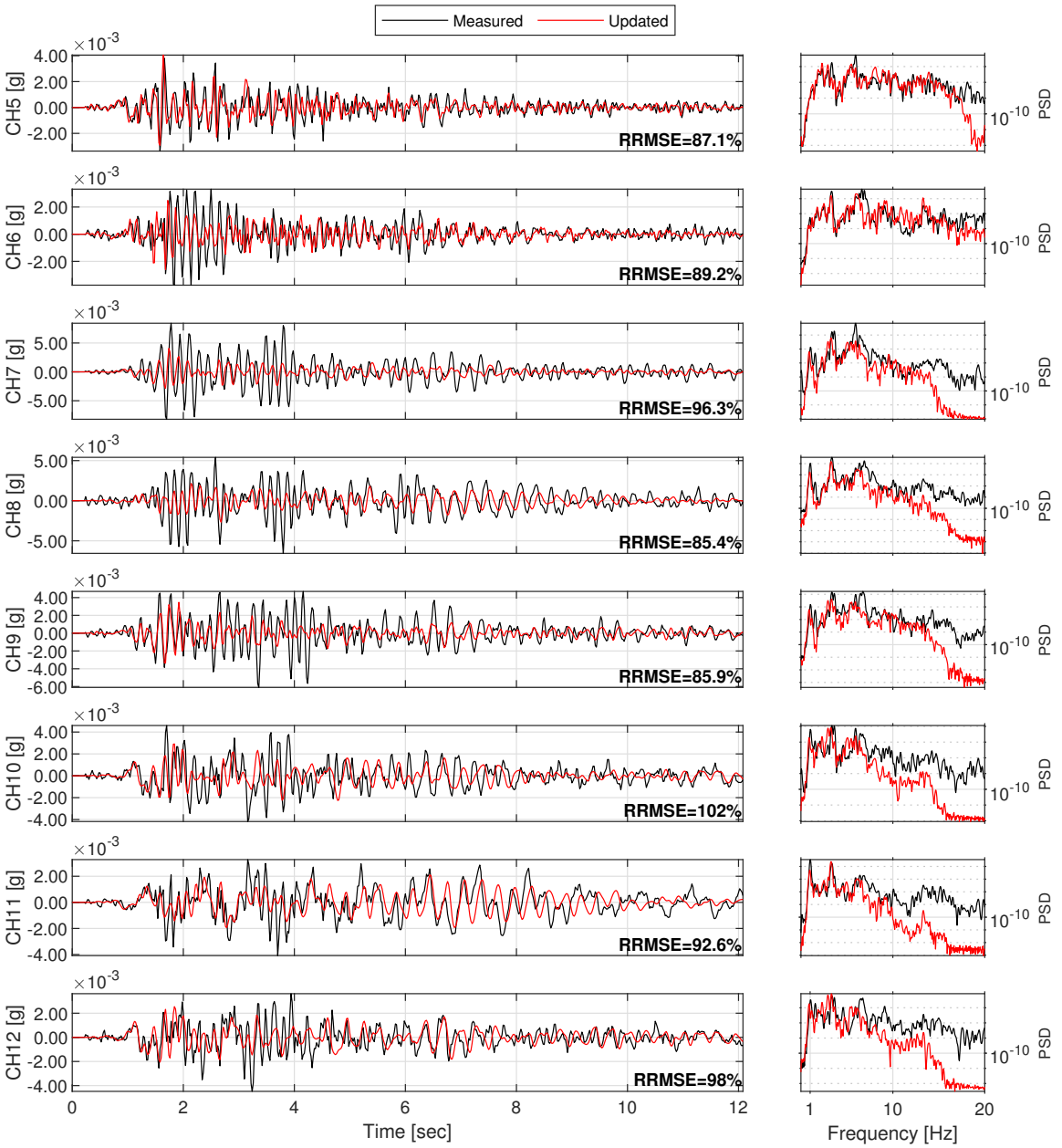

Figure D.21: Structural response comparison for seismic event #22.

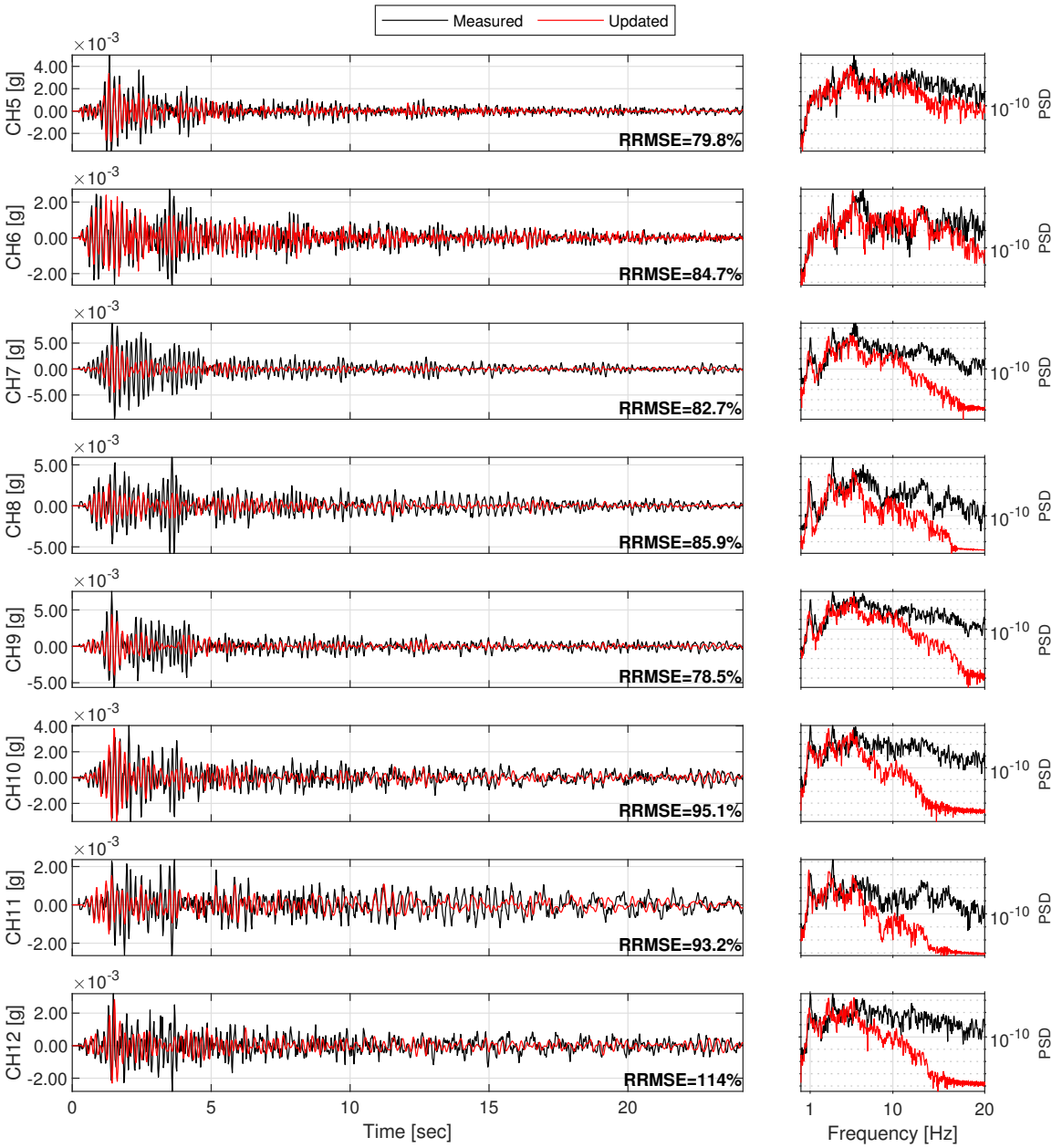

Figure D.22: Structural response comparison for seismic event #23.

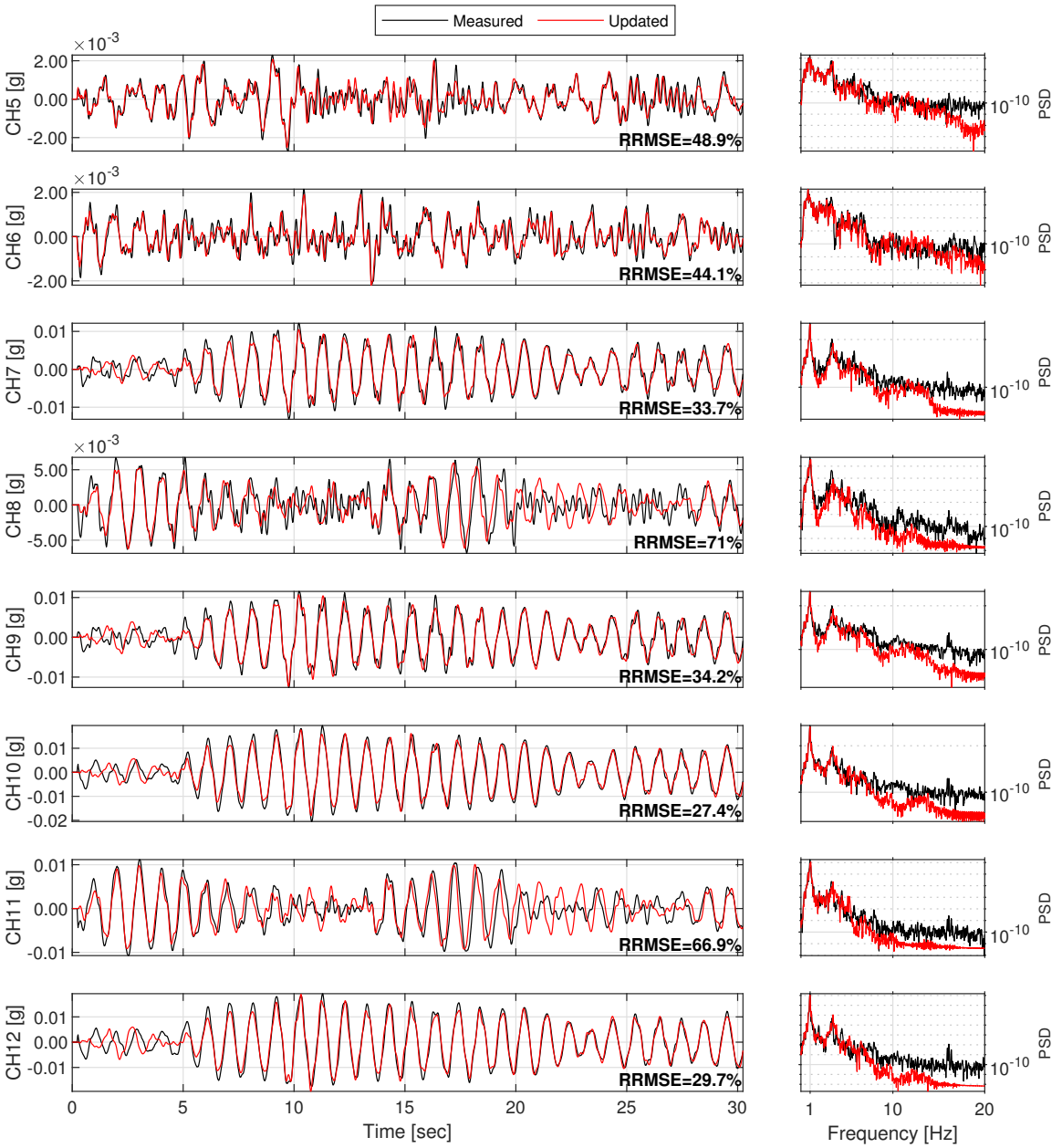

Figure D.23: Structural response comparison for seismic event #24.

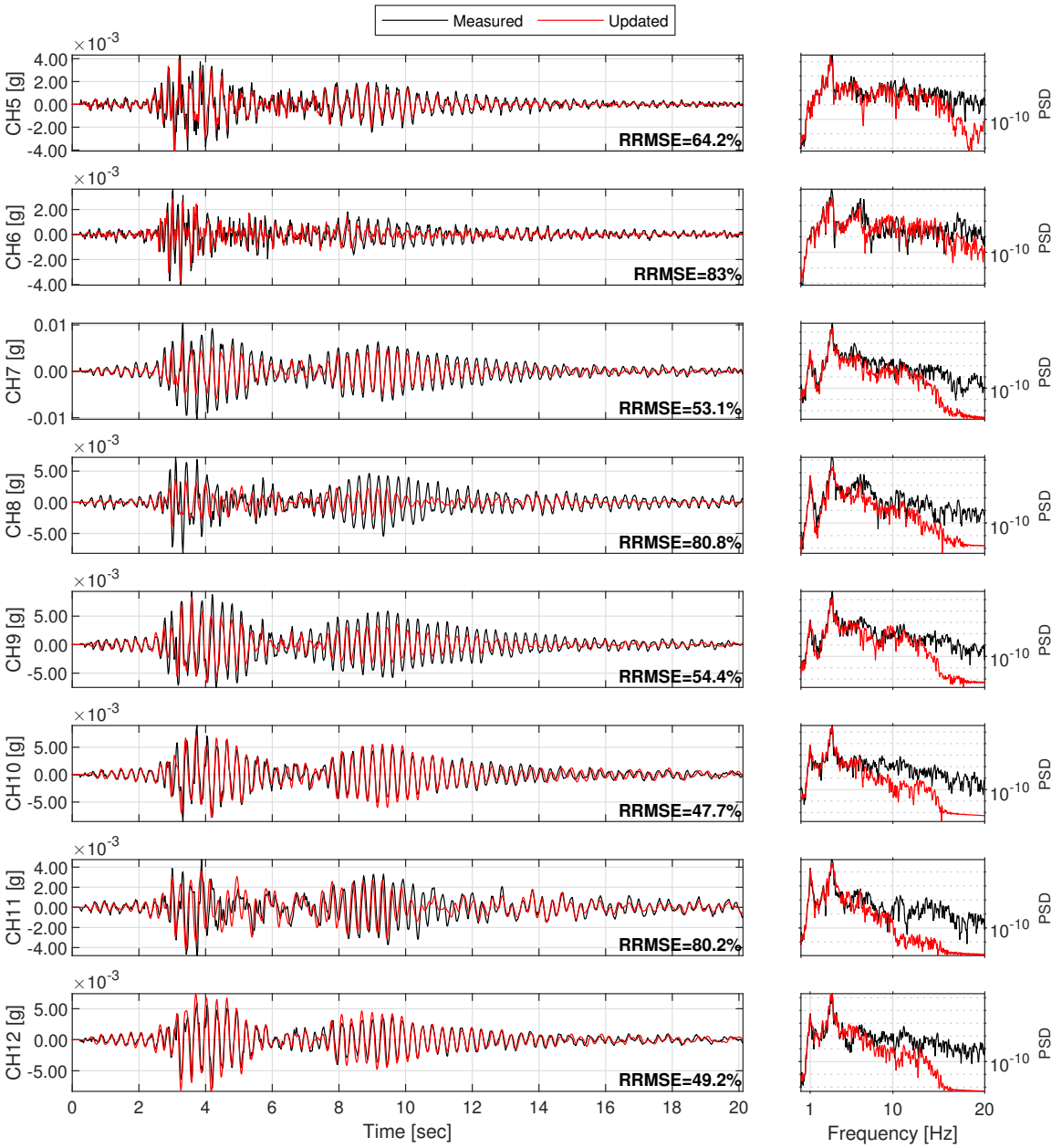

Figure D.24: Structural response comparison for seismic event #25.

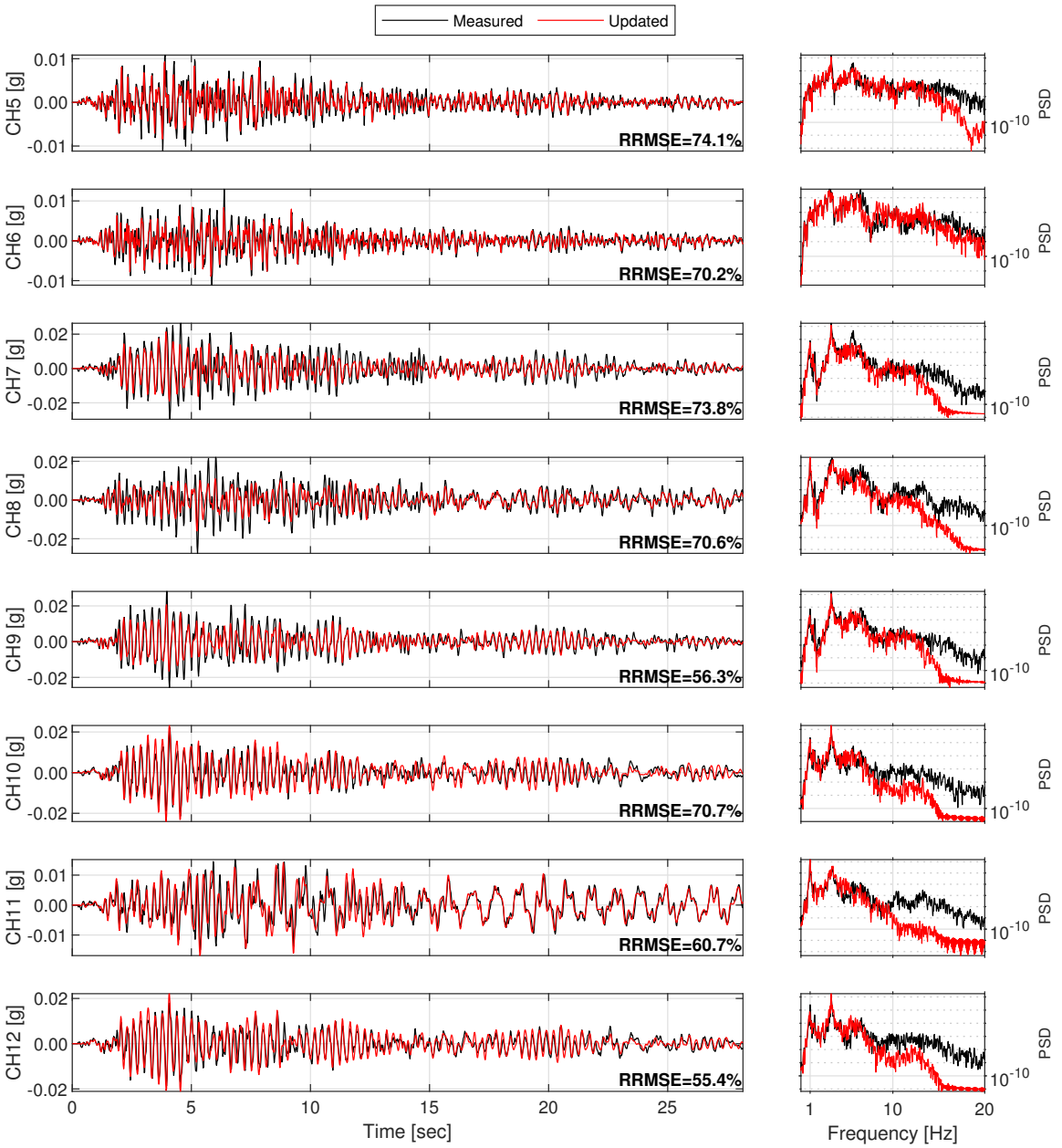

Figure D.25: Structural response comparison for seismic event #26.

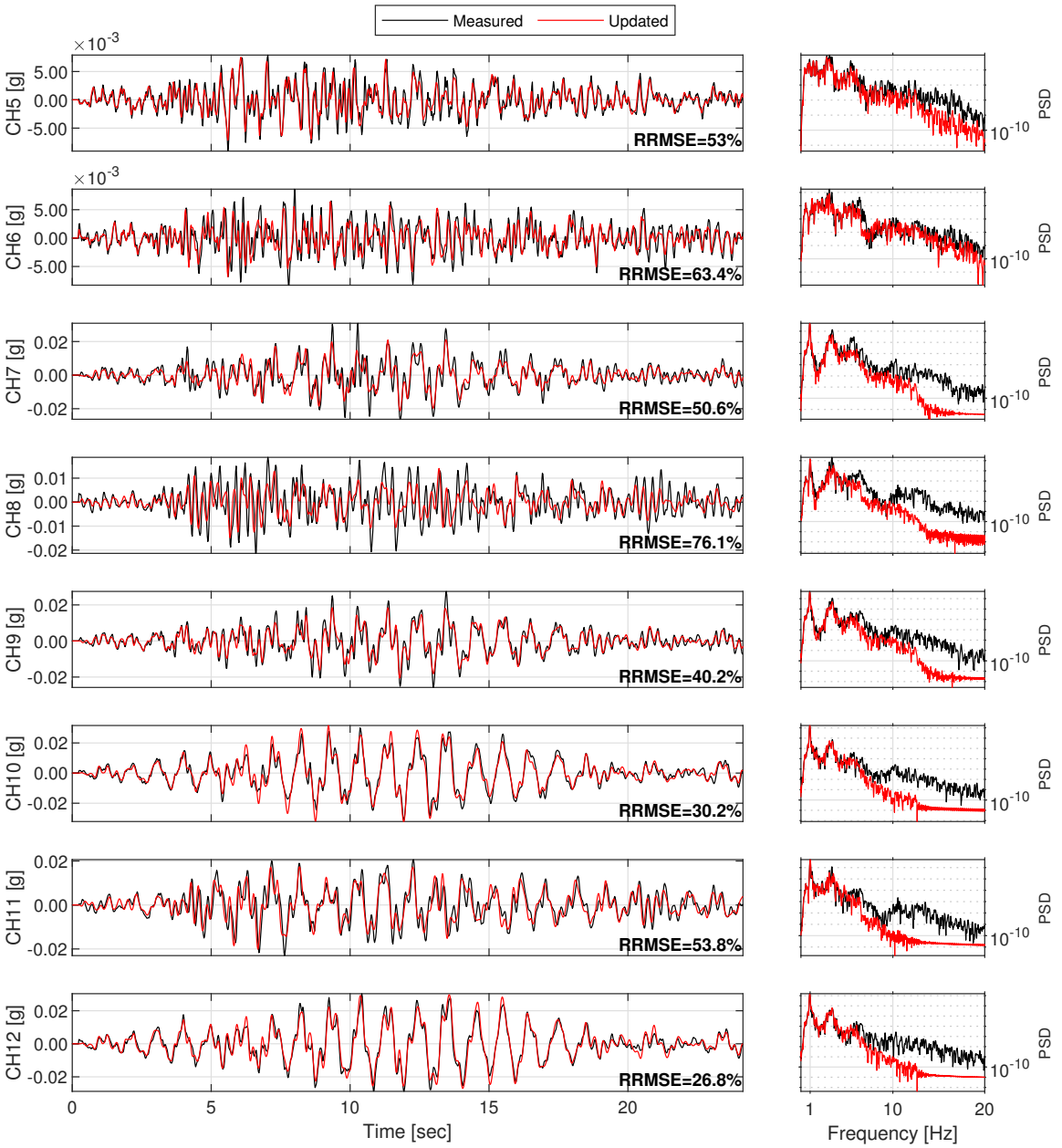

Figure D.26: Structural response comparison for seismic event #27.

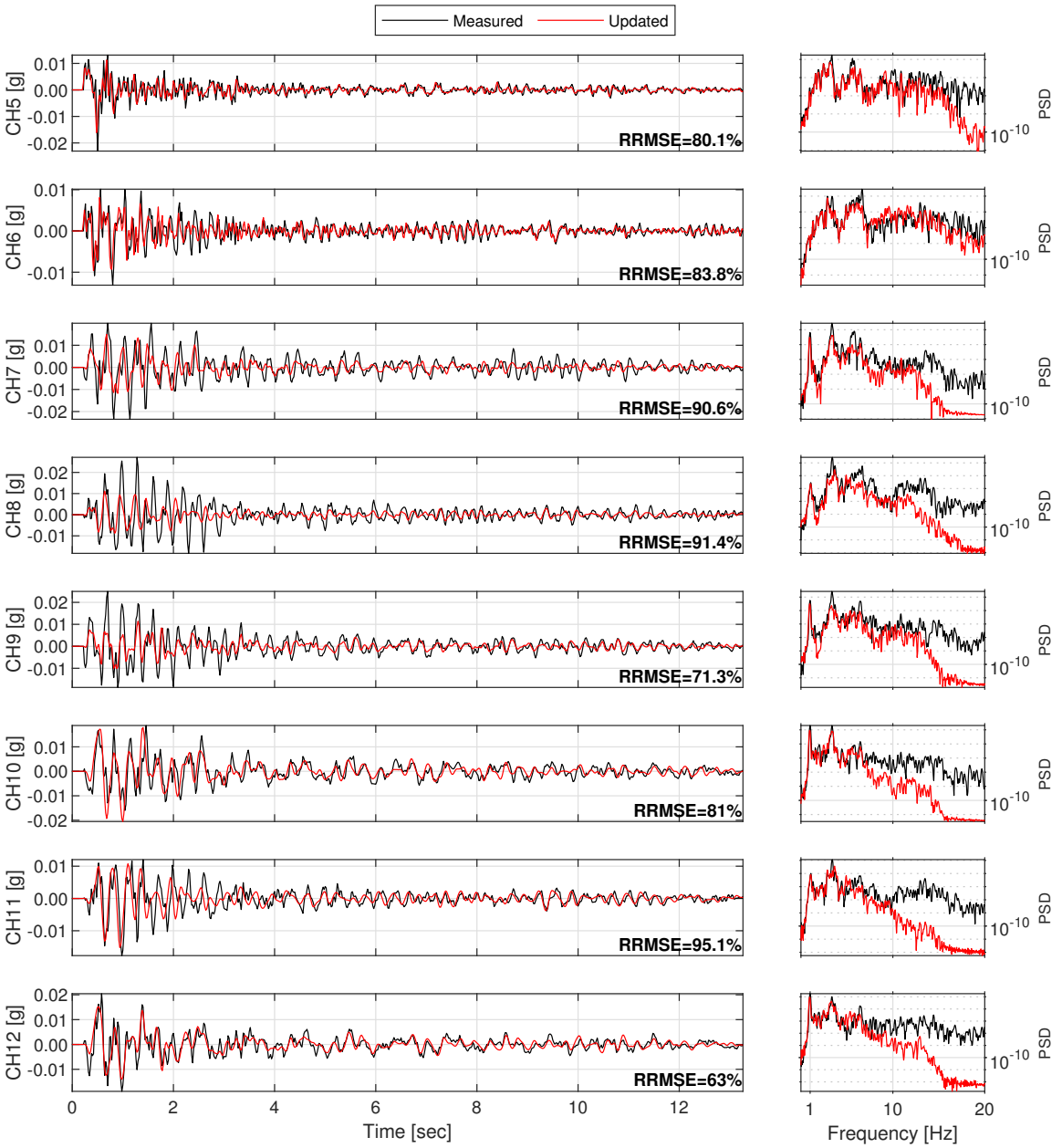

Figure D.27: Structural response comparison for seismic event #28.

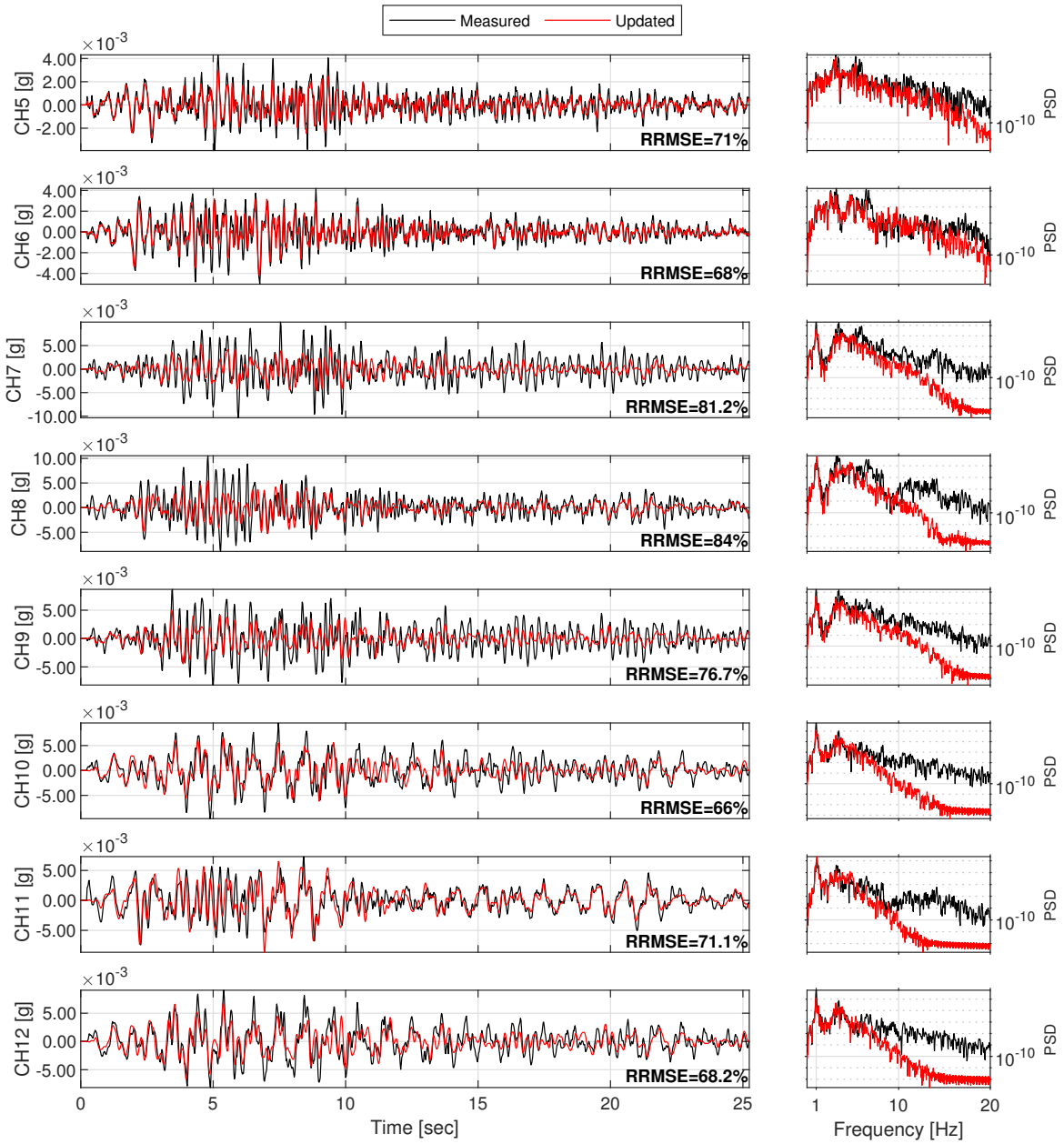

Figure D.28: Structural response comparison for seismic event #29.

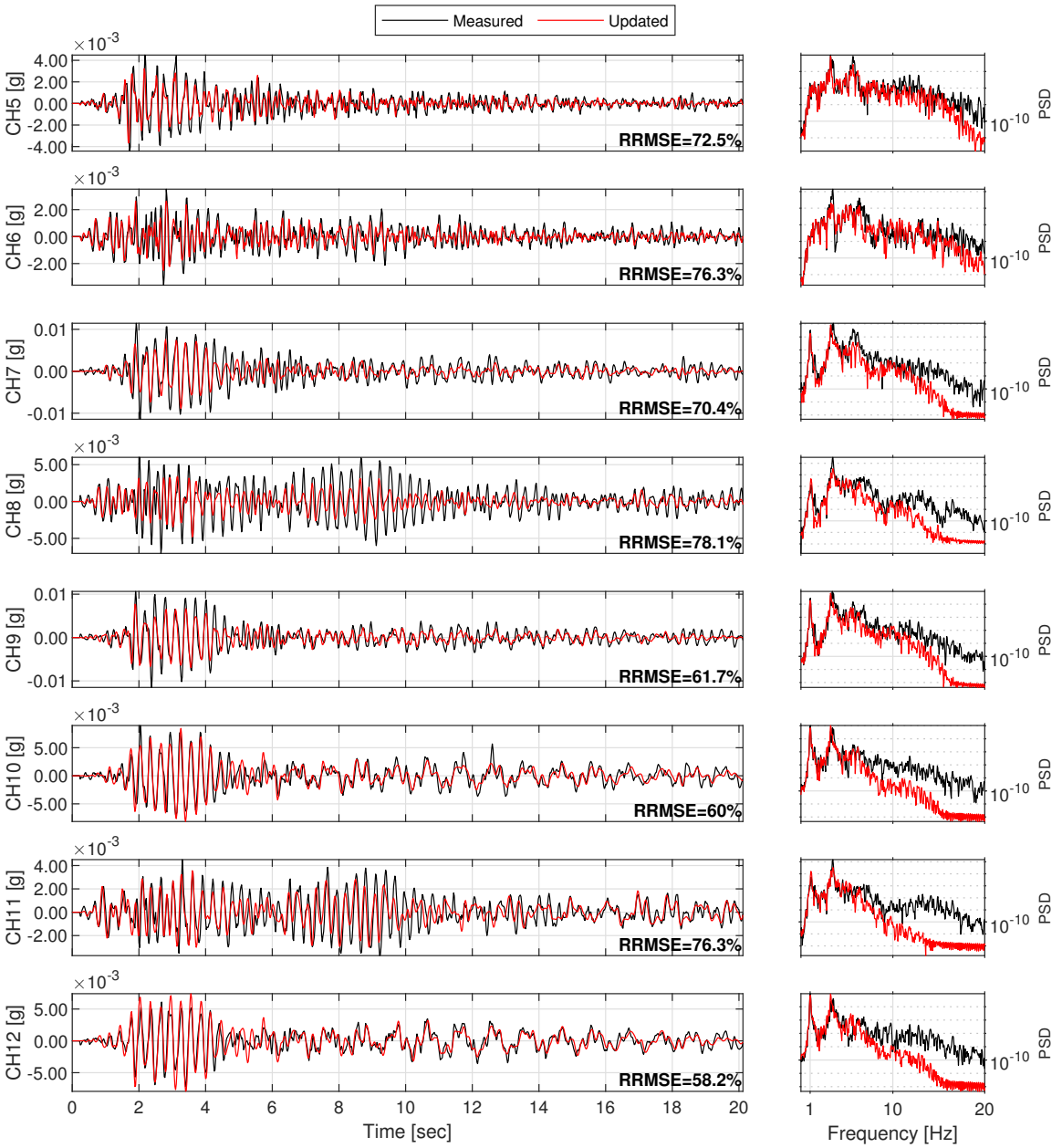

Figure D.29: Structural response comparison for seismic event #30.

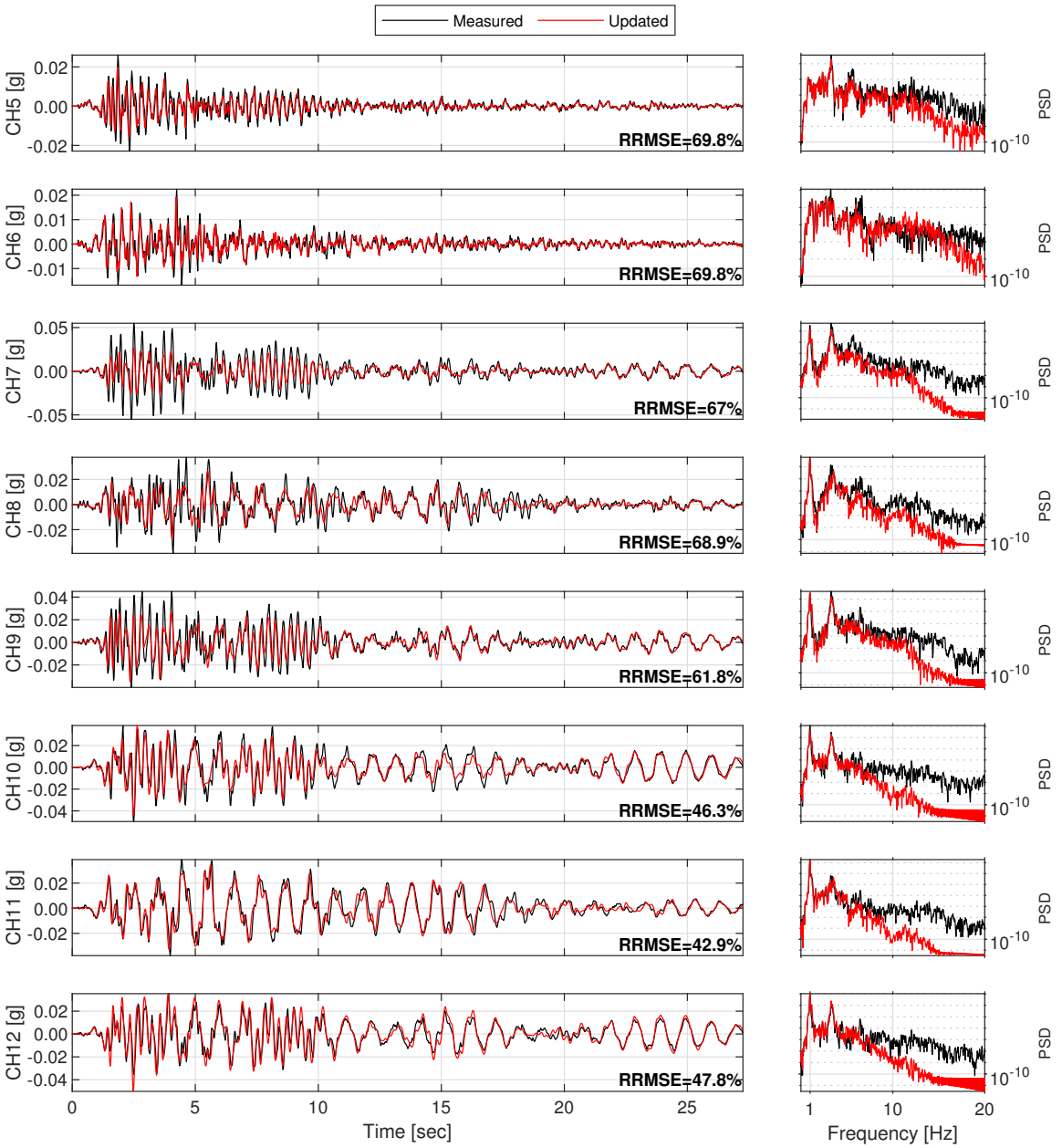

Figure D.30: Structural response comparison for seismic event #31.

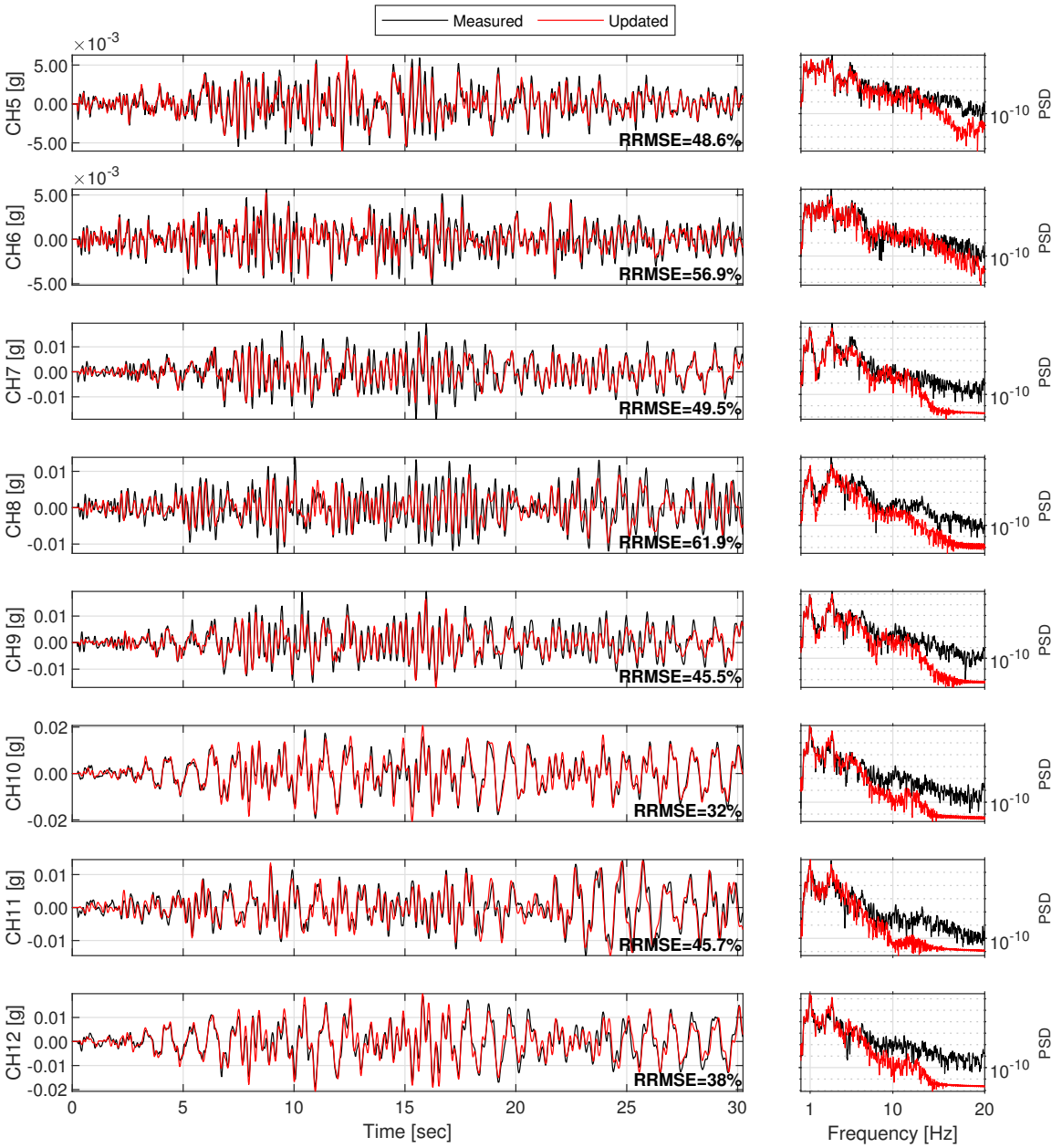

Figure D.31: Structural response comparison for seismic event #32.

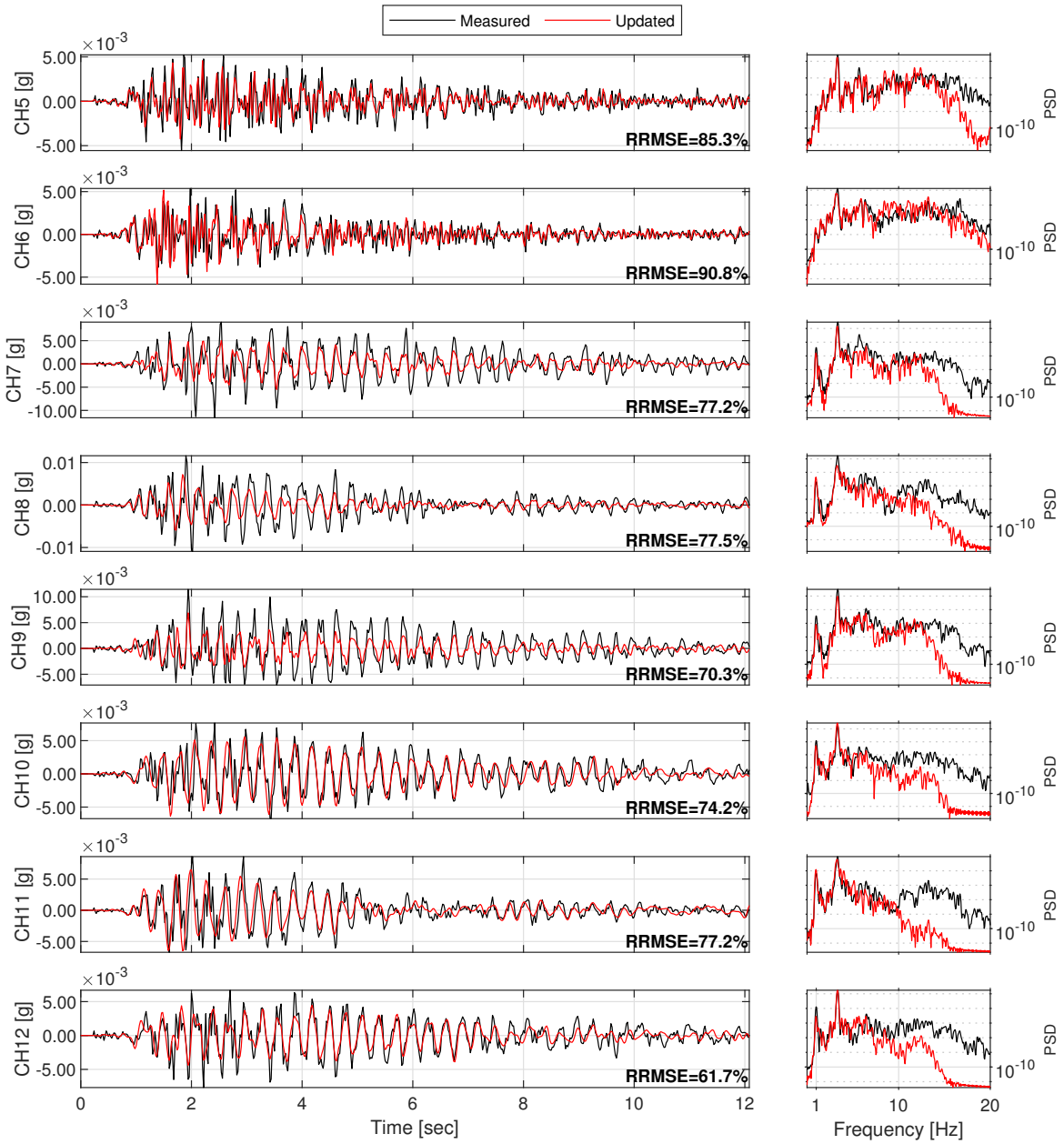

Figure D.32: Structural response comparison for seismic event #33.

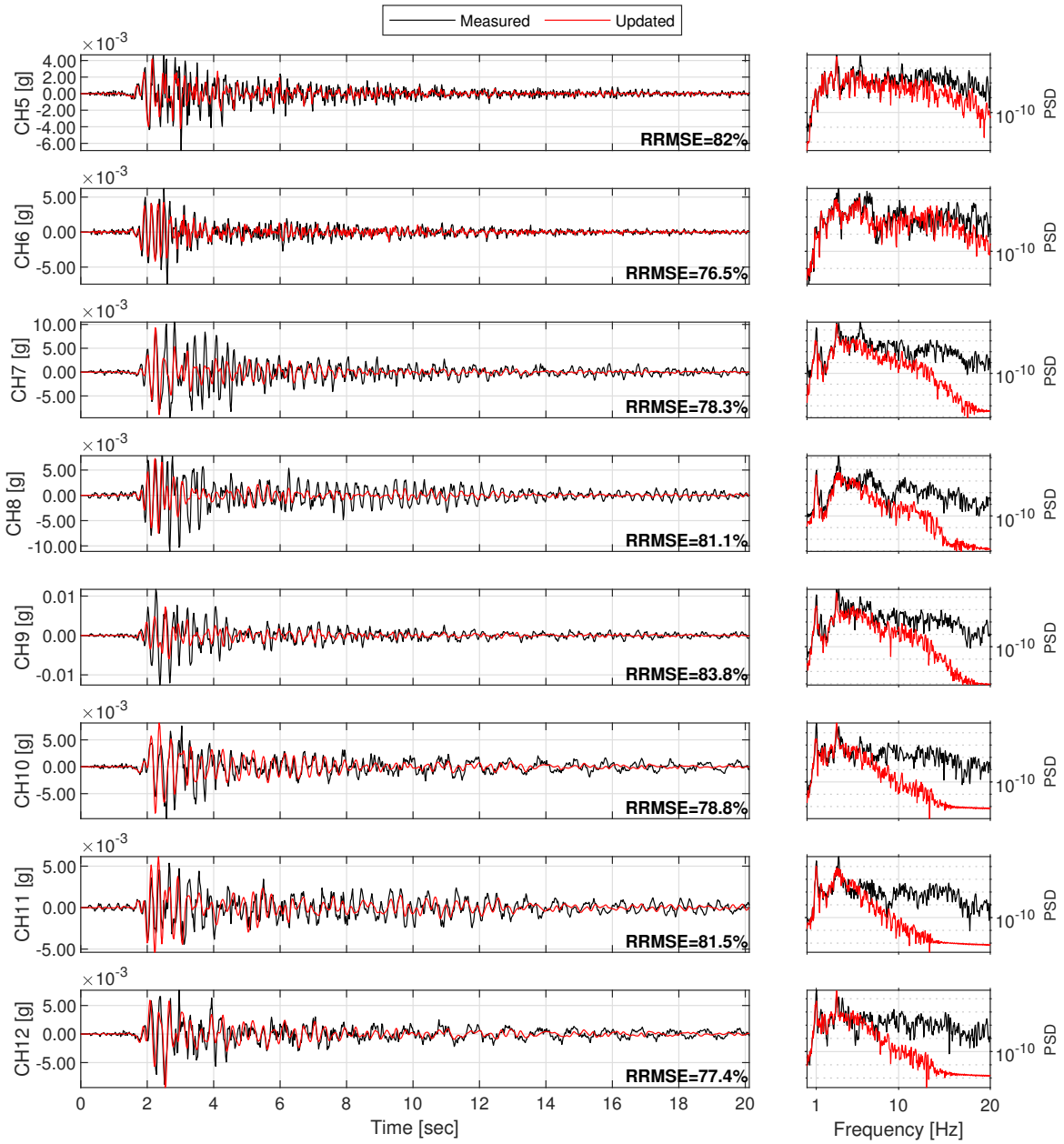

Figure D.33: Structural response comparison for seismic event #34.

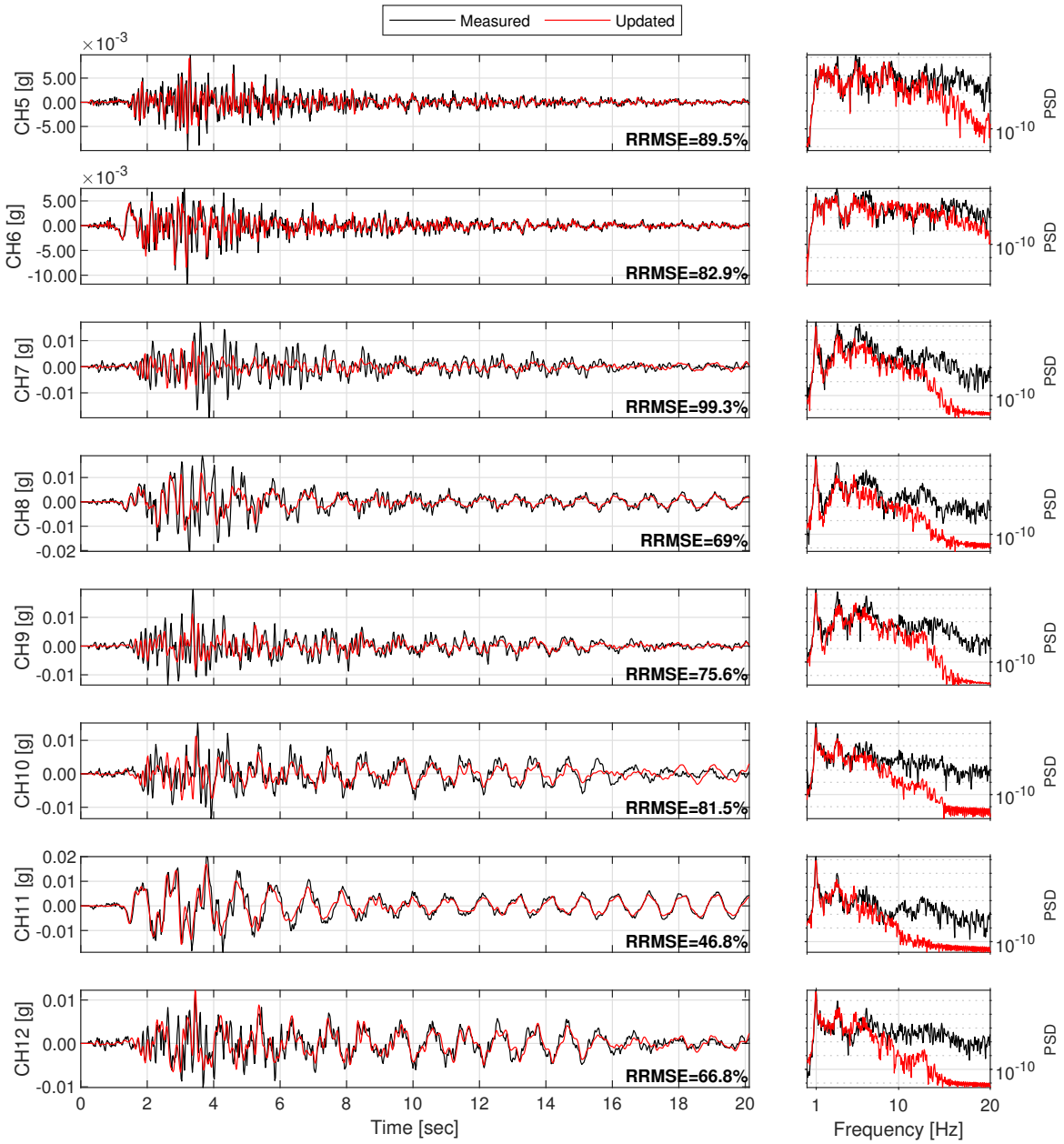

Figure D.34: Structural response comparison for seismic event #35.

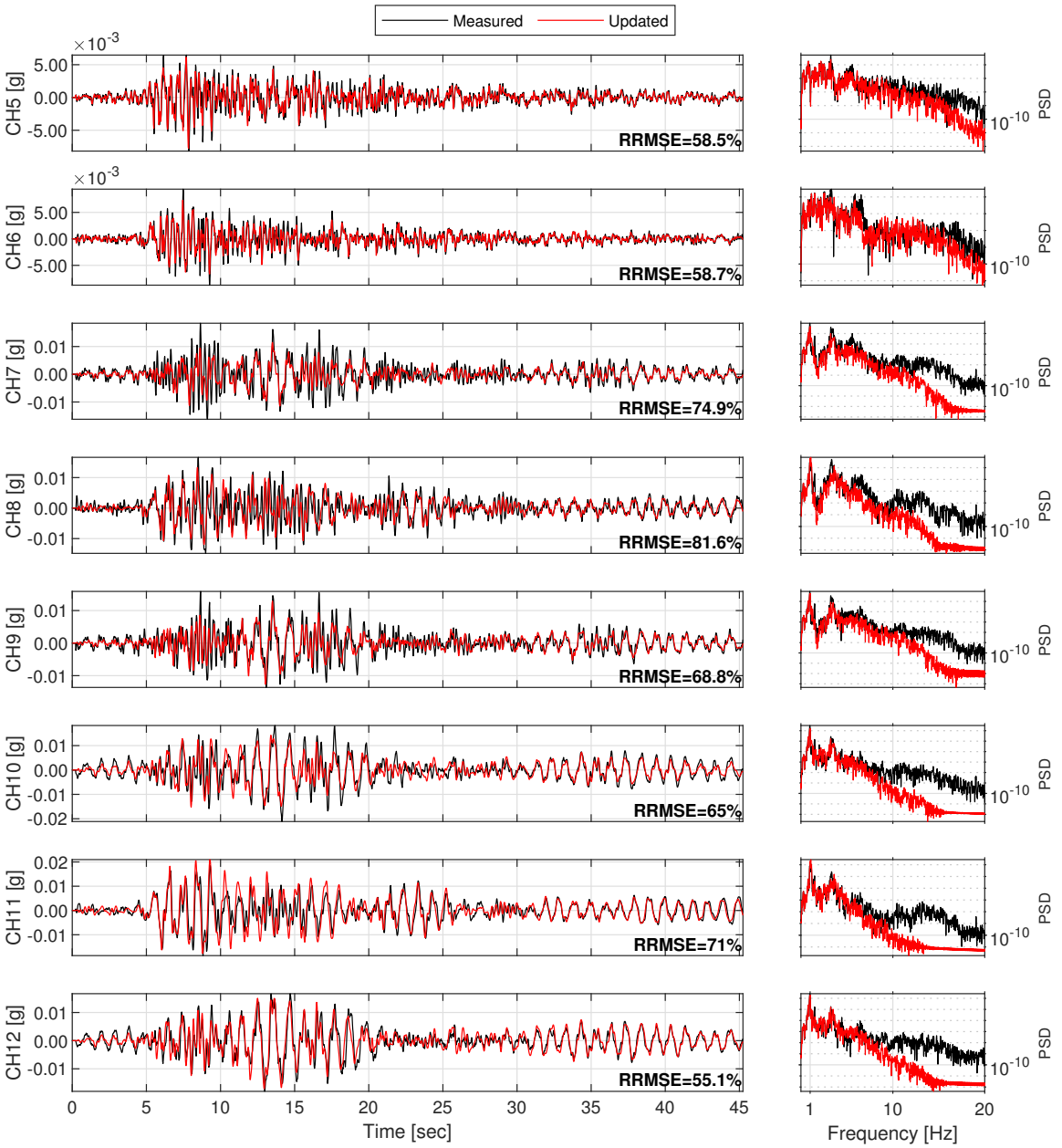

Figure D.35: Structural response comparison for seismic event #36.

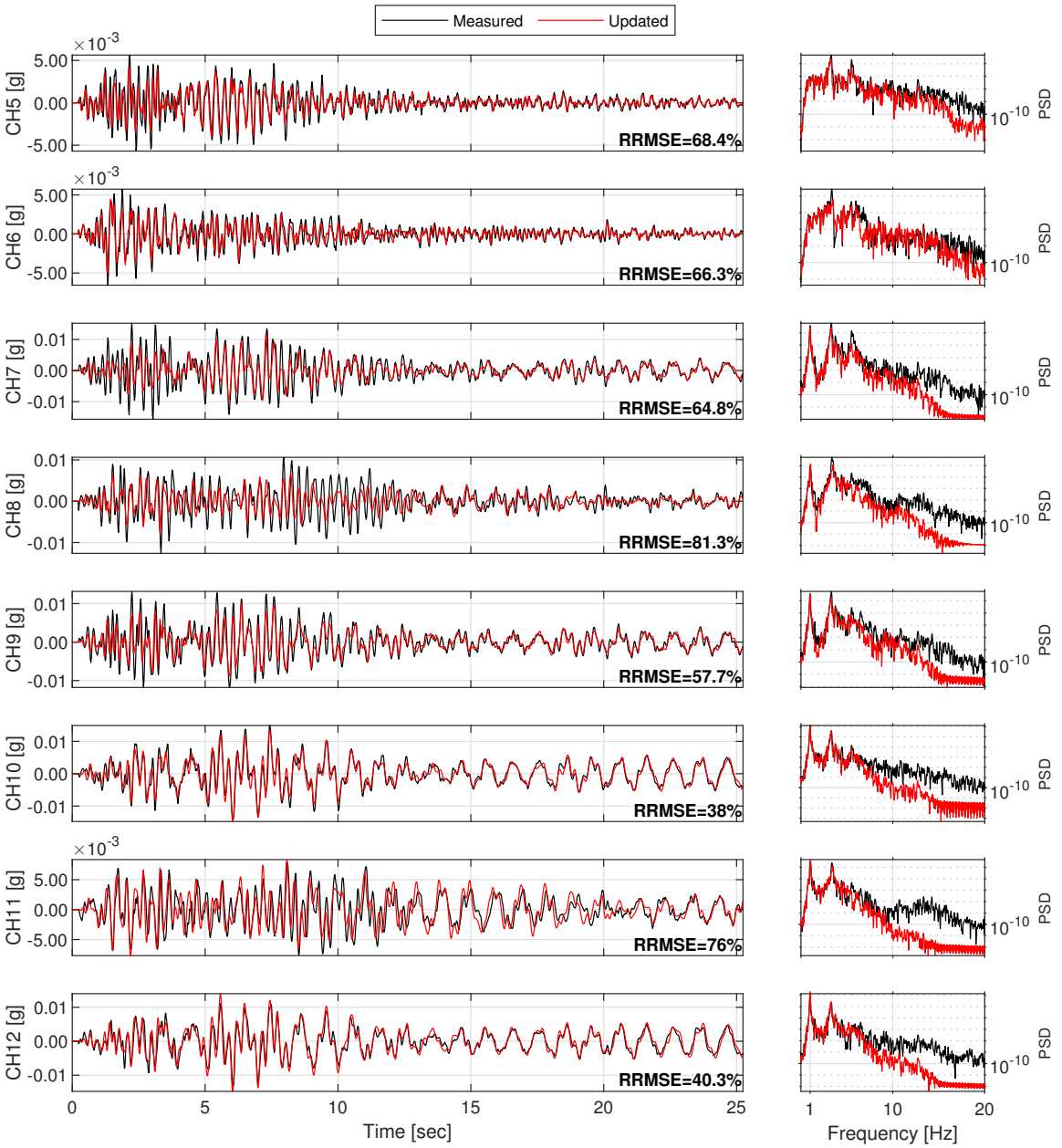

Figure D.36: Structural response comparison for seismic event #37.

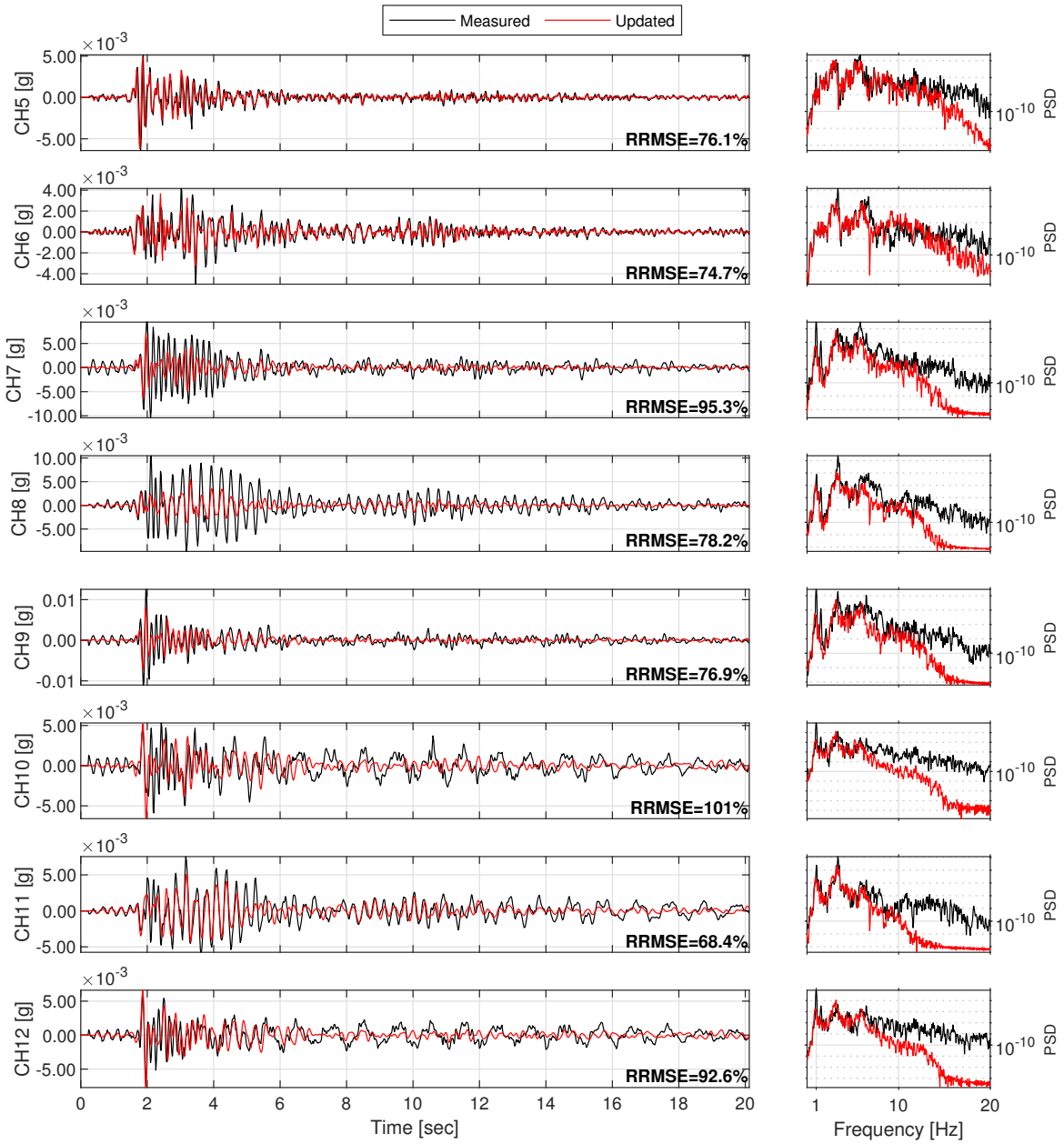

Figure D.37: Structural response comparison for seismic event #38.

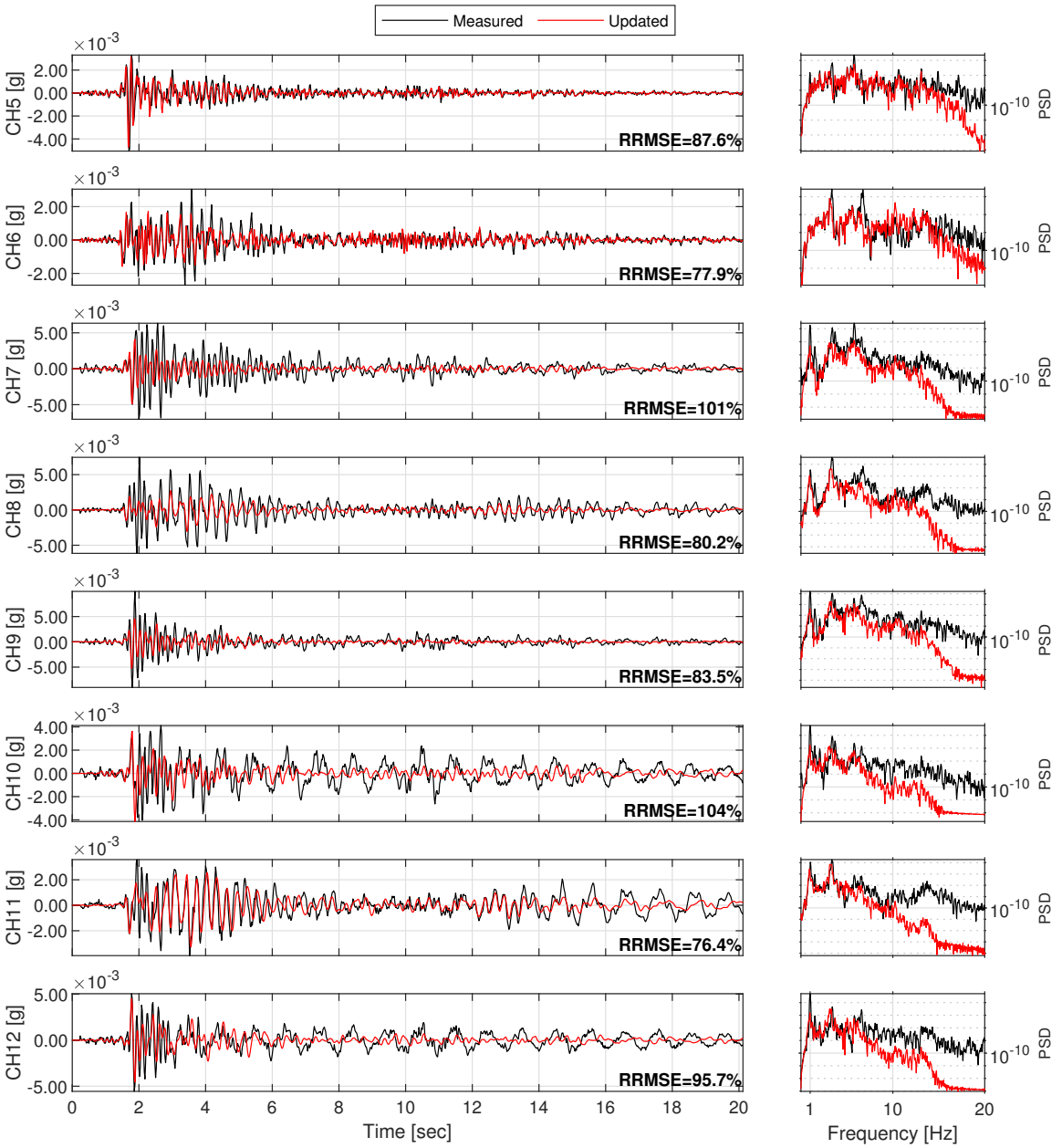

Figure D.38: Structural response comparison for seismic event #39.

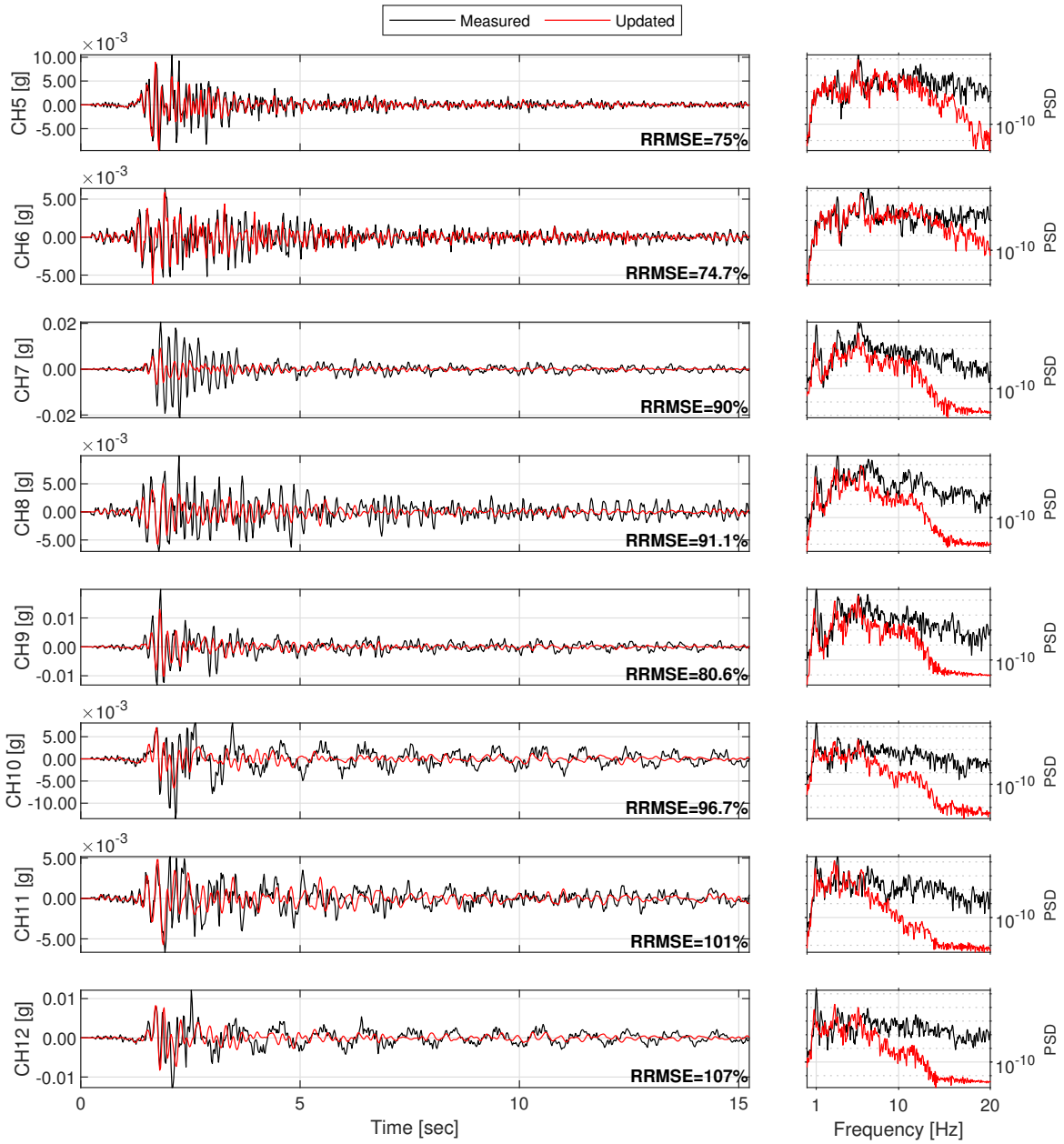

Figure D.39: Structural response comparison for seismic event #40.

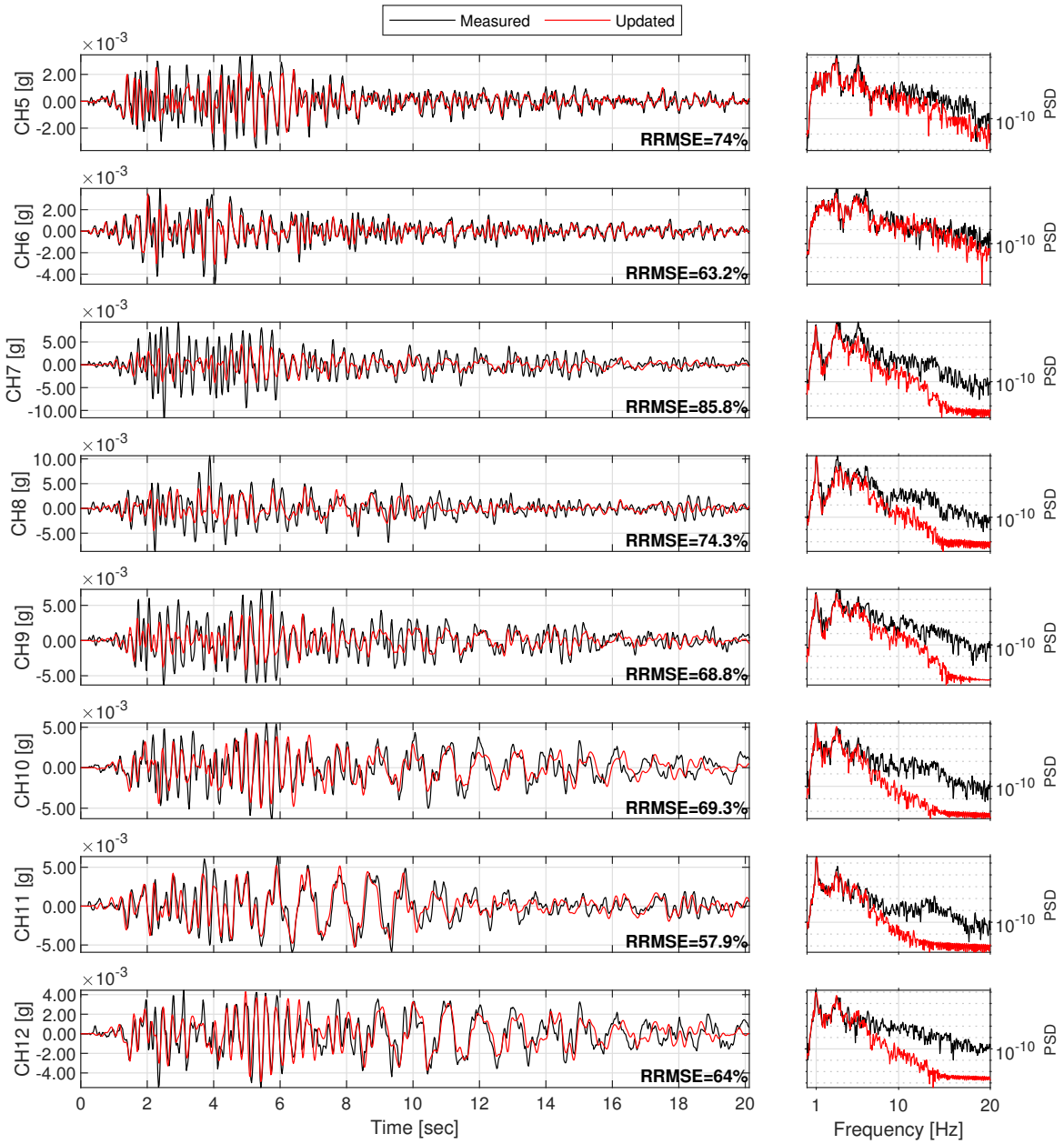

Figure D.40: Structural response comparison for seismic event #41.

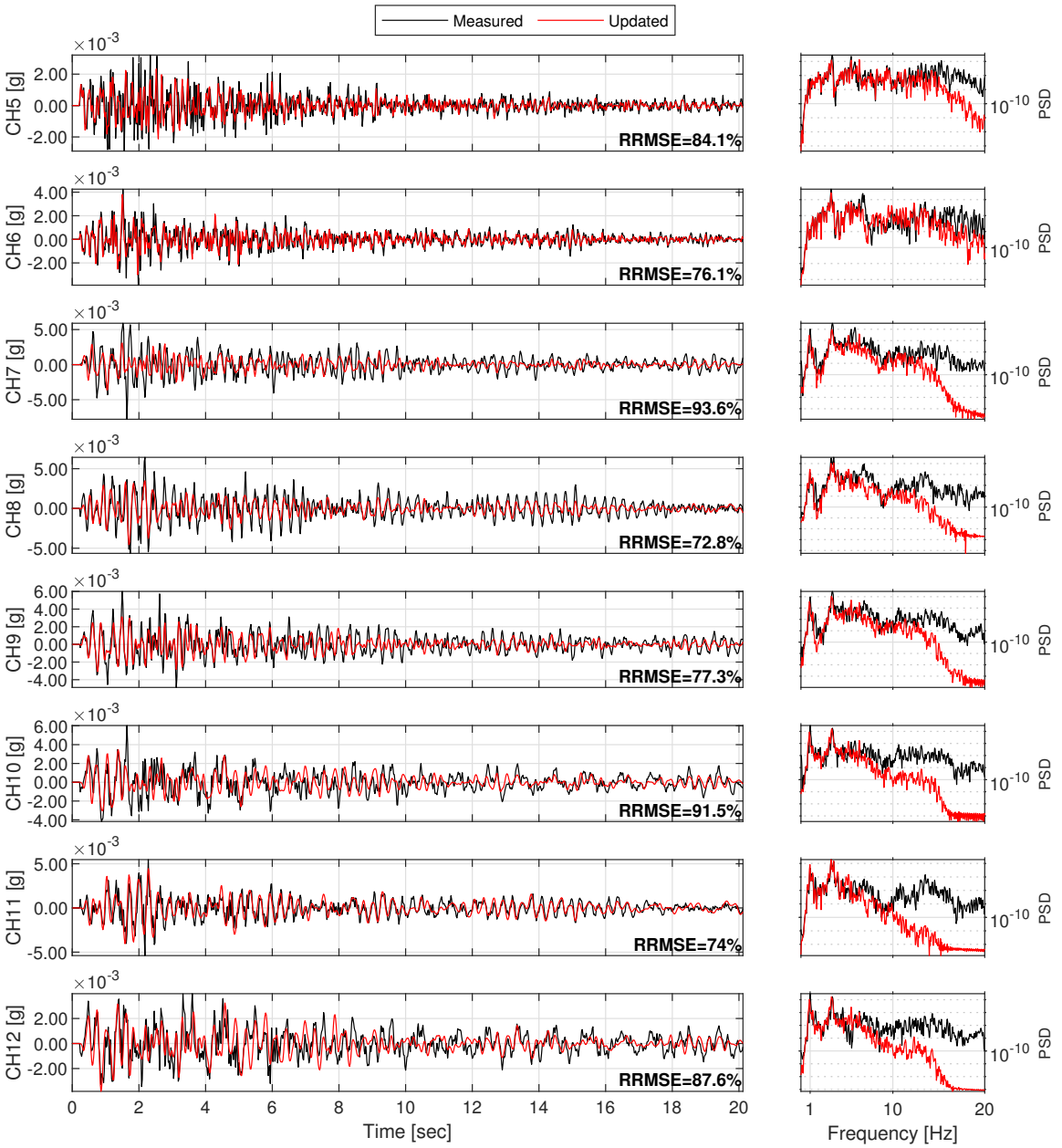

Figure D.41: Structural response comparison for seismic event #42.

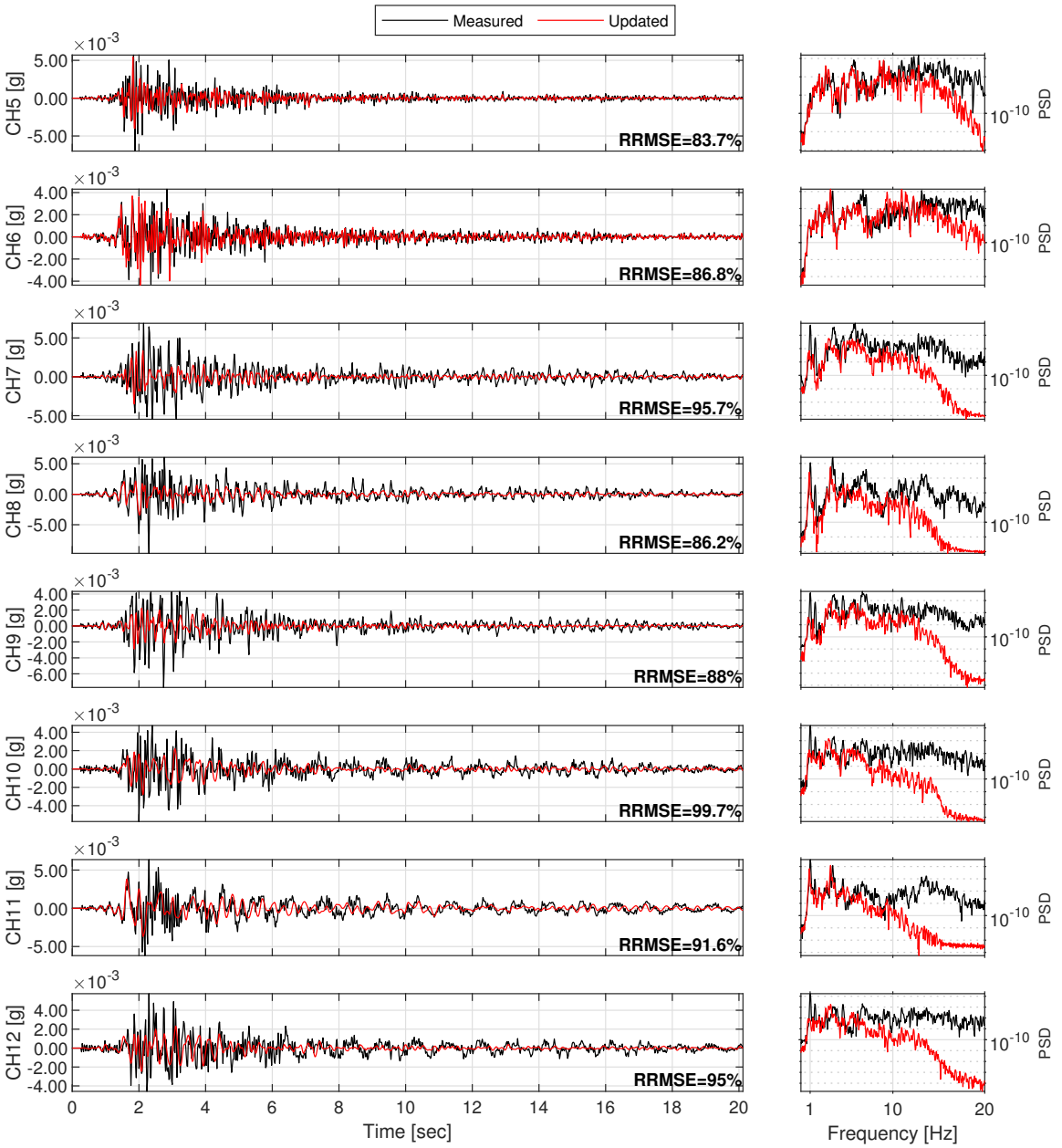

Figure D.42: Structural response comparison for seismic event #43.

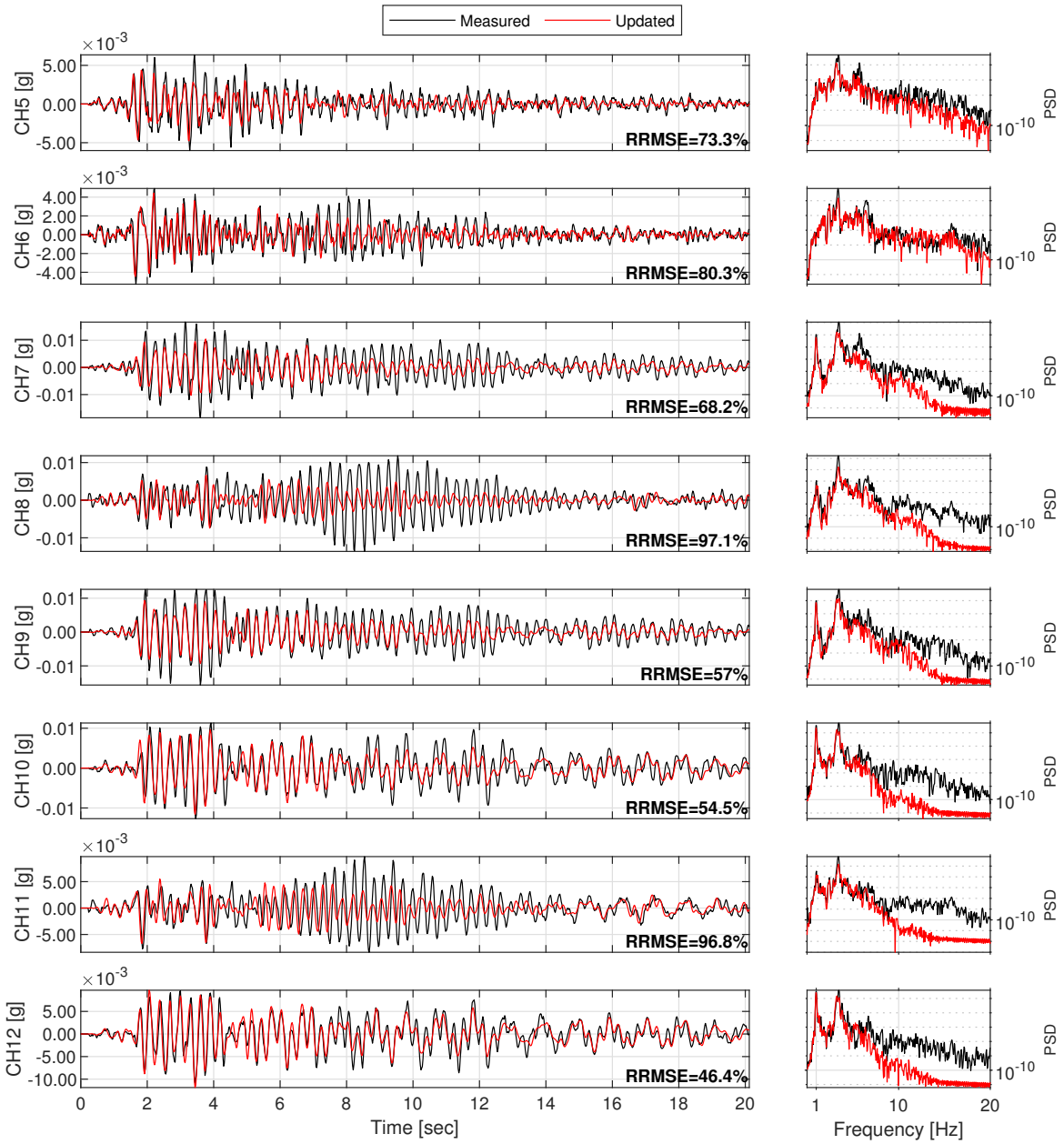

Figure D.43: Structural response comparison for seismic event #44.

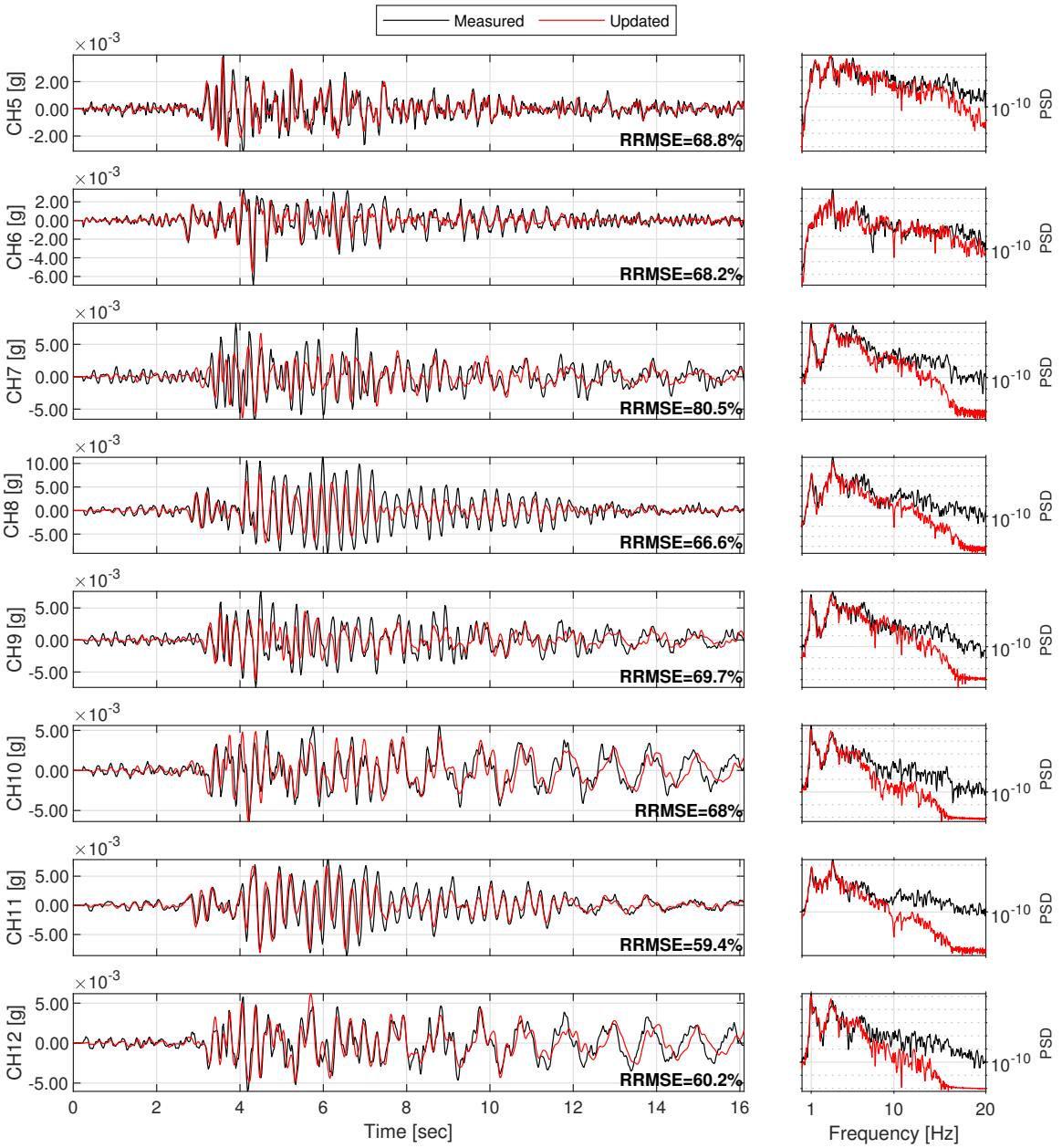

Figure D.44: Structural response comparison for seismic event #45.

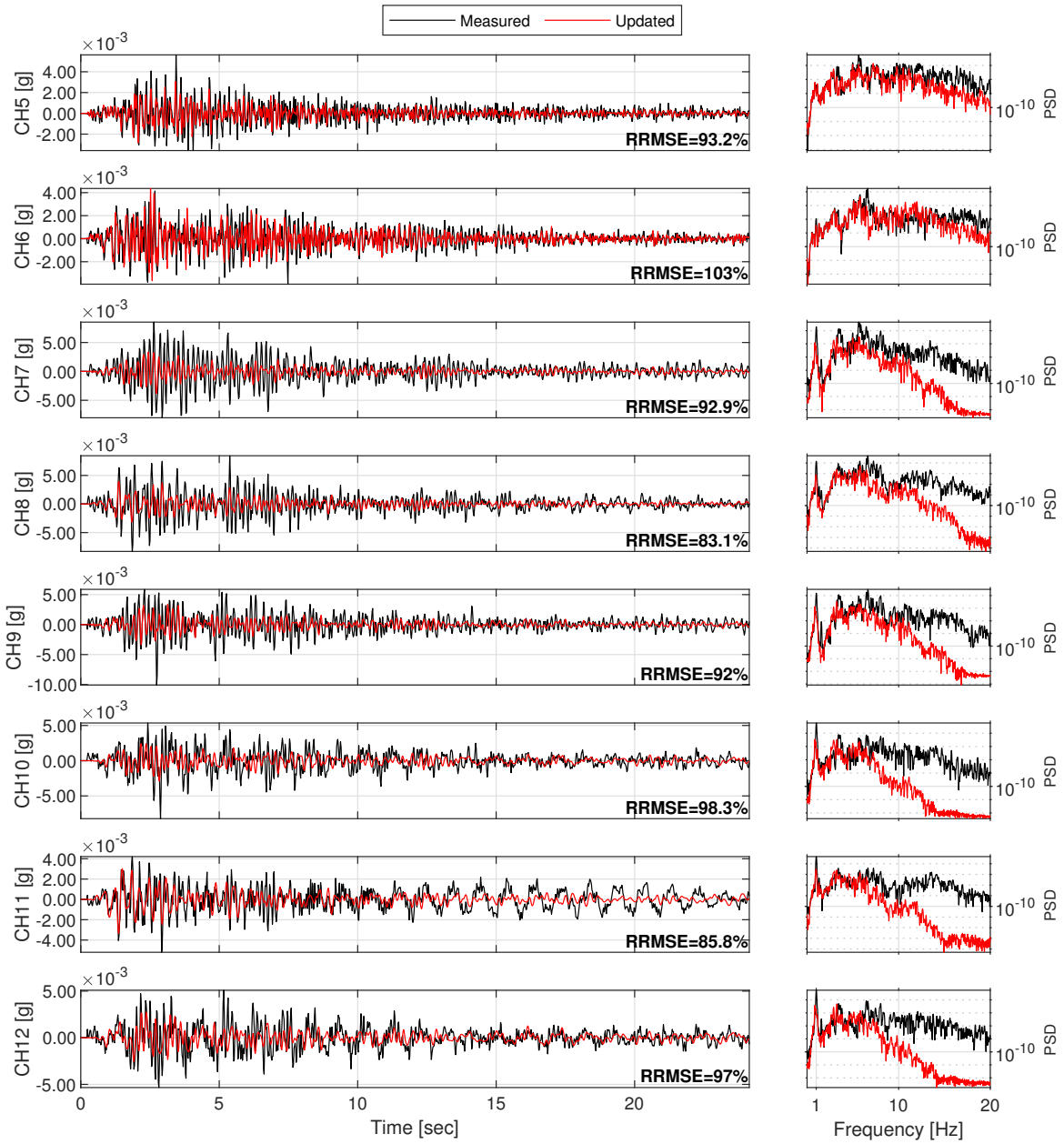

Figure D.45: Structural response comparison for seismic event #46.

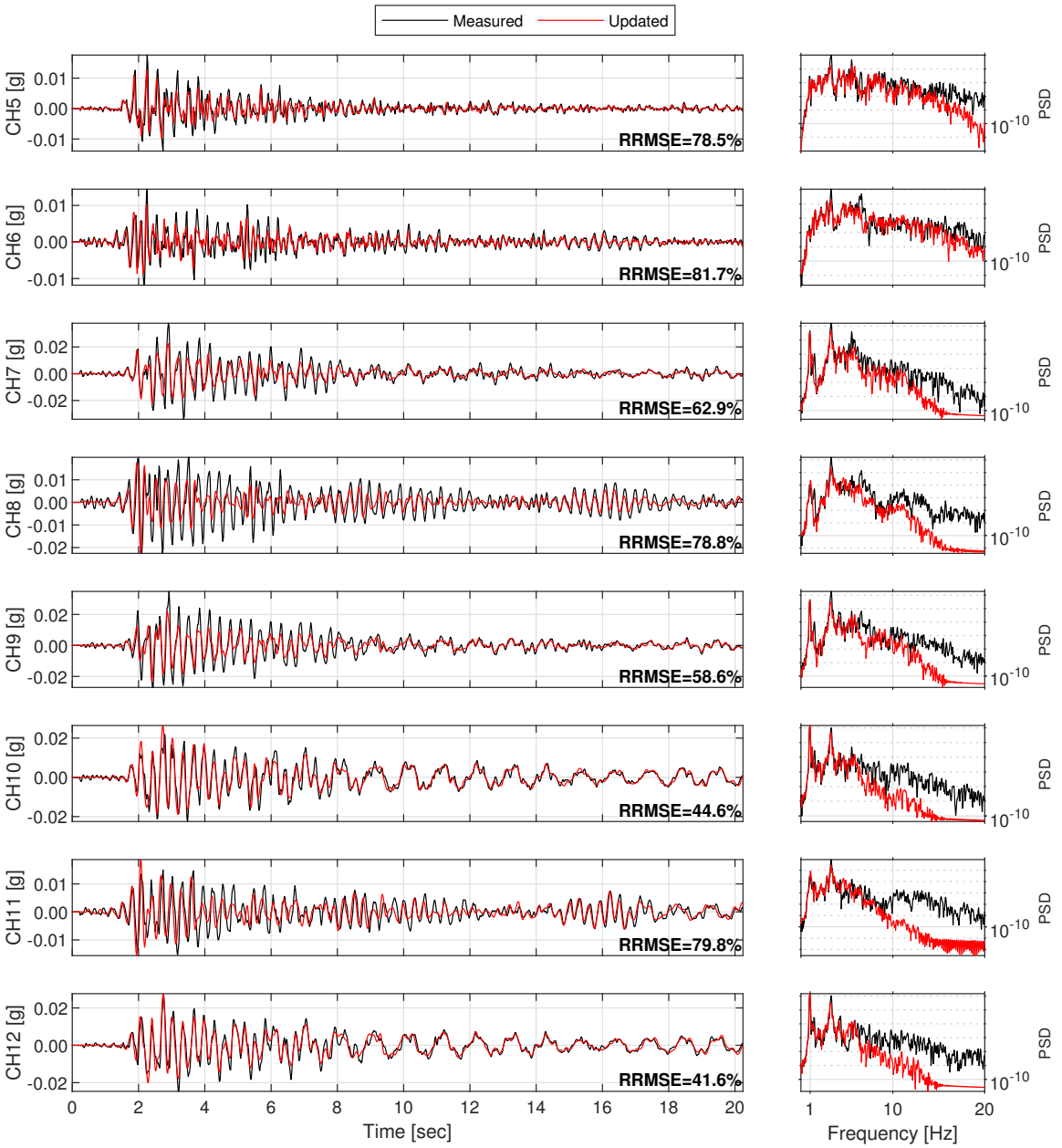

Figure D.46: Structural response comparison for seismic event #47.

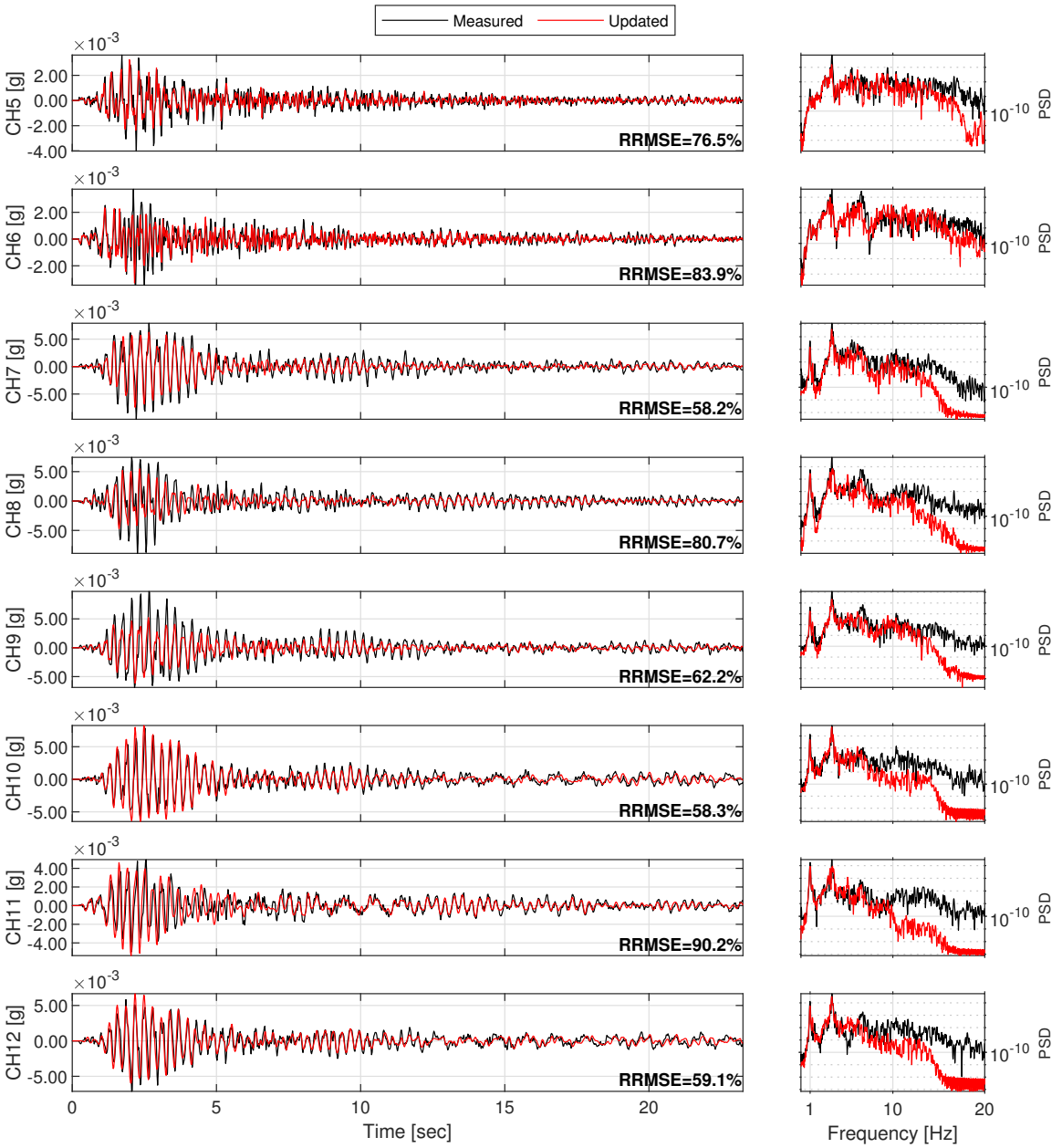

Figure D.47: Structural response comparison for seismic event #48.

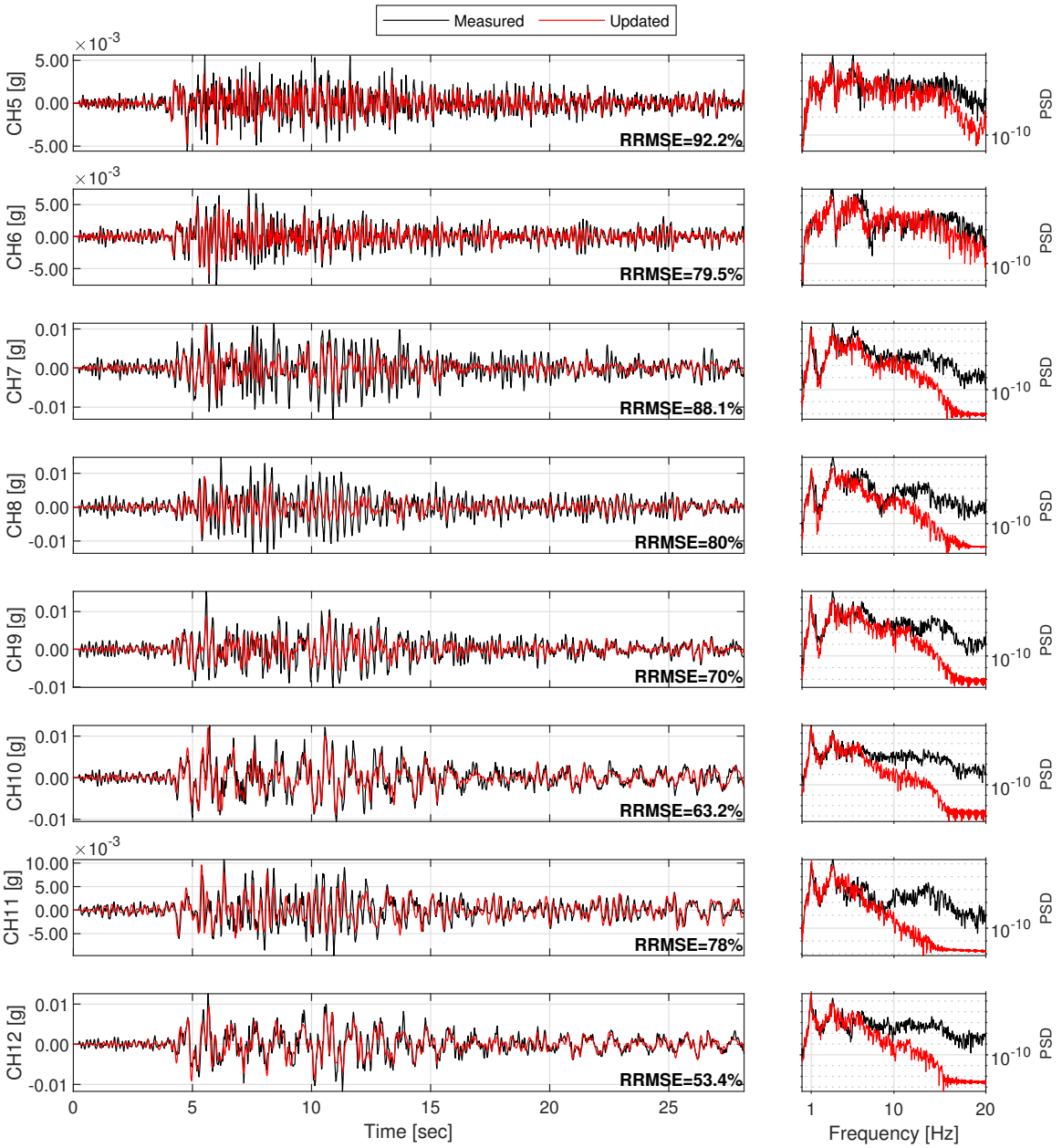

Figure D.48: Structural response comparison for seismic event #49.

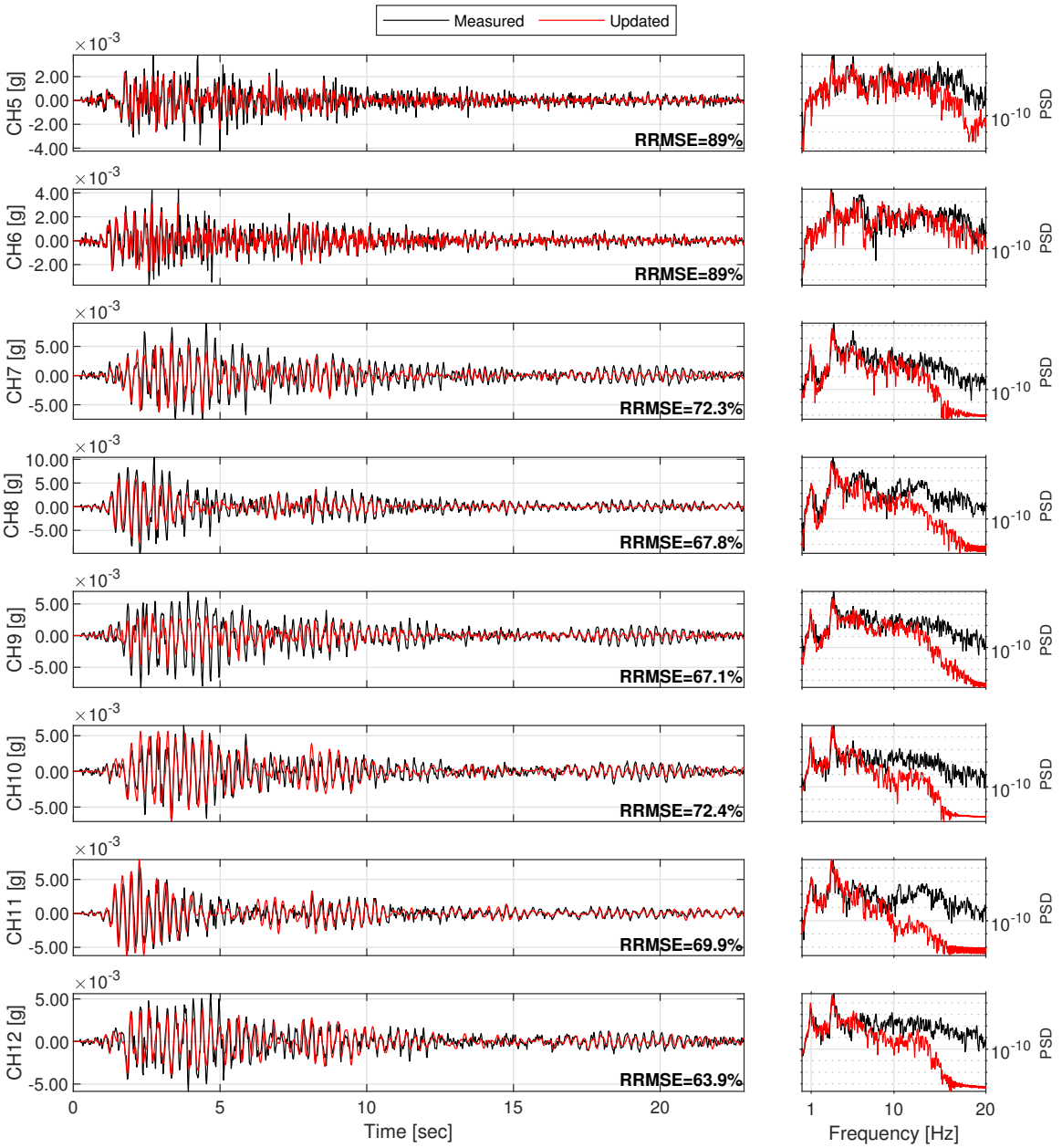

Figure D.49: Structural response comparison for seismic event #50.

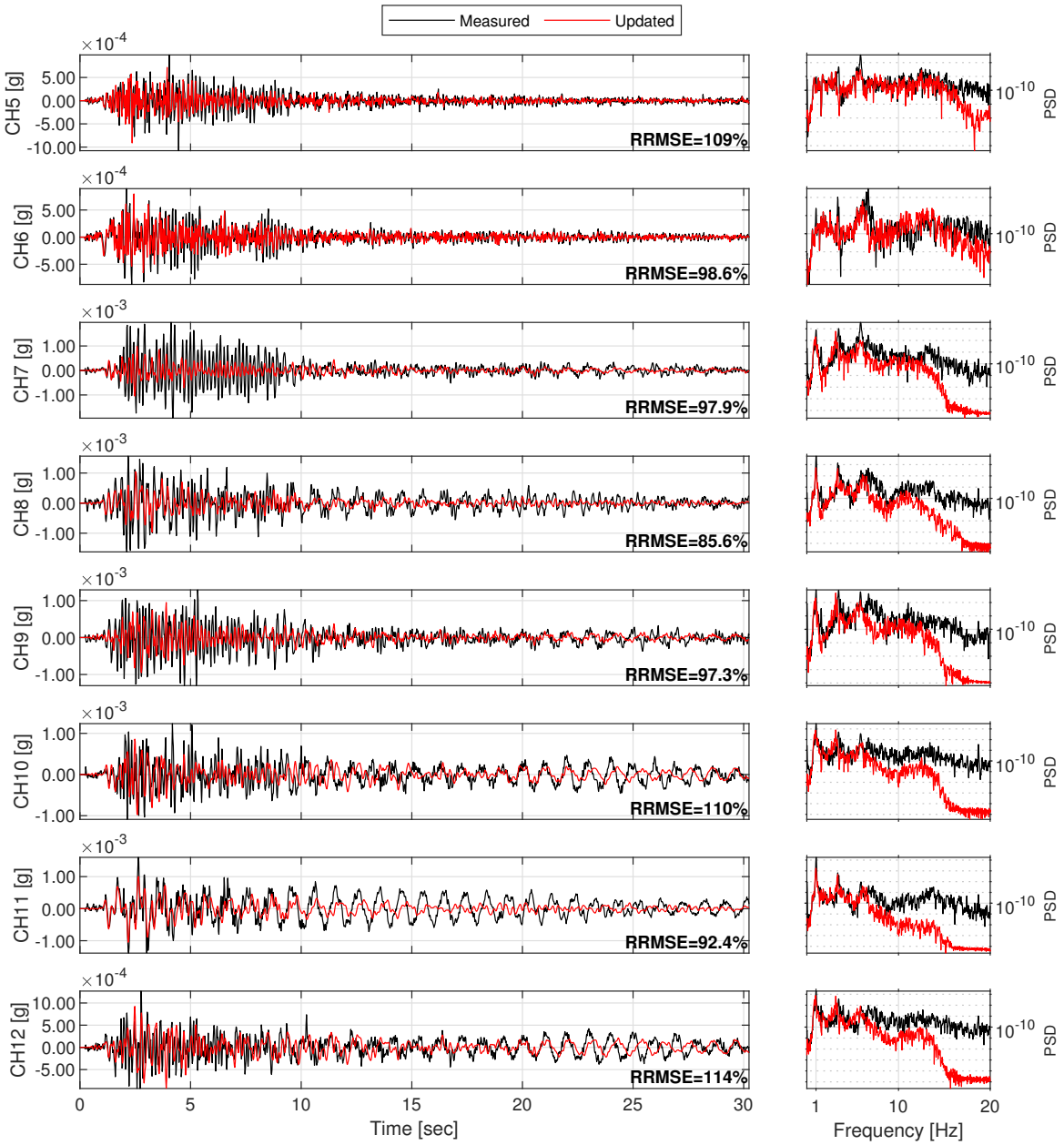

Figure D.50: Structural response comparison for seismic event #51.

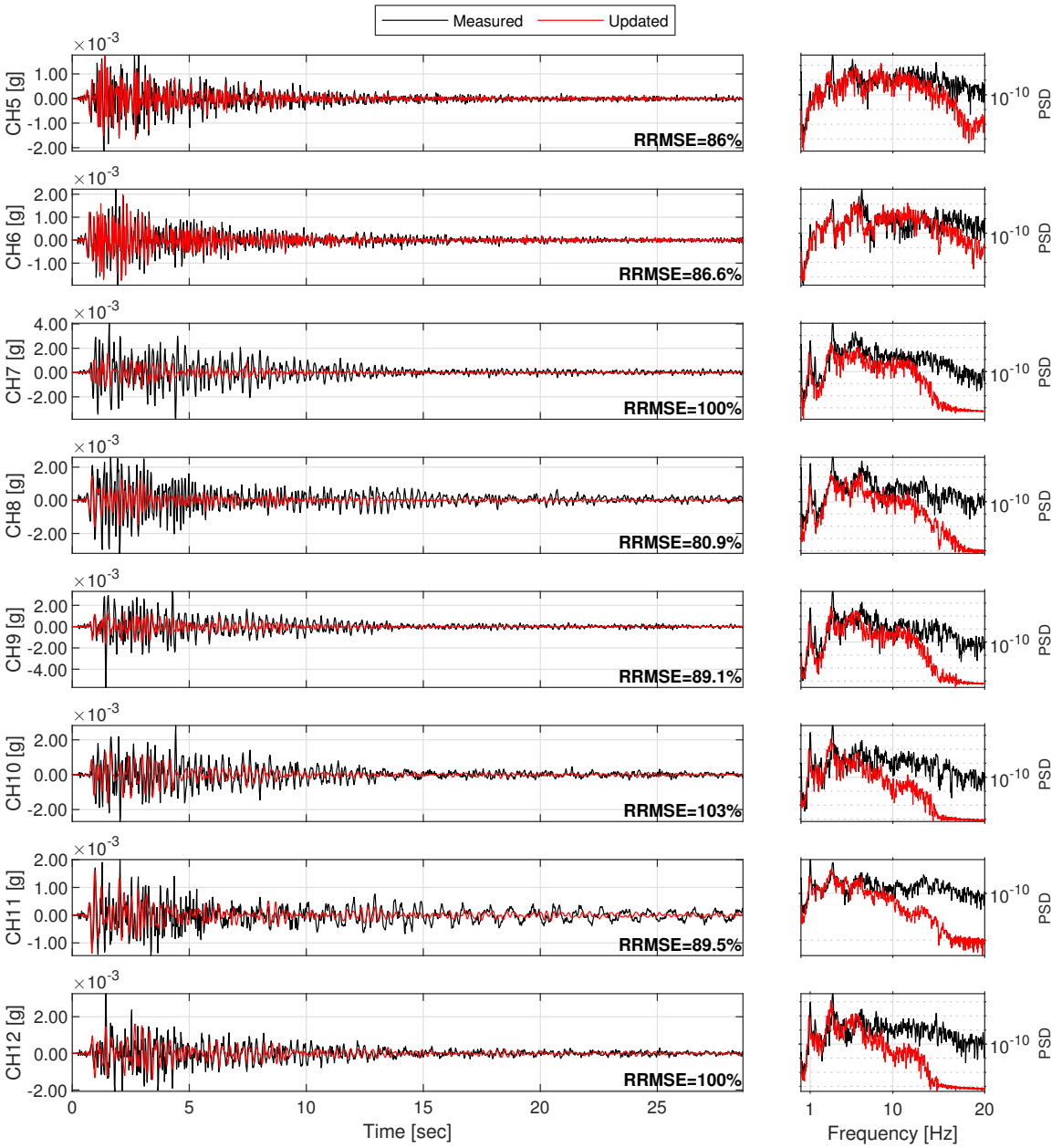

Figure D.51: Structural response comparison for seismic event #52.

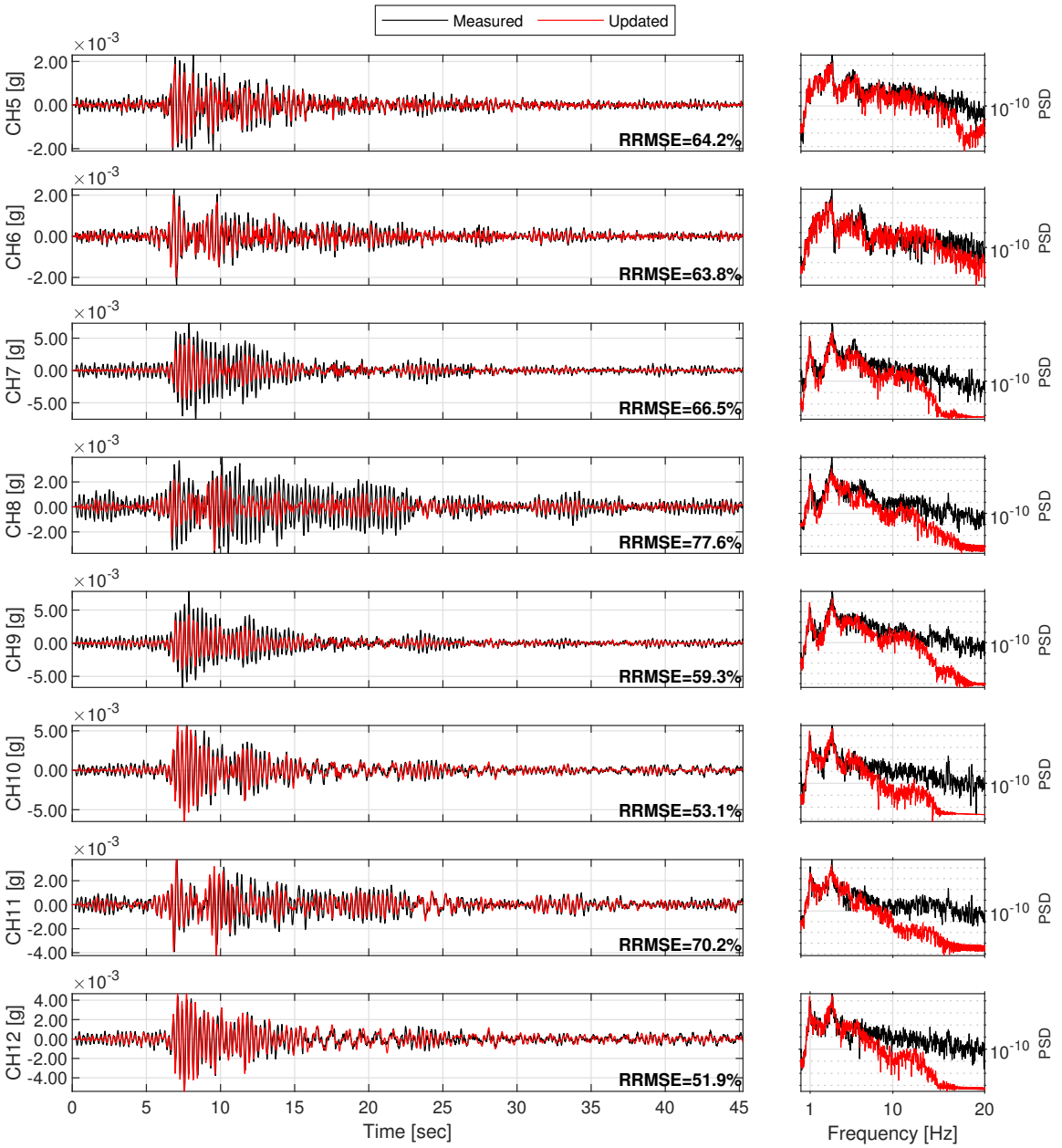

Figure D.52: Structural response comparison for seismic event #53.

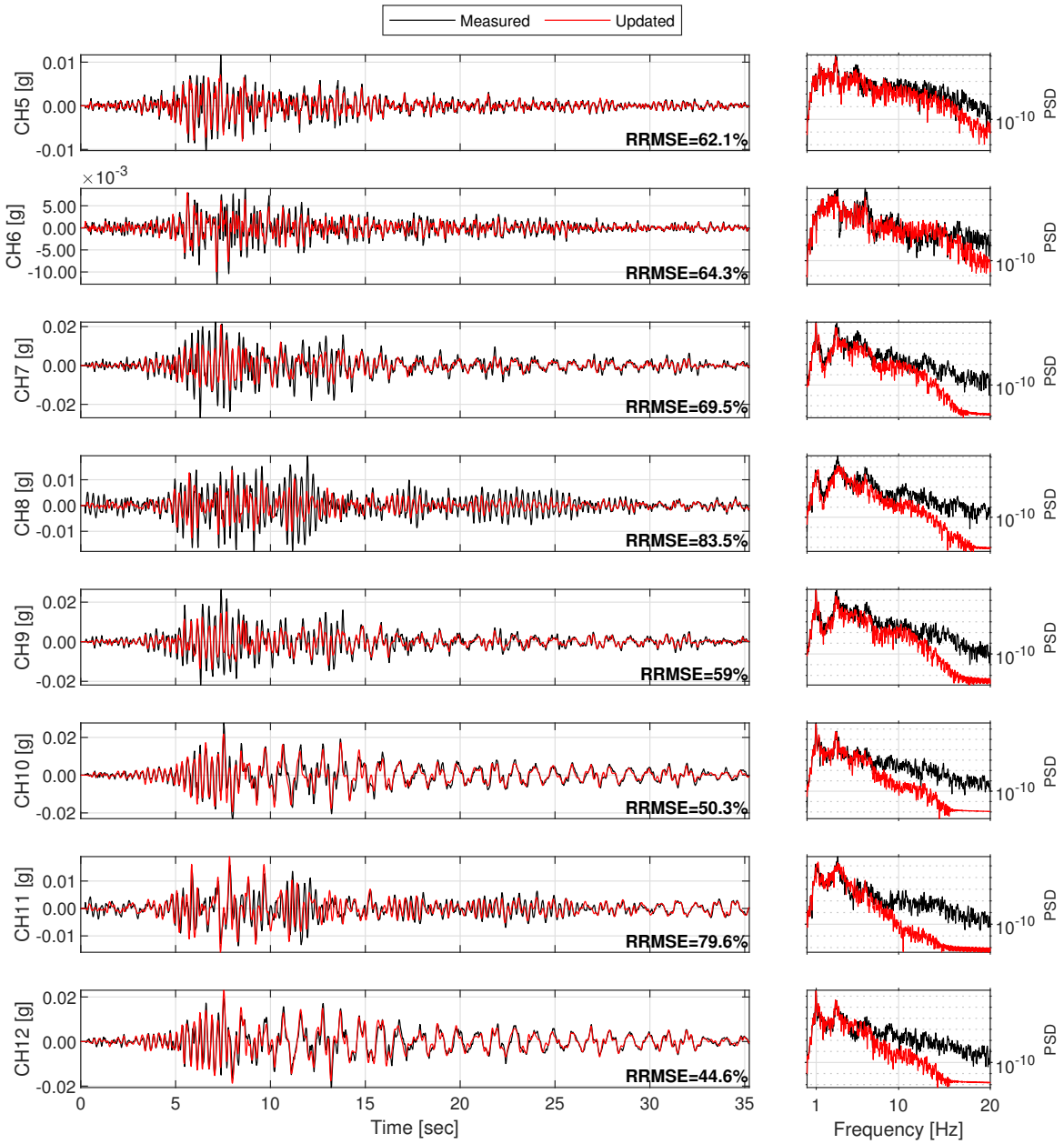

Figure D.53: Structural response comparison for seismic event #54.

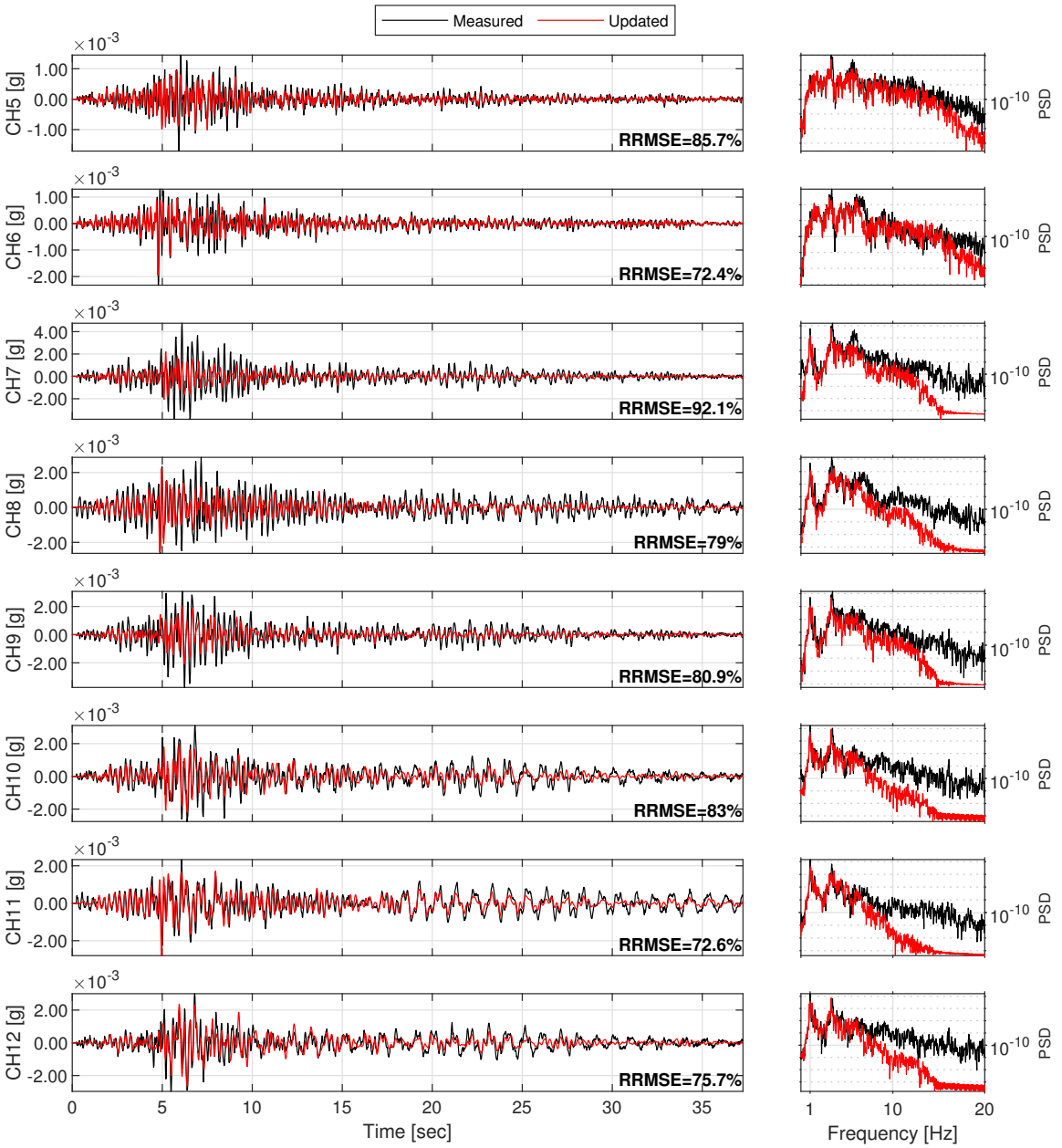

Figure D.54: Structural response comparison for seismic event #55.

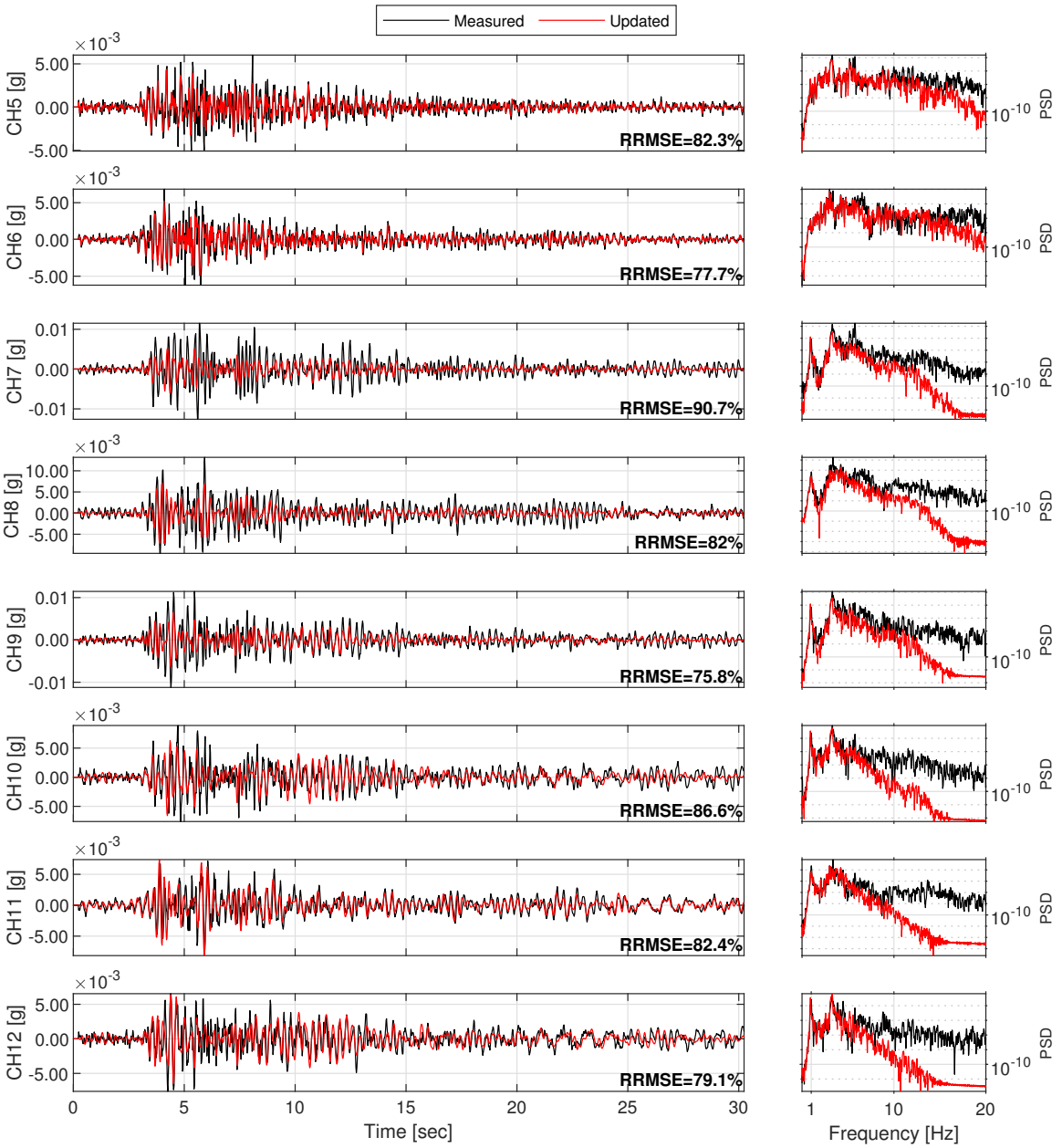

Figure D.55: Structural response comparison for seismic event #56.

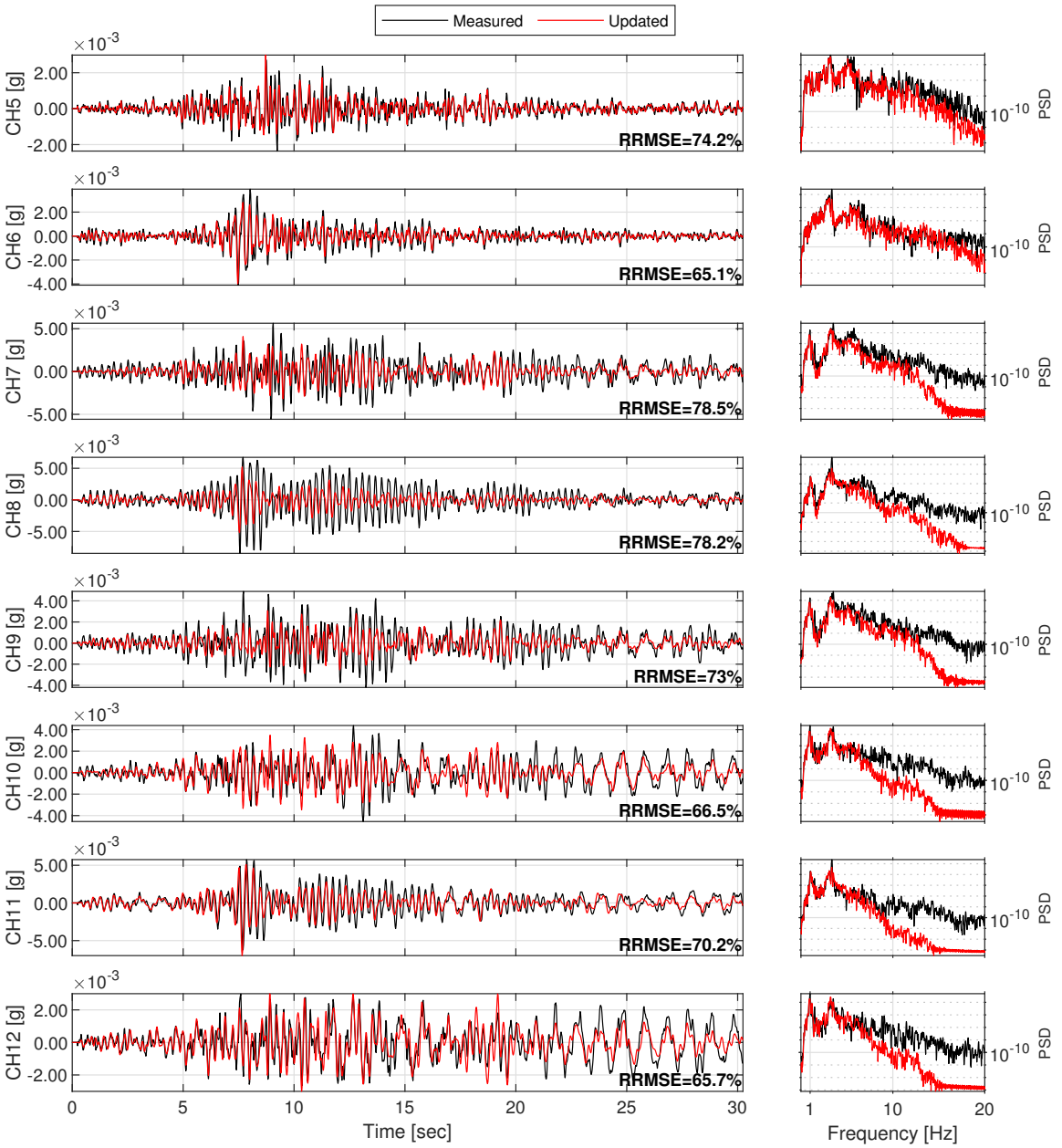

Figure D.56: Structural response comparison for seismic event #57.

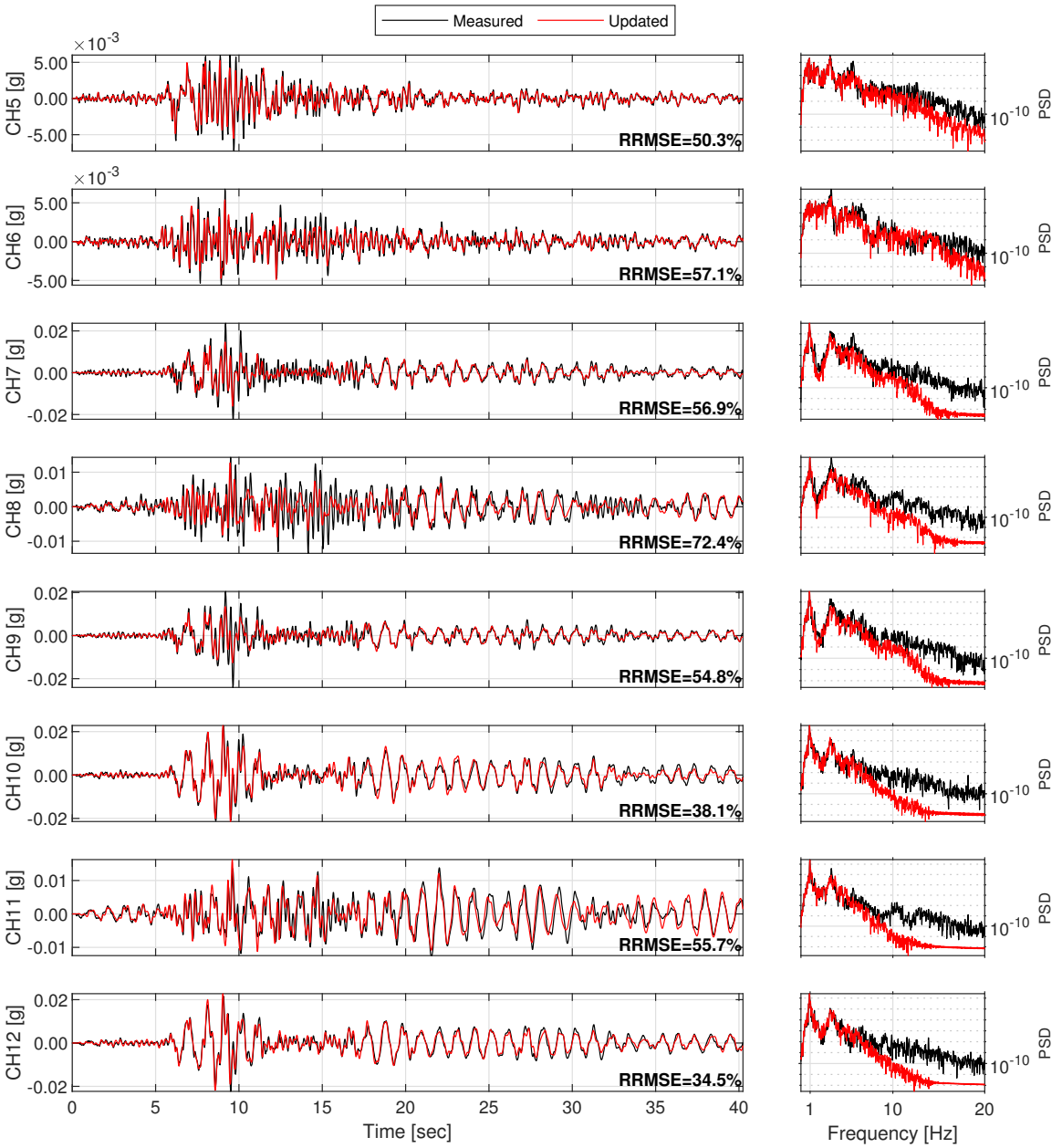

Figure D.57: Structural response comparison for seismic event #58.

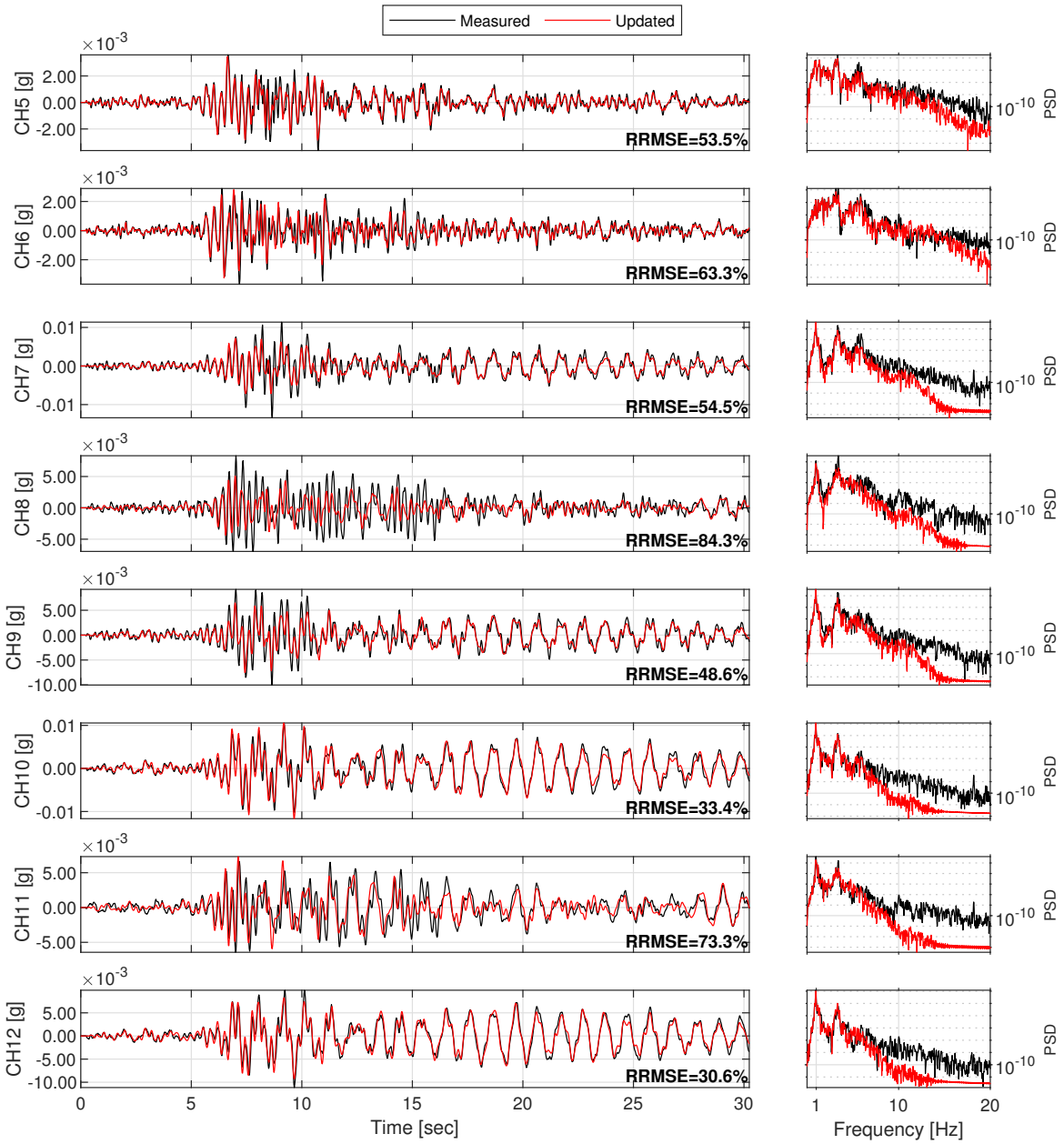

Figure D.58: Structural response comparison for seismic event #59.

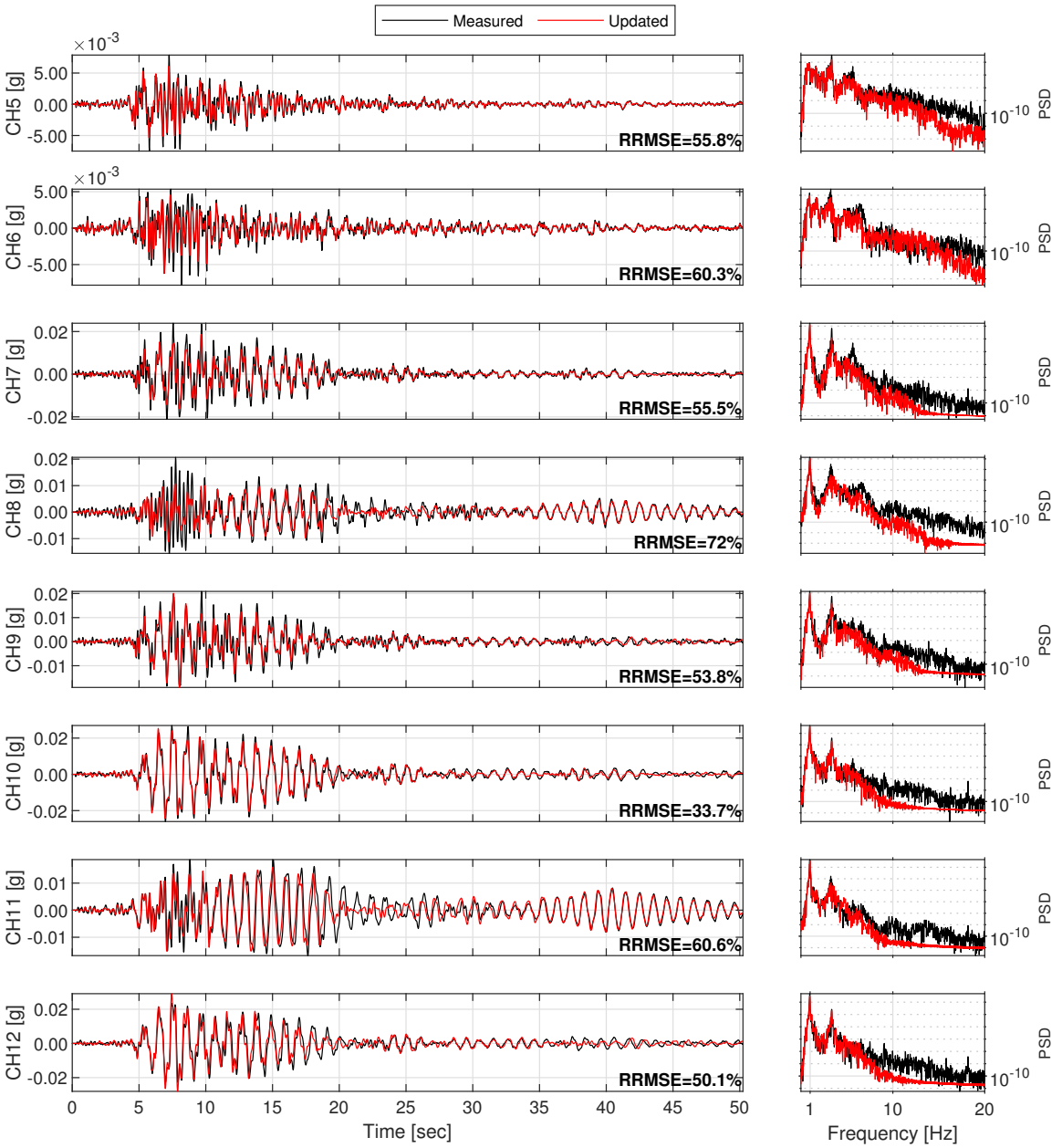

Figure D.59: Structural response comparison for seismic event #60.

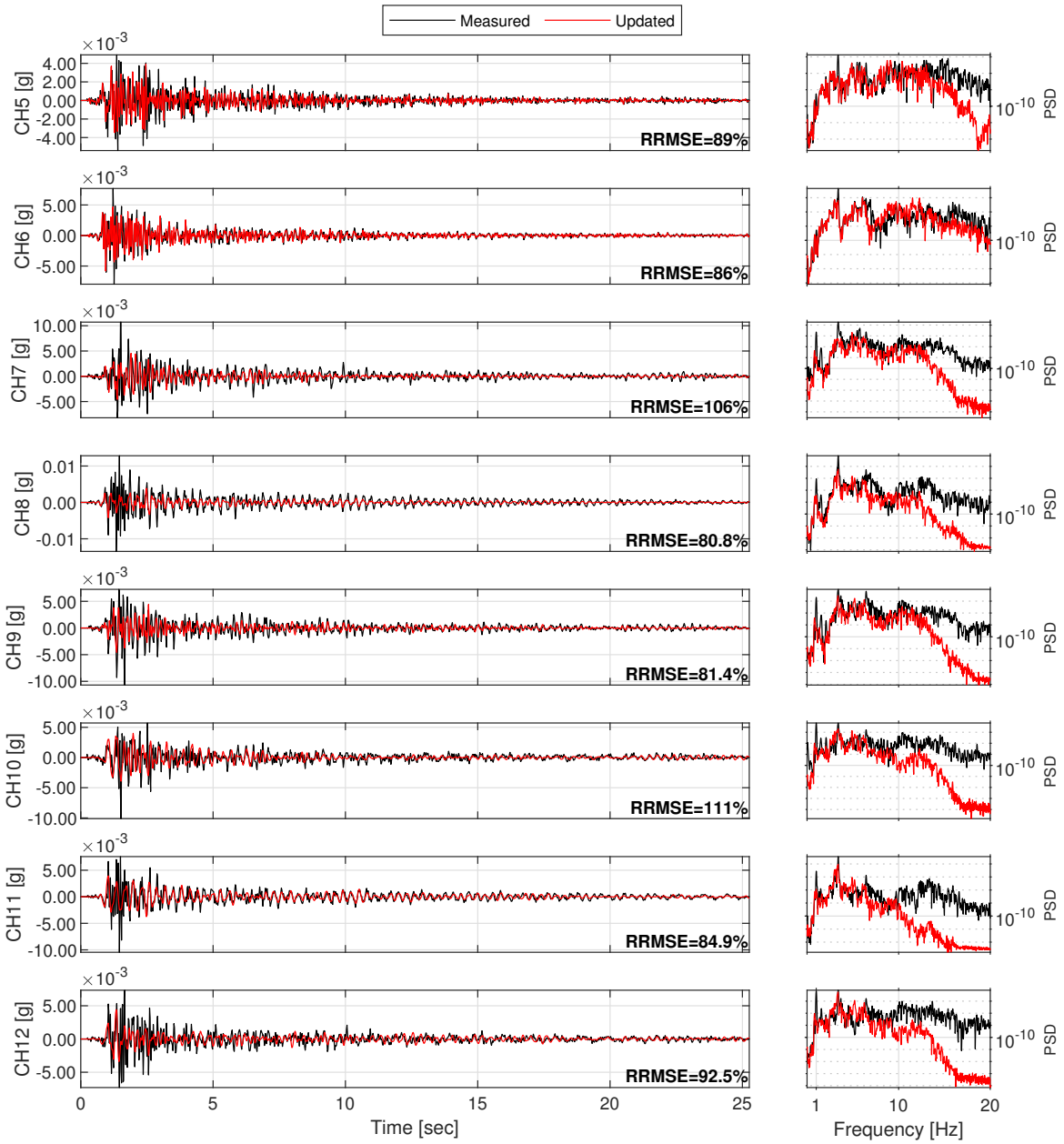

Figure D.60: Structural response comparison for seismic event #61.

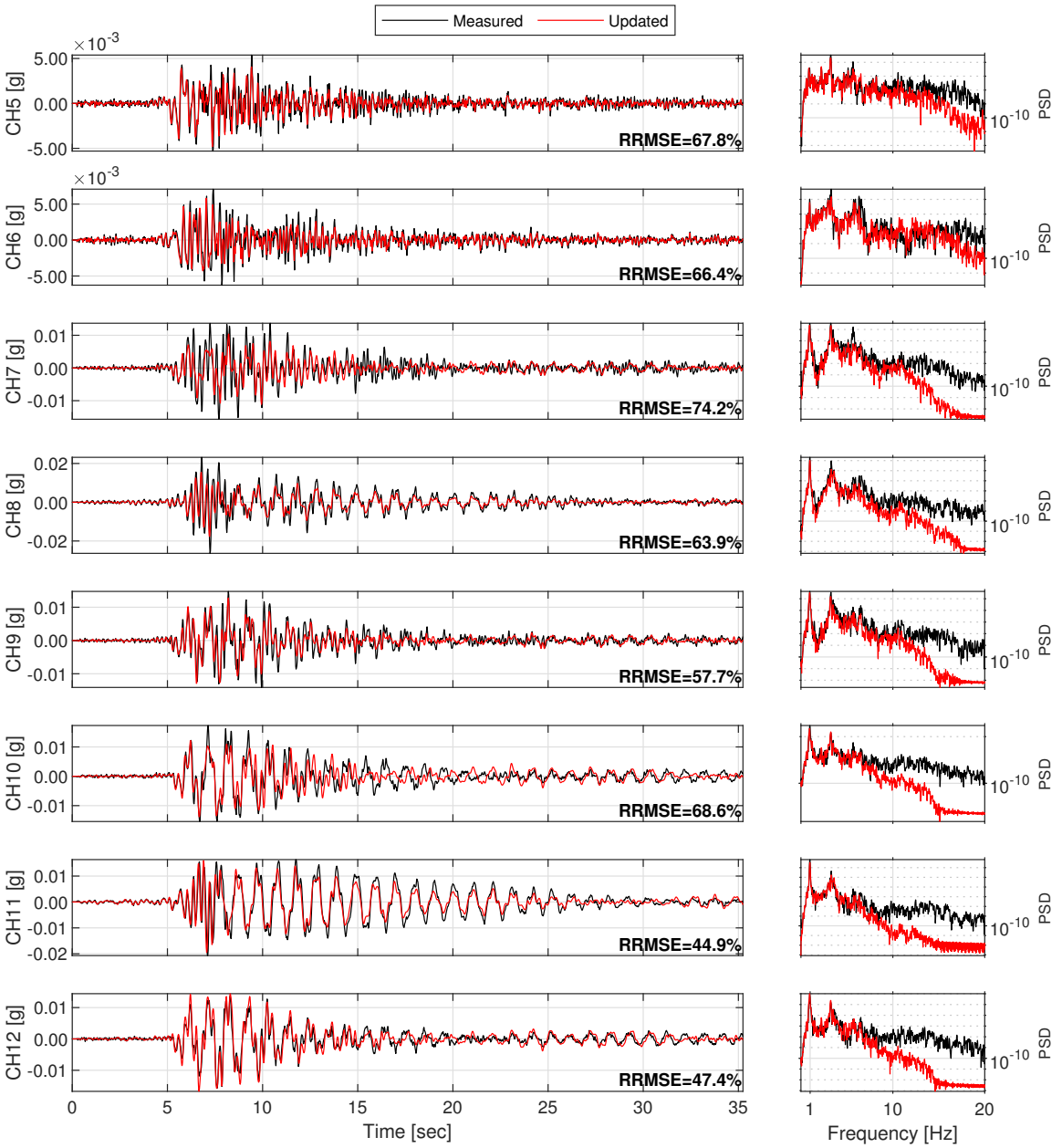

Figure D.61: Structural response comparison for seismic event #62.

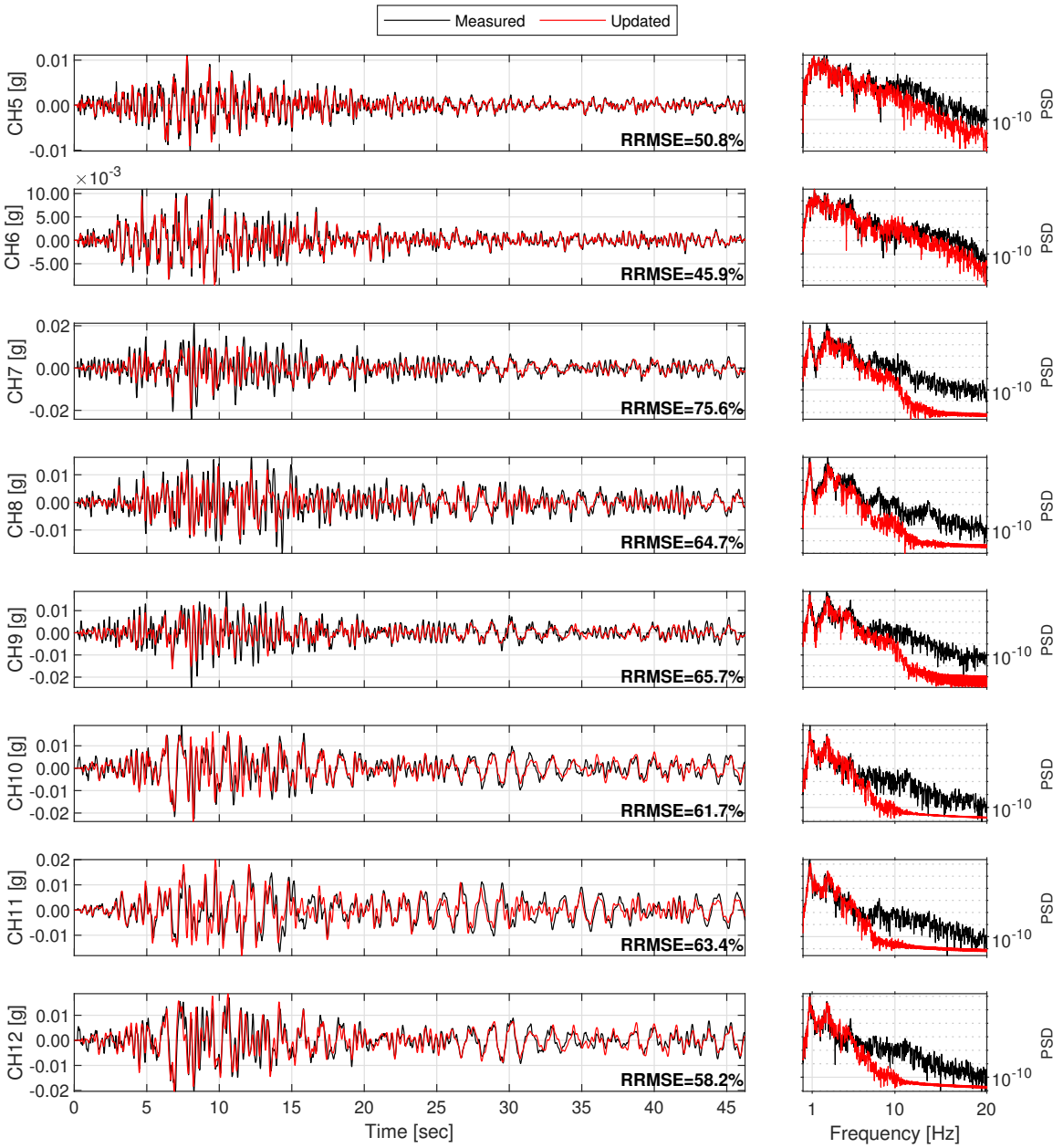

Figure D.62: Structural response comparison for seismic event #64.

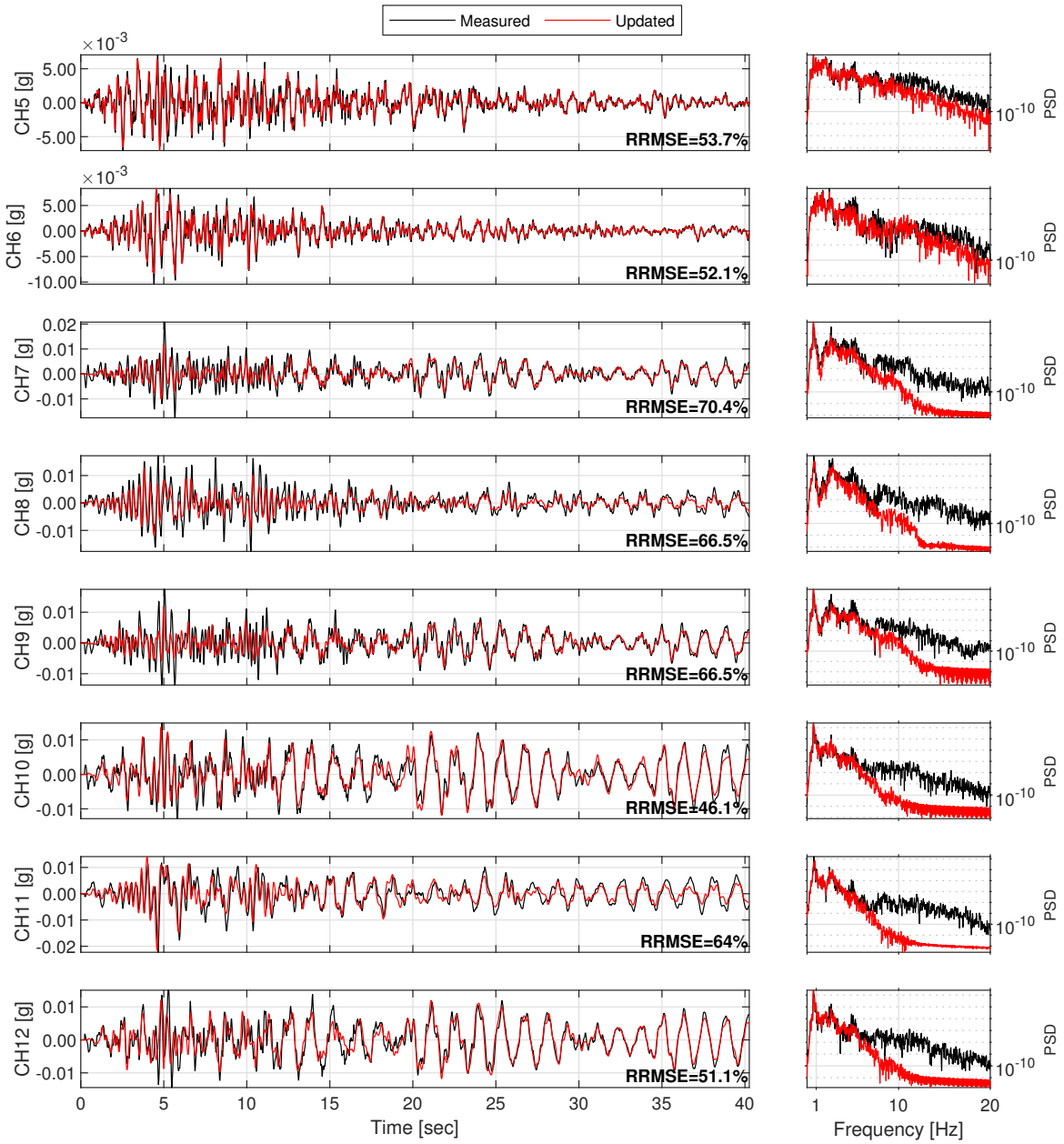

Figure D.63: Structural response comparison for seismic event #65.

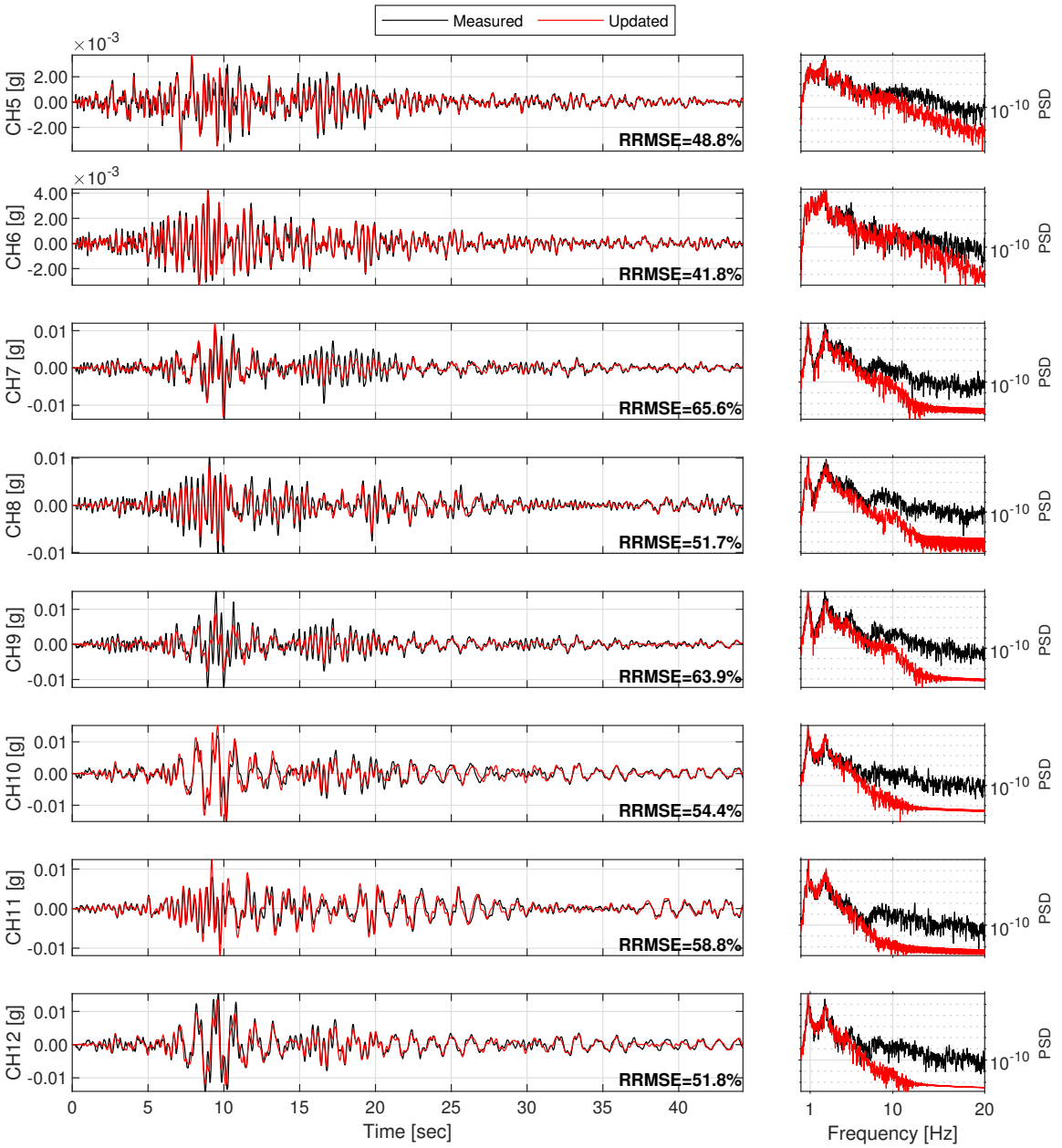

Figure D.64: Structural response comparison for seismic event #66.

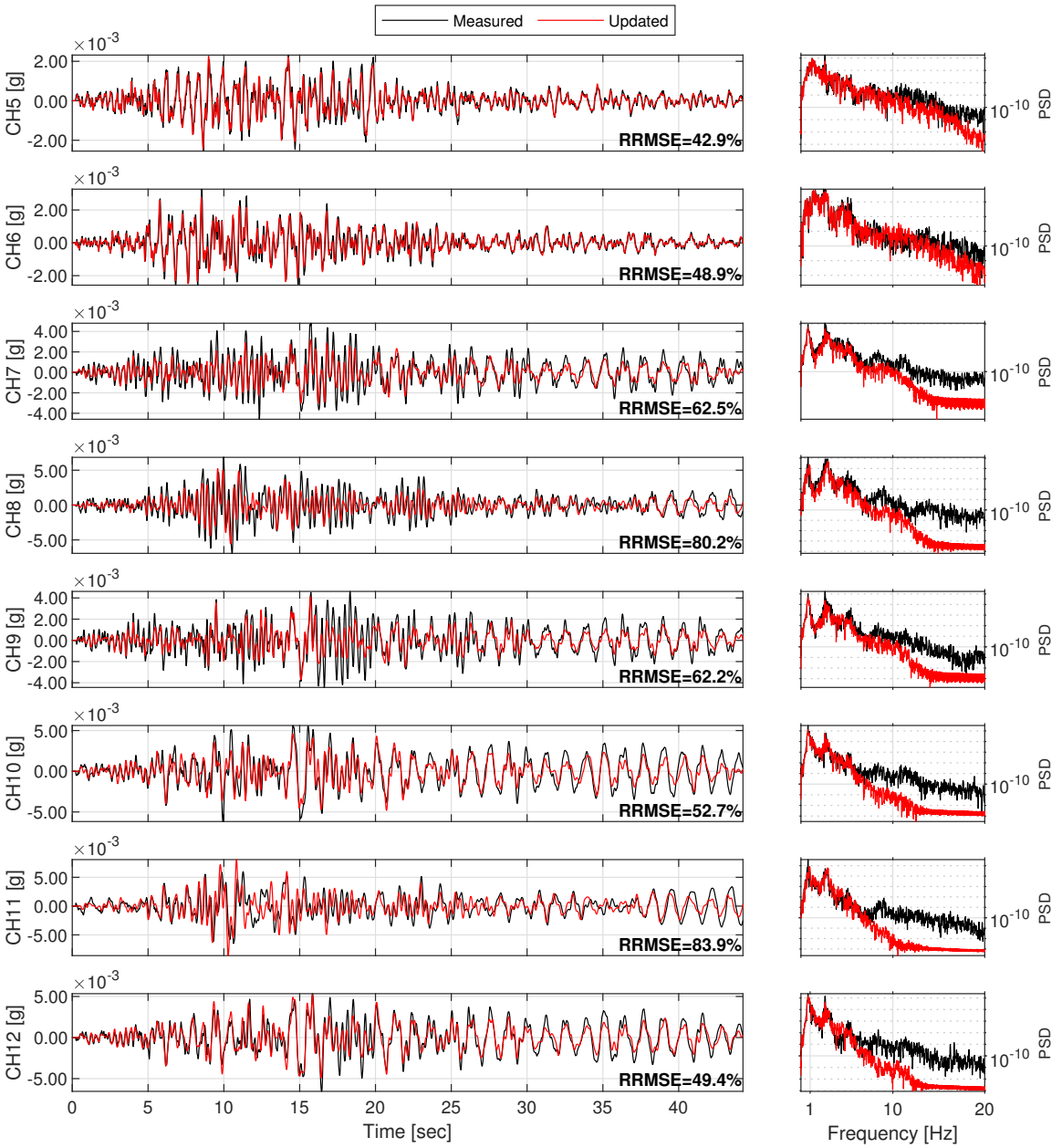

Figure D.65: Structural response comparison for seismic event #67.

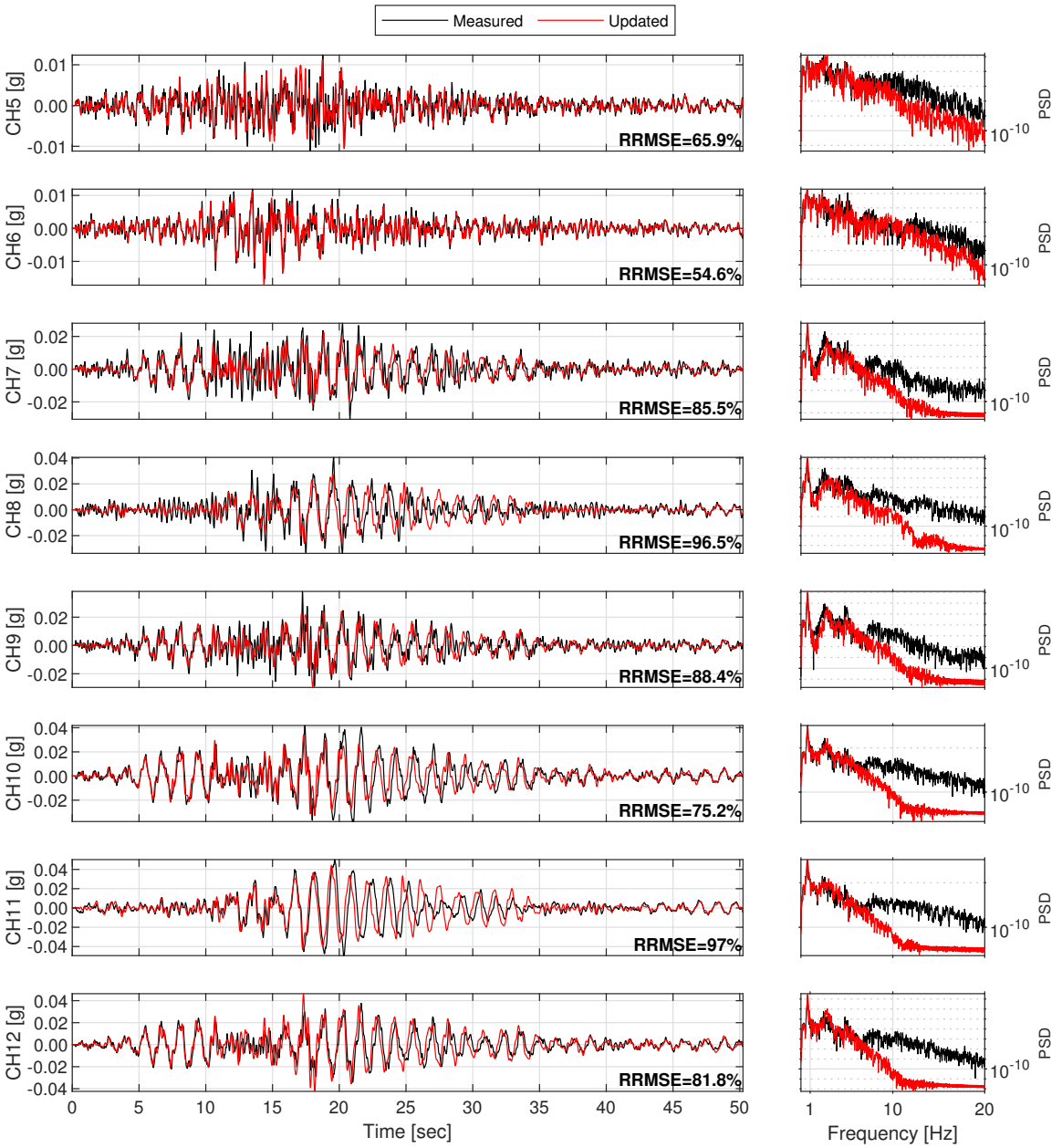

Figure D.66: Structural response comparison for seismic event #68.

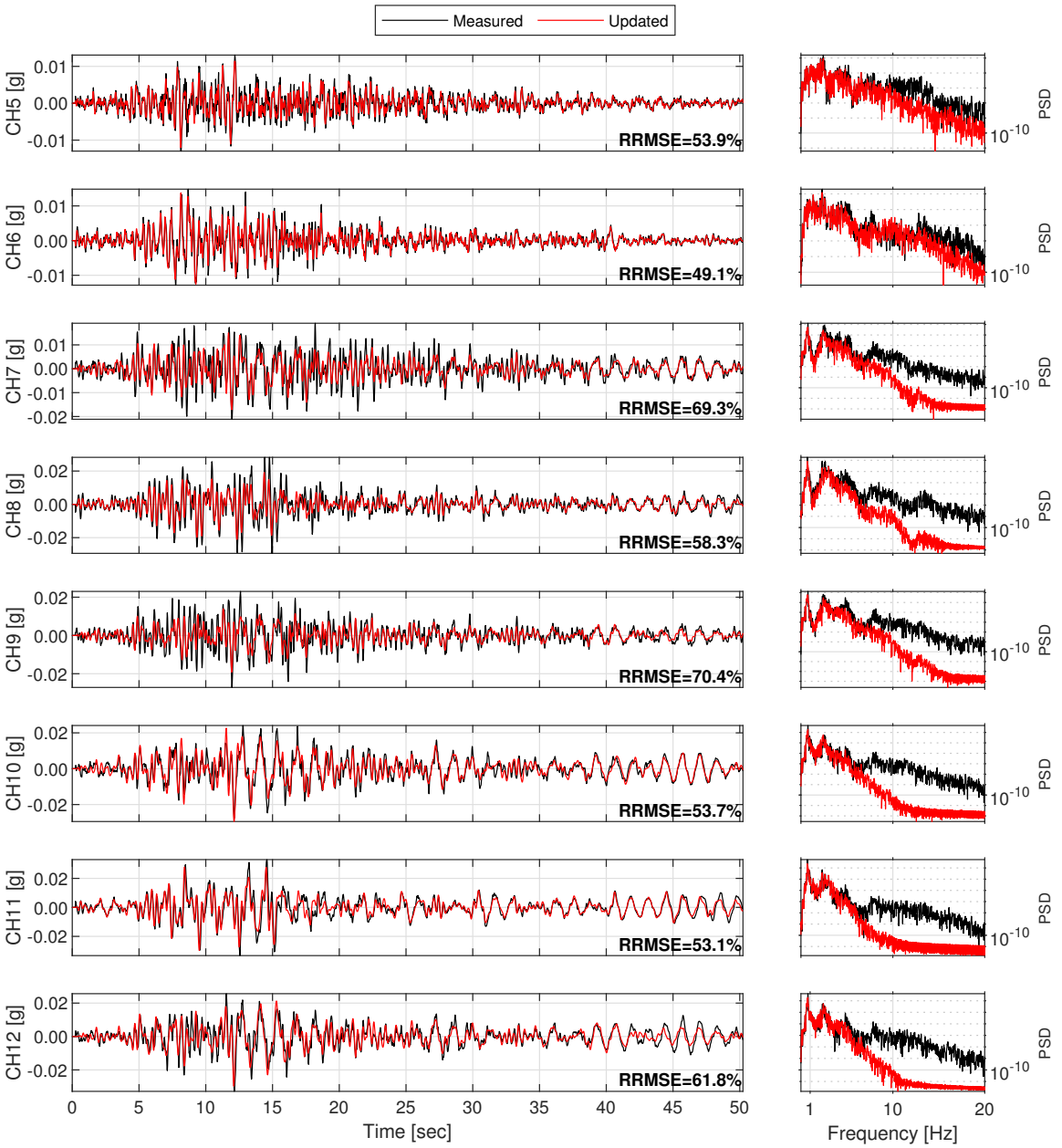

Figure D.67: Structural response comparison for seismic event #69.

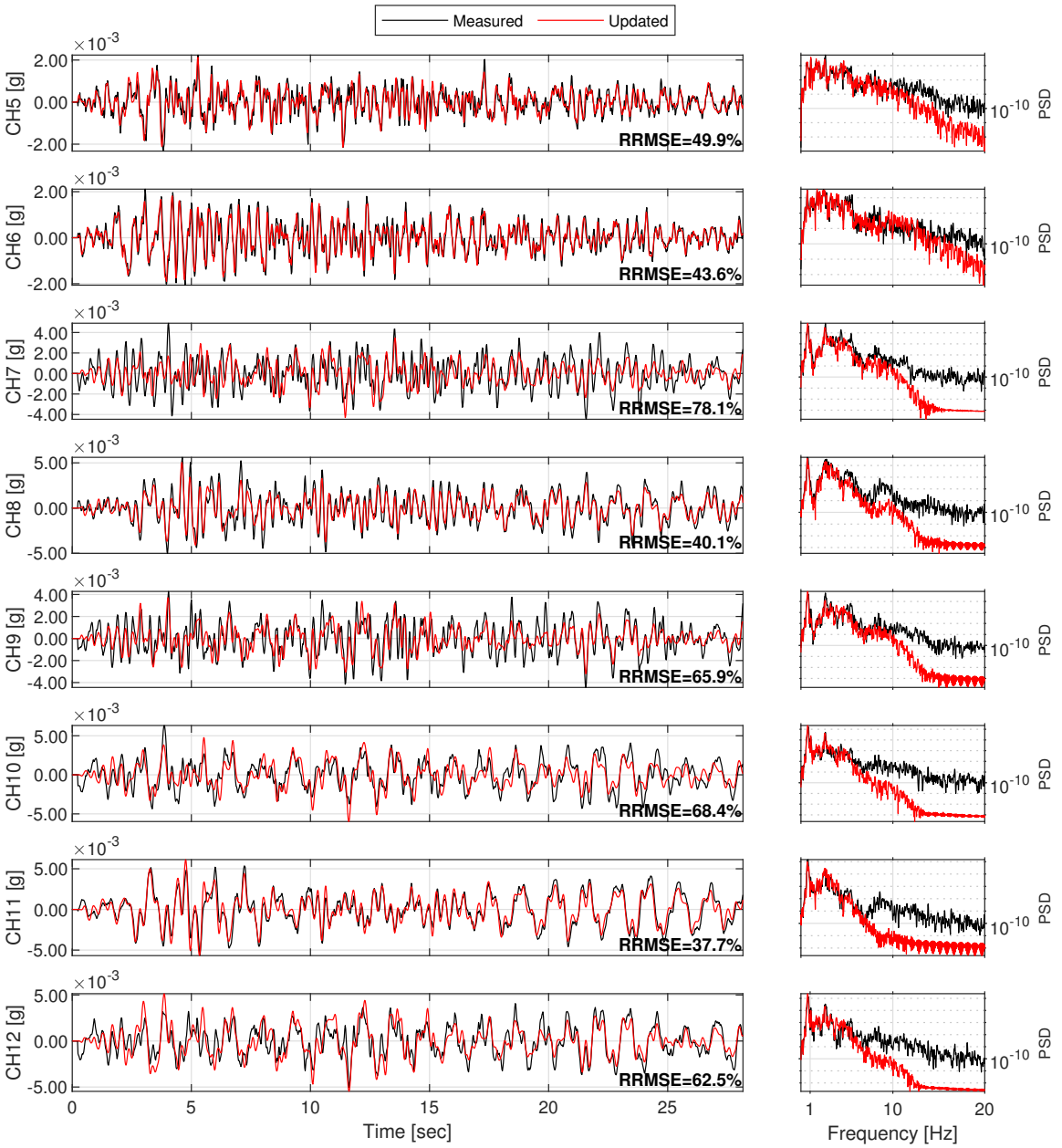

Figure D.68: Structural response comparison for seismic event #70.

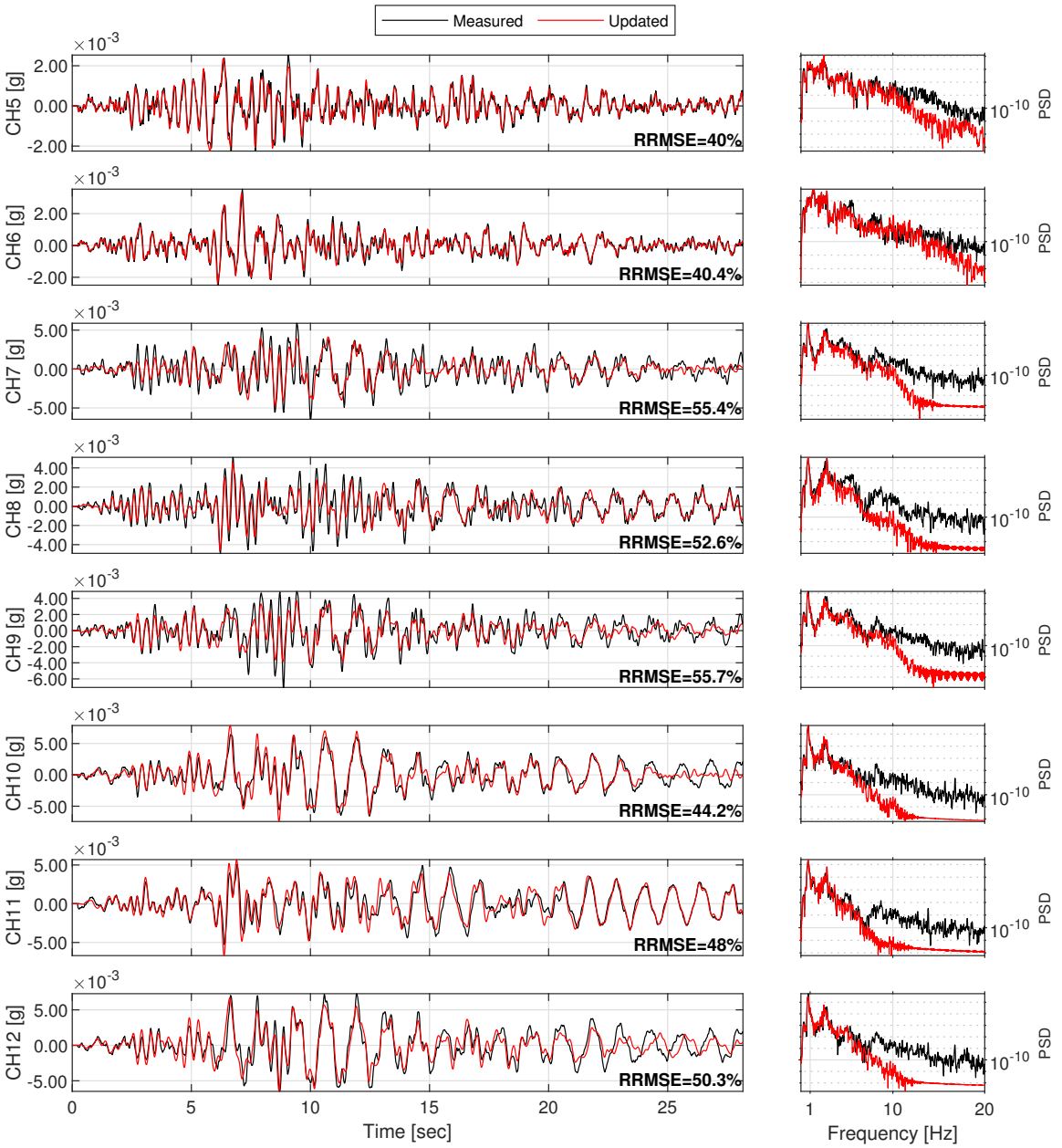

Figure D.69: Structural response comparison for seismic event #71.

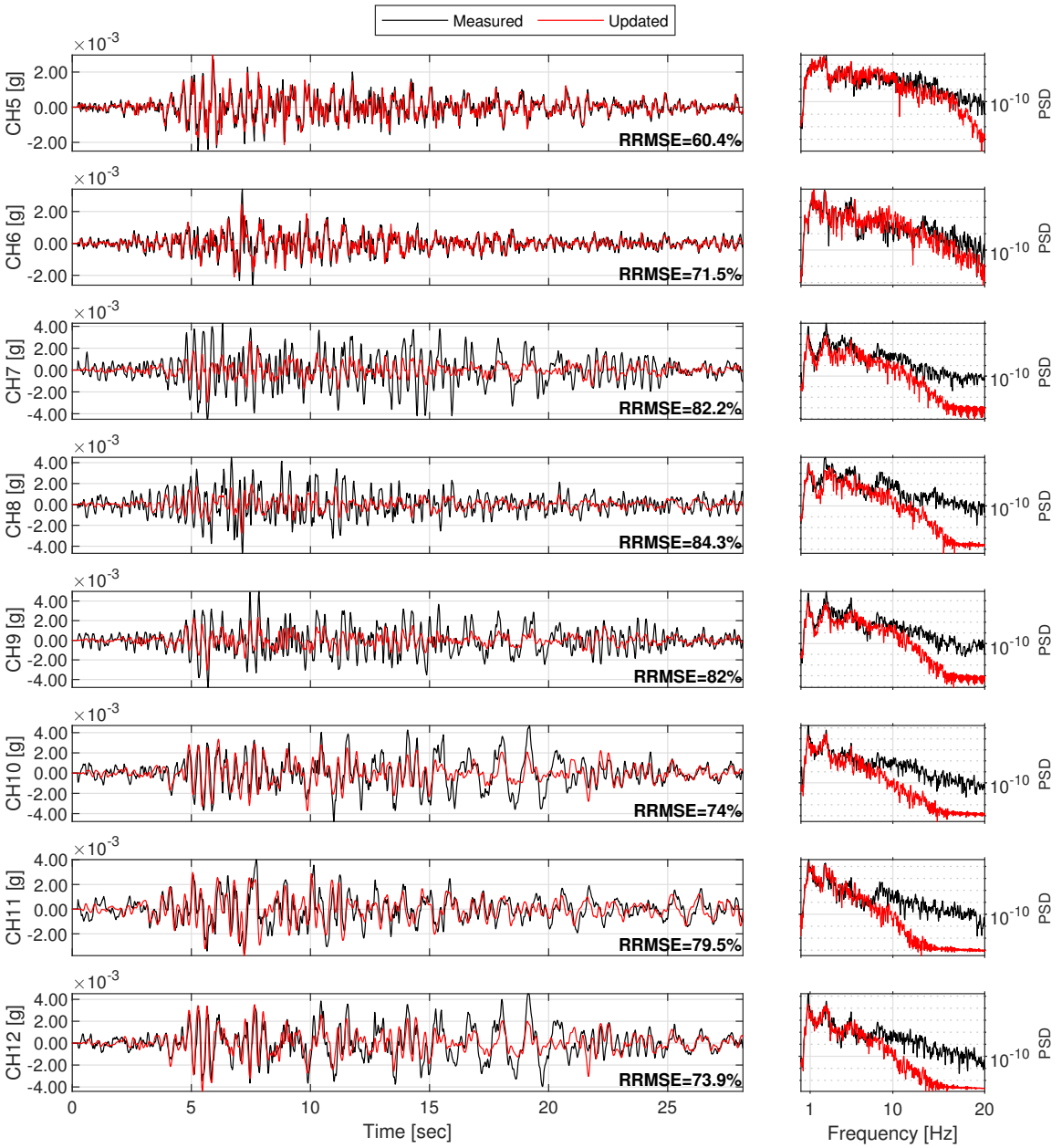

Figure D.70: Structural response comparison for seismic event #72.

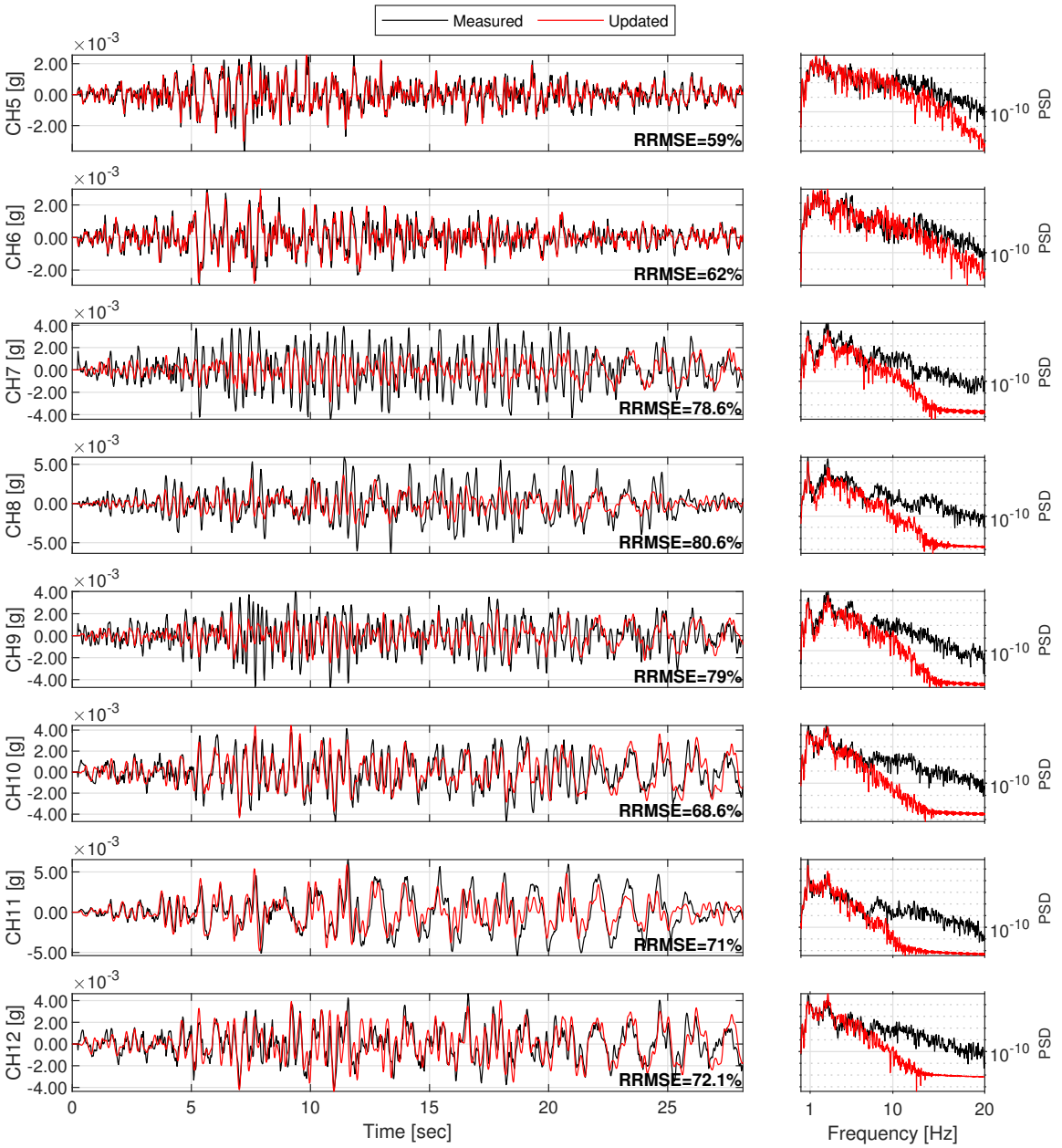

Figure D.71: Structural response comparison for seismic event #73.

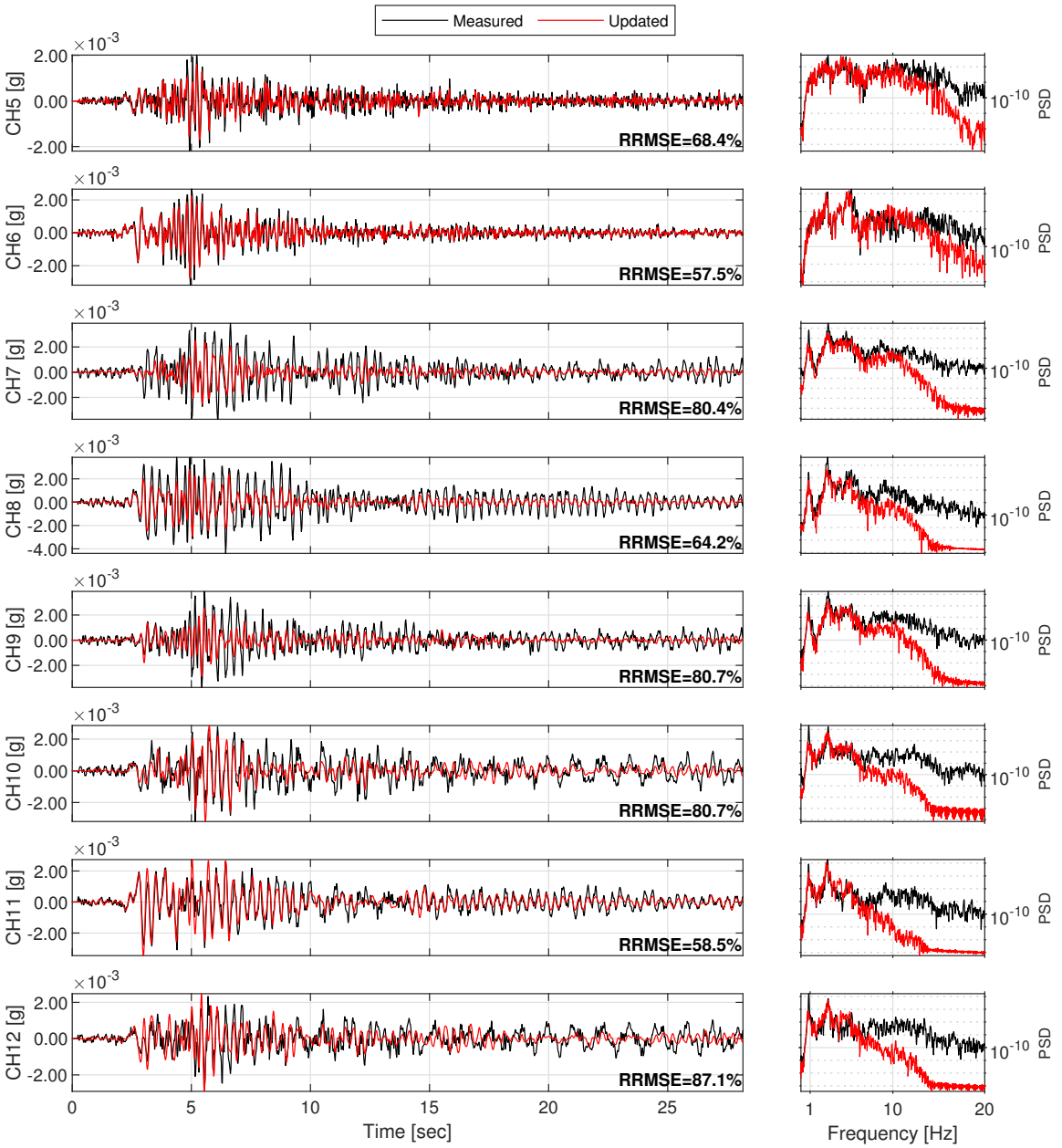

Figure D.72: Structural response comparison for seismic event #74.

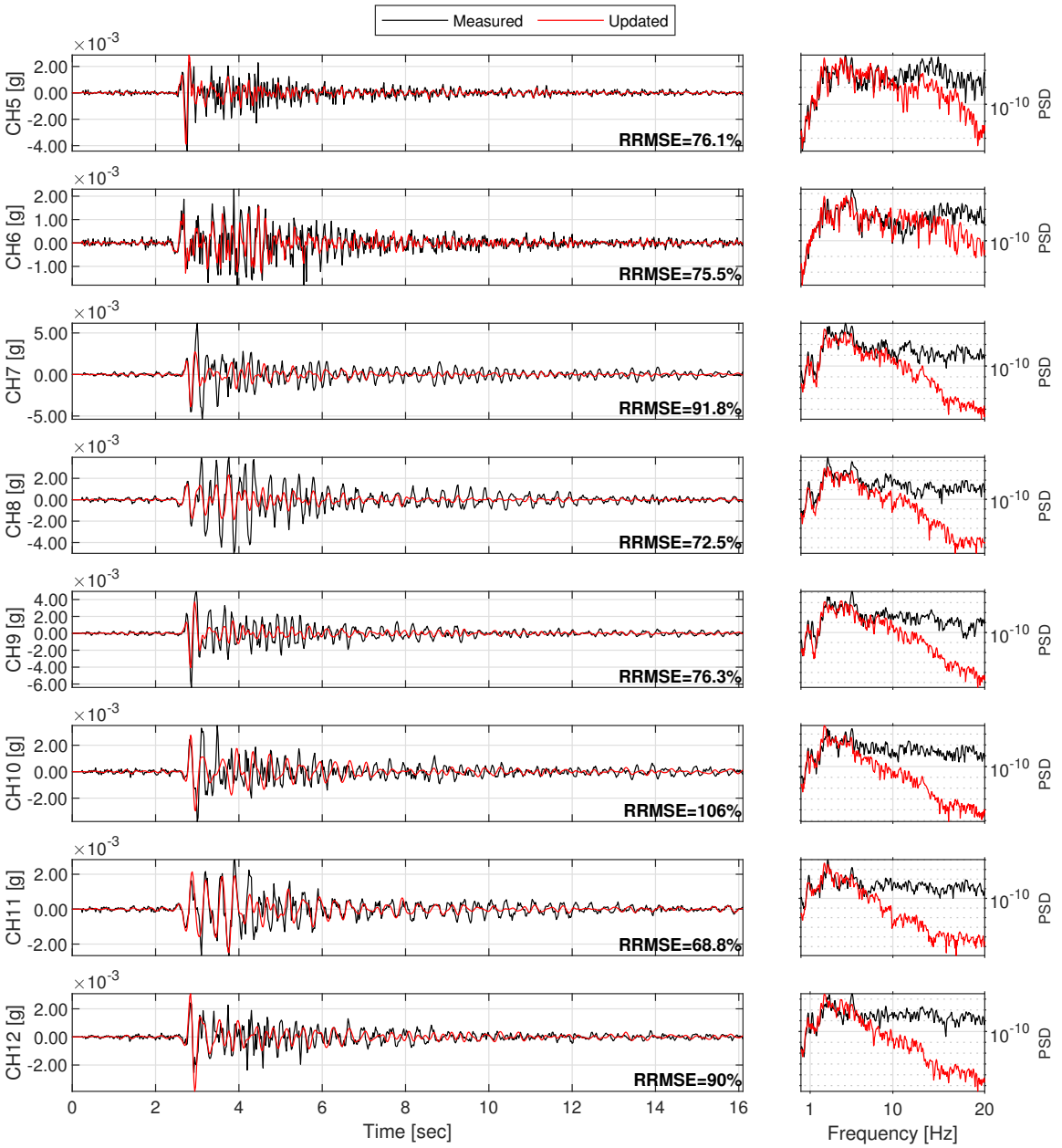

Figure D.73: Structural response comparison for seismic event #75.

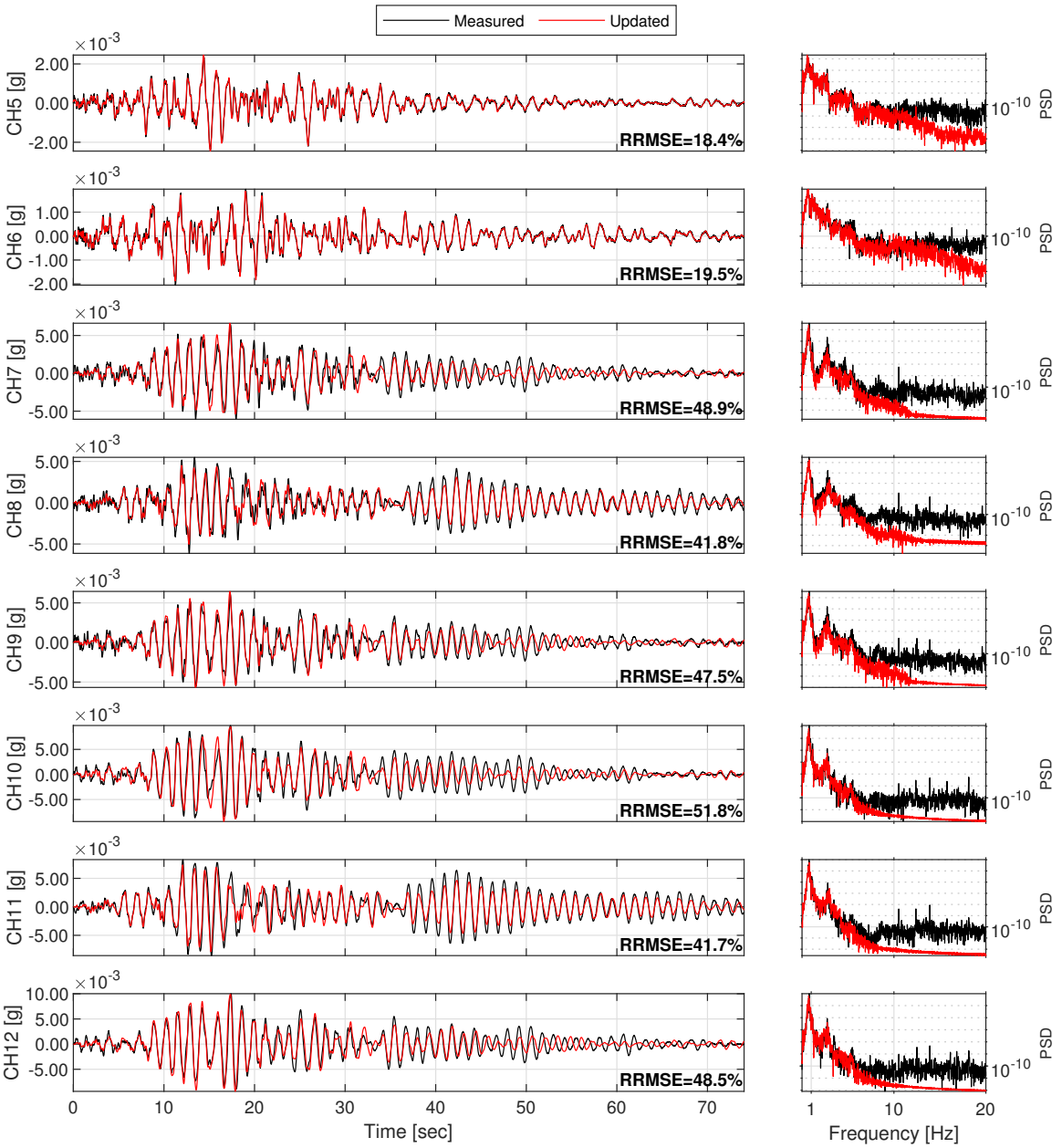

Figure D.74: Structural response comparison for seismic event #76.

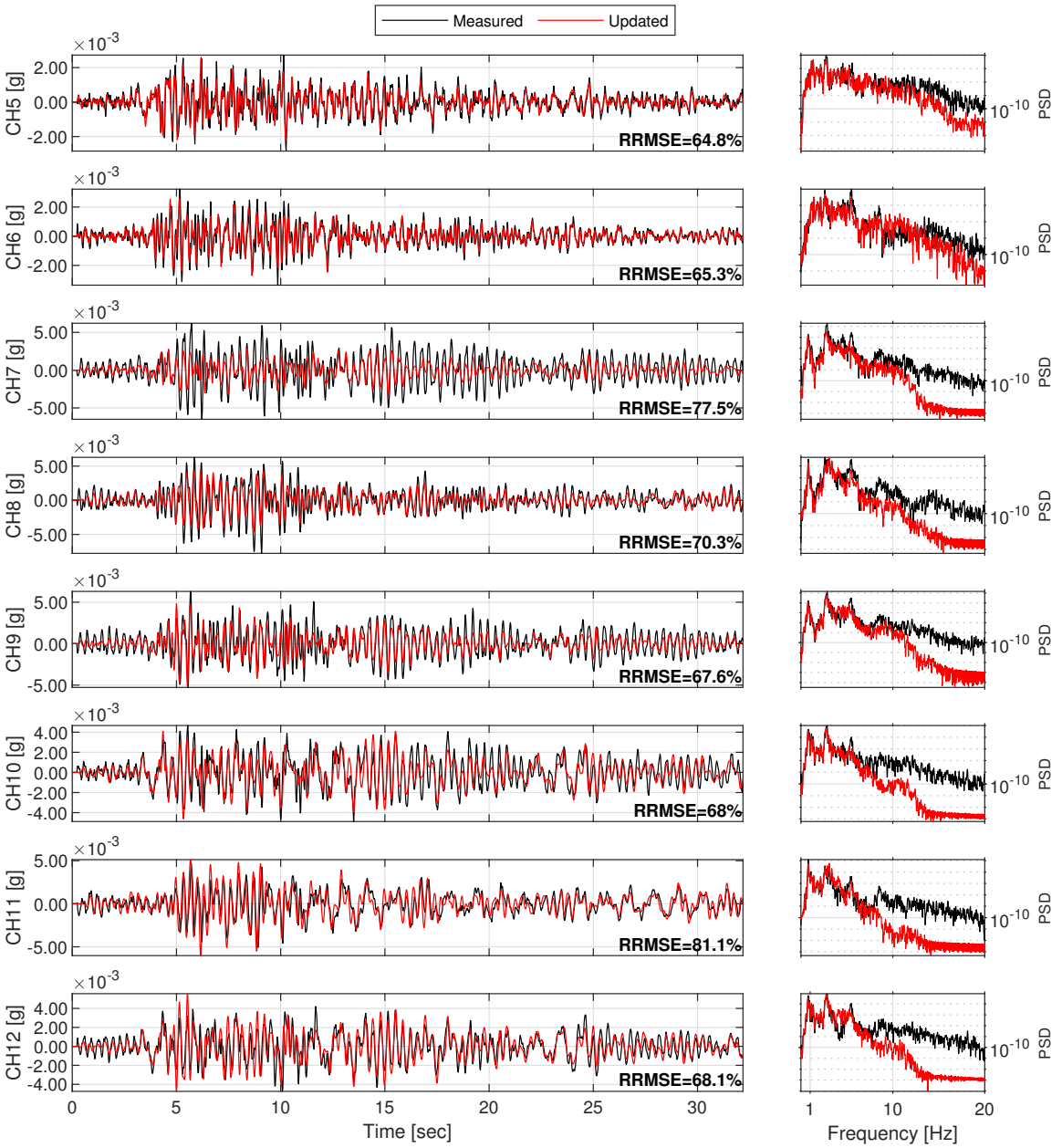

Figure D.75: Structural response comparison for seismic event #77.

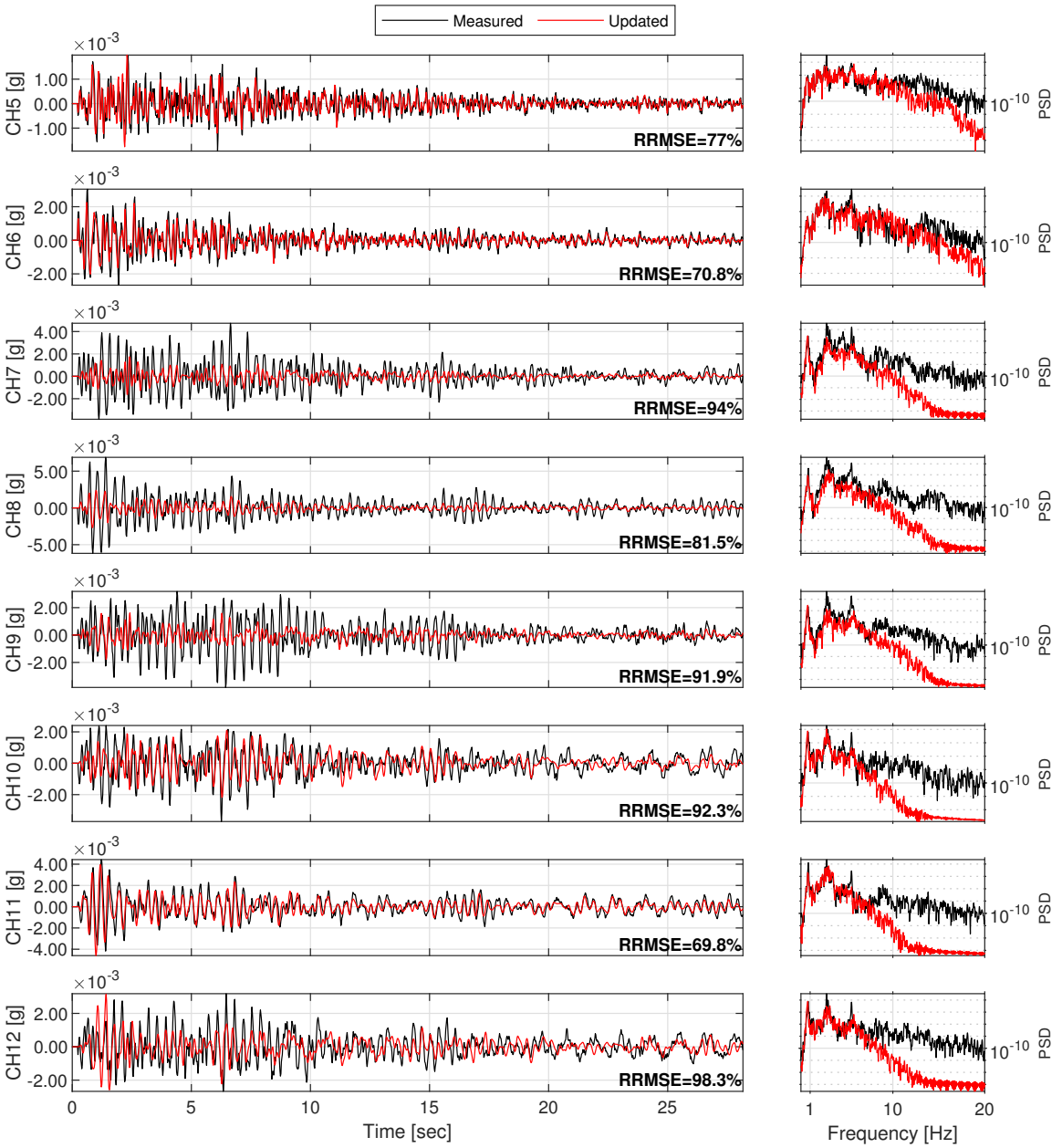

Figure D.76: Structural response comparison for seismic event #78.

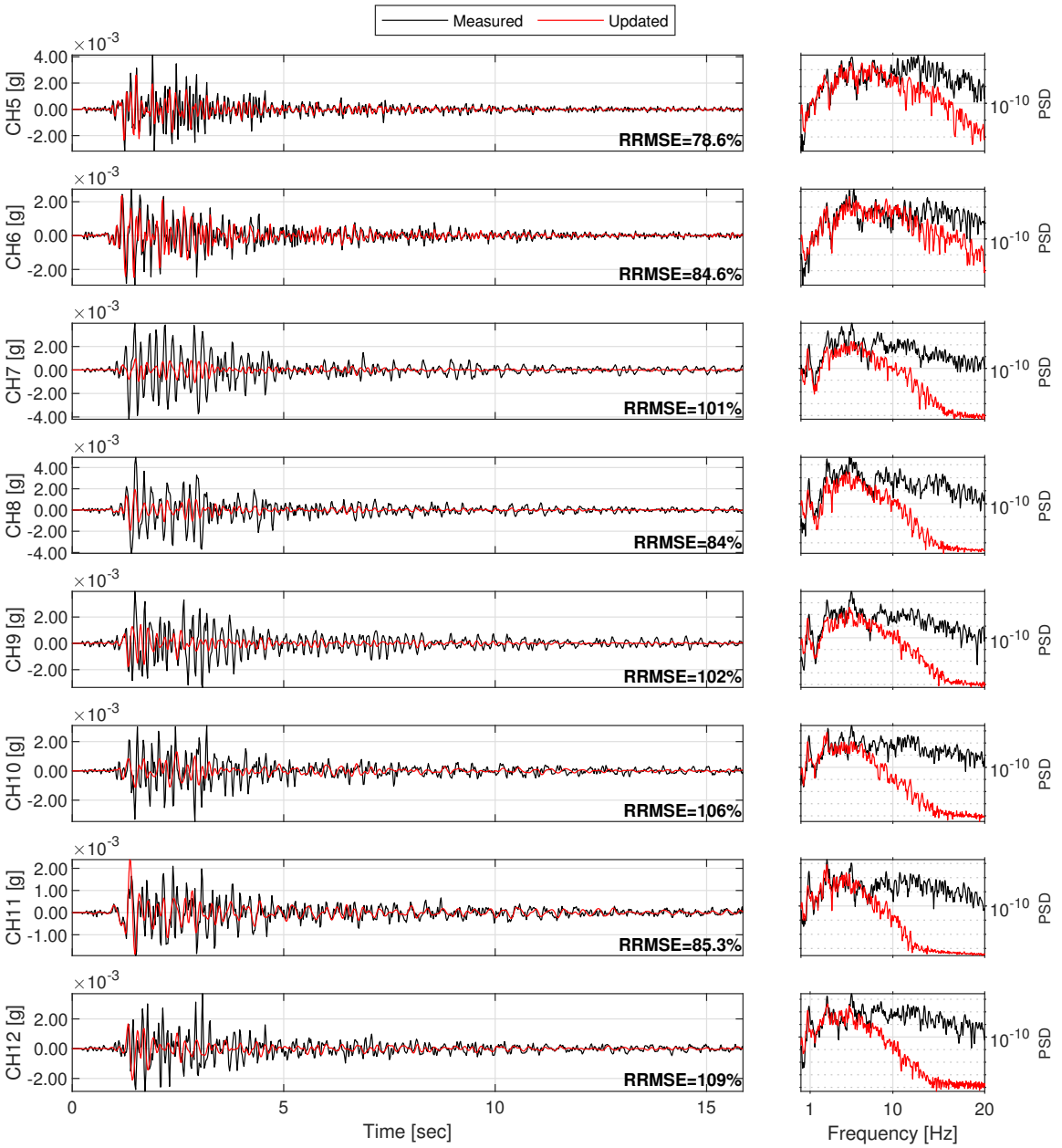

Figure D.77: Structural response comparison for seismic event #79.

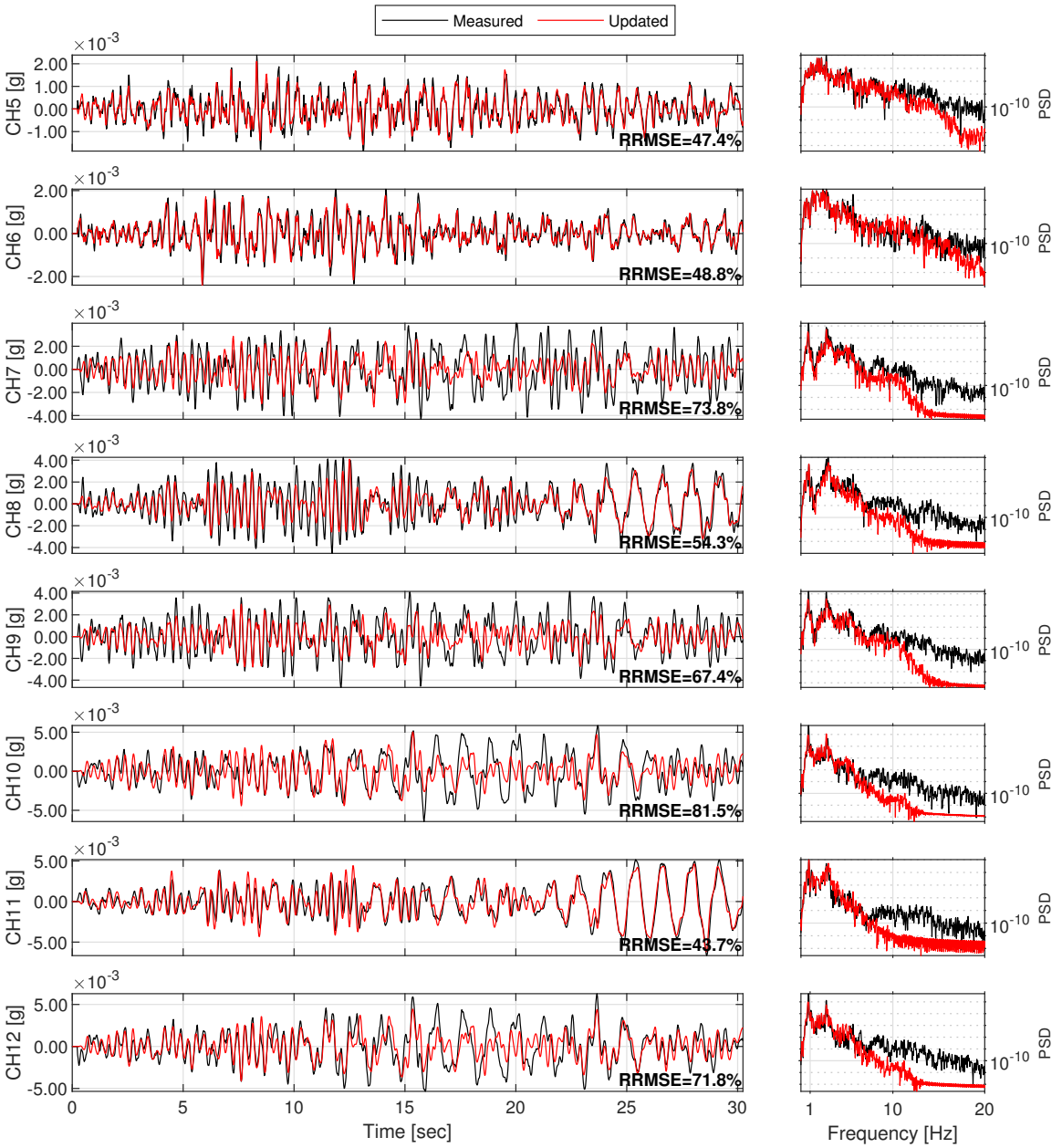

Figure D.78: Structural response comparison for seismic event #80.

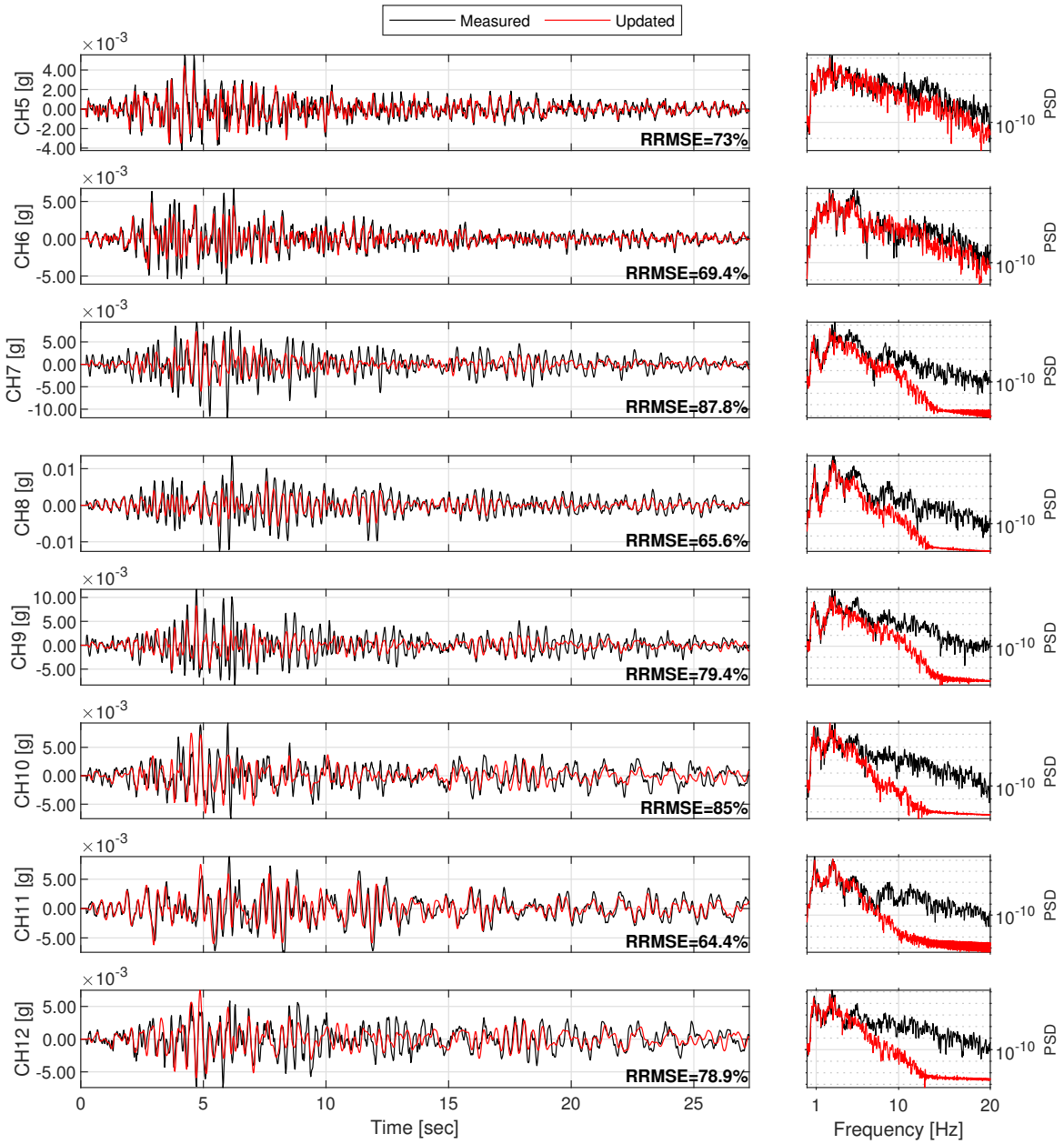

Figure D.79: Structural response comparison for seismic event #81.

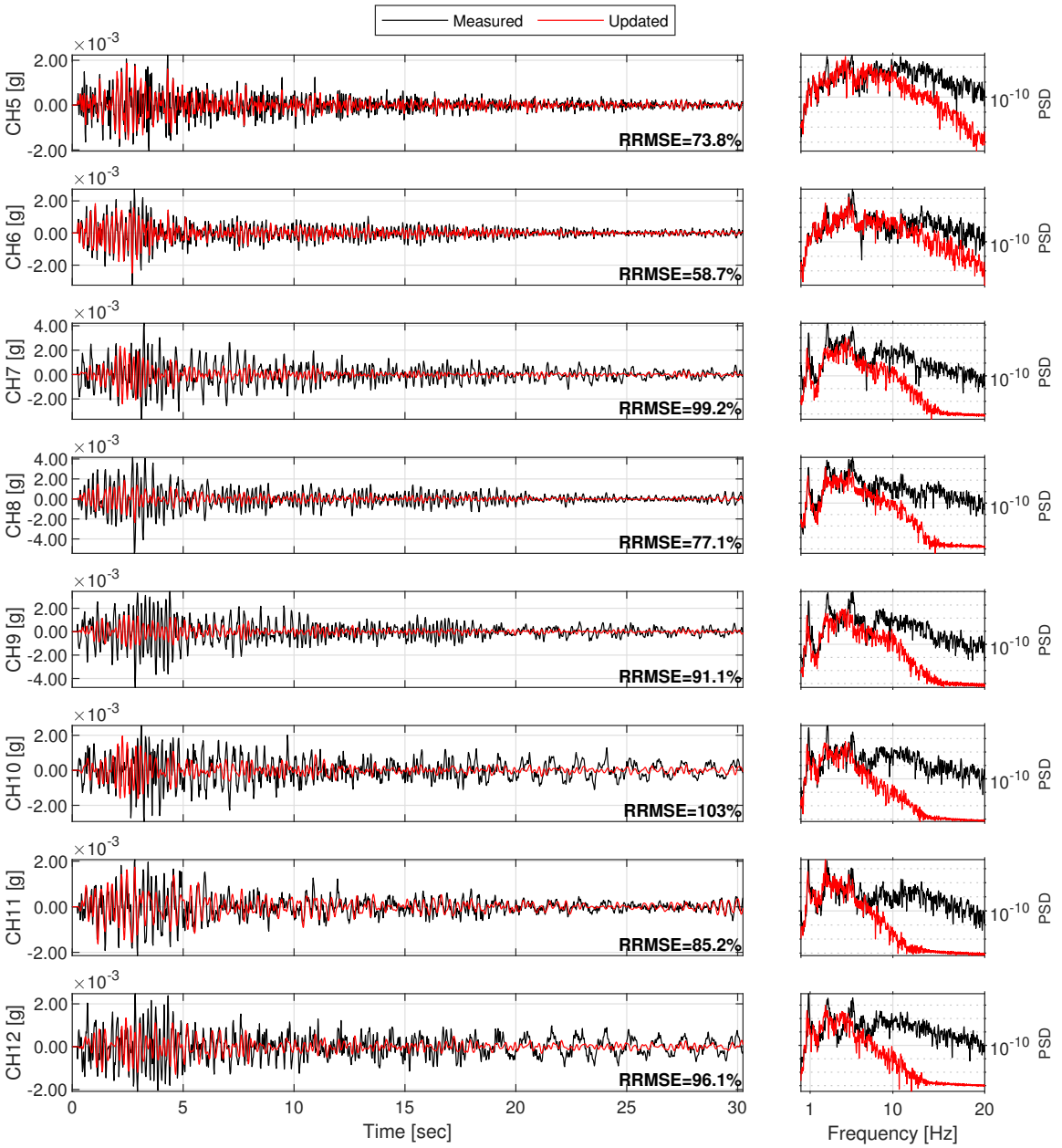

Figure D.80: Structural response comparison for seismic event #82.

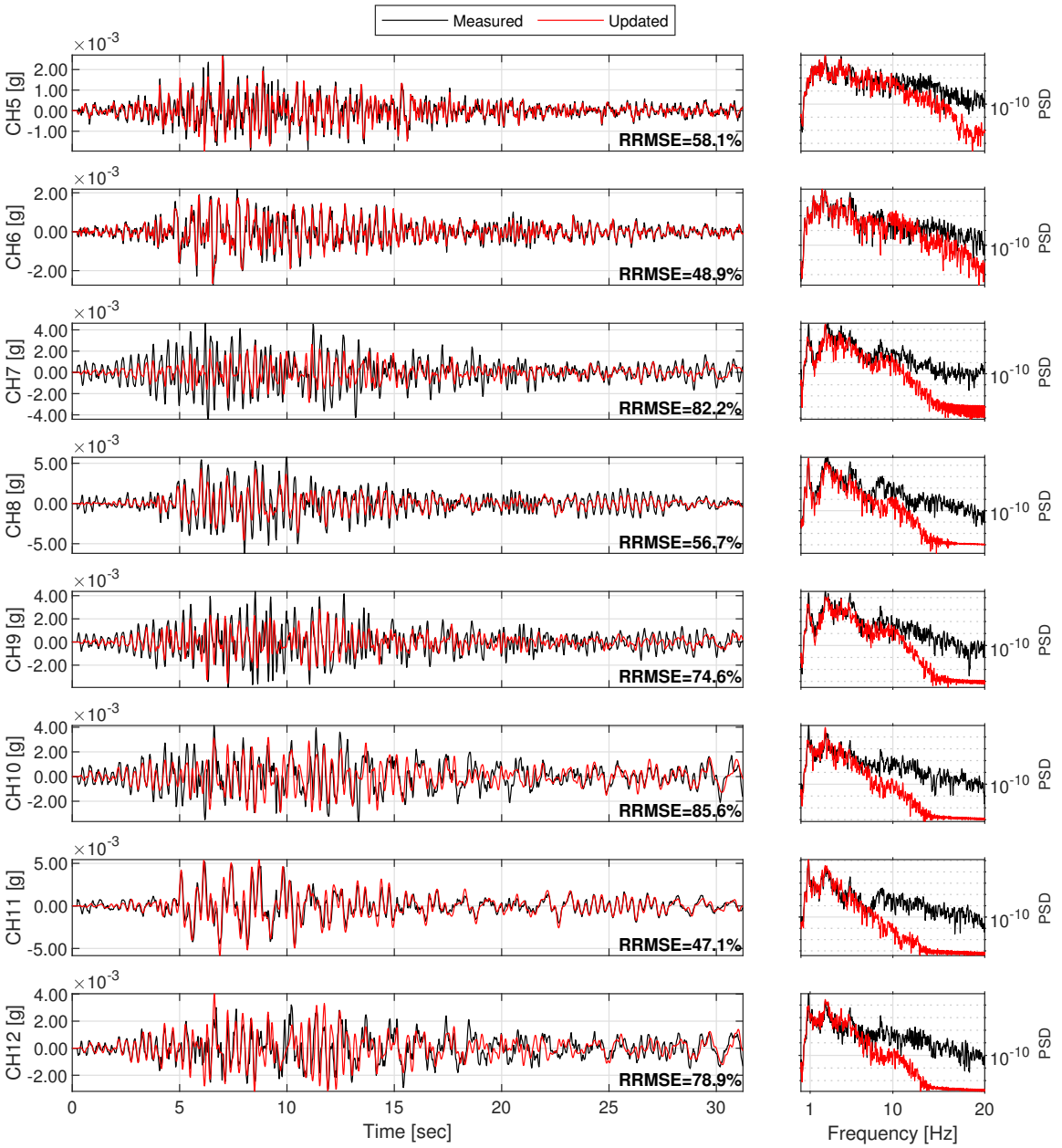

Figure D.81: Structural response comparison for seismic event #83.

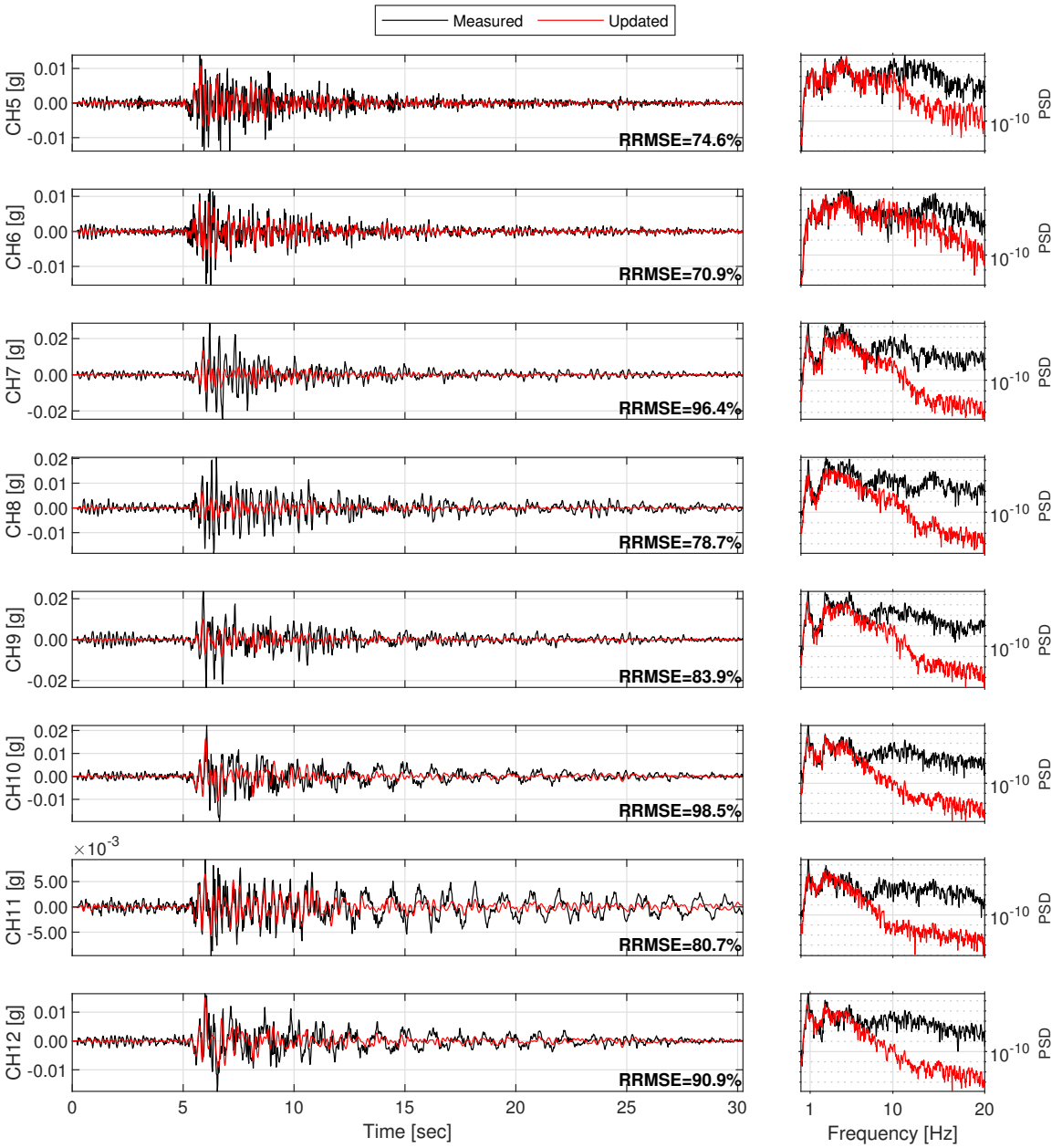

Figure D.82: Structural response comparison for seismic event #84.

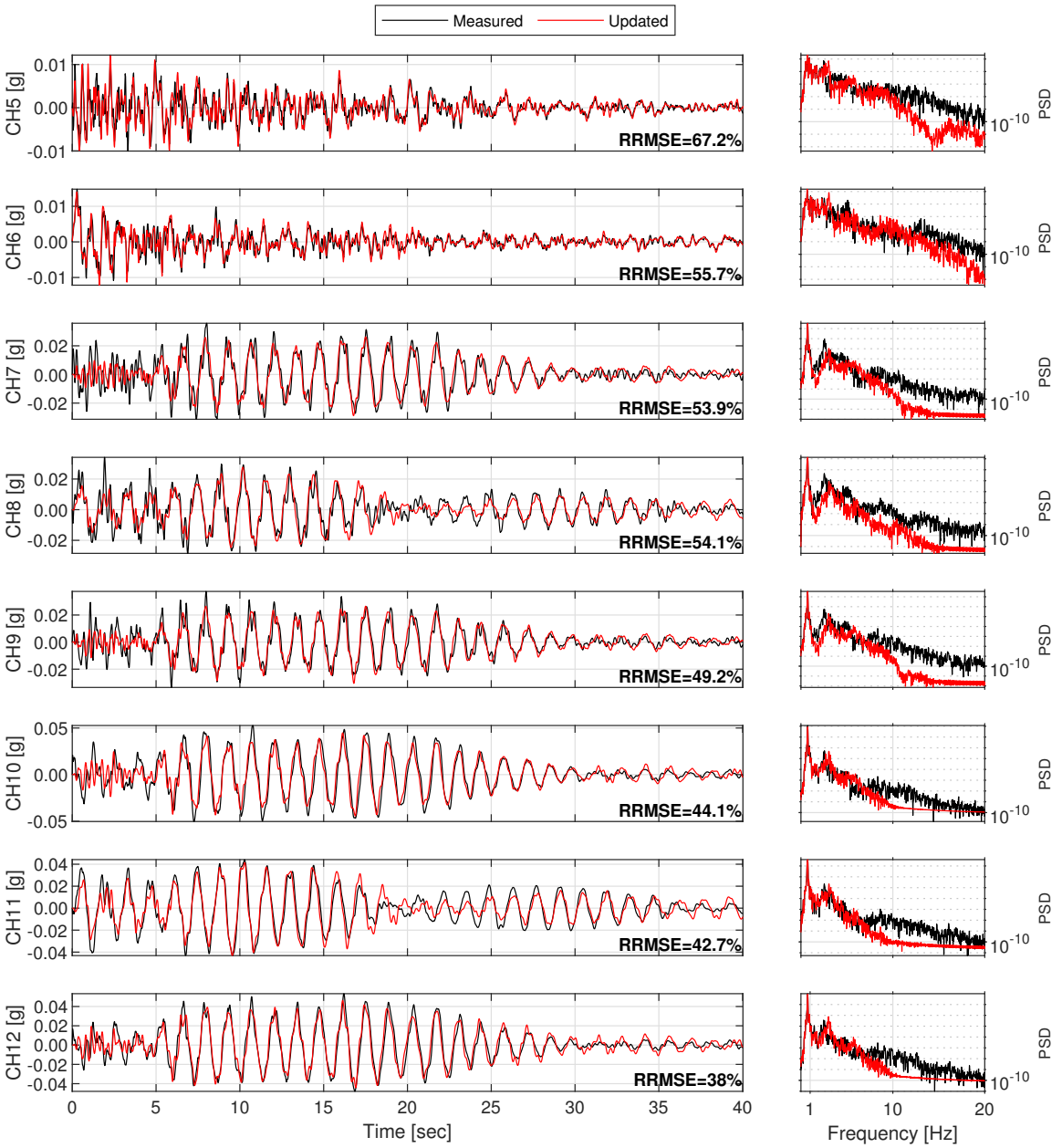

Figure D.83: Structural response comparison for seismic event #85.

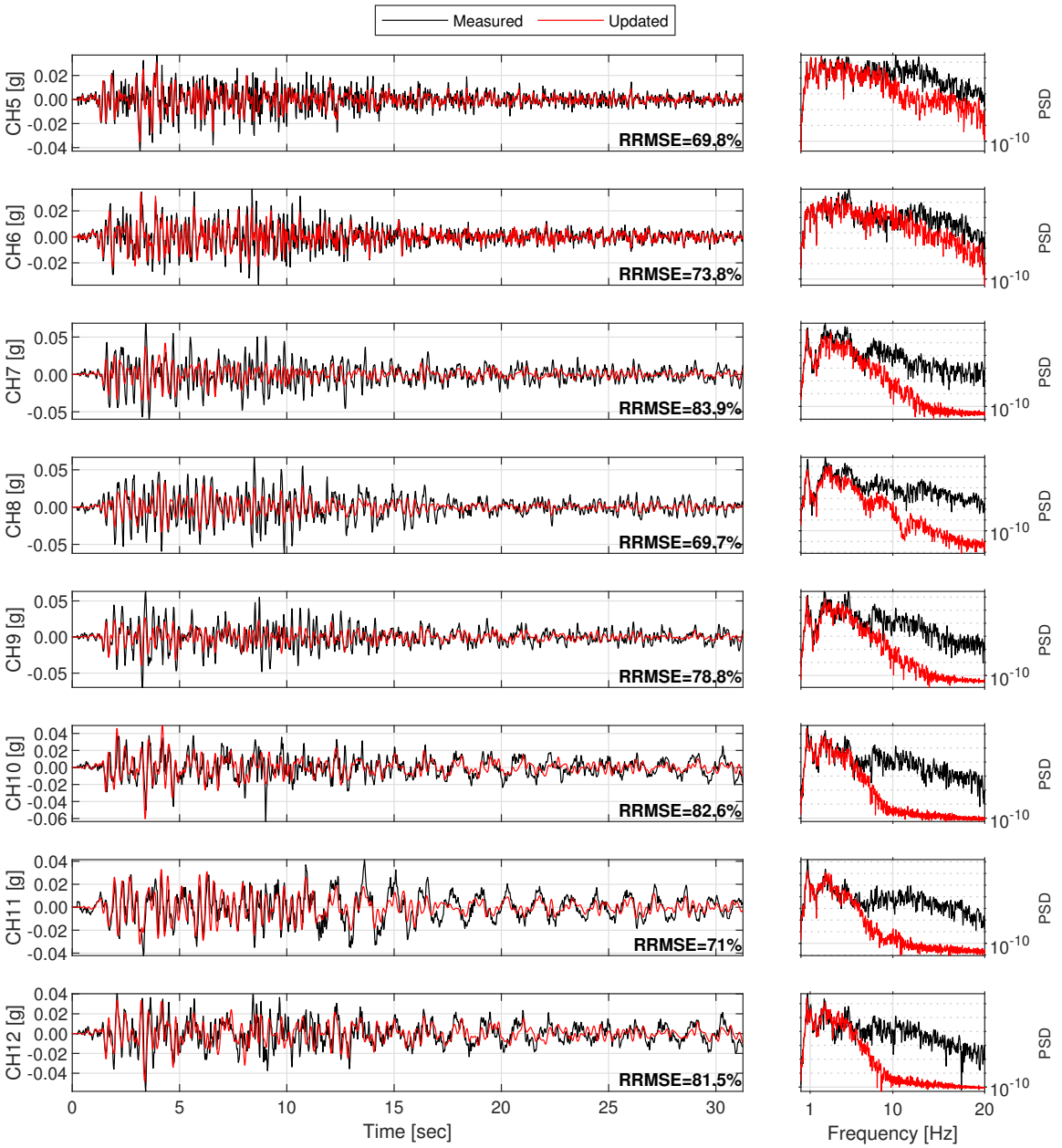

Figure D.84: Structural response comparison for seismic event #86.

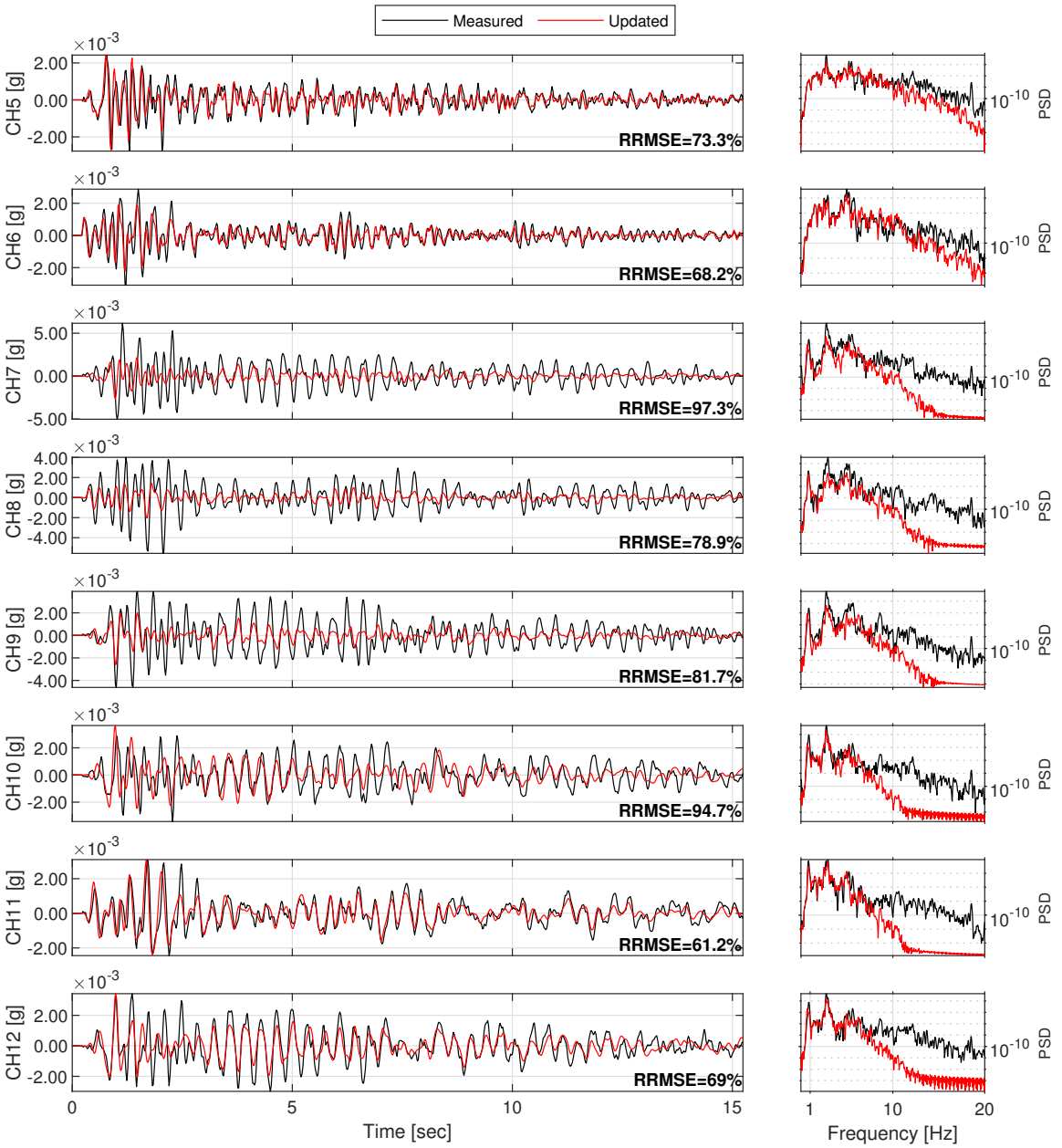

Figure D.85: Structural response comparison for seismic event #87.

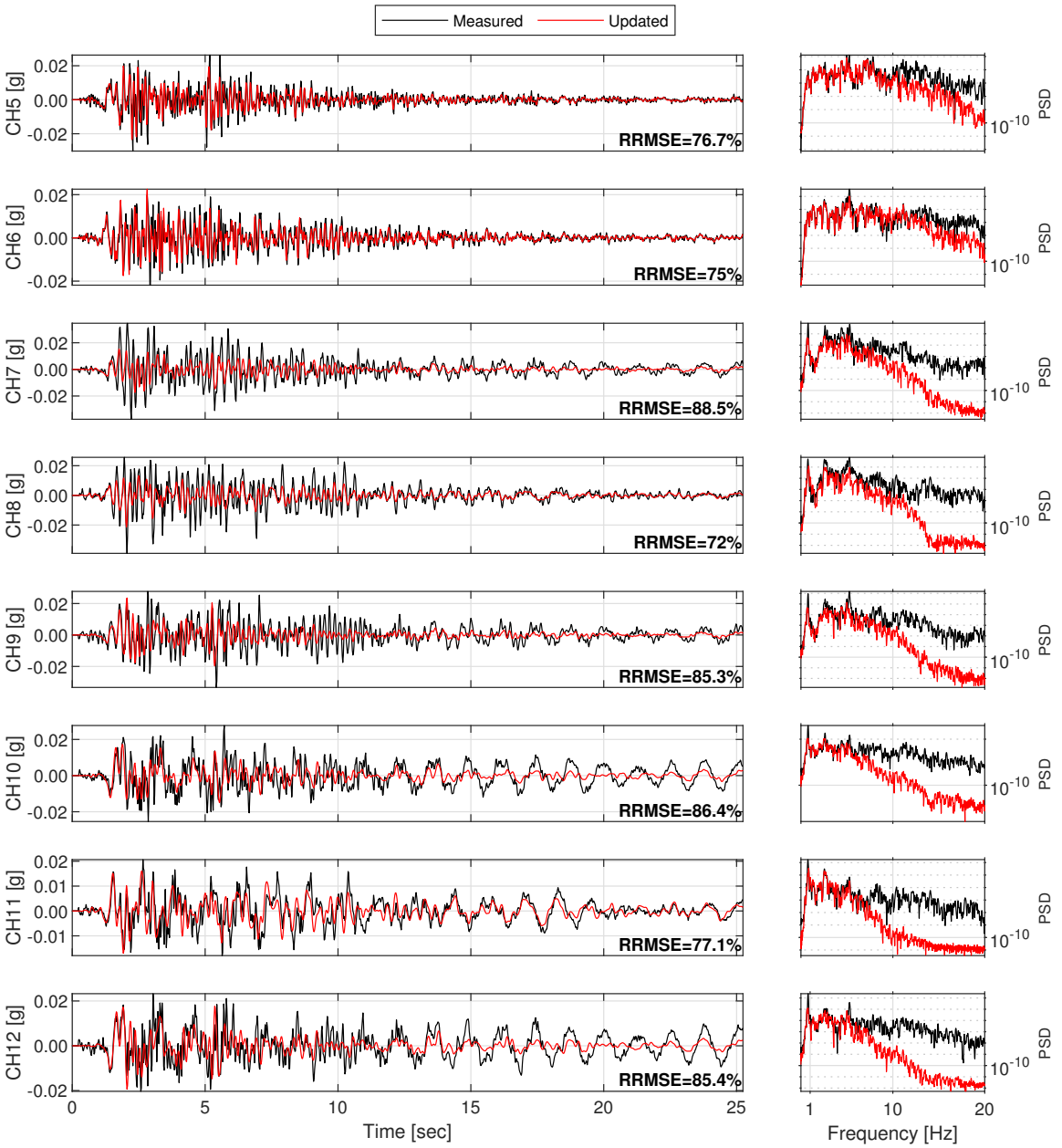

Figure D.86: Structural response comparison for seismic event #88.

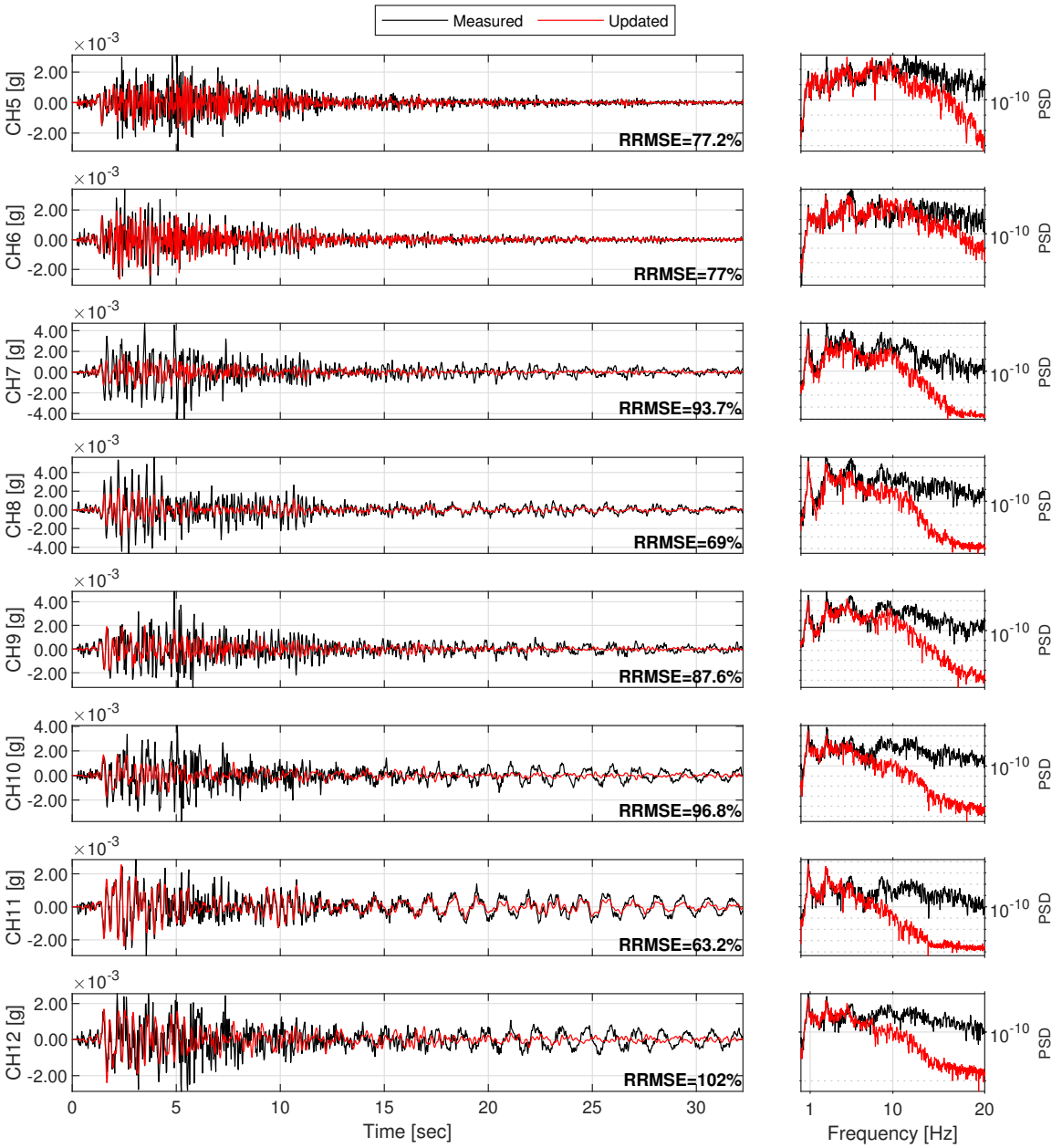

Figure D.87: Structural response comparison for seismic event #89.

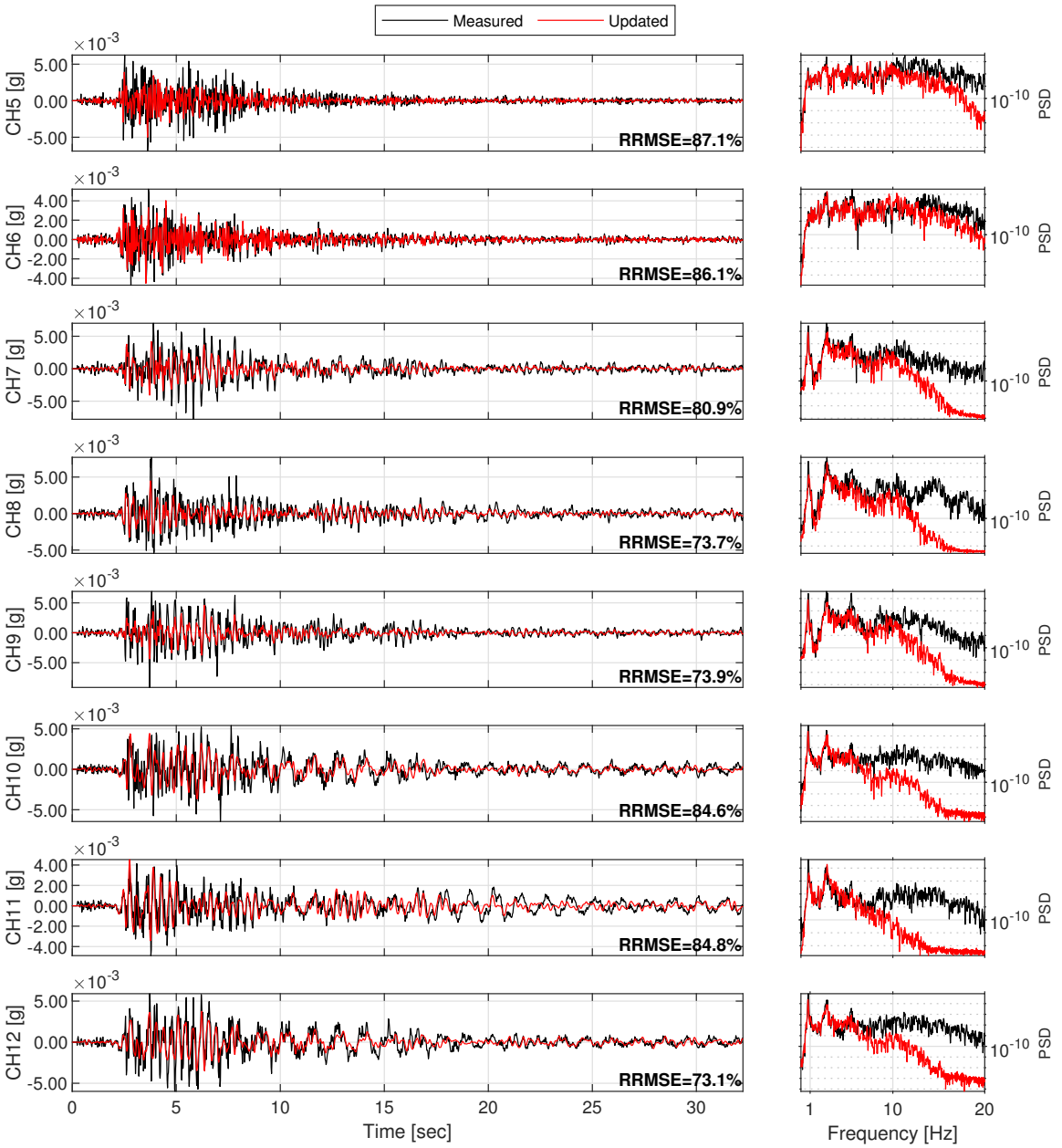

Figure D.88: Structural response comparison for seismic event #90.

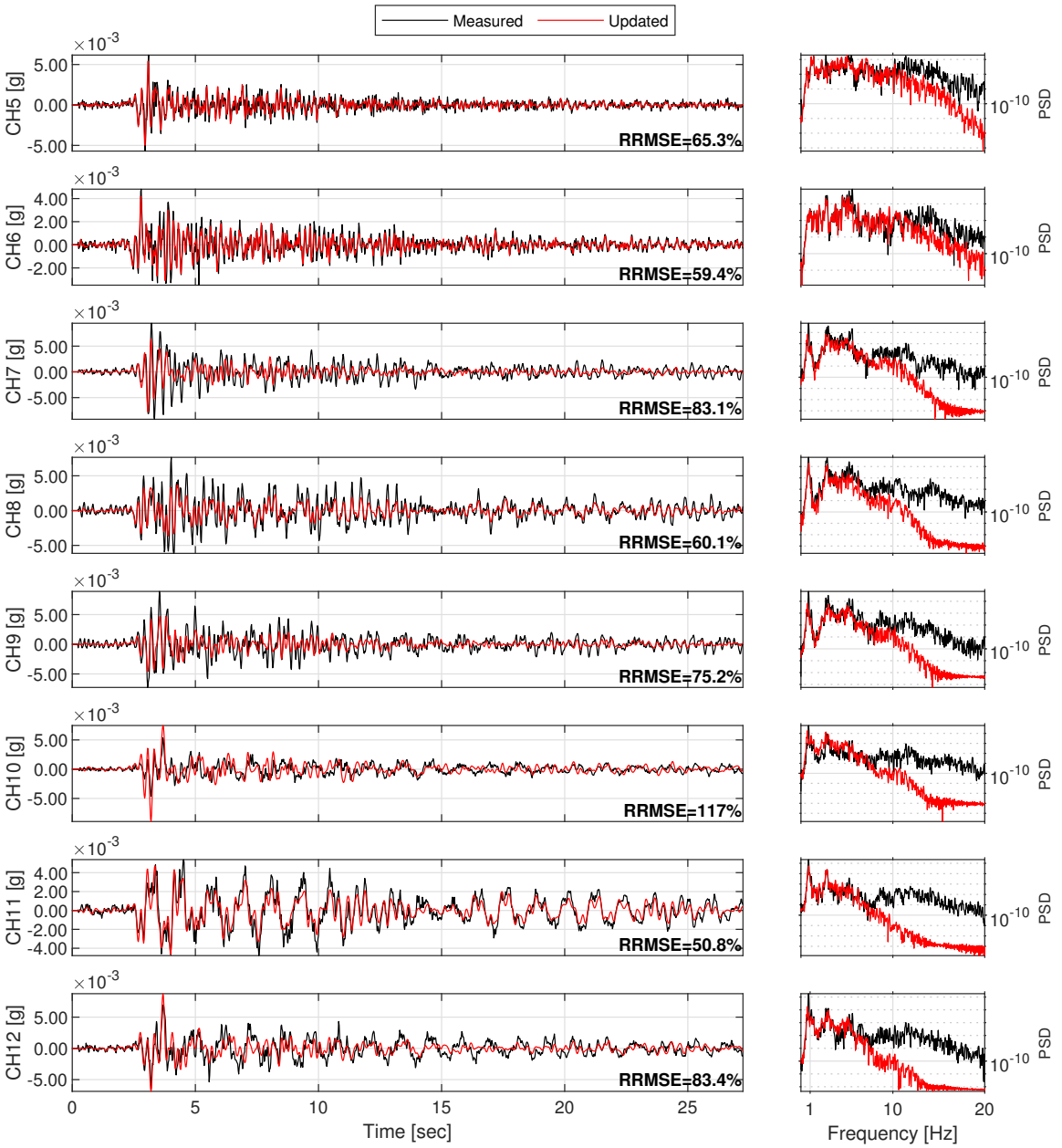

Figure D.89: Structural response comparison for seismic event #91.

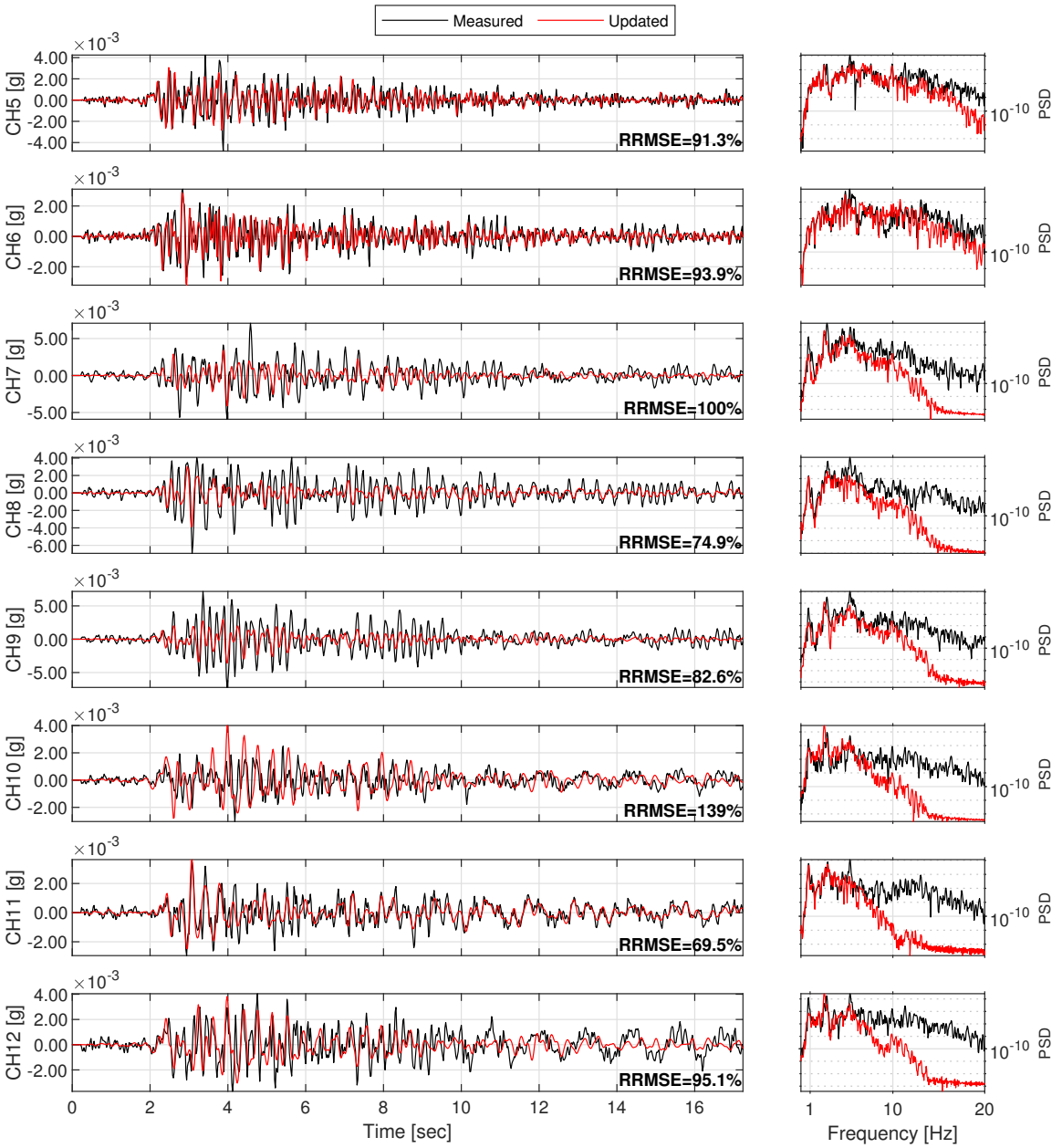

Figure D.90: Structural response comparison for seismic event #92.

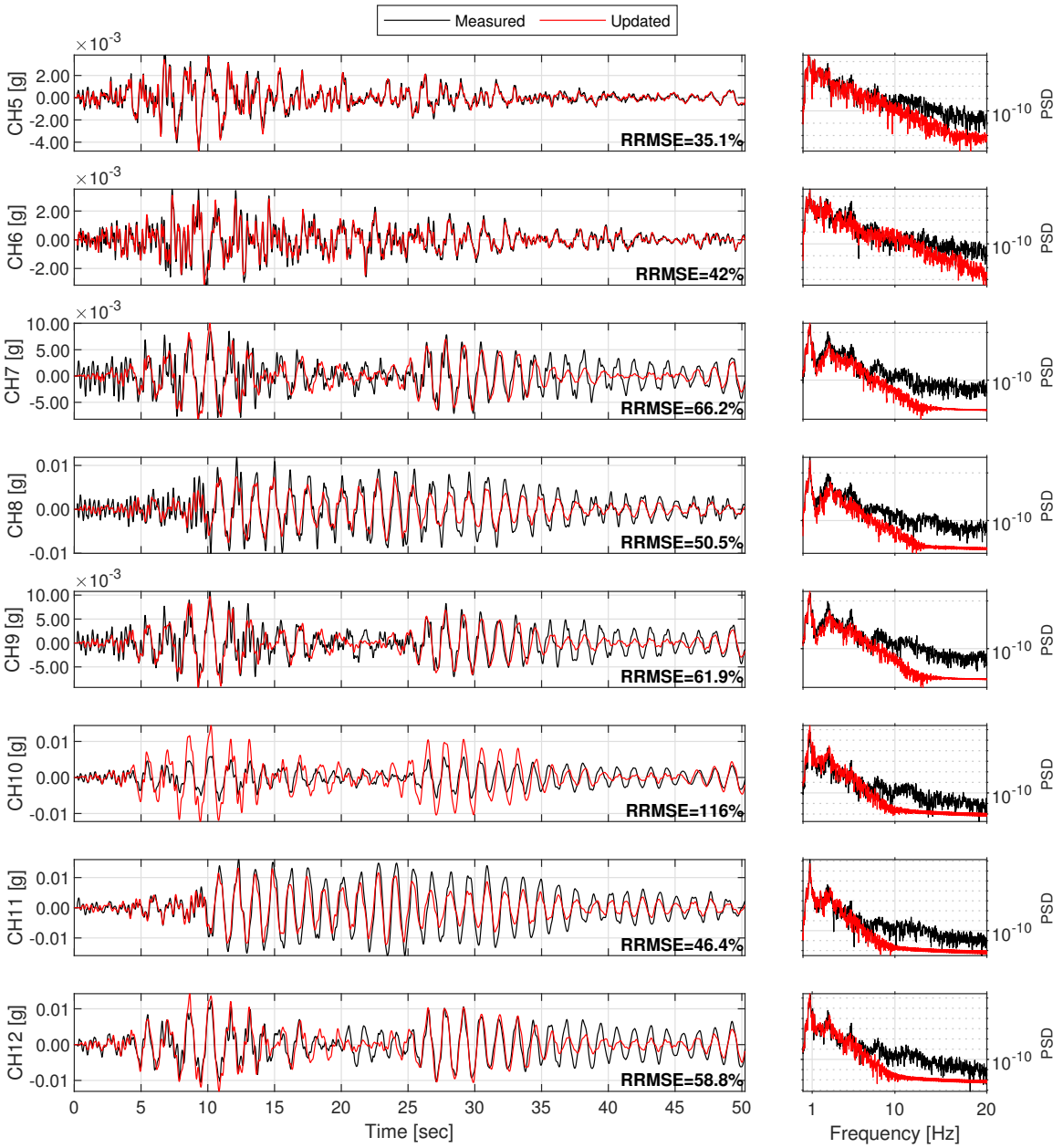

Figure D.91: Structural response comparison for seismic event #93.

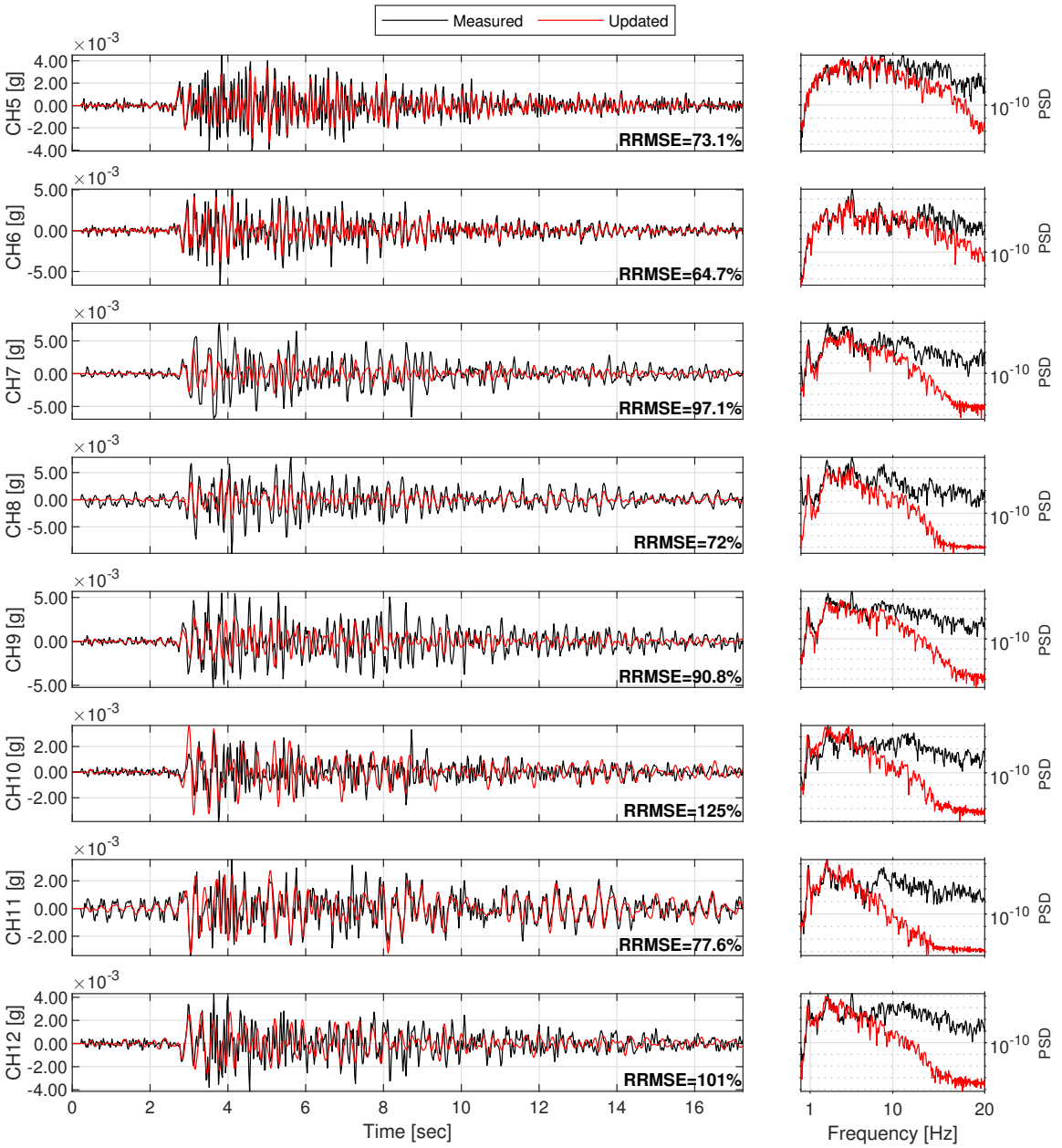

Figure D.92: Structural response comparison for seismic event #94.

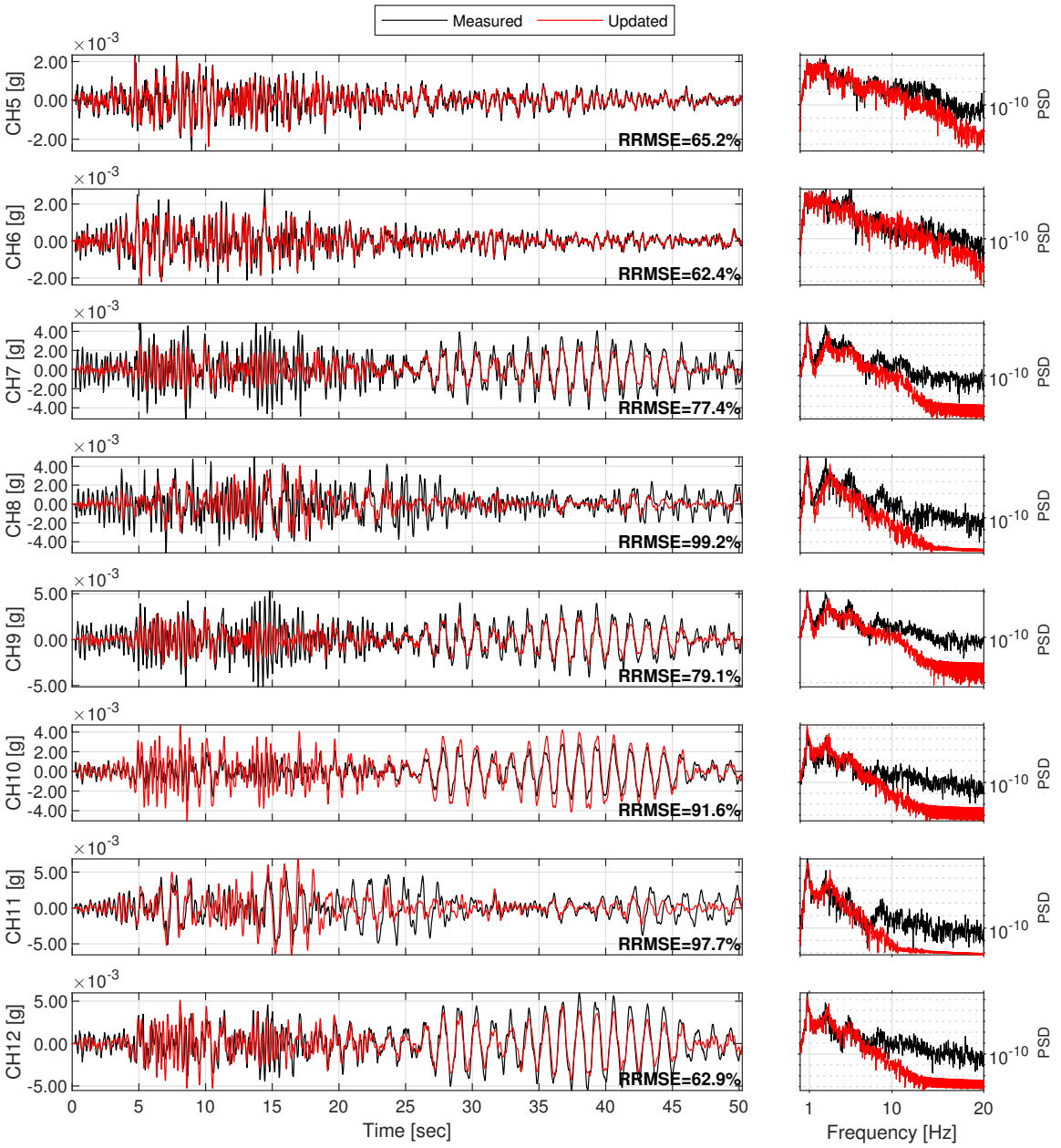

Figure D.93: Structural response comparison for seismic event #95.

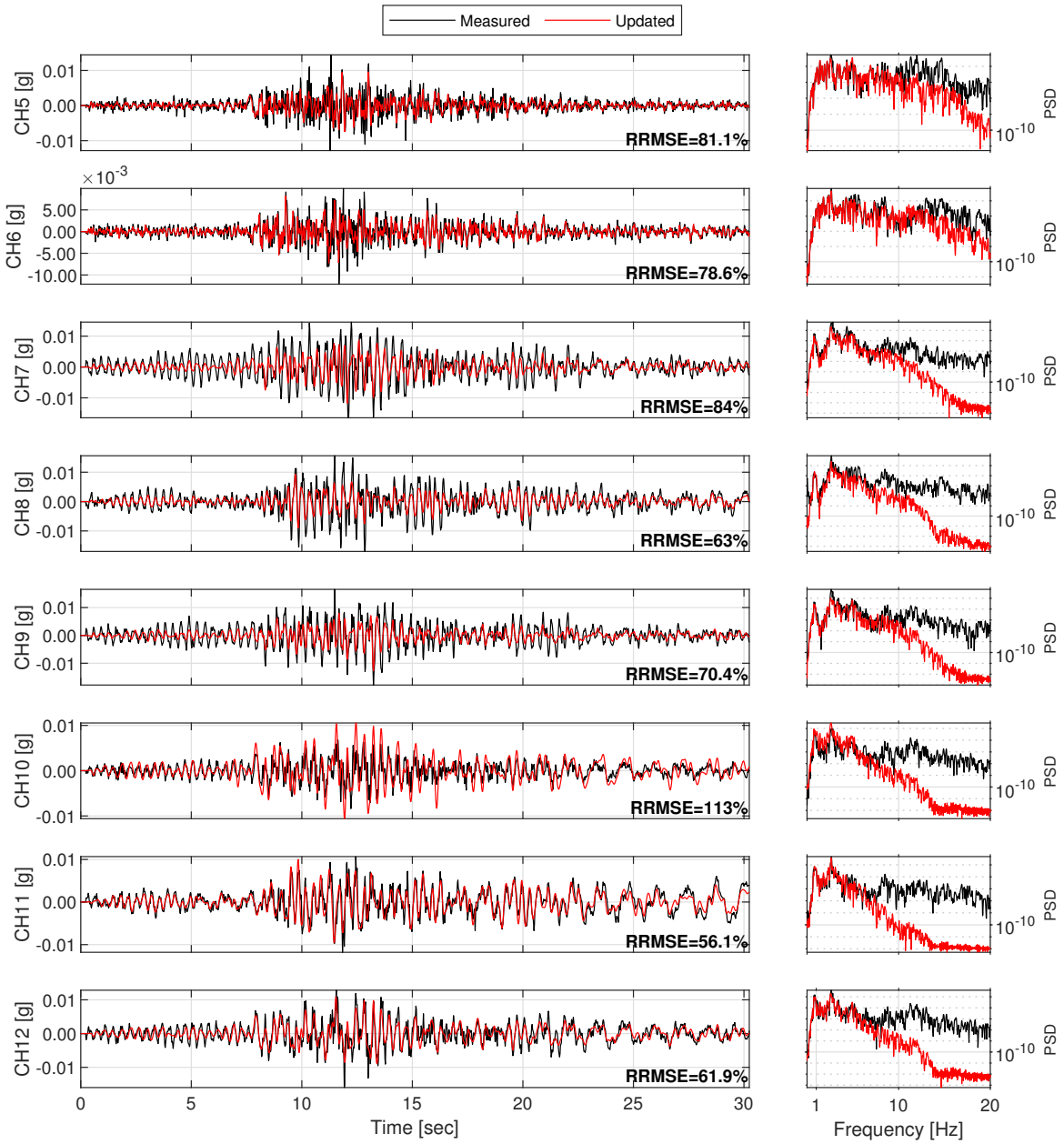

Figure D.94: Structural response comparison for seismic event #96.

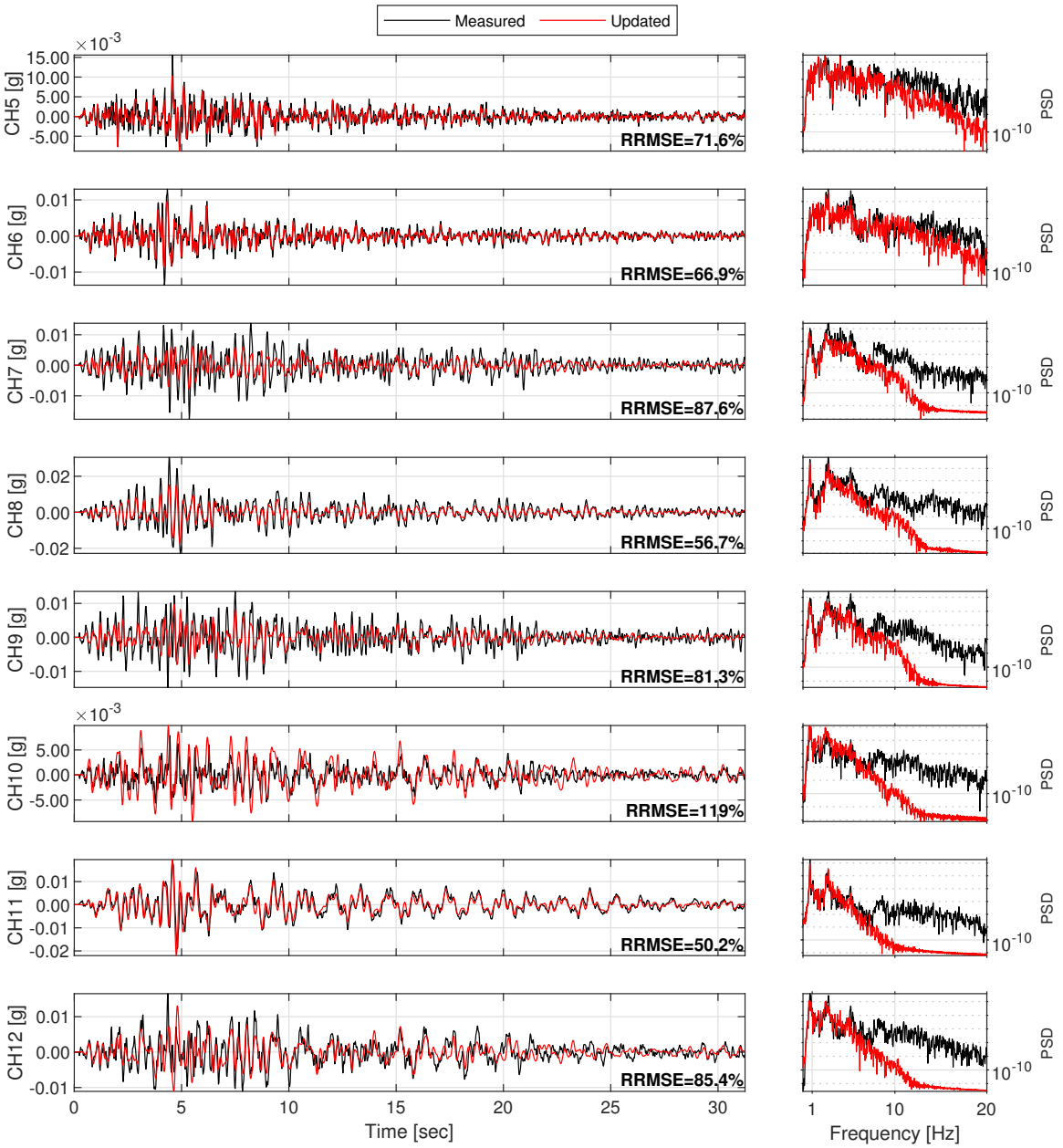

Figure D.95: Structural response comparison for seismic event #97.

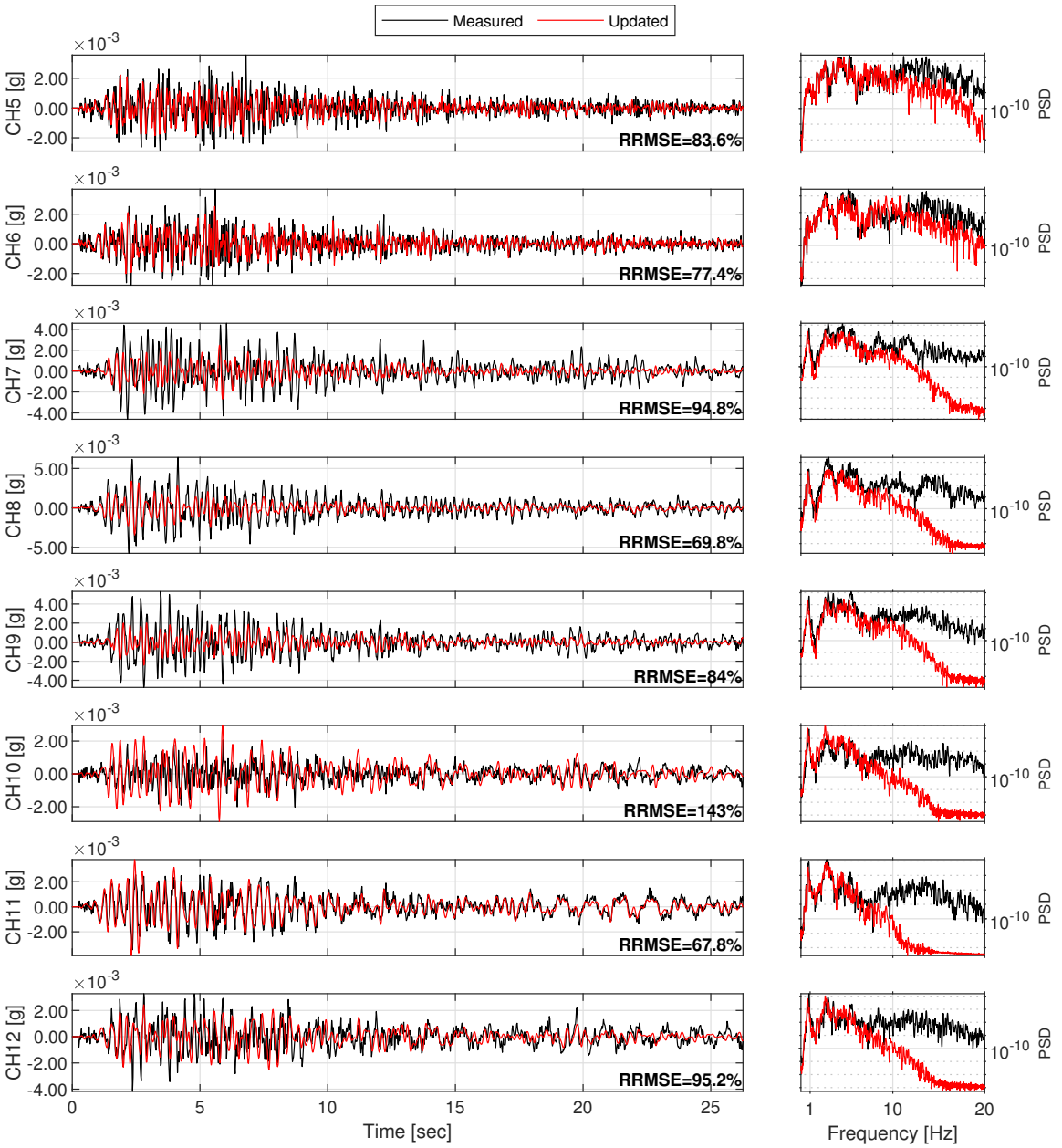

Figure D.96: Structural response comparison for seismic event #98.

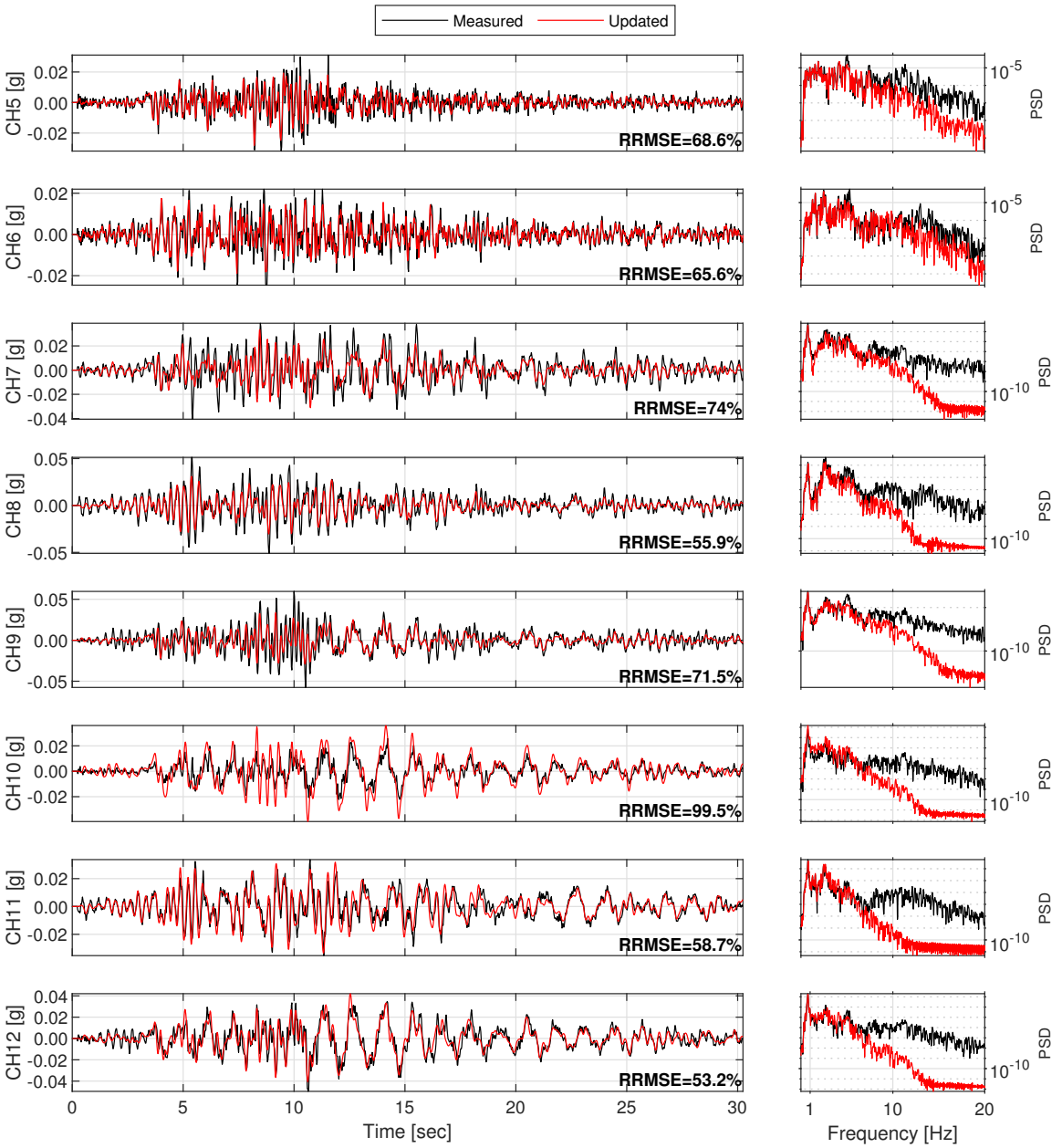

Figure D.97: Structural response comparison for seismic event #99.

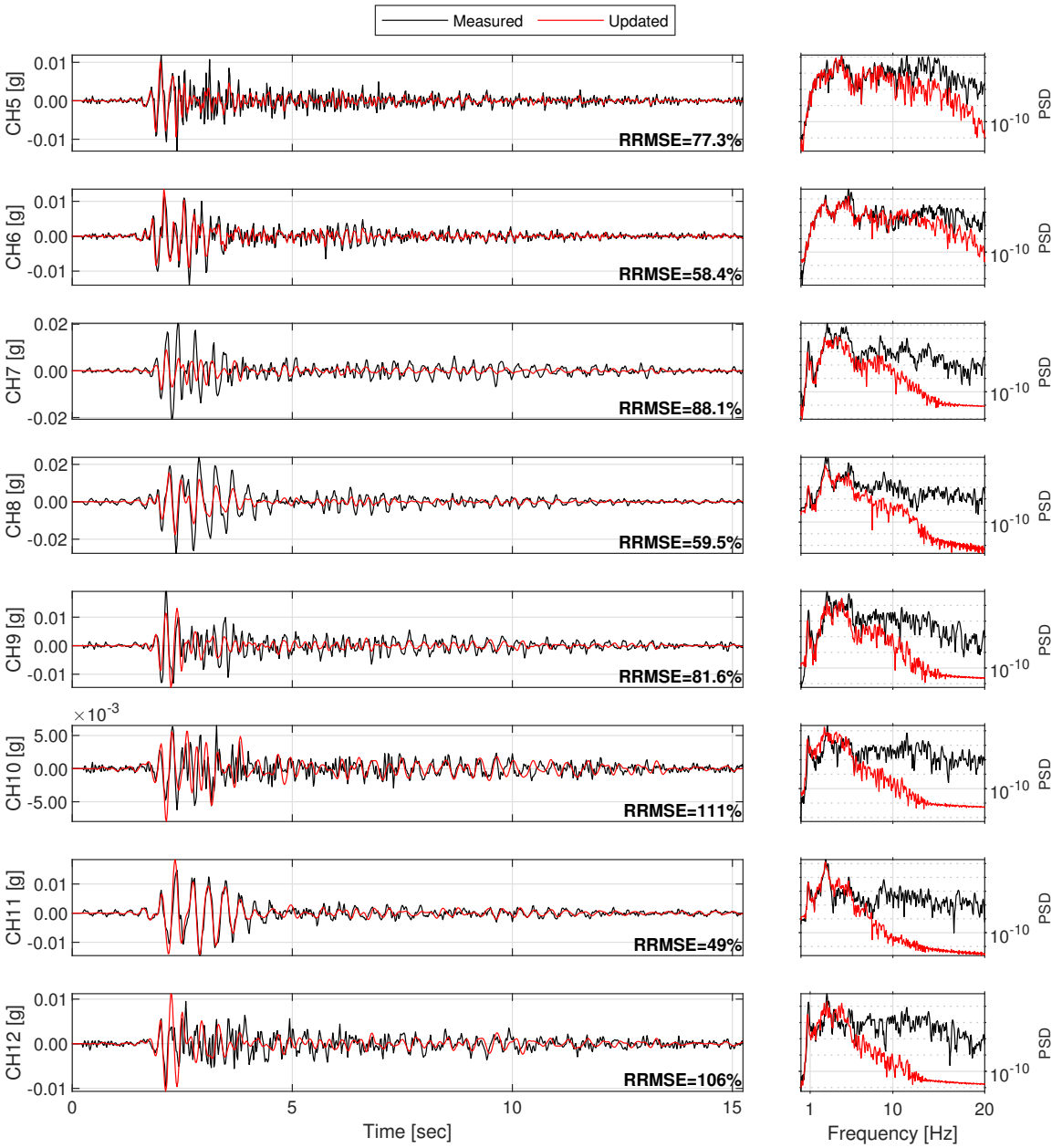

Figure D.98: Structural response comparison for seismic event #100.

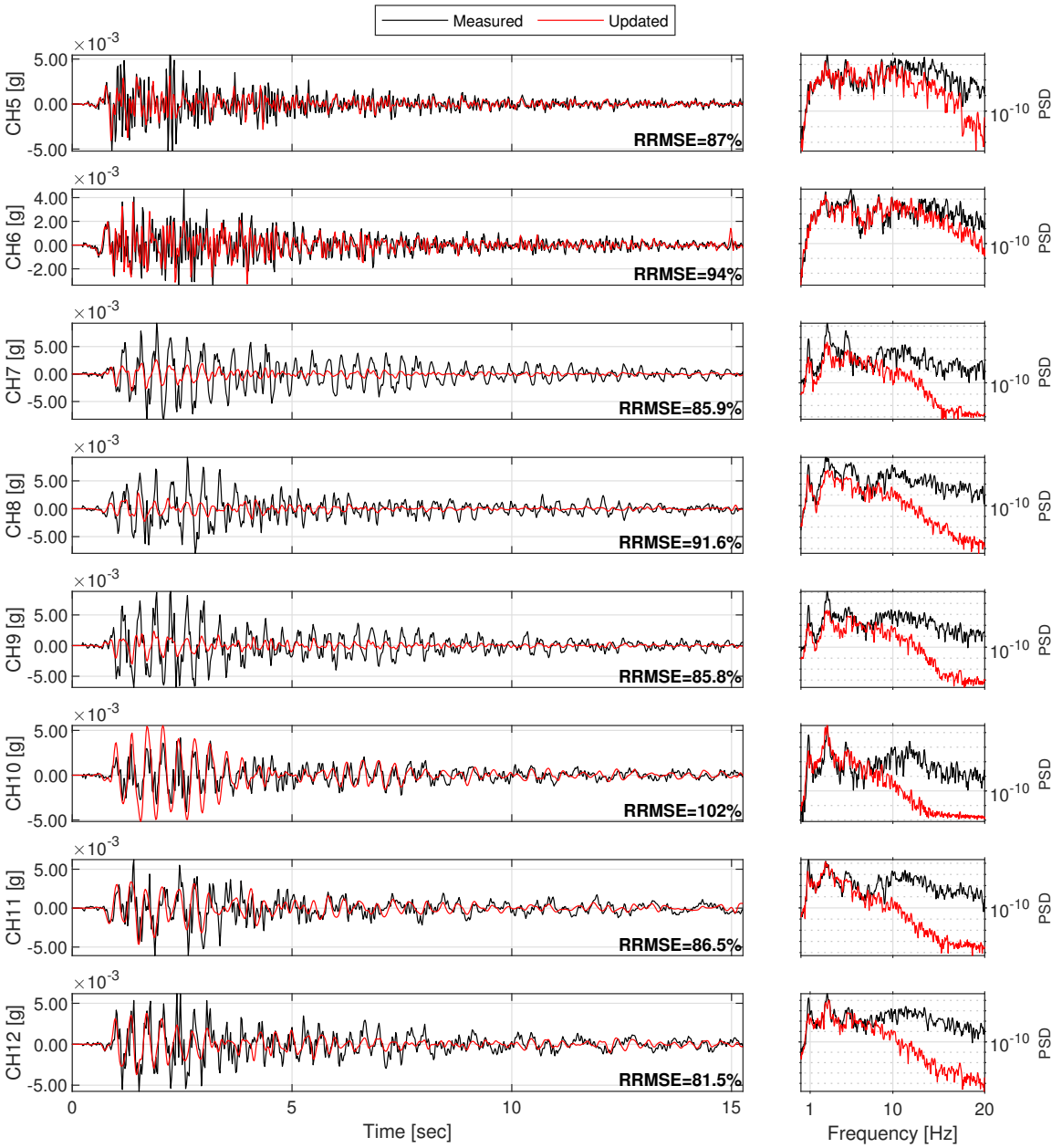

Figure D.99: Structural response comparison for seismic event #101.